



UNIVERSITÀ
DEGLI STUDI
DI PADOVA

UNIVERSITA' DEGLI STUDI DI PADOVA

Dipartimento di Ingegneria Industriale DII

Corso di Laurea in Ingegneria dell'Energia Elettrica

**Magnetic and thermal analysis of an internal permanent magnet motor
and a wound-rotor synchronous motor for automotive applications**

Relatore: Prof. Nicola Bianchi

Gambaretto Cristian 1197564

Anno Accademico 2019/2020

*Ai miei genitori e alla mia famiglia,
per avermi supportato in questi anni di studio.*

Sommario

Il corrente elaborato è composto di 6 parti fondamentali.

- **Capitolo 1, Introduzione**

In questa parte preliminare sono introdotte le problematiche derivanti dall'uso dei magneti permanenti composti di terre rare nei motori IPM. Le terre rare sono degli elementi metallici appartenenti al gruppo dei lantanoidi; essi trovano applicazione in moltissime tecnologie legate all'elettronica e all'informatica oltre che nei motori elettrici. L'estrazione delle terre rare e la loro lavorazione è molto dispendiosa sia da un punto di vista economico sia per l'impatto ambientale correlato. Le terre rare si trovano infatti disperse in piccole quantità in aree molto estese richiedendo enormi miniere a cielo aperto per essere estratte in quantità considerevoli; inoltre la lavorazione necessaria per renderle utilizzabili richiede l'uso di sostanze molto inquinanti quali l'acido cloridrico e l'idrossido di sodio e avviene ad elevate temperature (>1000 °C). Attualmente l'estrazione delle terre rare è quasi esclusivamente monopolio cinese, per questo motivo il loro prezzo è molto volatile e impatta pesantemente sul costo del prodotto finale (fino al 40 % nei motori IPM). Per tali ragioni la tendenza degli ultimi anni è di utilizzare quantità sempre minori dei suddetti materiali nei motori elettrici per la trazione o addirittura eliminarli del tutto, pur mantenendo le eccellenti prestazioni esibite da questi. Nel proseguo della tesi, dopo una breve panoramica sulle alternative proposte in letteratura, si decide di confrontare le prestazioni di un motore con magneti alle terre rare e un motore con rotore avvolto.

- **Capitolo 2, Motore IPM**

Viene presentato il motore a magneti permanenti interni (IPM) nelle sue caratteristiche generali quali disposizione dei magneti nel rotore, equazioni costitutive e strategia di controllo per la trazione. Una sezione è dedicata ai magneti permanenti, sono illustrati i principi di funzionamento e le caratteristiche fondamentali dei più utilizzati a livello industriale. Viene poi analizzato, tramite software agli elementi finiti, un motore IPM basato sul Lexus LS 600h, viene svolta l'analisi a vuoto per determinare l'induzione al traferro, i flussi concatenati e la f.e.m. indotta. Si procede poi con l'analisi a carico in cui viene mostrata la mappa delle correnti d e q, sono ricavate le traiettorie di corrente in MTPA, deflussaggio ed MTPV. Viene poi calcolata la coppia meccanica erogata al variare della posizione rotorica individuando la coppia media e la componente di ripple. Successivamente sono tracciate le caratteristiche meccaniche, sia in coppia che potenza, per vari valori di corrente oltre alla mappa dei punti di lavoro della macchina. Per concludere sono calcolate tutte le fonti di perdita e la mappa del rendimento.

- **Capitolo 3, WRSM**

Viene presentato il motore sincrono con rotore avvolto (WRSM) nelle sue caratteristiche generali quali equazioni costitutive e strategia di controllo per la trazione. Particolare attenzione viene posta su quest'ultimo aspetto in quanto la possibilità di variare la corrente di eccitazione (e quindi il flusso principale) permette di ottenere una maggiore libertà di

controllo. Nella successiva sezione vi è il progetto del rotore avvolto, svolto mediante formule empiriche e relazioni approssimate e poi ottimizzato tramite un semplice studio agli elementi finiti. Viene poi analizzato il motore ottenuto e un'altra variante con polo di rotore più stretto, ricalcando quanto già fatto con il motore IPM. Si conclude che la configurazione a polo più largo non è vantaggiosa in quanto caratterizzata da elevate perdite di eccitazione a causa della ridotta sezione di rame disponibile. Dopo il calcolo delle perdite e la mappa del rendimento il motore IPM e il WRSM sono messi a confronto. Si conclude come il WRSM possa essere un buon sostituto dell'IPM nella trazione elettrica.

- **Capitolo 4, Calcolo delle perdite meccaniche**

Sono analizzate nel dettaglio le perdite meccaniche dei motori sotto analisi, in particolare si suddividono le fonti di perdita in: perdite nei cuscinetti e perdite per ventilazione. Le prime sono studiate mediante delle relazioni analitiche e le tabelle dei costruttori mentre le seconde sono analizzate sia mediante un modello analitico sia mediante una simulazione fluidodinamica agli elementi finiti (Ansys fluent). Si osserva come le perdite nei cuscinetti siano trascurabili rispetto alle altre mentre quelle di ventilazione assumono un peso molto rilevante, soprattutto nel WRSM. I risultati ottenuti dal modello analitico e dalla simulazione numerica sono messi a confronto mostrandosi in ottimo accordo.

- **Capitolo 5, Analisi termica**

Viene svolta l'analisi termica delle macchine in esame. Il raffreddamento di statore e rotore sono analizzati separatamente; per il primo si adotta una camicia ad acqua esterna mentre per il secondo un albero cavo anch'esso raffreddato ad acqua. I due sistemi sono studiati sia mediante un modello analitico sia mediante una simulazione termofluidodinamica svolta nuovamente con Ansys fluent. I due approcci portano a dei risultati tra loro coerenti e il sistema di raffreddamento statorico si rivela adeguato. Il raffreddamento rotorico non si rende necessario nel motore IPM mentre risulta essenziale nel WRSM.

- **Capitolo 6, Conclusioni**

Si riassumono brevemente vantaggi e svantaggi di entrambe le topologie analizzate individuando per quali applicazioni siano maggiormente indicate.

Contents

1	Introduction	11
2	IPM motor	17
2.1	IPM general features	17
2.1.1	Permanent magnet	21
2.2	IPM analysis	25
2.2.1	No load analysis	28
2.2.2	Inductances	33
2.2.3	On load analysis	35
2.2.4	Losses	44
3	Wound-rotor synchronous motor	53
3.1	Working principles	54
3.2	Excitation system	58
3.2.1	Brushes and slip-ring	58
3.2.2	Rotary transformer	59
3.2.3	Comparison	62
3.3	WRSM rotor design	62
3.4	WRSM analysis	68
3.4.1	No load analysis	68
3.4.2	Inductances	72
3.4.3	On load analysis	75
3.4.4	Losses	86
3.5	Comparison	89
3.5.1	Cost estimation	92
4	Mechanical losses computation	95
4.1	Bearing losses	96
4.1.1	Analytical model	97
4.2	Windage losses	100
4.2.1	Analytical model	100
4.2.2	Numerical model	101
4.2.3	Comparison	103
5	Thermal analysis	109
5.1	Introduction to convective heat transfer	110
5.1.1	General features	110
5.1.2	Internal flows	113
5.2	Stator cooling system analysis	118

5.2.1	Analytical model	121
5.2.2	Numerical model	126
5.2.3	Comparison	130
5.2.4	Stator thermal analysis	131
5.3	Thermal transient	133
5.3.1	Conduction model	133
5.3.2	Numerical model	135
5.3.3	Analytical model	140
5.4	Rotor cooling	144
5.4.1	IPM motor rotor	144
5.4.2	WRSM rotor cooling	150
6	Conclusion	161

List of Figures

1.1	Average price per kilogram or tons in U.S. dollars of some rare earth metals . . .	12
1.2	Most promising topologies [19]	13
1.3	Comparison of performance of various rare earth-free magnets	15
2.1	Magnets possible positioning, PM are colored in purple	18
2.2	Working limits of IPM motor	20
2.3	Working limits of IPM motor, MTPA and MTPV in evidence [31]	21
2.4	Typical IPM torque versus speed with MTPV region [31]	21
2.5	B-H characteristic of a PM	22
2.6	Demagnetization point (knee)	23
2.7	Variation of B_{rem} and H_c with temperature	23
2.8	B-H characteristic for most used PMs	24
2.9	B-H curve	26
2.10	Geometry built in FEMM	27
2.11	Boundary conditions imposed	27
2.12	Phase a axis and rotor d-axis	28
2.13	Airgap flux density, the effect of slot openings is evident	29
2.14	Main flux density harmonics	29
2.15	Cogging torque computed in two ways	30
2.16	Linkage fluxes	31
2.17	Linkage flux armonics	31
2.18	No-load phase back electromotive force	32
2.19	Flux density map	32
2.20	d-axis apparent inductance	33
2.21	q-axis apparent inductance	34
2.22	Saliency ratio versus current	34
2.23	Numerical MTPA (green) and analytical MTPA (light blue)	35
2.24	Numerical MTPV (blue) and analytical MTPV (red)	36
2.25	MTPA (green) and MTPV (blue) loci	36
2.26	Torque versus rotor position at overload current $\hat{I} = 800 A$	37
2.27	Torque versus rotor position at $\hat{I} = 560 A$	38
2.28	Torque versus rotor position at nominal current $\hat{I} = 400 A$	38
2.29	Flux density map at $\hat{I} = 400 A$	39
2.30	Control stratagy at $\hat{I} = 800 A$	40
2.31	Current versus rotational speed	40
2.32	Torque versus rotational speed	41
2.33	Power versus rotational speed	41
2.34	Current levels analyzed	42
2.35	Torque versus rotational speed for various current levels	42

LIST OF FIGURES

2.36	Power versus rotational speed for various current level	43
2.37	IPM working points	43
2.38	FEMM model	44
2.39	Current density distribution at $\hat{I} = 400 A$	45
2.40	Resistance versus frequency	46
2.41	Joule losses distribution	46
2.42	Specific losses as function of B and f	47
2.43	Iron losses distribution	48
2.44	Mechanical losses distribution	48
2.45	Gemetry built in FEMM, notice the stator linear current density	50
2.46	Magneto motive force wave shape and harmonic spectrum	50
2.47	Flux lines due to MMF harmonics	51
2.48	Efficiency map	51
3.1	Wound-rotor	54
3.2	WRSM control zones [18]	55
3.3	Center of voltage ellipses outside the current limit	56
3.4	Power versus speed for decreasing excitation current	57
3.5	Power versus speed with optimal control	57
3.6	Slip-rings and brushes keyed on the rotor [37]	58
3.7	Integration concept of a rotary transformer inside a wound-rotor synchronous machine	59
3.8	Rotary transformer configurations	60
3.9	Adjacent winding [16]	60
3.10	Coaxial winding [16]	61
3.11	Resonant compensation circuit [17]	61
3.12	Torque and excitation current density versus pole length	64
3.13	Gemetries build in FEMM	65
3.14	Excitation winding	66
3.15	Current density versus current	67
3.16	Losses versus current	67
3.17	Geometries simulated in FEMM	68
3.18	Linkage flux versus excitation current	69
3.19	Airgap flux density	69
3.20	Airgap flux density harmonics	70
3.21	Cogging torque	70
3.22	Linkage fluxes	71
3.23	Linkage flux armonics	71
3.24	No-load phase back electromotive force	72
3.25	Flux density map	72
3.26	d-axis apparent inductance versus d-axis current	73
3.27	q-axis apparent inductance versus q-axis current	73
3.28	Saliency ratio versus current	74
3.29	d-q current plane, numerical MTPA (green) and analytical MTPA (light blue) at $I_{exc} = 600 A$	75
3.30	d-q current plane, numerical MTPV (blue) and analytical MTPV (red) at $I_{exc} = 600 A$	75
3.31	Numerical MTPA (green) and numerical MTPV (blue) at $I_{exc} = 600 A$	76
3.32	Torque at $I_{exc} = 1000 A$ and $\hat{I} = 800 A$	76
3.33	Torque at $I_{exc} = 800 A$ and $\hat{I} = 800 A$	77

3.34	Torque at $I_{exc} = 600 A$ and $\hat{I} = 800 A$	77
3.35	Flux density map at $I_{exc} = 1000 A$ and $\hat{I} = 800 A$	78
3.36	Current control path	78
3.37	Torque versus speed	79
3.38	Power versus speed	79
3.39	Current versus speed	80
3.40	Map of the working points	80
3.41	Current versus speed for varius current limits	81
3.42	Torque versus speed for varius current limits	82
3.43	Power versus speed for varius current limits	82
3.44	Torque versus speed for varius current limits	83
3.45	Power versus speed for varius current limits	83
3.46	Stator current magnitude	84
3.47	Control currents for cosfi=1 strategy	85
3.48	Joule losses distribution	86
3.49	Iron losses distribution	87
3.50	Mechanical losses distribution	87
3.51	Excitation losses distribution	88
3.52	Efficiency map	89
3.53	Torque versus speed comparison at $\hat{I} = 400 A$	90
3.54	Power versus speed comparison at $\hat{I} = 400 A$	90
3.55	Torque versus speed comparison at $\hat{I} = 260 A$	91
3.56	Power versus speed comparison at $\hat{I} = 260 A$	91
3.57	Efficiency map at $\hat{I} = 400 A$	92
4.1	High and low pressure zones created when a car moves	95
4.2	A cylindrical roller bearing [10]	96
4.3	Components contributing to the weight of rotor	98
4.4	Bearing losses: IPM versus WRSM	100
4.5	IPM geometry in Ansys	103
4.6	WRSM geometry in Ansys	103
4.7	Comparison between Ansys results and analitical results	104
4.8	Slotted IPM versus smooth stator IPM	104
4.9	Windage losses: IPM versus WRSM	105
4.10	IPM arrow plot at $n = 20000 rpm$	106
4.11	IPM velocity contour plot at $n = 20000 rpm$	106
4.12	WRSM arrow plot at $n = 20000 rpm$	107
4.13	WRSM velocity contour plot at $n = 20000 rpm$	107
4.14	Mechanical losses: IPM versus WRSM	108
5.1	Flow over a flat plane	110
5.2	Moody diagram	113
5.3	Thermal entrace region	114
5.4	h coefficient along thermal entrace region	114
5.5	Differential control volume	115
5.6	Axial temperature variations for heat transfer in a tube with constant heat flux	116
5.7	Axial temperature variations for heat transfer in a tube with constant surface temperature	117
5.8	Cooling frame geometry	118
5.9	Stator total losses at every working point	119

LIST OF FIGURES

5.10	Comparison on Nusselt number	121
5.11	Comparison on h coefficient	121
5.12	Temperature difference between intel and outlet	122
5.13	Reynolds number versus water mean velocity	122
5.14	Pressure drop	123
5.15	Power needed	123
5.16	Temperature distribution in the tube	124
5.17	Fluid temperature for varius tube surface temperature	125
5.18	Surface temperature calculation	125
5.19	Surface temperature calculation	126
5.20	Gemetry built in DesignModeler	127
5.21	Internal surface temperature distribution	129
5.22	Water streamlines	130
5.23	Thermal model and boundary conditions	132
5.24	Stator temperature distribution	133
5.25	Electric circuit for charging of a capacitor	134
5.26	Temperature (or voltage) versus time	135
5.27	Geometry simulated in Ansys and boundary conditions	136
5.28	Temperature distribution for the first condition	137
5.29	Maximum temperature versus time at $T = 241 Nm$ and $n = 5000 rpm$	137
5.30	Minimum temperature versus time at $T = 241 Nm$ and $n = 5000 rpm$	138
5.31	Temperature distribution at $\hat{I} = 682 A$ and $n = 20000 rpm$	138
5.32	Temperature versus time at $T = 46 Nm$ and $n = 20000 rpm$	139
5.33	Minimum temperature versus time at $T = 46 Nm$ and $n = 20000 rpm$	139
5.34	Thermal network	140
5.35	Temperature versus time for different parts of the stator	141
5.36	Comparison between Ansys and the equivalent thermal network, first condition	142
5.37	Comparison between Ansys and the equivalent thermal network, second condition	143
5.38	3D model simulated in Ansys	145
5.39	IPM rotor surface temperature distribution	146
5.40	Velocity arrow plot	146
5.41	Air gap temperature	147
5.42	FEMM model of the IPM rotor	148
5.43	Rotor temperature distribution	149
5.44	WRSM rotor 3D model built in DesignModeler	150
5.45	WRSM rotor surface temperature distribution	151
5.46	Velocity arrow plot	151
5.47	Air gap temperature	152
5.48	Hollow shaft for rotor cooling	153
5.49	Complete cooling system	153
5.50	Geometry built in DesignModeler	154
5.51	Shaft surface temperature distribution	155
5.52	Velocity stramlines	155
5.53	Analytical model	156
5.54	Heat flux removed versus shaft surface temperature	157
5.55	Geometry simulated in FEMM and boundary conditions	158
5.56	Rotor temperature distribution	159

List of Tables

2.1	Main properties of hard magnetic material	24
2.2	Initial data	25
2.3	Stator data	25
2.4	Rotor data	25
2.5	Magnet data	26
2.6	Parameters imposed in FEMM	50
3.1	Rotary transformer versus brushes and slip-ring	62
3.2	Poles main dimensions	64
3.3	Ribbon characteristics	65
3.4	Excitation net surface	65
3.5	Excitation main dimensions	66
3.6	Material price per kg	92
3.7	Material weight in the two motors	93
4.1	Friction coefficient $k_{bearing}$	97
4.2	IPM motor volumes	98
4.3	IPM motor mass weight	98
4.4	Narrow pole WRSM volumes	99
4.5	Narrow pole WRSM mass weight	99
4.6	Large pole WRSM volumes	99
4.7	Large pole WRSM mass weight	99
5.1	Frames main dimensions	119
5.2	Losses for two working points	120
5.3	Initial conditions	126
5.4	Comparisons	130
5.5	Thermal classes and their maximum temperature	131
5.6	Source losses in FEMM	132
5.7	Study conditions	136
5.8	Thermal network parameters	141
5.9	Sources	141
5.10	Initial conditions	145
5.11	Thermal analysis results	147
5.12	Material properties imposed in FEMM simulation	148
5.13	Initial conditions	150
5.14	Thermal analysis results	152
5.15	Simulation data	154
5.16	Rotor cooling system main dimensions	154
5.17	Thermal analysis results	156

LIST OF TABLES

5.18 Comparison between numerical and analytical model	157
5.19 Material properties and heat sources	158

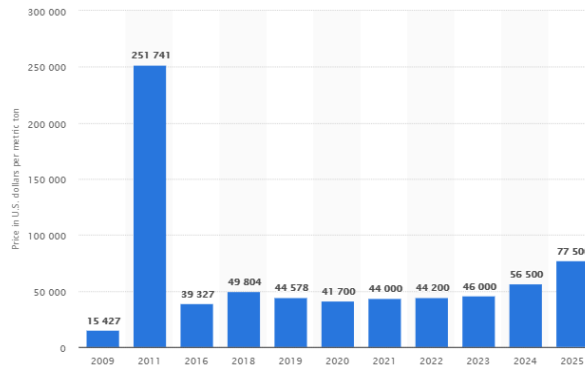
Chapter 1

Introduction

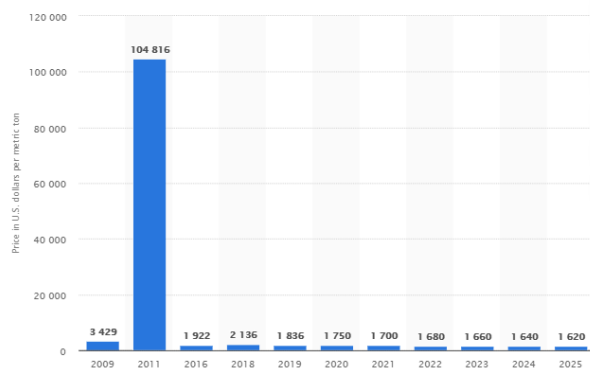
Over the years the interest in the application of electric motors to the automotive industry has increased exponentially. Electric motors in fact have considerable advantages compared to internal combustion engines, including:

- mechanical characteristic consisting of an area with constant torque for low (or even zero) speed and constant power for high speeds, excellent for traction;
- very high efficiency;
- possibility of energy recovery during braking and downhill (regenerative braking);
- very low noise;
- local emissions practically null;
- don't require clutches and gearboxes (or a very simple one);
- structurally much simpler and therefore less prone to failure.

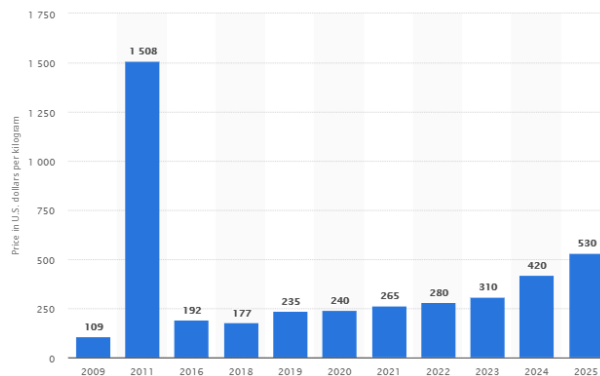
Among the many types of existing electric motors, those that have spreaded more in the automotive sector are internal permanent magnet motors (IPM). Among the many reasons, the most important are certainly the high torque and power density, the high efficiency and the possibility of operating in a very wide speed range [19]. Unfortunately, the permanent magnets most used for IPM motors are neodymium-iron-boron (NdFeB) and samarium-cobalt (SmCo). Neodymium and samarium are two metals belonging to the rare earth group which in the periodic table are part of the lanthanides. They are used in practically all electronic and computer applications making them indispensable for modern world. Although not as rare as the name implies, virtually all neodymium in the world market is exported from China (around 95 %), a majority of which comes from an area around Baotou in Inner Mongolia, China (around 65 %) [19]. Because of this monopoly, the price of neodymium is incredibly volatile; for example, in 2011 the price of neodymium rose by 1000 % in some months and then returned to the initial value in another few months. Even without such exaggerated price fluctuations the magnet determines about 25-40 % of the cost of the motor. The same criticalities can also be identified for samarium. In addition to the aforementioned neodymium and samarium, there is another widely used rare earth metal called dysprosium (Dy). It belongs to the group of so-called "heavy rare earths" due to its high density ($8551 \frac{kg}{m^3}$) and it is used to enhance the magnet coercivity to avoid demagnetization under both high temperatures as well as high d-axis currents [27]. Dysprosium is one of the most expensive rare earth, even more than neodymium. Figure 1.1 shows the average prices per tons and an estimate for the future years in U.S. dollars of neodymium and samarium while dysprosium is indicated in U.S. dollars per kg [28].



(a) Neodymium



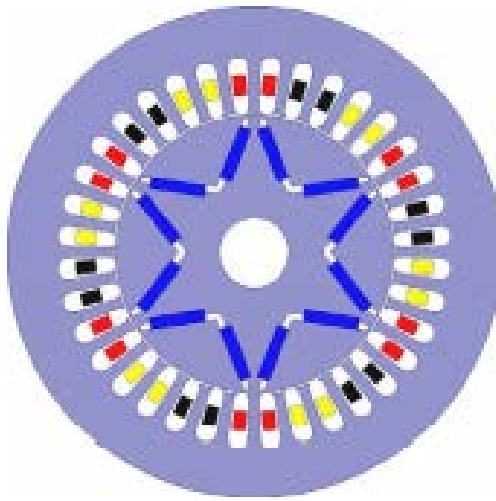
(b) Samarium



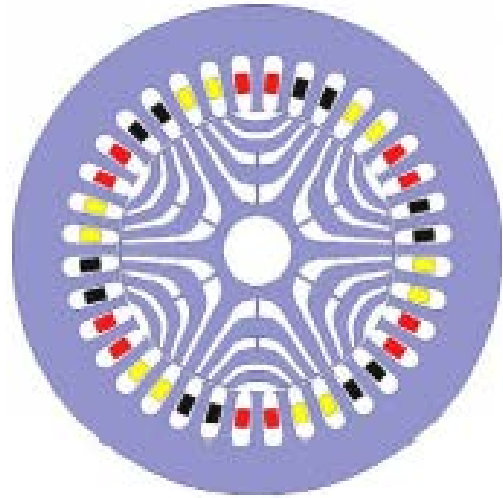
(c) Dysprosium

Figure 1.1: Average price per kilogram or tons in U.S. dollars of some rare earth metals

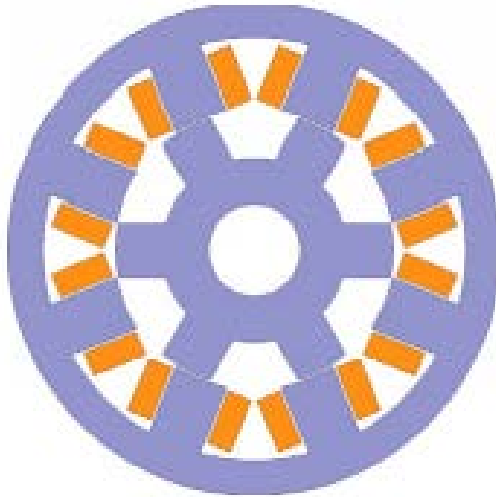
A second major problem is due to the environmental impact determined by the extraction of neodymium, samarium and dysprosium. In the first place, rare earths are rarely found concentrated in veins or deposits (as happens with other elements) but are dispersed in small quantities over very large areas. The mining therefore requires the excavation of a wide area and a geological damage of great impact. Furthermore, the extraction of rare earths from the minerals in which they are contained requires high temperatures ($\approx 1000\text{ }^\circ\text{C}$) and the use of very aggressive and polluting chemical compounds such as sulfuric acid, hydrochloric acid and sodium hydroxide [1]. For these reasons, looking for alternatives that do not use permanent magnets in electric motors but which still manage to maintain all the characteristics required in the automotive application has become of primary importance. Some alternative topologies are presented below.



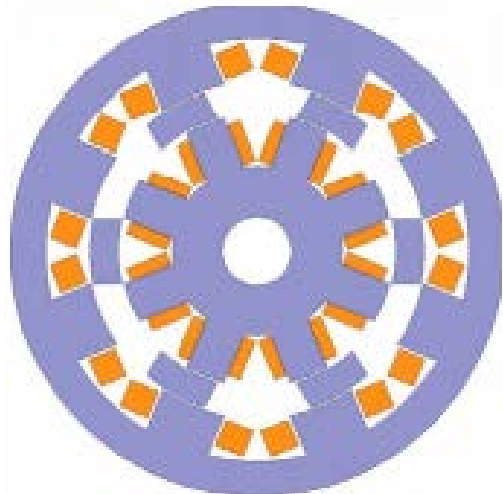
(a) Internal permanent magnet motor



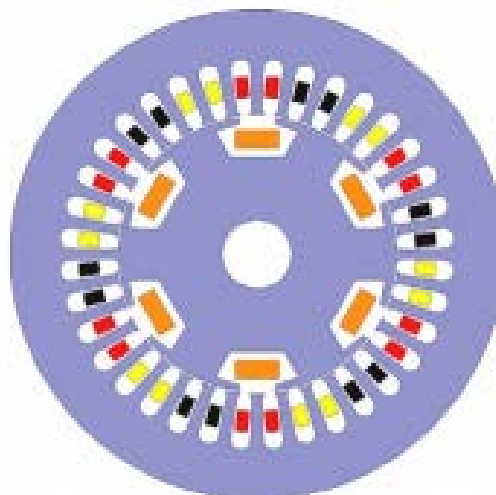
(b) Synchronous reluctance motor



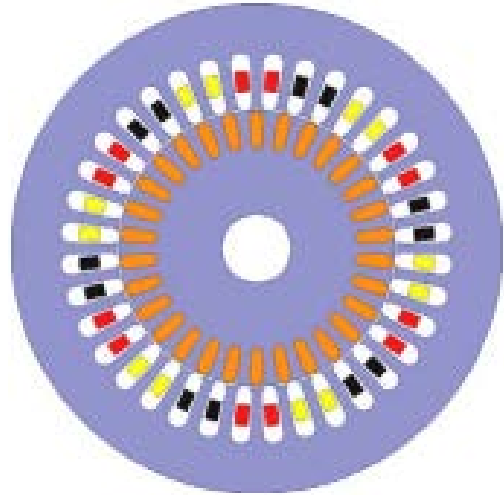
(c) Switched reluctance motor



(d) Double stator switched reluctance motor



(e) Electrically excited synchronous motor



(f) Induction motor

Figure 1.2: Most promising topologies [19]

- (a) IPM, the magnetizing flux is produced by the permanent magnets mounted on the rotor, it is characterized by high torque and power density and by a high efficiency. It is currently the most used topology in commercial cars, for example Toyota and Tesla use it;
- (b) synRM, The rotor does not have magnets or excitation, the whole torque is produced by the difference in reluctance between the d-axis and the q-axis. It is constructively very simple and therefore economic, it has a wide flux weakening zone and the possibility of always reaching an infinite theoretical speed. However, the torque density is not very high and the structural integrity of the rotor is a maior issues. Still it is one of the most promising PM-less topologies for electric vehicoles [19];
- (c) SRM, this machine typically has from two to five phases (Φ), $n \cdot \Phi$ poles and $n \cdot (\Phi + 1)$ stator teeth. This means that if one pole is aligned with a stator tooth, a total of n poles are aligned that way, while the other poles are more or less miss-aligned. The magnetic field is not rotating (as in the classic synchronous motors) but pulsating, that is, the stator windings are powered "in turn" in order to generate a constant torque, however the pulsating field causes a very high torque ripple. This type of topology has been known for a long time but lately it has increased in popularity thanks to the cheaper electronic converters. Land Rover used this type of topology [33];
- (d) DSSRM, works like the SRM, but with two stators, one outside the rotor and one inside the rotor. The rotor consists of a reluctance piece construction running in the gap between the two stators, the rotor pieces being pulled around by the pulses from both sides. The torque density is higher then the SRM while the ripple is lower, however the complex structure makes the machine very expensive;
- (e) EESM, the magnetizing flux is produced by DC powered windings and is therefore adjustable. This allows optimal control of the machine in all its operating areas without the risk of demagnetization. However, excitation losses reduce efficiency and make heat dissipation more problematic. In 2014, Renault was the only manufacturer with an EESM in the EV/HEV market [33]. Since in 2015 Renault Zoe was the number 2 most sold EV in Europe [19] and number 7 in the world so EESM is still represented in a fair amount of the total EV market;
- (f) IM, the magnetizing flux is produced by the stator and therefore does not require windings powered on the rotor which, for automotive applications, consists of an aluminum or copper squirrel cage. It is constructively simple and robust and has excellent performance both in terms of torque density and flux weakening area. On the other hand, however, it has lower efficiencies compared to synchronous motors due to losses in the rotor. It is widely used in the automotive industry for example it is mounted on: Renault Kangoo, Chevrolet Silverado, Daimler Chrysler Durango, BMW 5 and Tesla model S [33];

Another type of possible approach is to maintain the topology of the IPM motor by replacing the permanent magnets composed of rare earths (expecially dysprosium) with other more sustainable magnets; in particular, the most used are ferrite magnets. A ferrite is a ceramic material made by mixing and firing large proportions of iron oxide (Fe_2O_3 , rust) blended with small proportions of one or more additional metallic elements, such as barium, manganese, nickel, and zinc. They are electrically nonconductive, and ferrimagnetic. Ferrites can be divided into two families based on their resistance to being demagnetized (magnetic coercivity) [29].

- Hard ferrites have high coercivity, so are difficult to demagnetize. They are used to make permanent magnets for applications such as refrigerator magnets, loudspeakers, and electric motors;

- Soft ferrites have low coercivity, so they easily change their magnetization and act as conductors of magnetic fields. They are used in the electronics industry to make efficient magnetic cores called ferrite cores for high-frequency inductors, transformers and antennas, and in various microwave components.

Ferrite compounds are extremely low cost, being made of mostly rusted iron (iron oxide), and their production is much less polluting than rare earth magnets. Figure 1.3 shows the peak power of some motors with low (or zero) presence of rare earth magnets [30].

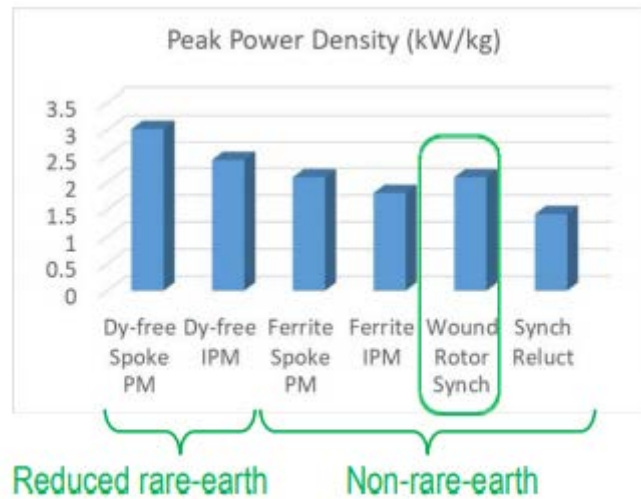


Figure 1.3: Comparison of performance of various rare earth-free magnets

Once again, WRSM proves to be very promising for automotive application.

Contents of the thesys

The main body of the thesis develops after the current introductory chapter and consists of 5 parts:

- In chapter 2 the operating and control principles of the IPM motor are briefly presented and then an IPM motor similar to the Lexus LS 600h motor is analyzed [32]. Both no-load and on-load analysis are performed, the mechanical characteristic is calculated and losses are also computed in detail. FEMM finite element software is used for greater accuracy.
- In chapter 3 the operating and control principles of the WRSM are briefly presented. A wound rotor is then designed to be inserted in the stator already used for the IPM motor and the motor thus obtained is analyzed in a similar way to what is done in chapter 1. Finally, the two motors are compared, highlighting the advantages and disadvantages of both. FEMM finite element software is used for greater accuracy.
- In chapter 4 the mechanical losses computation of the two motors presented is analyzed in detail. Both an analytical approach and a finite element analysis are proposed using the Ansys Fluent software.
- In chapter 5, after a brief introduction on the convection phenomenon, the thermal analysis of the two motors is presented. Both regime and transient operation is investigated.

Again both an analytical approach and a finite element analysis through Ansys Fluent are proposed.

- In chapter 6, the final conclusions are drawn.

Chapter 2

IPM motor

Electrical machines for automotive applications required some basic characteristics, i.e., high torque density and power density, wide operating speed range, high efficiency over wide speed and torque range, and intermittent overload capability for short durations. Therefore internal permanent magnet (IPM) machines are usually preferable choice for EVs for their excellent driving performance. The main flux is produced by some permanent magnets (PM) so there is no need of brushes or excitation systems and therefore the efficiency is very high. Also PM are very performing with high residual magnetization. However there are also several disadvantages:

- high working temperature degrade the magnetic performances of PM; in particular a lower residual magnetization and an higher chance of demagnetization;
- in order to achieve a wide constant power region the IPM is driven with a negative d-current that weakens the flux produced by PM, this means that the efficiency in this region is lower and there are higher chances of demagnetization of the PM;
- PM are composed by rare earth elements (i.e. Samarium and Neodimium) which are very expensive and their mining is very polluting.

2.1 IPM general features

IPM motors are composed by a stator where three phase windings are located and a rotor where there are several holes that host the magnets. Thanks to the fact that PM are inside the iron rotor an higher rotational speed and also more protection from demagnetization is achivable. Furthermore PM have a similar differential magnetic permeability to air so it is possible to use them also to increase the anisotropy of the rotor and consequently the reluctance torque. Figure 2.1 presents various arrangements for PM inside the rotor.

- (a) surface permanent magnets, (isotropic rotor);
- (b) inset PM, (anisotropic rotor);
- (c) salient pole, (isotropic/anisotropic rotor);
- (d) IPM, (anisotropic rotor);
- (e) spoke PM, (anisotropic rotor);
- (f) IPM, (anisotropic rotor);

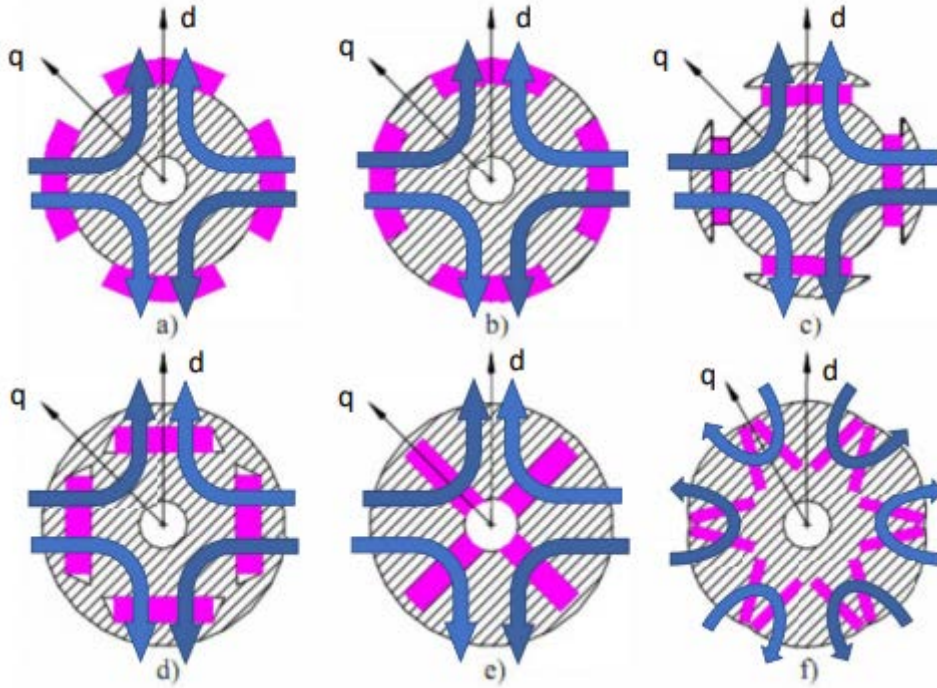


Figure 2.1: Magnets possible positioning, PM are colored in purple

Main equations

The governing equations of the IPM motor model are [31]

$$u_a(t) = R \cdot i_a(t) + \frac{d\Lambda_a(t)}{dt} \quad (2.1)$$

$$u_b(t) = R \cdot i_b(t) + \frac{d\Lambda_b(t)}{dt} \quad (2.2)$$

$$u_c(t) = R \cdot i_c(t) + \frac{d\Lambda_c(t)}{dt} \quad (2.3)$$

where:

- $i_a(t), i_b(t), i_c(t)$ are the currents flowing inside the three phases;
- $\Lambda_a, \Lambda_b, \Lambda_c$ are the linkage fluxes with each phase;
- R is the resistance of each phase which are supposed equal;

Equations (2.1),(2.2) and (2.3) can be written using a space vector representation:

$$\vec{u}(t) = R \cdot \vec{i}(t) + \frac{d\vec{\Lambda}(t)}{dt} \quad (2.4)$$

Because of its anisotropic structure the rotor presents different inductances along different axes so it is more convenient to write the voltage equations in a rotating reference frame synchronous with the rotor. This way we can define a d-axis, which points in the direction of PM's flux lines, and a q-axis which is rotated by 90 electrical degrees with respect of d-axis.

$$u_d = R \cdot I_d + \frac{d\Lambda_d}{dt} - \omega_{me} \cdot \Lambda_q \quad (2.5)$$

$$u_q = R \cdot I_q + \frac{d\Lambda_q}{dt} + \omega_{me} \cdot \Lambda_d \quad (2.6)$$

where $\omega_{me} = p \cdot \omega_m$ is the electrical speed. Now we can consider a linear working condition (without iron saturation) and re-write fluxes as follow:

$$\Lambda_d = \Lambda_{PM} + L_d \cdot I_d \quad (2.7)$$

$$\Lambda_d = L_q \cdot I_q \quad (2.8)$$

Finally by plugging (2.7) and (2.8) into (2.5) and (2.6) we get:

$$u_d = R \cdot I_d + L_d \cdot \frac{dI_d}{dt} - \omega_{me} \cdot L_q \cdot I_q \quad (2.9)$$

$$u_q = R \cdot I_q + L_q \cdot \frac{dI_q}{dt} + \omega_{me} \cdot \Lambda_{PM} + \omega_{me} \cdot L_d \cdot I_d \quad (2.10)$$

From (2.9) and (2.10) torque can be computed as:

$$M = \frac{3}{2} \cdot p \cdot (\Lambda_{PM} \cdot I_q + (L_d - L_q) \cdot I_d \cdot I_q) \quad (2.11)$$

It's easy to notice the "cylindrical" torque $\Lambda_{PM} \cdot I_q$, generated by PM and the "reluctance" torque $(L_d - L_q) \cdot I_d \cdot I_q$, generated by the anysotropy and also that, since $(L_d - L_q < 0)$, I_d has to be negative to have a positive torque.

Control strategy

An important feature is the ability to control effectively the motor with variable speed and load. First it is necessary to map the d-q current plane to find torque and voltage for each possible operating current and speed. Then, a maximum operating current and voltage depending on the inverter limits or other security issues is define

$$U_d^2 + U_q^2 \leq U_{lim}^2 \quad (2.12)$$

$$I_d^2 + I_q^2 \leq I_{lim}^2 \quad (2.13)$$

It can be seen that the current limit is a circle.

By considering equations (2.10) at steady state (derivatives are equal to zero) and plugging it into equation (2.13) we obtain

$$(\Omega_{me} \cdot L_q \cdot I_q)^2 + (\Omega_{me} \cdot L_d \cdot I_d + \Omega_{me} \cdot \Lambda_{PM}) \leq U_{lim}^2 \quad (2.14)$$

and with some basic algebraic the equation of an ellipse can be obtain.

$$\left(I_d + \frac{\Lambda_{PM}}{L_d}\right)^2 + \left(\frac{L_d \cdot I_q}{L_q}\right)^2 \leq \left(\frac{U_{lim}^2}{\Omega_{me} \cdot L_d}\right)^2 \quad (2.15)$$

At low rotational speed the ellipse is very wide and it gets smaller and smaller as speed increses until it collapse in its own centre which has coordinates

$$I_d = -\frac{\Lambda_{PM}}{L_d} \quad (2.16)$$

$$I_q = 0 \quad (2.17)$$

Notice how equations (2.16) and (2.17) represent also the short circuit current of the machine. By re-arranging equation (2.11) it can be seen that the torque has an hyperbolic dependence with current.

$$I_q = \frac{2 \cdot M}{3 \cdot p \cdot (\Lambda_{PM} + (L_d - L_q) \cdot I_d)} \quad (2.18)$$

By plotting everything in the same plane, current circle, voltage ellipse and hyperbolic torque something similar to figure 2.2 can be obtain [31].

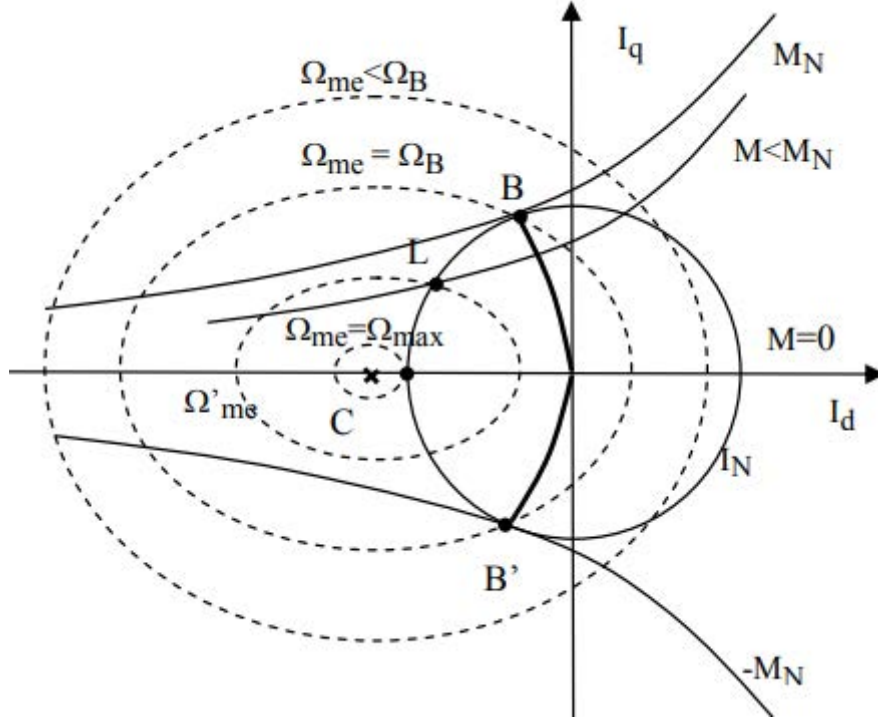


Figure 2.2: Working limits of IPM motor

Point B is called *base point* and the associated speed is called *base speed*; it is the highest speed at which maximum torque is available and also the point where maximum voltage is reached. There is a specific path that allows the maximum output torque with minimum current, it can be obtained by finding the tangential point between current circles and torque hyperbole and it is called maximum torque per ampere (MTPA) locus. It has the following analytical expression, valid in linear conditions only

$$I_q = \pm \sqrt{\frac{I_d \cdot \Lambda_{PM} + (L_d - L_q) \cdot I_d}{L_q - L_d}} \quad (2.19)$$

If the center of voltage ellipses is inside the current limit there is another locus which is called maximum torque per voltage (MTPV) and it is obtain by finding the tangential point between voltage ellipses and torque hyperbols; in this case the theoretical rotational speed is infinite. The availability of the MTPV is very important in traction motors as it allows to obtain an optimal mechanical characteristic. During the machine design the linkage flux and d-axis inductance must be carefully calculated to gain access to the MTPV.

$$I_q = \pm \frac{L_d}{L_q} \cdot \sqrt{\frac{-(I_d + \Lambda_{PM}) \cdot (\Lambda_{PM} + (L_d - L_q) \cdot I_d)}{L_q - L_d}} \quad (2.20)$$

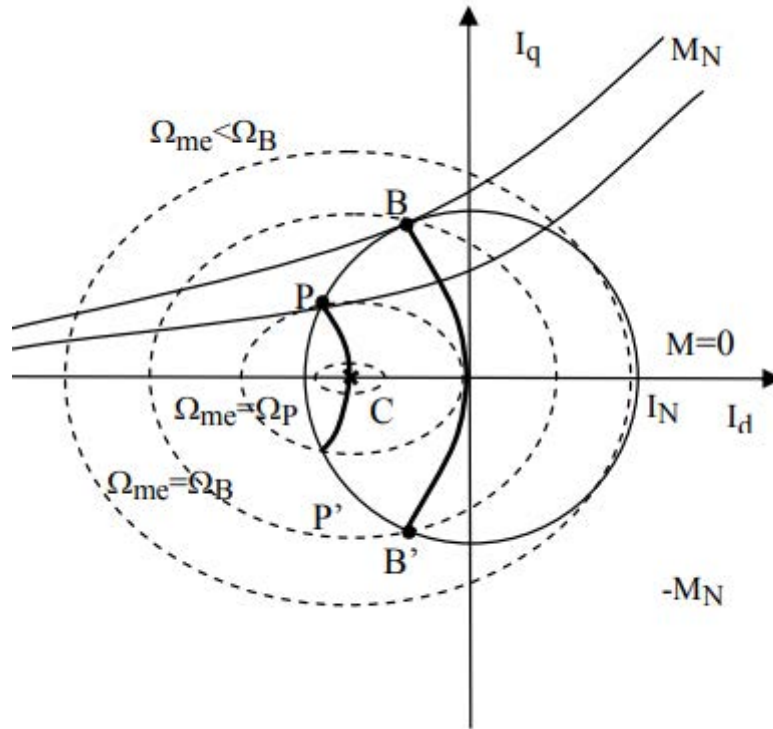


Figure 2.3: Working limits of IPM motor, MTPA and MTPV in evidence [31]

Knowing the d-q map it is possible to control the motor in the most efficient way; in particular currents are moved along the MTPA for low rotational speed, increasing voltage with increasing speed then along the current limit circle (once the base speed is reached), keeping the voltage at its maximum value, and finally along MTPV locus if possible (or needed). The typical torque versus speed characteristic is shown below in figure 2.4.

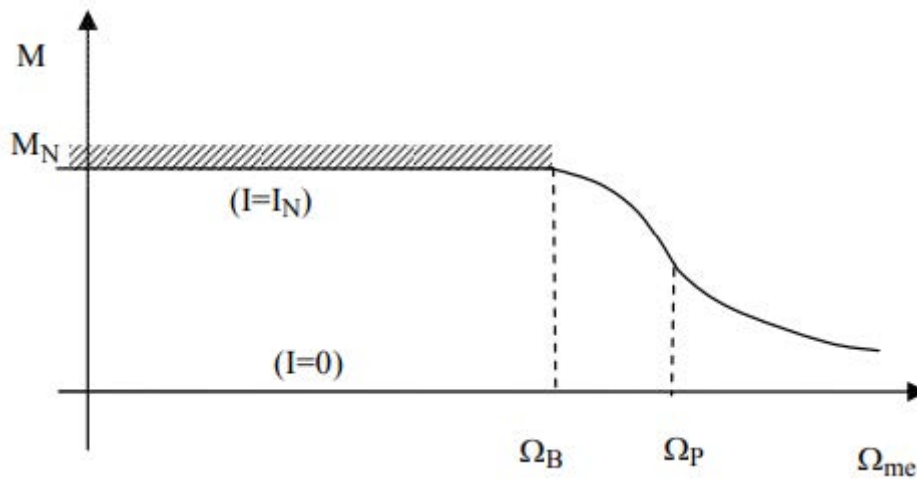


Figure 2.4: Typical IPM torque versus speed with MTPV region [31]

2.1.1 Permanent magnet

A permanent magnet is a hard magnetic material. It is characterized by a very wide hysteresis cycle and therefore a lot of energy is needed to magnetize or demagnetize it. Figure 2.5 shows

the typical B-H characteristic for a permanent magnet. Both the intrinsic (dashed line) and normal (solid line) hysteresis loops are drawn as reported in most PM data sheets. The intrinsic curve represents the added magnetic flux density that the PM material produces. The normal curve represents the total magnetic flux density which is carried in combination by the air and by the PM [25]. There are four important parameters to characterize a magnet

- B_{rem} is the residual flux density;
- H_c is the coercive force;
- μ_{rec} is the differential relative permeability, it usually have value slightly higher than unit;
- H_{ci} is the intrinsic coercive force.

Once magnetized, the magnet works in the second quadrant of the characteristic and its operation is approximated by the recoil line:

$$B_m = B_{rem} + \mu_{rec} \cdot \mu_0 \cdot H_m \quad (2.21)$$

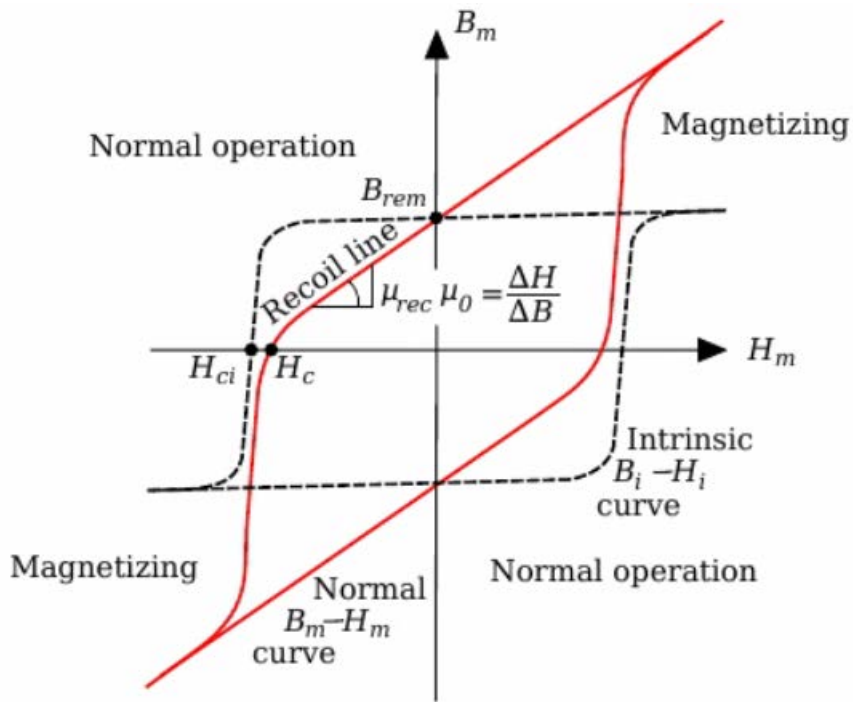


Figure 2.5: B-H characteristic of a PM

When the flux density becomes lower than B_{knee} (see figure 2.6), where the hysteresis curve exhibits a knee in quadrant II, the PM is irreversibly demagnetized and its next operating points move on a locus with lower flux density versus field strength. The minimum flux density in the PMs has to be verified during the magnetic analysis of the machine. Since B_{knee} depends on the temperature, the worst operating condition has to be considered [25]. In particular, almost all the magnetic materials used worsen their performance with increasing temperature, both from the point of view of the residual flux density and the coercive force. This means that at high temperatures the risk of demagnetization is higher (figure 2.7). The exception is barium ferrite which increases its coercive field with increasing temperature.

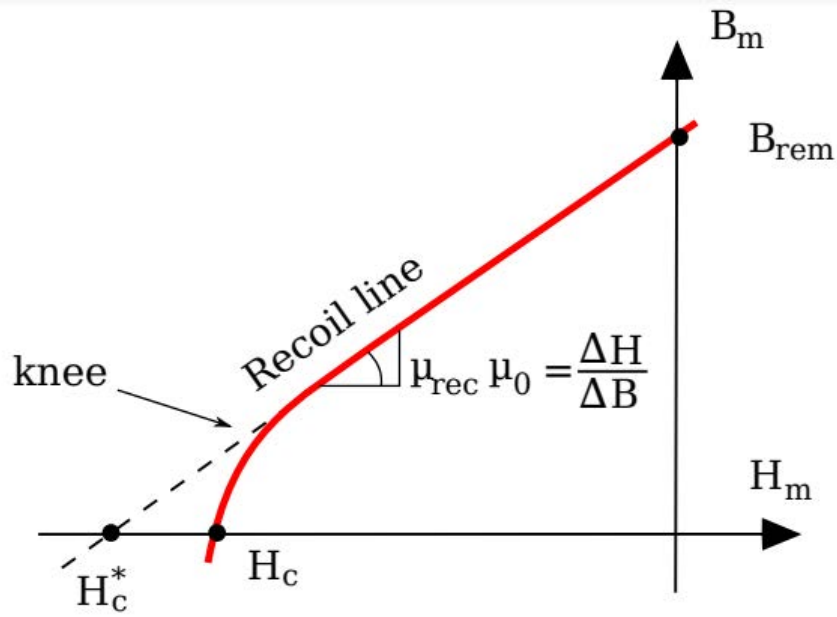


Figure 2.6: Demagnetization point (knee)

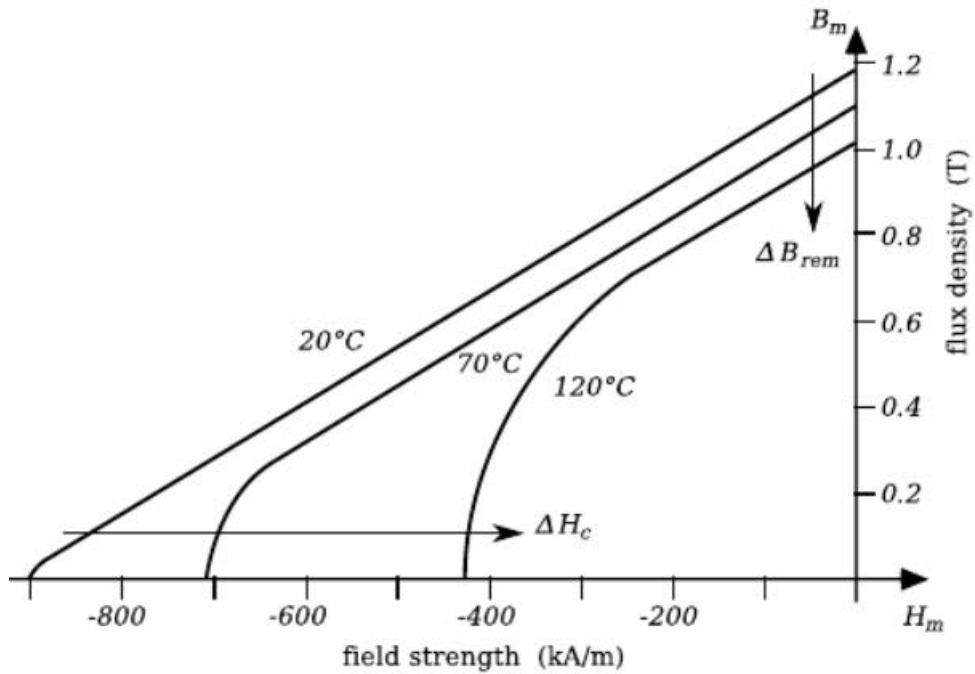


Figure 2.7: Variation of B_{rem} and H_c with temperature

Table 2.1 shows the main properties of the permanent magnets most used in electric machines while figure 2.8 presents their B-H characteristics [22].

	Mesure unit	Ferrite	AlNiCo	SmCo	NdFeB
B_{rem}	T	0.38	1.2	0.85	1.15
H_c	$\frac{kA}{m}$	250	50	570	880
Curie T	$^{\circ}C$	450	860	775	310
T_{max}	$^{\circ}C$	300	540	250	180
Density	$\frac{kg}{m^3}$	4800	7300	8300	7450
$(B \cdot H)_{max}$	$\frac{kJ}{m^2}$	30	45	140	260
$\frac{\Delta B_{rem}}{\Delta T}$	$\frac{\%}{^{\circ}C}$	-0.2	-0.02	-0.04	-0.12
$\frac{\Delta H_c}{\Delta T}$	$\frac{\%}{^{\circ}C}$	0.4	-0.02	-0.2	-0.7

Table 2.1: Main properties of hard magnetic material

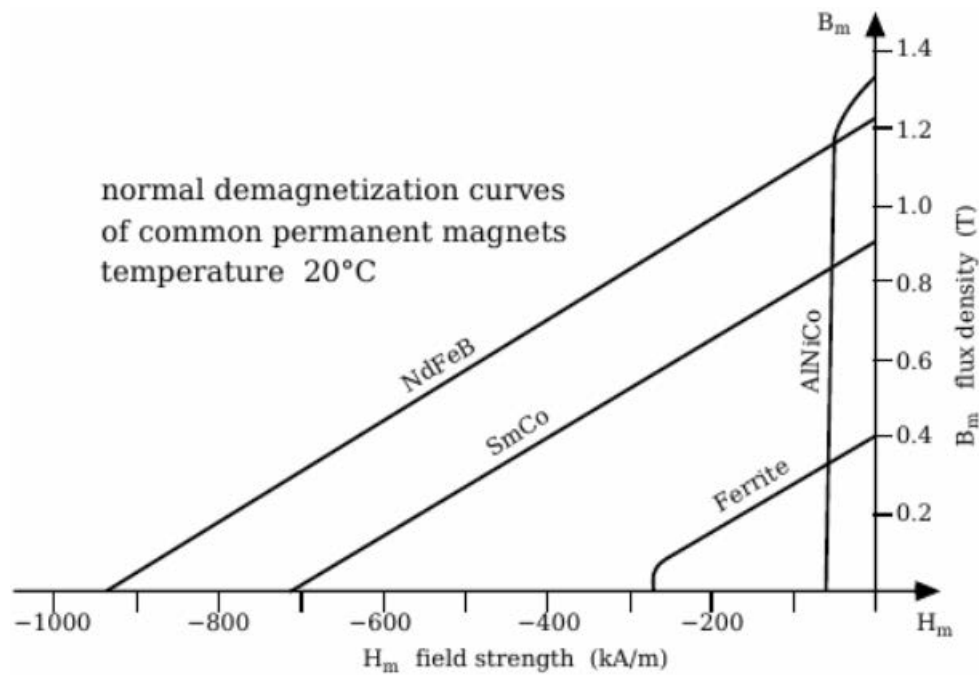


Figure 2.8: B-H characteristic for most used PMs

Ferrite magnets are often used in applications where the magnet does not have to be particularly performing for example in permanent magnet assisted synchronous reluctance motor (PMASRM). They are also highly appreciated as they are not composed of rare earths. Cobalt nickel aluminum (AlNiCo) magnets are rarely used due to the extreme low demagnetization resistance. Practically, internal permanent magnet motors mount almost exclusively NdFeB and SmCo magnets. The latter is highly appreciated for its ability to work effectively even at high temperatures.

As already mentioned in the introduction, dysprosium is added to increase the resistance to demagnetization.

2.2 IPM analysis

The reference motor under analysis has the following initial data

	Symbol	Value	Mesure unit
Pole pairs	p	4	/
Stack length	L_{stk}	130	mm
Packing coefficient	k_{pak}	0.97	/
Number of series conductors per slot	n_{cs}	1	/
Number of slots	Q_s	72	/
Nominal peak current	\hat{I}_n	400	A
Overload peak current	\hat{I}_{ol}	800	A
DC bus voltage	V_{DC}	300	V

Table 2.2: Initial data

In table 2.3 and 2.4 geometrical data of stator and rotor are respectively indicated.

	Symbol	Value	Mesure unit
Outer diameter	D_{ext}	200	mm
Inner diameter	D_{int}	140	mm
Tooth width (minimum)	w_t	3.24	mm
Slot area	S_{slot}	38.76	mm ²
Slot opening width	w_{so}	0.6	mm
Slot height	h_s	14	mm
Slot opening height	h_{so}	0.8	mm
Wedge height	h_{wed}	0.7	mm
Slot width	w_s	3	mm
Back iron height	h_{bi}	16	mm

Table 2.3: Stator data

	Symbol	Value	Mesure unit
Outer rotor diameter	D_r	138.4	mm
Shaft diameter	D_{shaft}	50	mm
Air gap	g	0.8	mm

Table 2.4: Rotor data

Stator and rotor are made of non oriented electrical steel with 0.27 mm sheets (NO27) that

has the following B-H characteristic (figure 2.9).

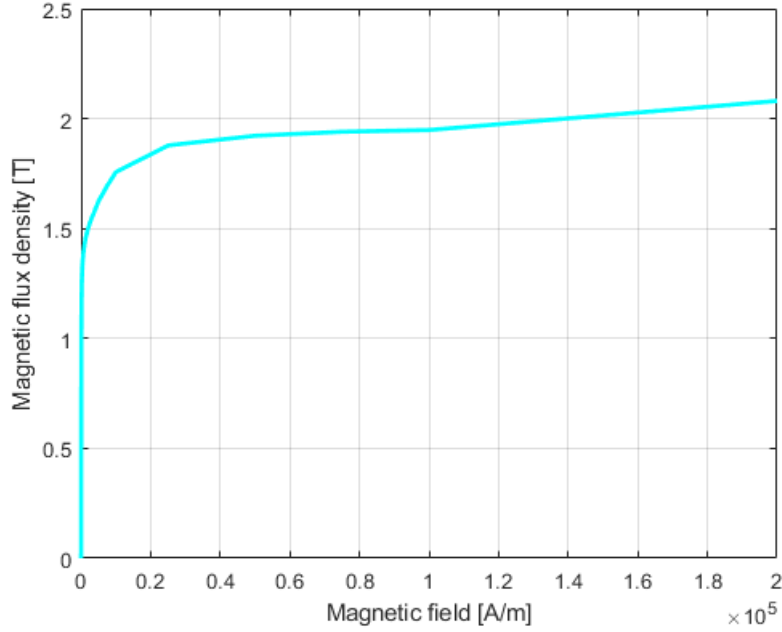


Figure 2.9: B-H curve

In table 2.5 magnet's properties are listed, a NdFeB 40 MGO is chosen:

	Symbol	Value	Mesure unit
Differential permeability	μ_{rec}	1.049	/
Residual magnetization at 20 °C	B_{rem}	1.24	T
Coercivity	H_c	939	$\frac{kA}{m}$
Polarization	H_{cj}	1989	$\frac{kA}{m}$
Magnetic energy	$(B \cdot H)_{max}$	302	$\frac{kJ}{m^3}$
Reverse temperature coefficient (B)	α	-0.1	/
Reverse temperature coefficient (H)	β	-0.55	/

Table 2.5: Magnet data

Finally copper conductivity is set to $\sigma = 36 \frac{MS}{m}$. This value is calculated assuming an operating temperature of 150 °C and applying the following relationship

$$\rho_{cu,150} = \rho_{cu,20} \cdot (1 + 0.004 \cdot (150 - 20)) = 2.73 \cdot 10^{-8} \Omega \cdot m \quad (2.22)$$

$$\sigma_{cu,150} = \frac{1}{\rho_{cu,150}} = 36 \frac{MS}{m} \quad (2.23)$$

The analysis of the motor is carried out by using a 2D finite element software called FEMM. The built geometry is shown in figure 2.10. Considering the periodic structure of the machine it is possible to reduce the study to a single pole; to do this, anti-periodic conditions are imposed on lateral borders. To confine the magnetic flux inside the stator, dirichlet conditions are also

imposed on the periphery. Finally, in order to study the rotation of the rotor more effectively, an antiperiodic air gap condition is established; in this way it is not necessary to build a new mesh at each rotor movement thus avoiding numerical errors. An explanatory drawing is shown in figure 2.11

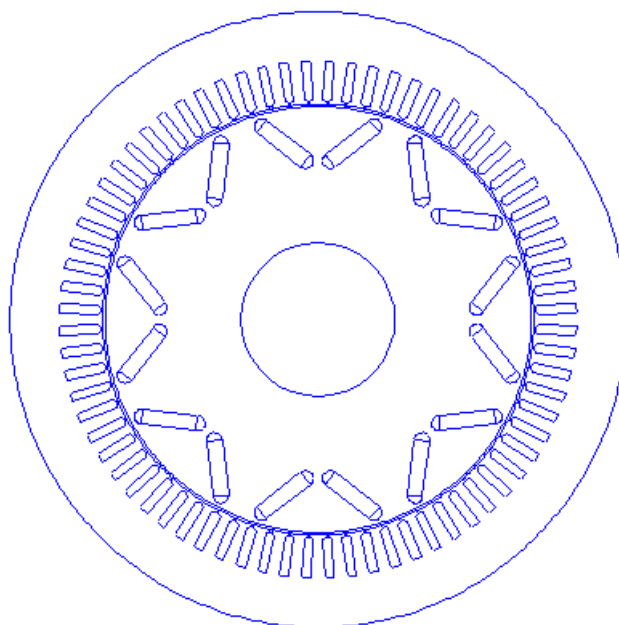


Figure 2.10: Geometry built in FEMM

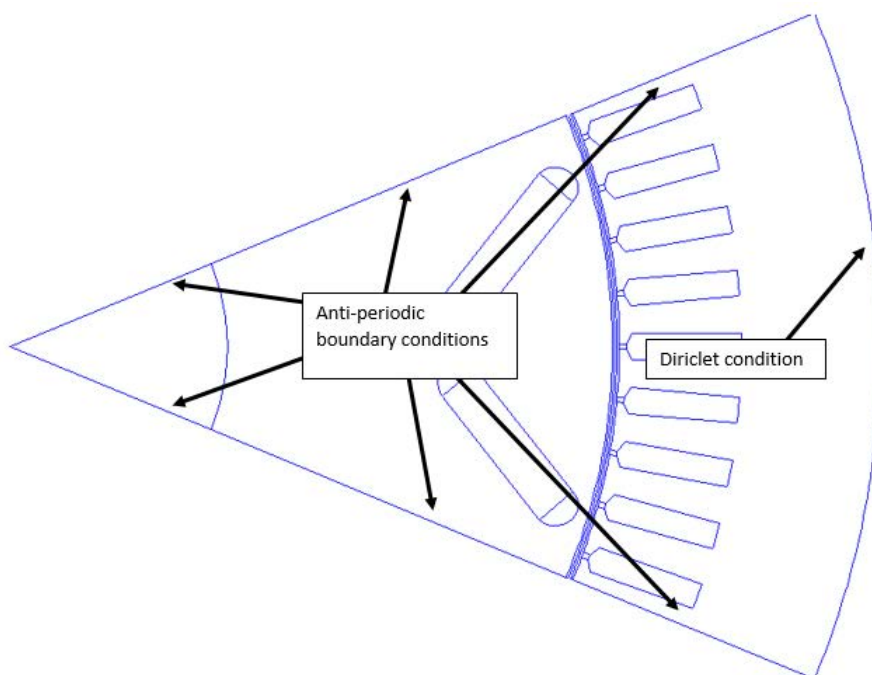


Figure 2.11: Boundary conditions imposed

In order to facilitate the simulations, it is chosen to position the conductors in the slots so

that the axis of phase a lies as shown in figure 2.12. To do this, the following slot matrix is used:

$$\begin{pmatrix} 0 & -1 & 0 \\ 0 & -1 & 0 \\ 0 & -1 & 0 \\ 1 & 0 & 0 \\ 1 & 0 & 0 \\ 1 & 0 & 0 \\ 0 & 0 & -1 \\ 0 & 0 & -1 \\ 0 & 0 & -1 \end{pmatrix}$$

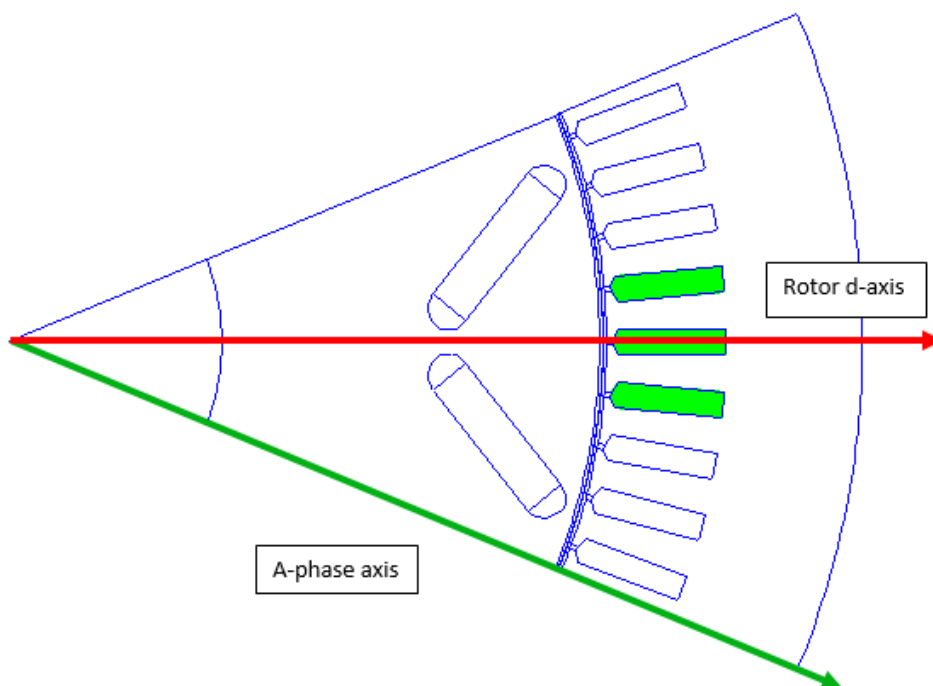


Figure 2.12: Phase a axis and rotor d-axis

2.2.1 No load analysis

The no load analysis is carried out with zero currents in the stator, its purpose is to derive the no load linkage flux and cogging torque.

Airgap

The airgap flux density is characterized by a first harmonic of 0.709 T and some higher order harmonics caused by slot openings in the stator (figure 2.13 and 2.14). The main harmonics are: a fifth one with amplitude of 11% with respect to the fundamental and a seventh one with amplitude 10%.

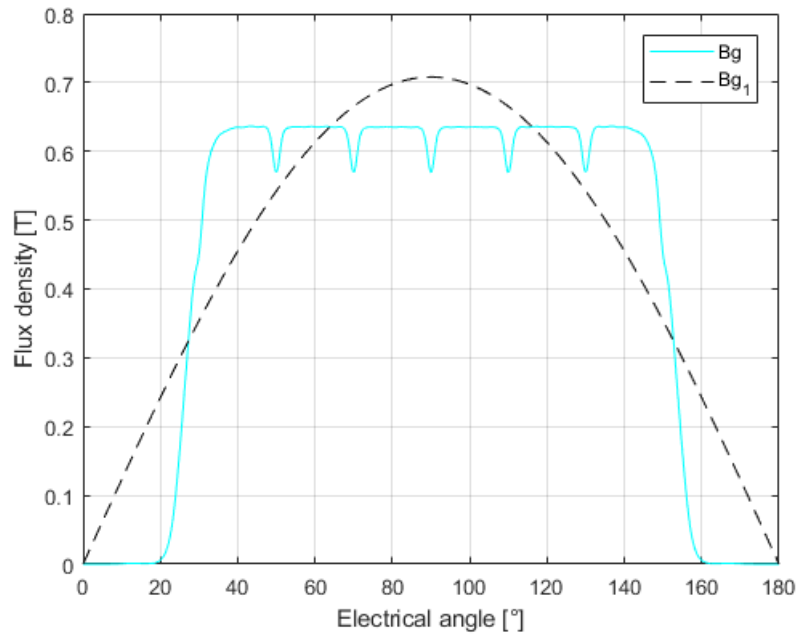


Figure 2.13: Airgap flux density, the effect of slot openings is evident

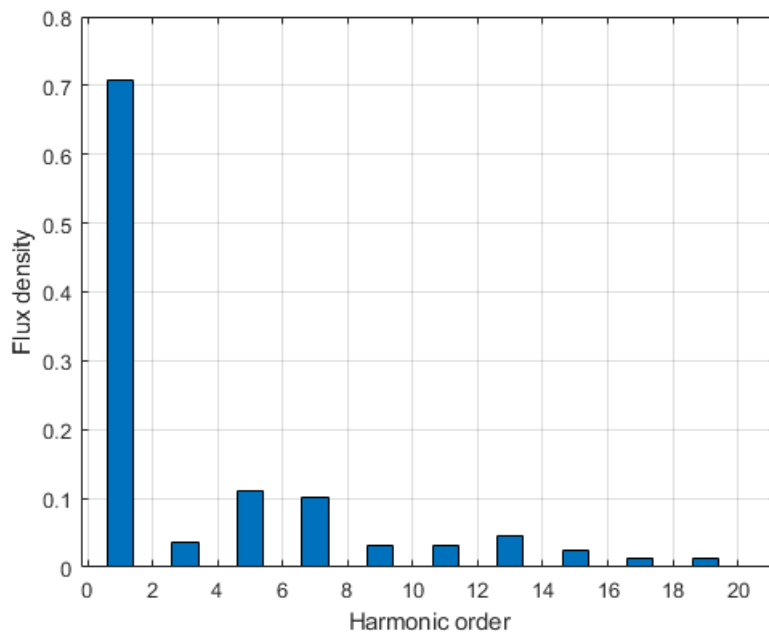


Figure 2.14: Main flux density harmonics

Cogging torque

The cogging torque is a torque caused by the interaction between rotor and stator. In particular, the alternation of slot openings and tooth creates paths with different reluctance in the stator. The rotor tends to align with the path of lower reluctance thus determining a parasitic torque. It is important to note that the cogging torque does not have an average value but is oscillating

and the number of N_p periods during a slot pitch rotation can be calculated as [25]

$$N_p = \frac{2p}{\text{GCD}\{Q, 2p\}} = \frac{8}{\text{GCD}\{72, 8\}} = 1 \quad (2.24)$$

where GCD means Greater Common Divisor. Thus, the mechanical angle corresponding to each period is

$$\alpha_{\text{cogging}} = \frac{2 \cdot \pi}{N_p \cdot Q} = \frac{2 \cdot \pi}{1 \cdot 72} = 5^\circ \quad (2.25)$$

Higher number of periods lower the amplitude of the cogging torque. The computation can be performed in two ways: through the maxwell stress tensor (already implemented in the software) or through the derivative of the magnetic co-energy between two different positions of the rotor. Figure 2.15 shows the values obtained by this two methods. It is noted how the oscillation period is 5° , like predicted with equation 2.25.

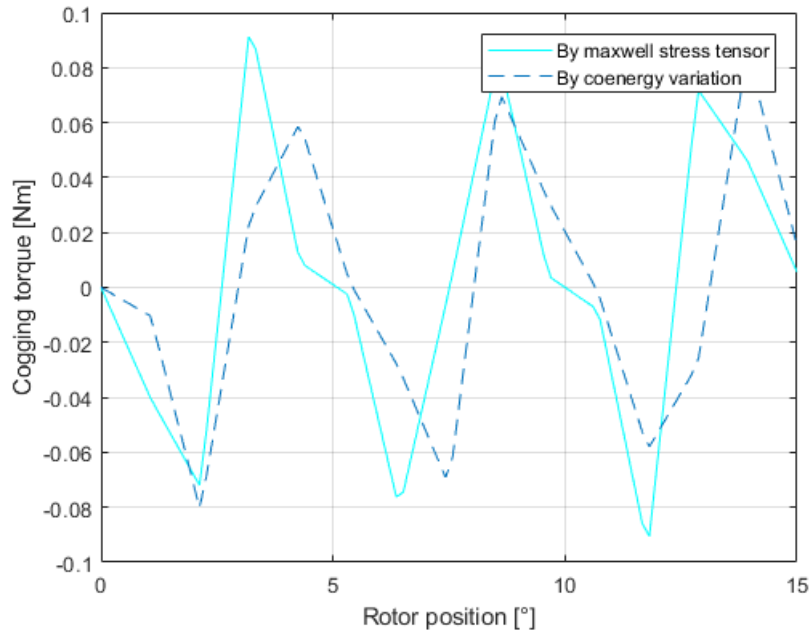


Figure 2.15: Cogging torque computed in two ways

Linkage fluxes and emf

Linkage fluxes by the three phases are then calculated at various rotor positions and reported in figure 2.16. It can be seen that the peak of phase a is 0.0037 Vs and it corresponds to the zero position of the rotor. When this happens the rotor d -axis is aligned with the phase a axis.

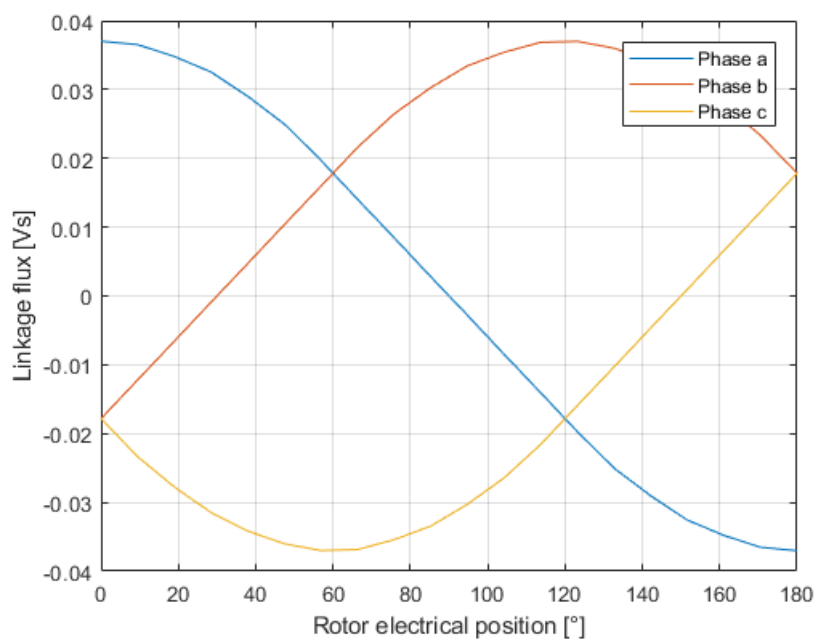


Figure 2.16: Linkage fluxes

By breaking down the waveform of the flux linkage of phase *a* into its series of Fourier, it is possible to obtain the harmonic spectrum of figure 2.17. A very low harmonic content can be noted.

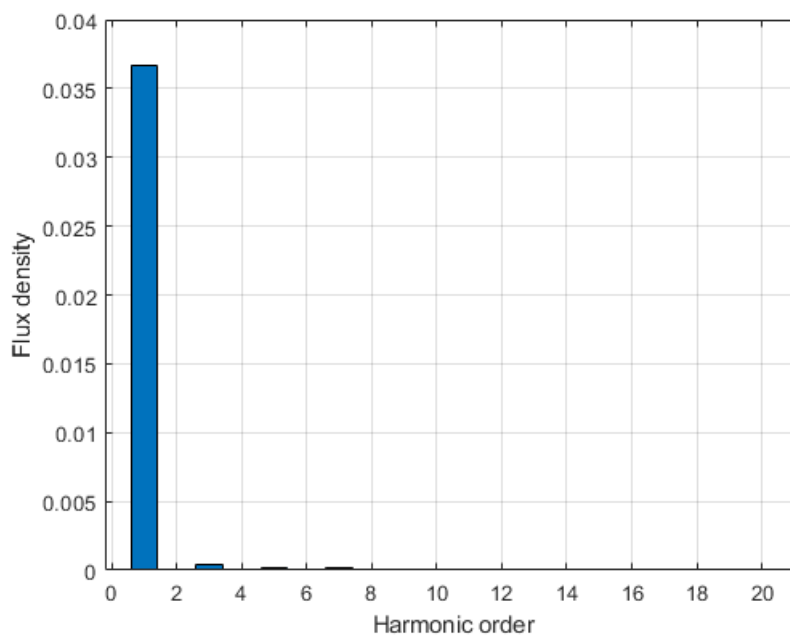


Figure 2.17: Linkage flux armonics

From the flux linkage waveform, it is possible to compute the induced voltage (also called back EMF) waveform, assuming a constant mechanical speed. According with the machine convention,

it is [25]

$$e(t) = \frac{d\Lambda(t)}{t} = \omega \cdot \frac{d\Lambda(\theta)}{d\theta} \quad (2.26)$$

The flux linkage waveform is expressed by means of its Fourier series expansion. Then, each harmonic of the series is derived, and all harmonics of EMF are summed together.

$$e(t) \approx \omega_{me} \cdot [\Lambda^{(1)} \sin(\omega_{me}t) + 3\Lambda^{(3)} \sin(3\omega_{me}t) + 5\Lambda^{(5)} \sin(5\omega_{me}t) \dots] \quad (2.27)$$

Given the tendency of the derivation to amplify noises, the waveform of the induced voltage will be much richer in harmonics than the flux that caused it. This is confirmed by figure 2.18

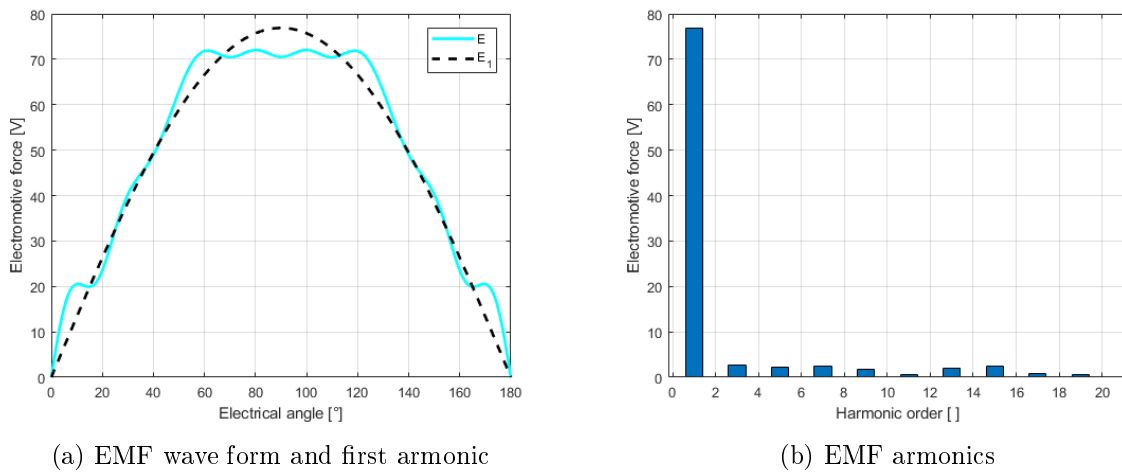


Figure 2.18: No-load phase back electromotive force

In figure 2.19 magnetic flux density and flux lines are shown.

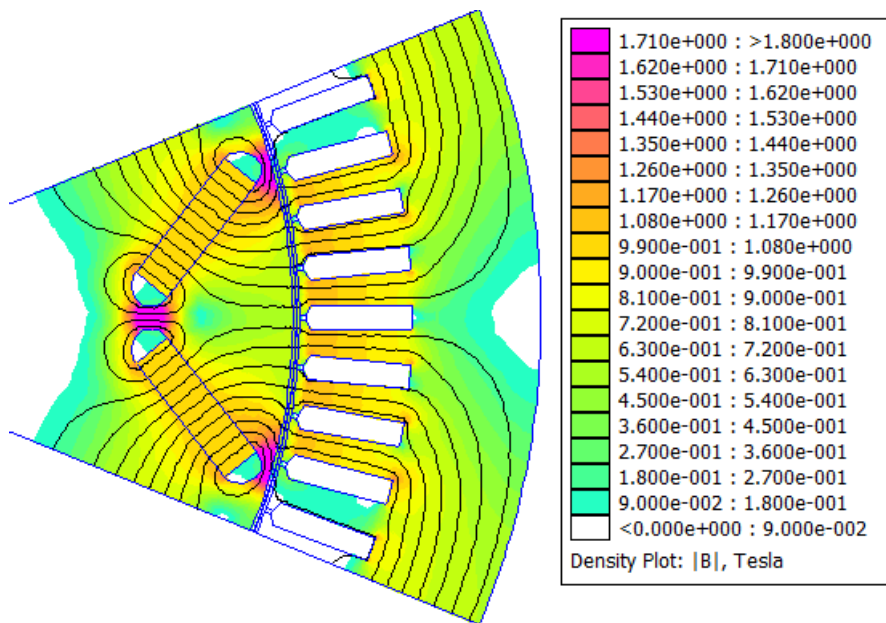


Figure 2.19: Flux density map

2.2.2 Inductances

As already stated in Section 2.1, the IPM motor has an anisotropic structure and is therefore studied in a rotating reference frame synchronous with the rotor. For this reason it is convenient to define an inductance L_d associated with the magnetic path of the d-axis and an inductance L_q associated with the magnetic path of the q-axis. To calculate the d-axis inductance the stator is fed with a d-axis current, then calculate the d-axis linkage flux and finally apply the following relationship

$$L_d = \frac{\Lambda_d - \Lambda_{PM}}{I_d} \quad (2.28)$$

As shown in figure 2.20 the inductance is not constant but depends on the current.

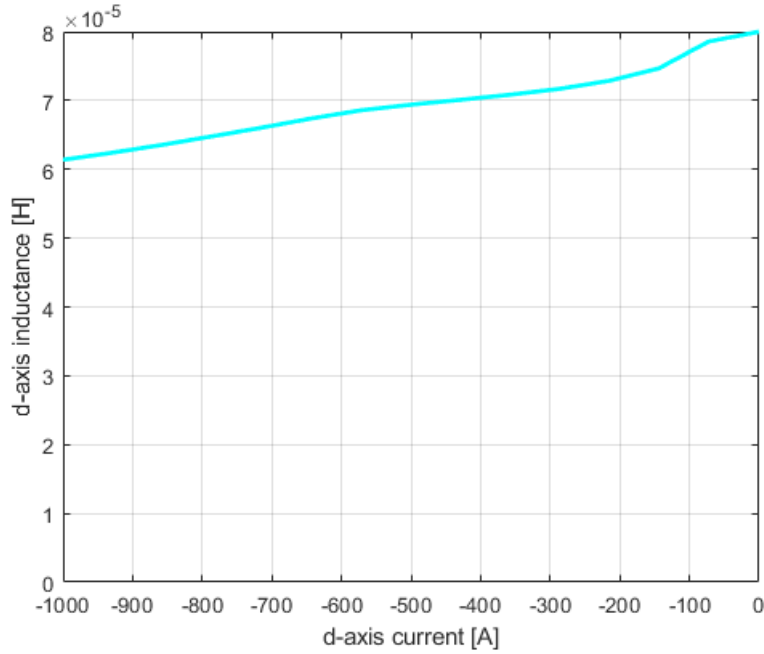


Figure 2.20: d-axis apparent inductance

To calculate the q-axis inductance the stator is fed with a q-axis current, then calculate the q-axis linkage flux and finally apply the following relationship

$$L_q = \frac{\Lambda_q}{I_q} \quad (2.29)$$

Alternatively it can be calculate using the product $A \cdot J$ (energy plus co-energy)

$$L_q = \frac{2 \cdot 2 \cdot \int A \cdot J}{3 \cdot I_q^2} \quad (2.30)$$

Also L_q depends on the current.

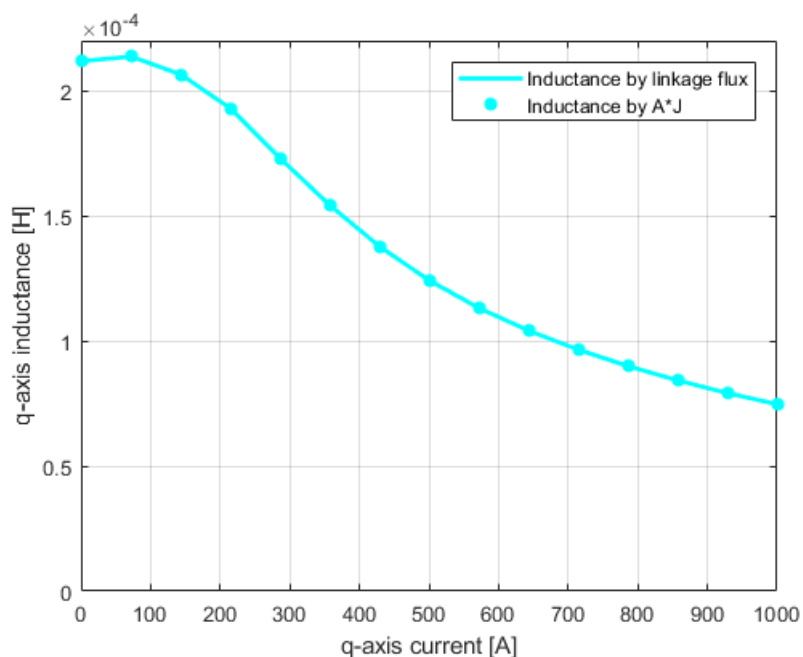


Figure 2.21: q-axis apparent inductance

Another important parameter is the so-called saliency ratio. It is the ratio between the greater and the lesser inductance and is indicative of how intense the reluctance torque will be. Figure 2.22 shows saliency ratio for different current values.

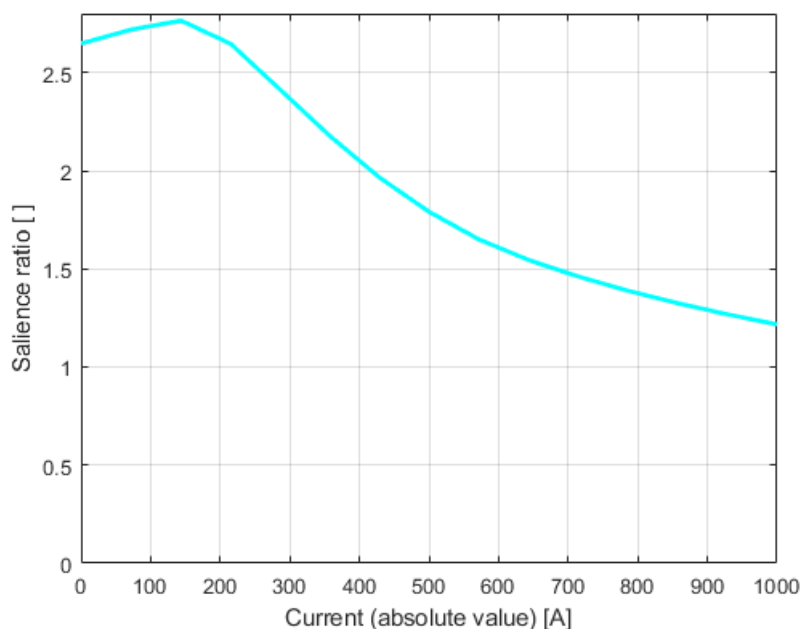


Figure 2.22: Saliency ratio versus current

Note how the relationships used to calculate the inductances require that the machine operate without saturation. Otherwise the two axes are no longer separate but the variations of current in one axis influence the flux of the other one, this phenomenon is called cross coupling.

2.2.3 On load analysis

For the on load analysis it is first of all necessary to map the d-q current plane. The motor is fed with variable d-axis and q-axis currents and the mechanical torque, d-axis and q-axis linkage fluxes, mechanical speed and the corresponding voltage are calculated for each point on the map. The current limit circle, voltage limit ellipses, MTPA and MTPV are then drawn. Figure 2.23 shows the location of the MTPA calculated by the analytical formula (equation 2.19) and the one calculated numerically. In particular, the calculation involves the use of a simple matlab script in which the torque on current circles from zero to maximum angle is calculated and then the point with maximum torque is identified. By performing this operation for various circles it is possible to obtain the real trend of the MTPA. It is noted that the analytical formula is able to give a fairly reliable estimate, especially for low current values, for first orientation analysis.

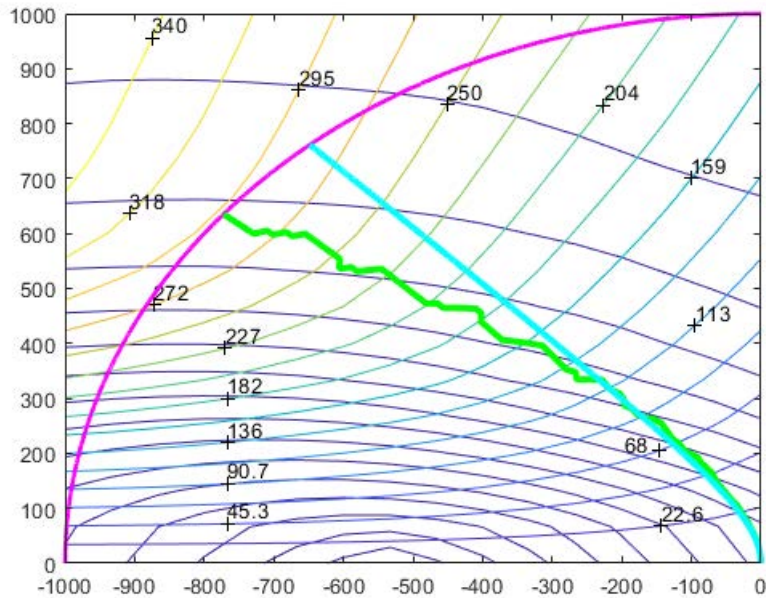


Figure 2.23: Numerical MTPA (green) and analytical MTPA (light blue)

Figure 2.24 shows the MTPV calculated analytically (through equation 2.20) and numerically. The approach is very similar to that applied for the calculation of the MTPA this time looking for the point at maximum torque on the voltage ellipses instead of on the current circles. It is noted that the two trends are quite different, however, it remains good starting point for a first orientation and does not require a large number of simulations. Note also how the MTPV can be used as long as the center of the voltage limit ellipses is within the current limit. If the current limit is reduced to lower values, it may no longer be possible to follow the path of MTPV.

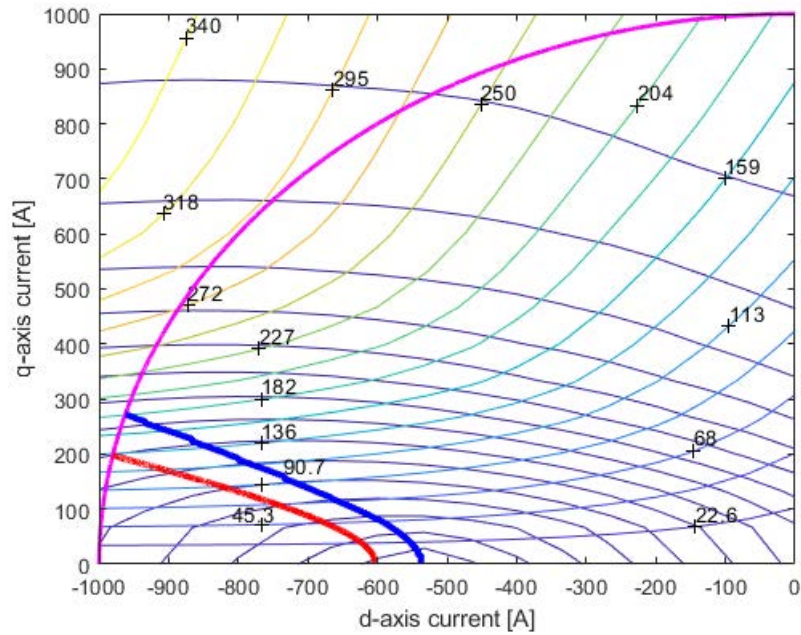


Figure 2.24: Numerical MTPV (blue) and analytical MTPV (red)

Finally, the two loci are shown together on the same plane in figure 2.25.

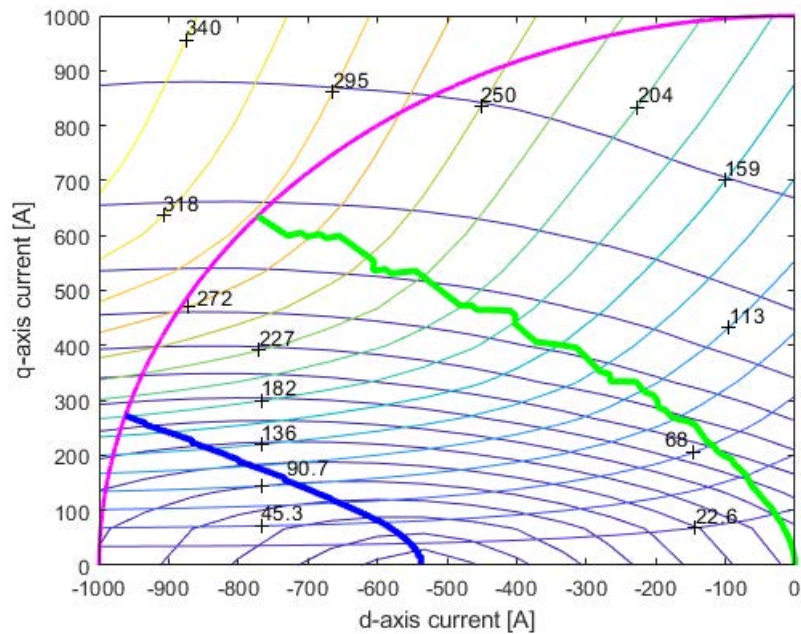


Figure 2.25: MTPA (green) and MTPV (blue) loci

The mechanical torque delivered when the rotor position changes is then calculated; the motor is fed with a fixed amplitude current and a phase obtained from the map of the d-q plane supposing to work in MTPA conditions. The calculation is done in two ways [23]:

- integrating the maxwell stress tensor along the rotor periphery:

$$T = \frac{D^2 \cdot L_{stk}}{4} \cdot \int_0^{2\pi} \frac{B_{g,n} \cdot B_{g,\theta}}{\mu_0} d\theta \quad (2.31)$$

- using the following analytical formula obtained from equations 2.6

$$T_{dq} = \frac{3}{2} \cdot p \cdot (\Lambda_d \cdot I_q - \Lambda_q \cdot I_d) \quad (2.32)$$

Since it is derived from non-punctual quantities, it is necessary to add an additional contribution to obtain the effective torque which is the variation of coenergy between one position and another:

$$T = \frac{3}{2} \cdot p \cdot (\Lambda_d \cdot I_q - \Lambda_q \cdot I_d) + \frac{dW_{coenergy}}{d\theta} \quad (2.33)$$

The results obtained for three different current values are reported below.

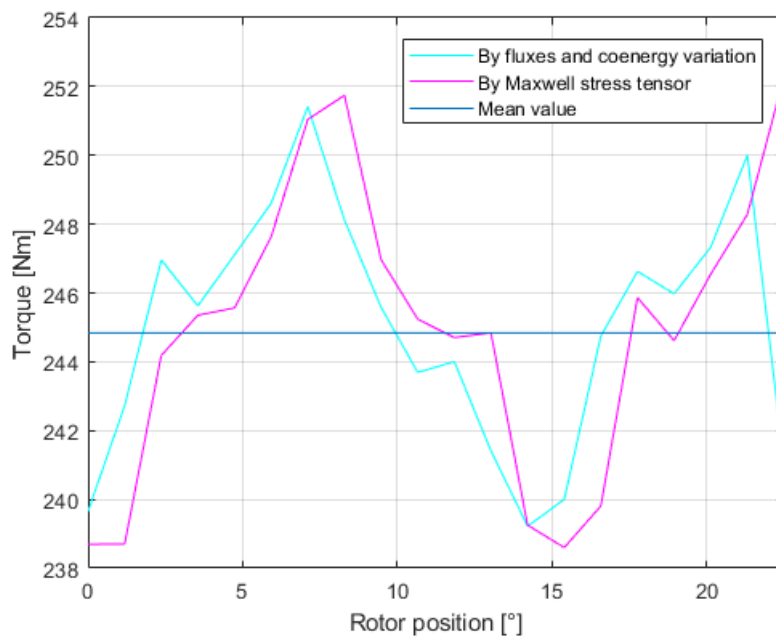


Figure 2.26: Torque versus rotor position at overload current $\hat{I} = 800 A$

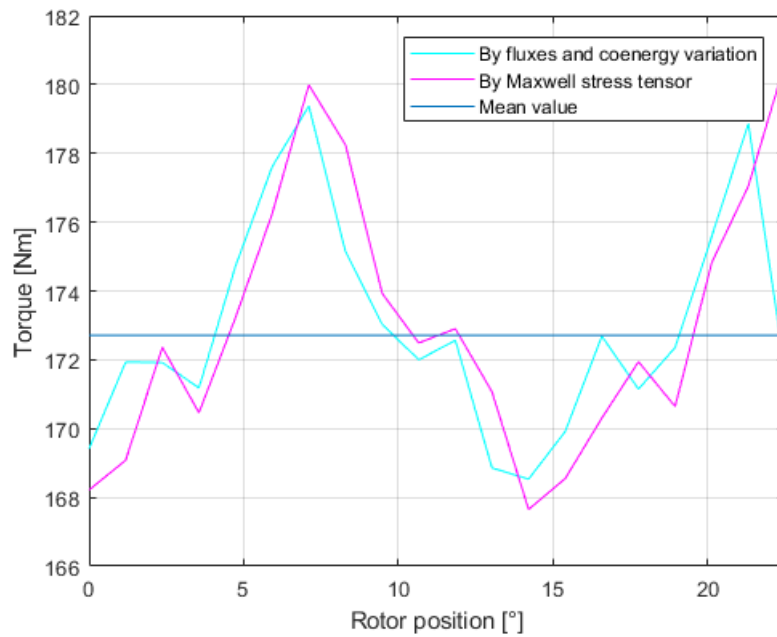


Figure 2.27: Torque versus rotor position at $\hat{I} = 560 A$

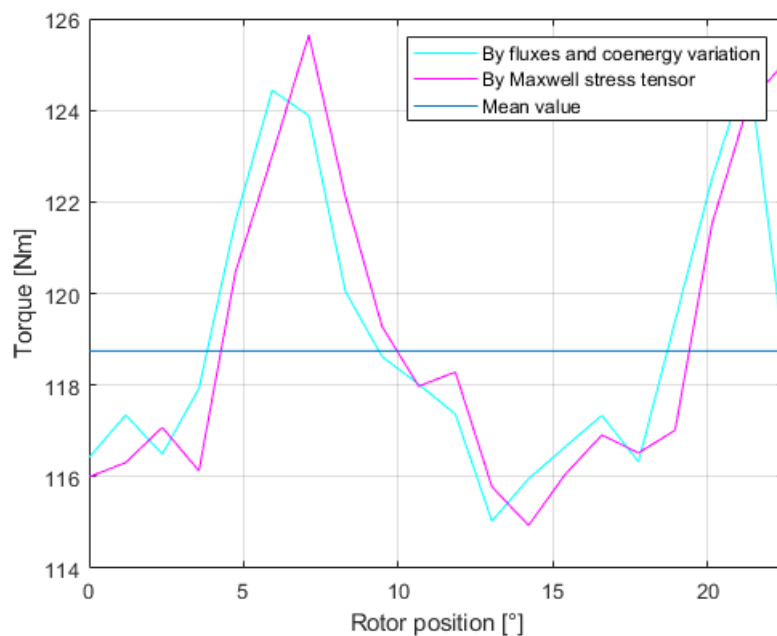
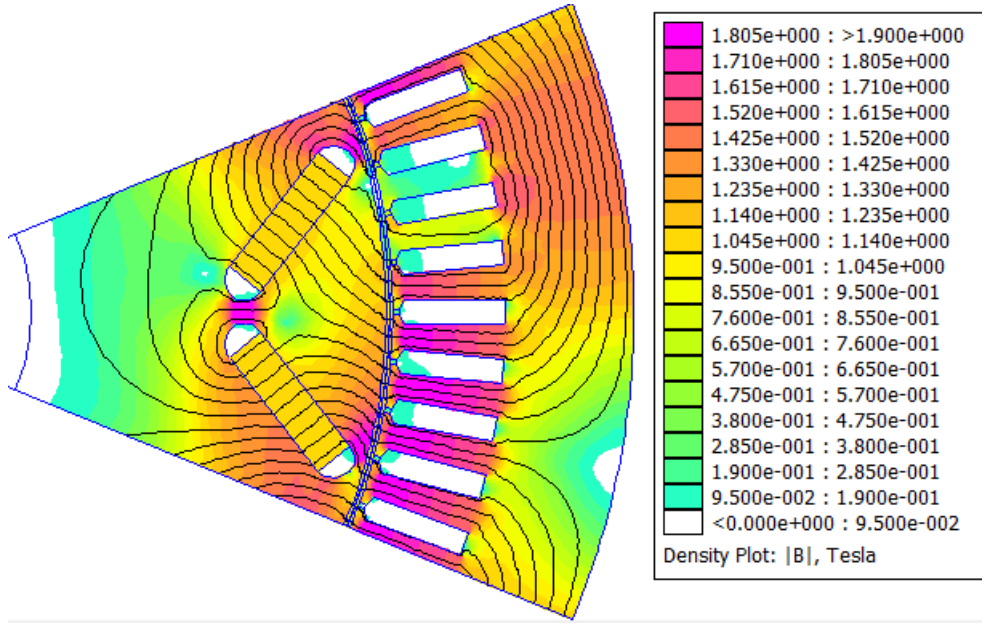


Figure 2.28: Torque versus rotor position at nominal current $\hat{I} = 400 A$

The flux density map with current $\hat{I} = 400 A$ is shown in figure 2.29, the maximum value (in a tooth) reaches 1.9 T.


 Figure 2.29: Flux density map at $\hat{I} = 400 A$

Mechanical characteristic

To complete the on load analysis, the variation in torque and power with the rotation speed must be calculated. For each value of current module, it is necessary to identify the most efficient path in the current plan. For example if we consider a current $\hat{I} = 800 A$ the best way to control currents is the path reported in figure 2.30; first the MTPA locus is followed until base speed and rated voltage are reached, thus working with constant linkage flux, then the current limit circle is followed until MTPV locus is reached and then follow it until maximum allowed speed is achieved. It is possible to determine the rotational speed at each operating point by applying the relationships [23]

$$\omega_m = \left(\sqrt{\frac{V^2}{\Lambda_d^2 + \Lambda_q^2}} \right) \cdot \frac{1}{p} \quad (2.34)$$

$$n = \frac{\omega_m \cdot 60}{2 \cdot \pi \cdot p} \quad (2.35)$$

V is the phase voltage and its values increase until its maximum value is reached (at base speed), then it is kept constant at that value and finally adapted according to MTPV locus. By analyzing all the operating points up to the maximum allowed speed (20000 rpm) it is possible to obtain figure 2.31, 2.32 and 2.33. The three working zones can be seen clearly.

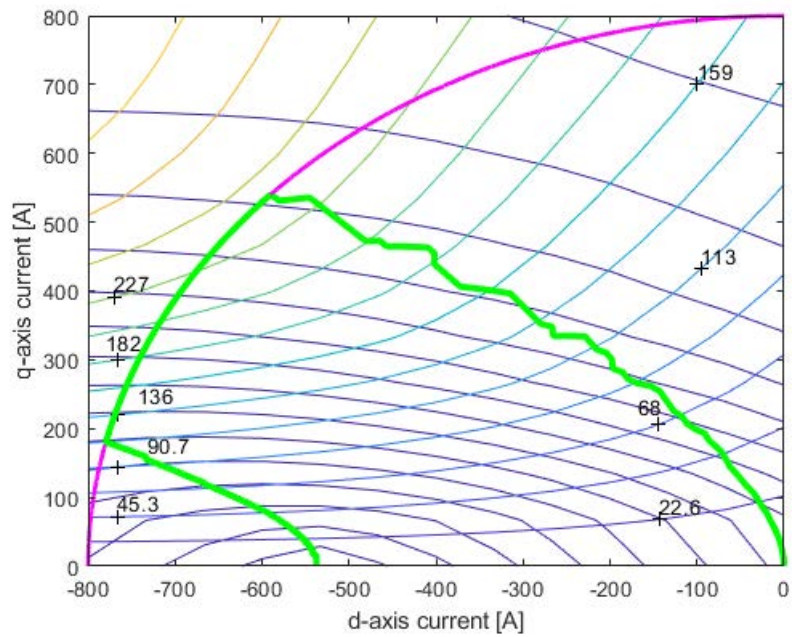


Figure 2.30: Control strategy at $\hat{I} = 800 A$

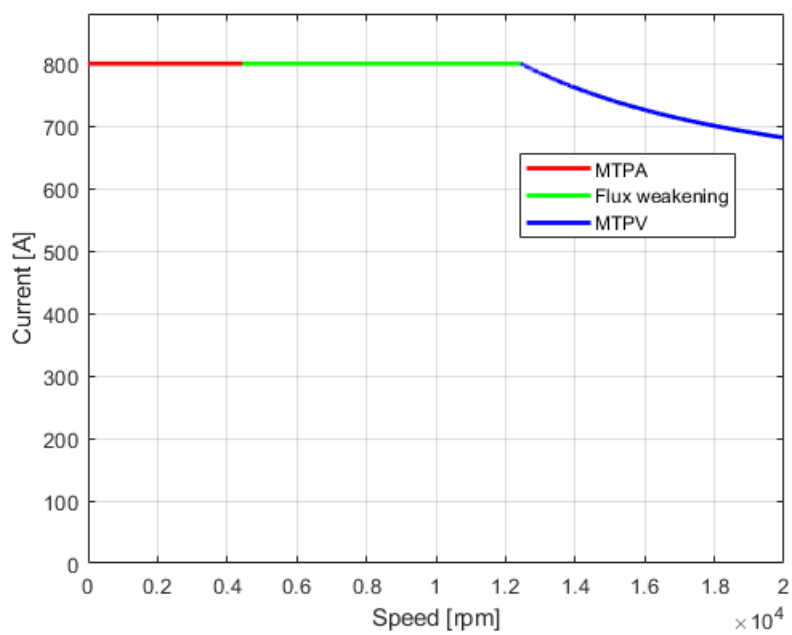


Figure 2.31: Current versus rotational speed

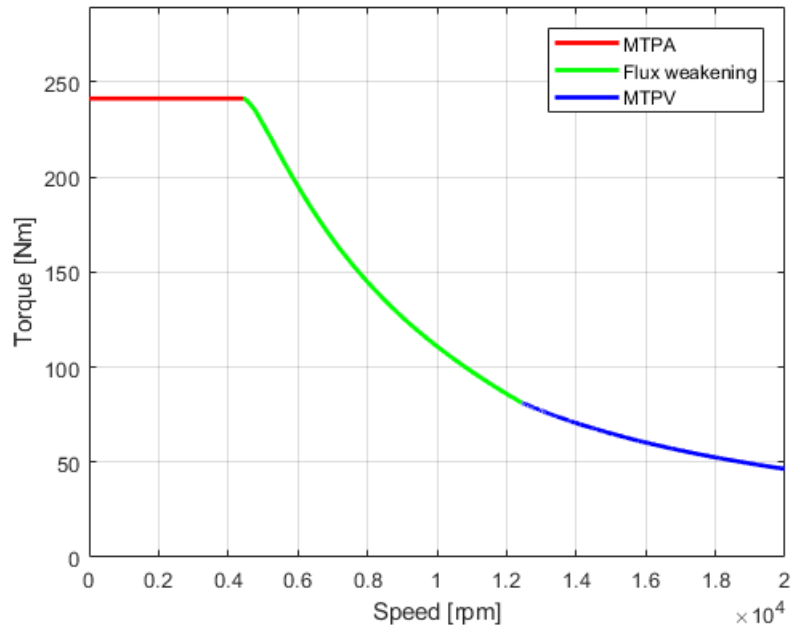


Figure 2.32: Torque versus rotational speed

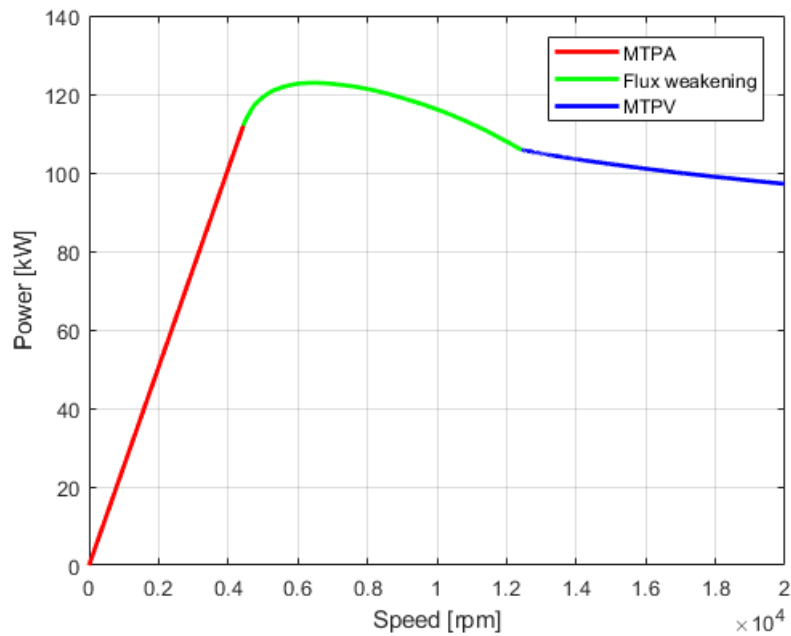


Figure 2.33: Power versus rotational speed

Variable current limit circle

By repeating the above procedure for various current limit values it is possible to obtain the characteristics shown in figure 2.34, 2.35 and 2.36.

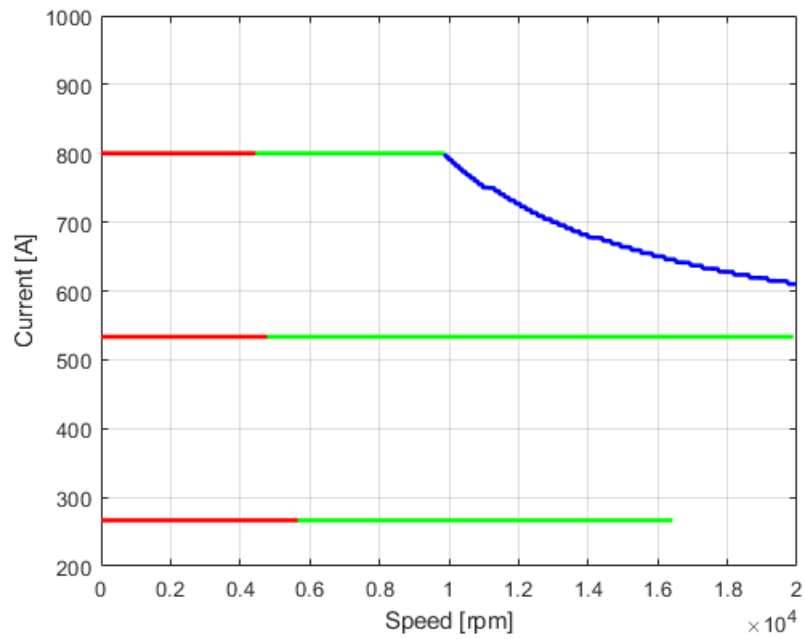


Figure 2.34: Current levels analyzed

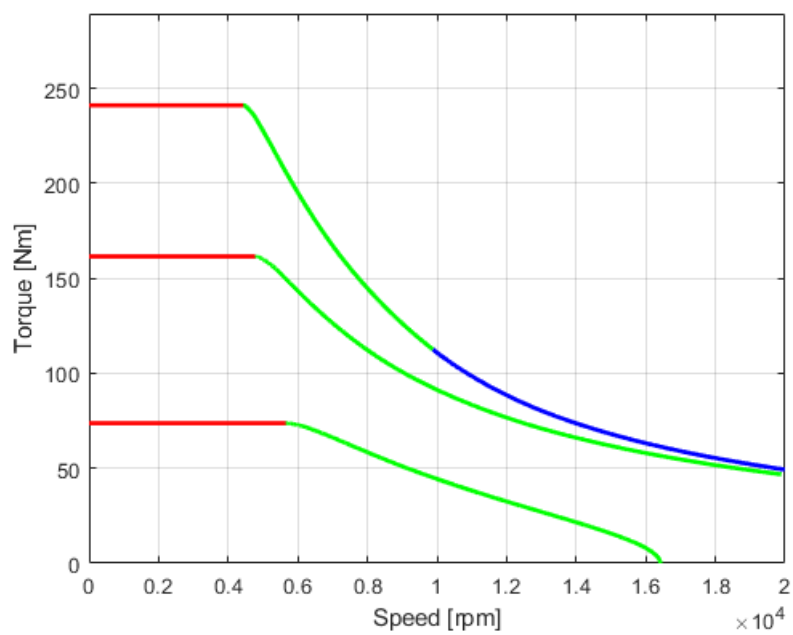


Figure 2.35: Torque versus rotational speed for various current levels

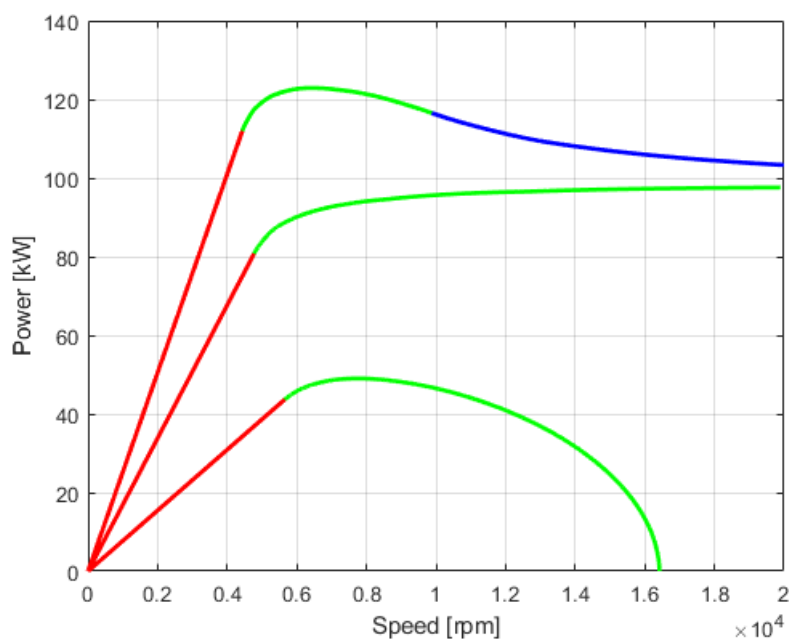


Figure 2.36: Power versus rotational speed for various current level

Note that for low limit current values it is not possible to exploit the MTPV as the center of the voltage ellipses is external to it. For this reason it is not possible to reach the required speed. In figure 2.37 the complete map of all the possible working points of the machine is shown. Note how the map also includes overload operation.

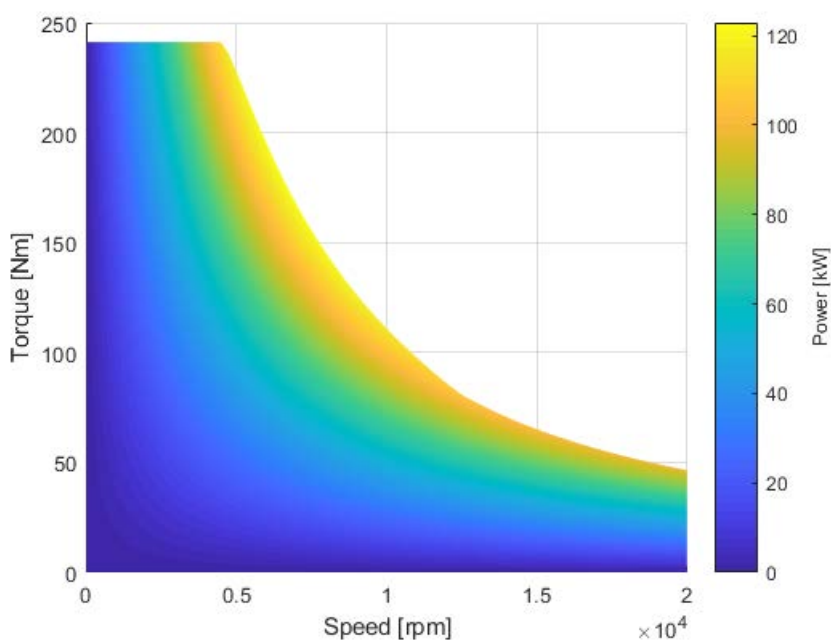


Figure 2.37: IPM working points

2.2.4 Losses

An IPM motor has four main sources of losses during operation:

- copper losses due to the current flowing in the windings;
- iron losses due to the variable induction in the stator;
- magnet and rotor losses due to high order MMF harmonics (neglected);
- mechanical losses due to air and bearings friction;

Losses for all working conditions are calculated.

Copper losses

Losses in copper can be calculated with the following equation

$$P_j = \frac{3}{2} \cdot R \cdot I_{peak}^2 = 3 \cdot R \cdot I_{eff}^2 \quad (2.36)$$

Nevertheless the calculation must take into account the high frequency at which the machine operates; in fact the current tends to thicken on the surface of conductors decreasing the effective section and increasing resistance. This effect, called the "skin effect", is characterized by the penetration depth which is the thickness in which most of the current density is concentrated; the penetration depth is computed as follow

$$\delta = \sqrt{\frac{\rho_{cu}}{\mu_0 \cdot \mu_{rel} \cdot \pi \cdot f}} \quad (2.37)$$

$$\text{with } \mu_0 = 4 \cdot \pi \cdot 10^{-7} \quad \mu_{rel} = 1 \quad (2.38)$$

Finite elements are used to accurately calculate the resistance assumed by conductors at high frequency. In particular, a slot is built with the actual conductors and simulations are performed at increasing frequency. Phase resistance can be calculated as follow:

$$R_{AC} = \frac{2}{3} \cdot N \cdot \frac{\sum P_{conductors}}{\hat{I}^2} \quad (2.39)$$

In figure 2.38 the slot and conductors built in FEMM can be seen; diriclet conditions have been imposed to confine the flux inside the domain.

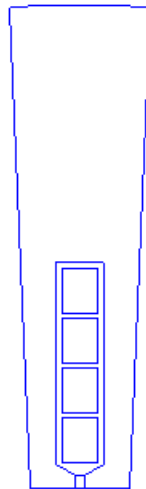


Figure 2.38: FEMM model

Figure 2.39 shows the current density at various frequencies, it is noted how the current distribution is very uneven at high frequency.

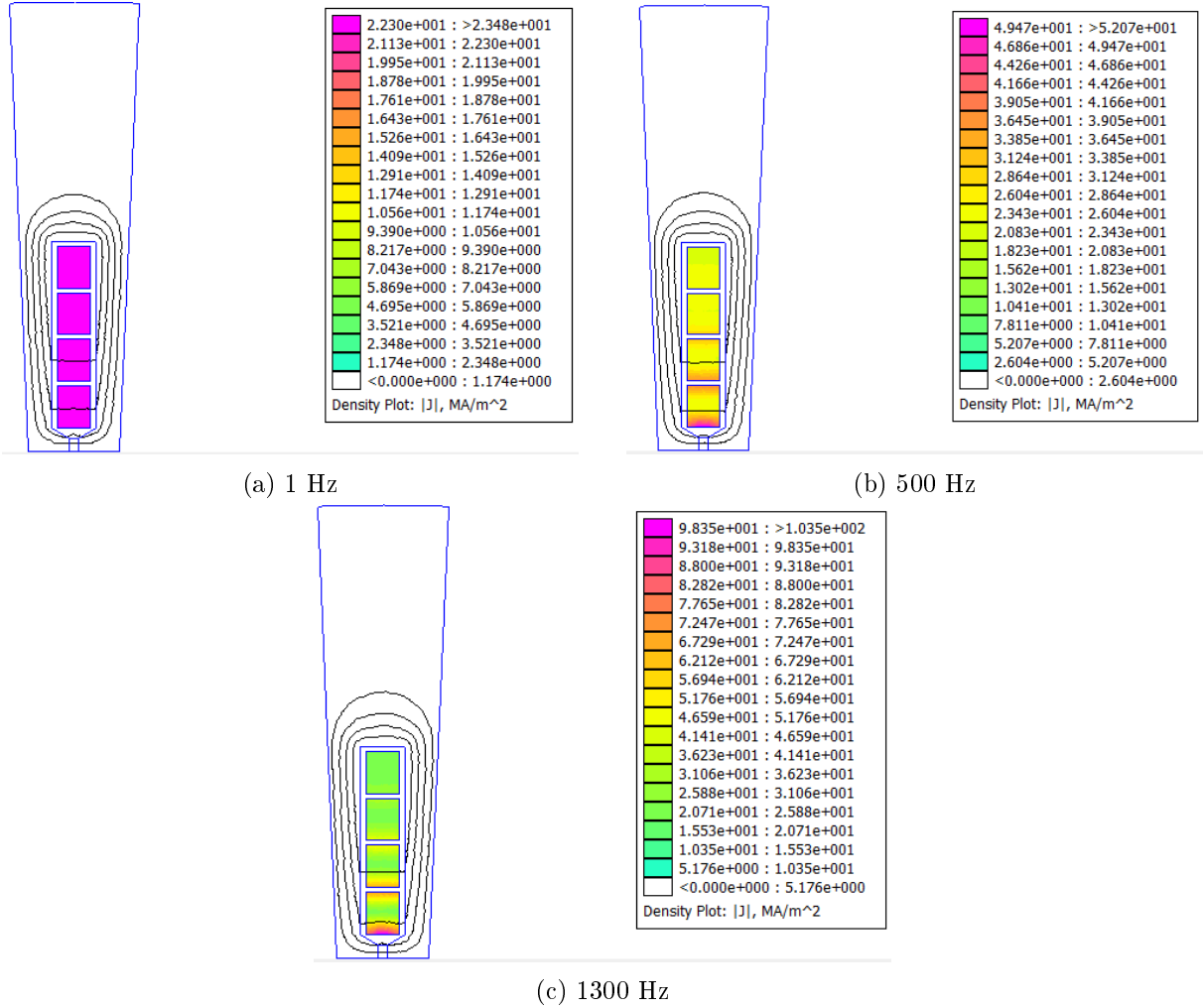


Figure 2.39: Current density distribution at $\hat{I} = 400 A$

Since the simulation is in two dimensions it is necessary to add the resistive contributions deriving from the winding heads. The length of the latter is estimated as

$$L_{end} = 2.5 \cdot \frac{D_{int}}{p} = 87.5 \text{ mm} \quad (2.40)$$

Finally the effective resistance at various frequencies is reported in figure 2.40.

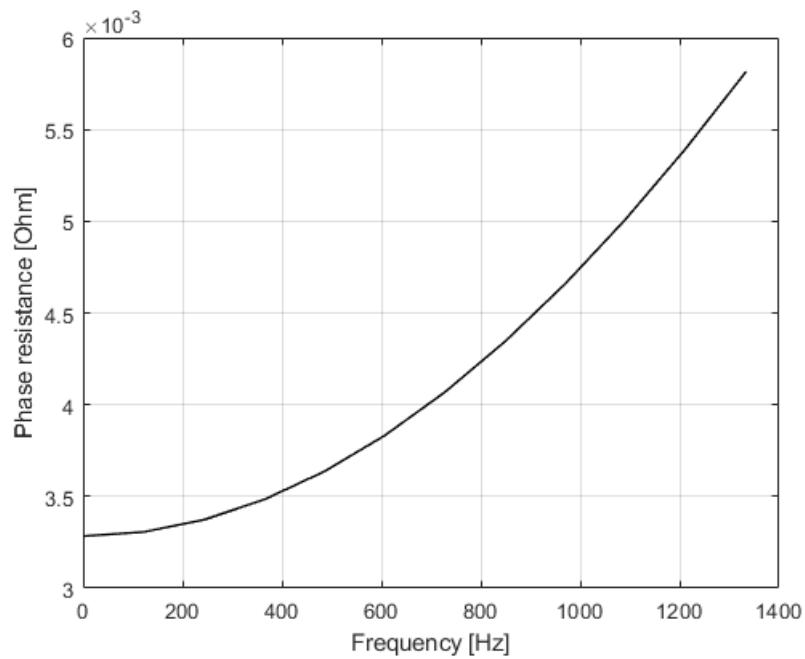


Figure 2.40: Resistance versus frequency

Copper losses can now be computed with equation 2.36. Figure 2.41 shows the distribution of losses due to the joule effect for all working conditions. It can be seen that, although at high speed current magnitude is lower, the thickening effect of the high frequency leads to higher losses.

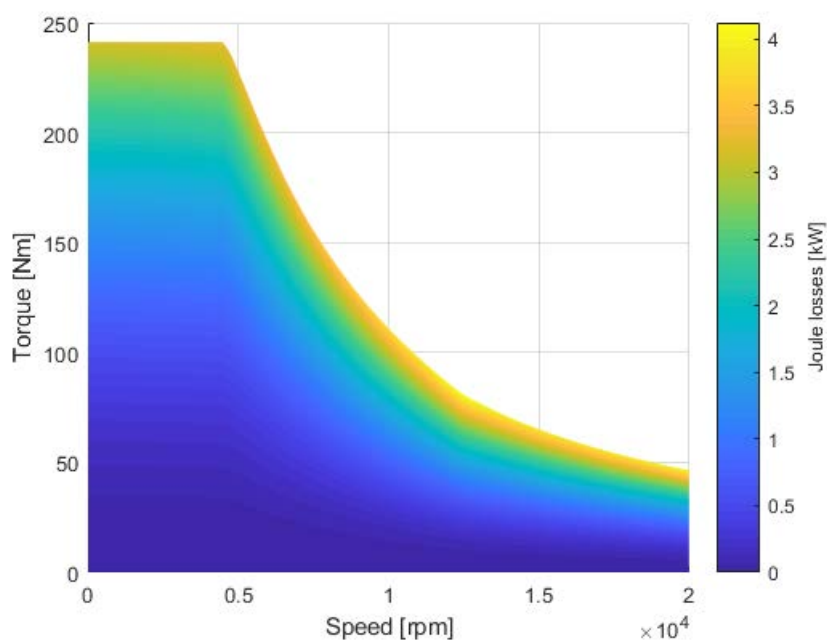


Figure 2.41: Joule losses distribution

Iron losses

To calculate the losses in the iron it is necessary to obtain the maximum induction value in the teeth and in the stator back iron; this is easily done through the FEMM software creating a grid of points and sampling the flux density magnitude. From the electrical steel datasheet specific loss values are extrapolated through the steinmetz formula.

$$p_{spec} = K_{hist} \cdot \left(\frac{B}{B^*}\right)^2 \cdot \left(\frac{f}{f^*}\right) + K_{ec} \cdot \left(\frac{B}{B^*}\right)^2 \cdot \left(\frac{f}{f^*}\right)^2 \quad (2.41)$$

Figure 2.42 shows in a colored graph the double dependence (B and f) of specific losses.

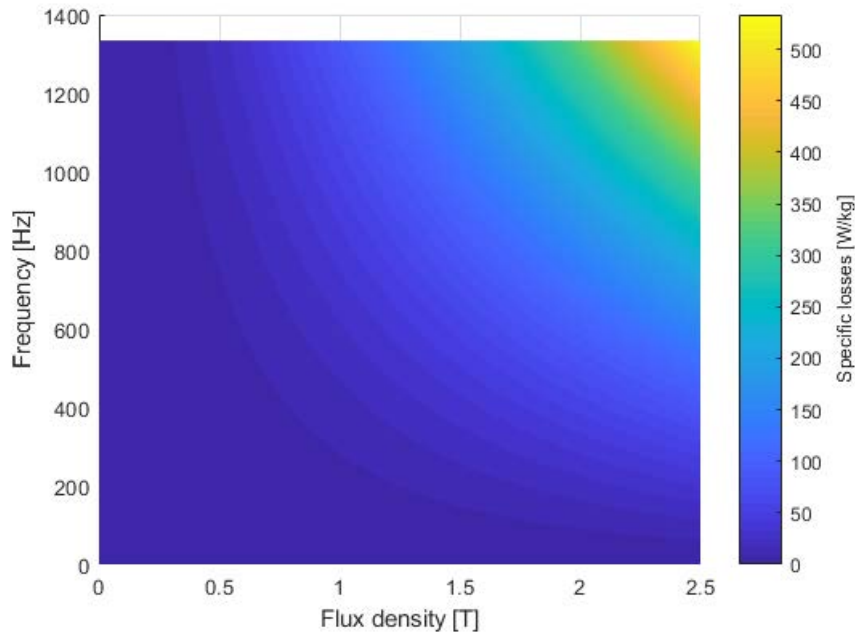


Figure 2.42: Specific losses as function of B and f

Teeth and back iron weight are now calculated multiplying the volume by specific weight of iron ($\gamma_{iron} = 7800 \frac{kg}{m^3}$):

$$G_{iron,t} = \gamma_{iron} \cdot Q_s \cdot w_t \cdot h_s \cdot L_{fe} = 3.17 \text{ kg} \quad (2.42)$$

$$G_{iron,bi} = \gamma_{iron} \cdot \frac{\pi}{4} [D_e^2 - (D_e - 2 \cdot h_{bi})^2] \cdot L_{fe} = 9.36 \text{ kg} \quad (2.43)$$

Total losses are finally calculated by multiplying specific losses by the weight of iron and also by a safety coefficient that takes into account the stress suffered by the steel during processing (e.g. drilling, cutting, lamination...).

$$P_{iron,t} = p_{spec,t} \cdot G_{fe,t} \cdot 2 \quad (2.44)$$

$$P_{iron,bi} = p_{spec,bi} \cdot G_{fe,bi} \cdot 1.5 \quad (2.45)$$

$$P_{iron} = P_{iron,t} + P_{iron,bi} \quad (2.46)$$

Figure 2.43 shows the distribution of iron losses in the stator for all working conditions. It can be seen that the greatest losses occur at high speed.

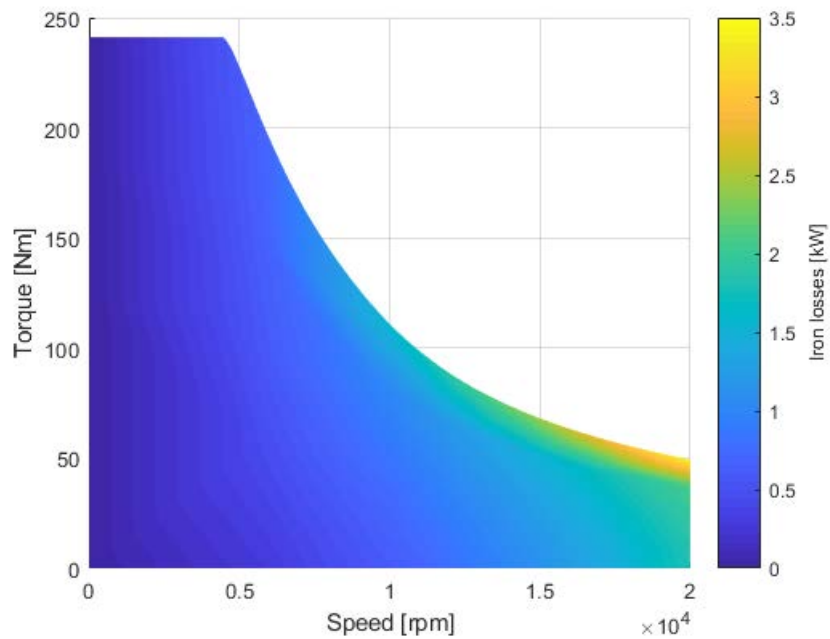


Figure 2.43: Iron losses distribution

Mechanical losses

Mechanical losses computation will be presented in detail in chapter 4, here the results are shown as a map (figure 2.44) for each machine operating point. Obviously mechanical losses do not depend on the torque delivered but only on the rotation speed.

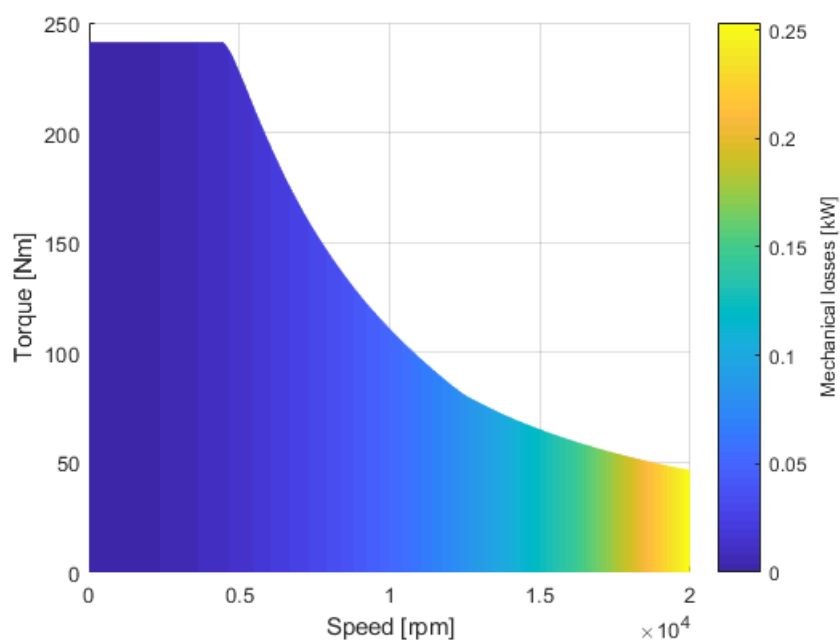


Figure 2.44: Mechanical losses distribution

Rotor losses

Although the rotational speed of the rotor is synchronous with that of the fundamental component of stator magnetomotive force, this does not apply to higher order harmonics that rotate at higher speeds [25]. The rotation speed of the M.M.F. can be expressed by equation 2.47 where it can be seen that high order harmonics have a higher rotational speed. This creates an effect very similar to the slip of asynchronous motors and therefore currents are induced in all the conductive parts of the rotor.

$$\Omega = \frac{2 \cdot \pi i \cdot \nu \cdot f_{\text{fundamental}}}{p} \quad (2.47)$$

These currents cause losses which can be calculated by equation [25]:

$$P_{rl} = \int_{Vol} \frac{J_r^2}{\sigma} dVol = \int_{Vol} \sigma \frac{\partial A_z}{\partial t} \quad (2.48)$$

where

- J is the current density induced in the rotor;
- σ is the electric conductivity of the rotor;
- A_z is the magnetic vector potential along z direction;
- t is the time.

A practical finite element computation of rotor losses is based on the superposition of the effects: the total rotor losses P_{rl} result as the sum of the rotor losses computed for each harmonic order ν , that is $P_{rl} = \sum P_{rl,\nu}$ [26]. A correct simulation would require rotation of the rotor and therefore a transient analysis. However, it is possible to use a stationary analysis, with constant frequency sinusoidal currents, using the following model.

- The stator is replaced by a linear current density positioned on the stator inner diameter. A linear current density $k_{s\nu}(\theta)$, sinusoidally distributed in space, is imposed in such a stator sheet. The peak value of the linear current density can be obtained for each harmonic by

$$\hat{k}_{s\nu} = 2 \cdot \nu \cdot \frac{\hat{U}_{s\nu}}{D} \quad (2.49)$$

where $\hat{U}_{s\nu}$ is the MMF peak value for each harmonic.

- The circumference is divided into a large number of points (N_p) to which a certain current is assigned

$$\hat{I}_{p,\nu} = \frac{\hat{k}_{s\nu} \cdot \pi \cdot D}{N_p} \quad (2.50)$$

$$I_{p,\nu} = \hat{I}_{p,\nu} \cdot e^{j \cdot \nu \cdot \theta} \quad (2.51)$$

- The frequency of the simulation is computed for each harmonic order as

$$f_{\nu r} = f \cdot \left(\text{sgn} \cdot \frac{\nu}{p} - 1 \right) \quad (2.52)$$

where sgn is equal to +1 if the harmonic rotates in the same direction as the rotor and -1 if it rotates the opposite way.

In figure 2.45 the geometry built in FEMM is shown while in table 2.6 the parameters imposed for the analysis are reported.

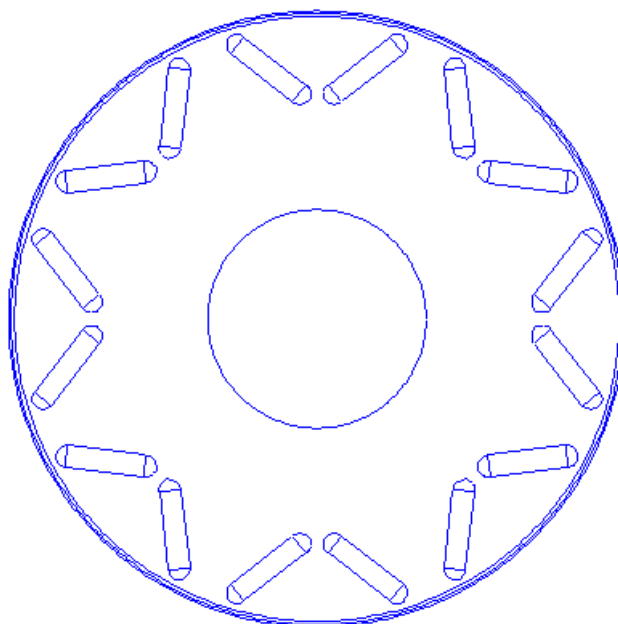
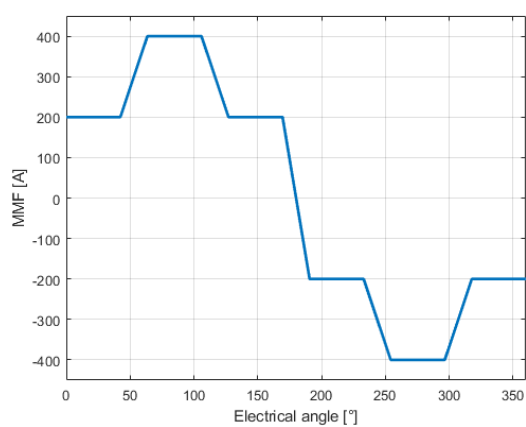


Figure 2.45: Gemetry built in FEMM, notice the stator linear current density

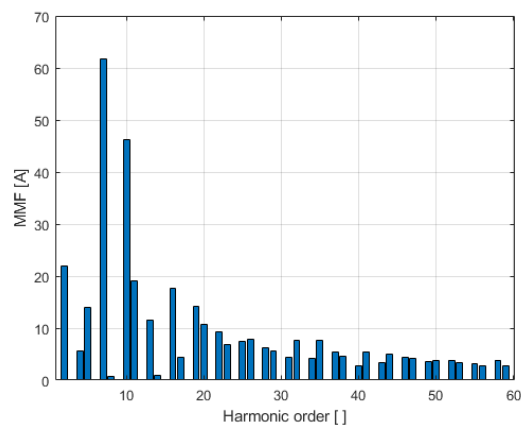
Magnet electrical conductivity	1.16	$\frac{MS}{m}$
Rotor electrical conductivity	0	$\frac{MS}{m}$

Table 2.6: Parameters imposed in FEMM

It is decided to analyze the first 60 harmonics of MMF, as shown in figure 2.46. In figure 2.46b the fondamental component is not shown as it is not a source of loss.



(a) MMF wave shape for one pole pair



(b) MMF harmonics

Figure 2.46: Magneto motive force wave shape and harmonic spectrum

Figure 2.47 shows the flux lines produced by three different harmonics.

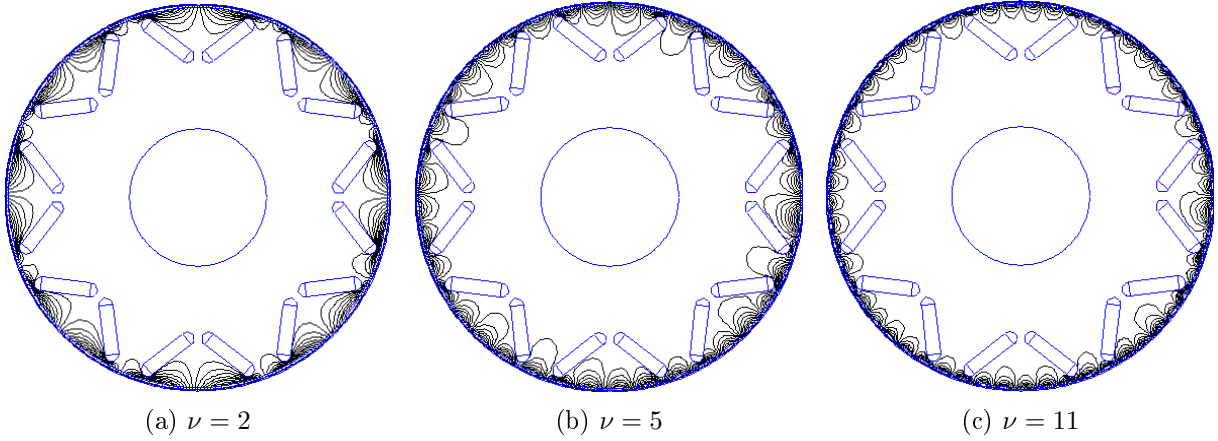


Figure 2.47: Flux lines due to MMF harmonics

Total losses in magnets are equal to $P_{magnet} = 0.95 W$ so they are negligible.

Total losses and efficiency

Total losses are obtained by summing up all losses previously calculated and multiplying them by a safety factor which takes into account any non-calculable contribution.

$$P_{loss} = (P_j + P_{iron} + P_{mech}) \cdot 1.1 \quad (2.53)$$

Efficiency is finally computed as:

$$\eta = \frac{P_n}{P_n + P_{loss}} \cdot 100 \quad (2.54)$$

The efficiency map is shown in figure 2.48; it can be seen how the machine works very well for low speeds and medium torques while at high speeds it has lower efficiency. However most of the working points have an efficiency higher than 80%.

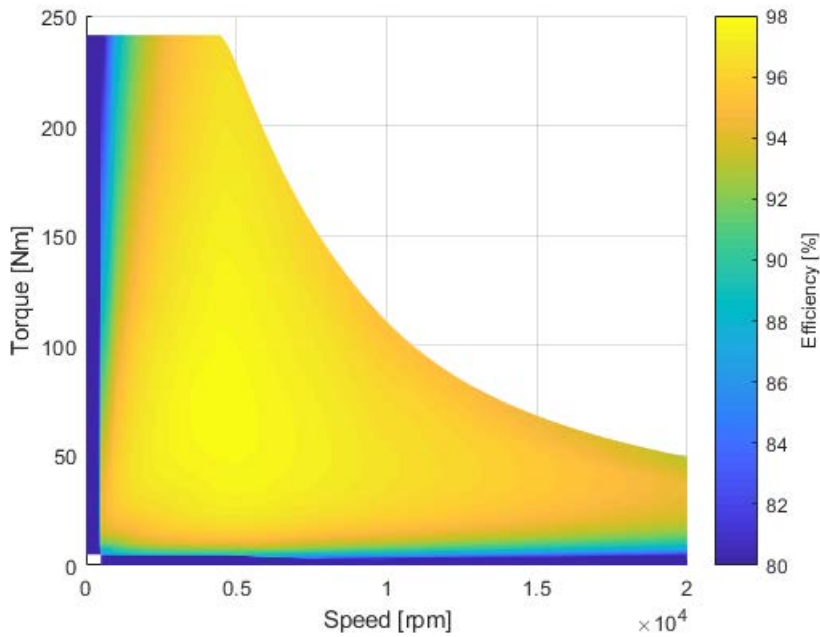


Figure 2.48: Efficiency map

Chapter 3

Wound-rotor synchronous motor

Wound-rotor synchronous motors (WRSM) also known as electrically excited synchronous motors (EESM) are synchronous machines, i.e. the rotation speed of the rotor is synchronous with the speed of the stator rotating field, which have excitation windings housed in the rotor. The purpose of these windings is to produce a magnetic flux which interacts with the flux produced by the stator in order to generate a driving torque. WRSM have significant advantages over IPM motors that come mostly thanks to the fact that they do not need permanent magnets:

- they are much less expensive;
- there is no pollution due to the mining of the rare earth necessary for the realization of magnets;
- the working temperature does not degrade performances so severely;
- there is no risk of demagnetization;
- the fact of being able to control the excitation flux allows a much more effective control in the constant power region making this type of motor excellent for traction.

However, they also have some disadvantages:

- losses in the excitation circuit lowered efficiency;
- the excitation system can be cumbersome and lowered efficiency;
- in the constant torque region, the IPM motor is more performing;
- the torque and power density is lower than motors with magnets;
- the shape that the rotor takes to house the windings is less aerodynamic and therefore windage losses are greater;
- heat removal in the excitation circuit is not trivial.

3.1 Working principles

The governing equations of the WRSM model are the same as the IPM motor, in fact, the presence of a permanent magnet can always be traced back to a current density distribution and vice versa

$$u_a(t) = R \cdot i_a(t) + \frac{d\Lambda_a(t)}{dt} \quad (3.1)$$

$$u_b(t) = R \cdot i_b(t) + \frac{d\Lambda_b(t)}{dt} \quad (3.2)$$

$$u_c(t) = R \cdot i_c(t) + \frac{d\Lambda_c(t)}{dt} \quad (3.3)$$

Because of the anisotropy of the rotor, WRSM is also studied in the d-q rotating system. This time, however, the direct axis is the one with the least reluctance as it has a higher iron content (figure 3.1); this implies that the d-axis inductance is greater than the q-axis inductance.

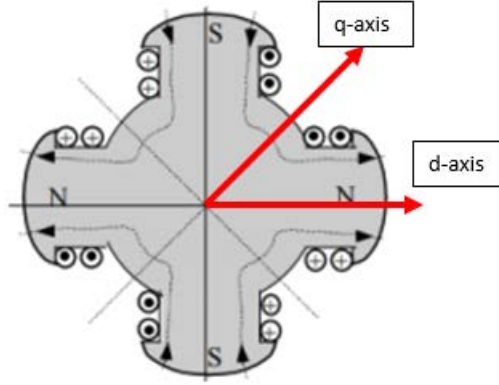


Figure 3.1: Wound-rotor

Again equations (3.1), (3.2), (3.3) are written in terms of space vectors and then written separately for the two axes thus obtaining

$$u_d = R \cdot I_d + \frac{d\Lambda_d}{dt} - \omega_{me} \cdot \Lambda_q \quad (3.4)$$

$$u_q = R \cdot I_q + \frac{d\Lambda_q}{dt} + \omega_{me} \cdot \Lambda_d \quad (3.5)$$

Linkage fluxes are then written as currents and inductances

$$\Lambda_d = \Lambda_{exc} + L_d \cdot I_d \quad (3.6)$$

$$\Lambda_q = L_q \cdot I_q \quad (3.7)$$

Equation structure is the same as the IPM one but this time the magnetization flux (Λ_{exc}) is not constant but depends on the excitation current. As with IPM the torque equation can be written as

$$M = \frac{3}{2} \cdot p \cdot (\Lambda_{exc} \cdot I_q + (L_d - L_q) \cdot I_d \cdot I_q) \quad (3.8)$$

Since $L_d > L_q$ a positive d-axis current is used to get a positive torque.

Control strategy

The control strategy of WRSM is different from IPM motor in fact the excitation flux is variable and therefore there is greater freedom of control. In particular, a strategy identified in [18] and [21] is based on dividing the working operation into three areas as shown in figures 3.2:

- Zone I: voltage limit in this area is not reached, the produced torque is limited by current so we move on the MTPA locus. With increasing speed, the maximum voltage will be reached, and then the machine has to leave MTPA and goes over zone II;
- Zone II: in this area the torque is limited simultaneously by current and voltage. Furthermore, the rotor excitation stays at its maximum.
- Zone III: the torque in this area is limited by voltage. Current must be reduced to keep voltage equation fulfilled. The green curve BC is then the trajectory of various points of torque hyperbolas, which tangent to voltage ellipses over different speed (MTPV).

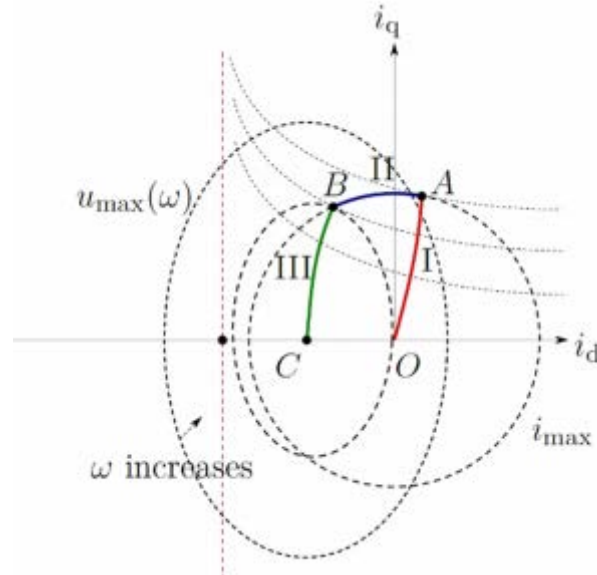


Figure 3.2: WRSM control zones [18]

The above mentioned three operation areas are the same as for an IPM. Since the rotor excitation of WRSM can be actively varied, there is still a further operation state for WRSM to achieve maximum torque characteristic, which is defined as SSB2 (current voltage limitation 2) [21]. The prerequisite is that the origin of the voltage ellipse lies outside the maximum current circle, as shown in figure 3.3.

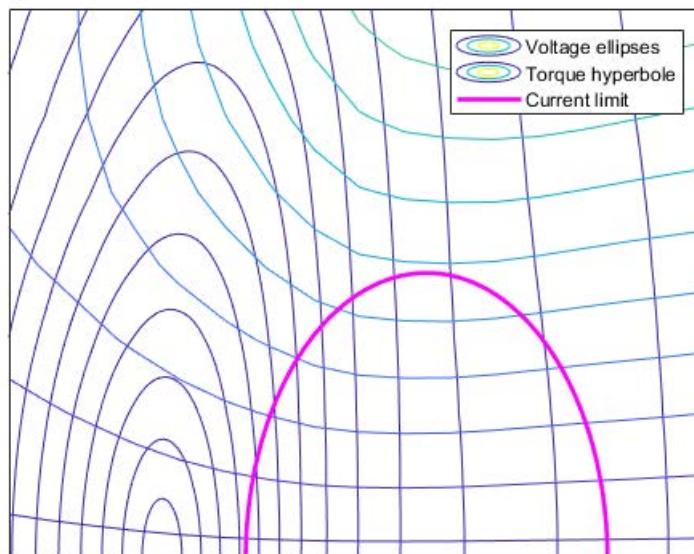


Figure 3.3: Center of voltage ellipses outside the current limit

In this case, IPM has a finite maximum speed. Instead of MTPV operation (which is not available), the current continues along maximum current circle until $I_q = 0 A$, where no more torque can be generated. In contrast, the current phasor of WRSM runs up to the position where voltage phasor and current phasor coincide with the same phase position, i.e. $\cos\phi = 1$. The theoretical maximum mechanical power is reached. Then the current and voltage stay at the maximum, rotor excitation should be reduced gradually and from now on SSB2 begins. For higher speed, the rotor excitation will be adjusted so that $\cos\phi = 1$ remains. In fact, as can be seen from figure 3.4, the maximum power point tends to move towards higher speeds for lower excitation currents. The idea is therefore to move from one curve to another as the speed increases so that the machine always operates at maximum power. When the center of the voltage ellipses coincides with the maximum d-axis current, the excitation is kept constant while the stator current follows the current limit circle. It is important that the center of the ellipses never enter the current circle otherwise the trajectory of the MTPV must be follow which is characterized by significantly lower torques and powers. It is also noted that it is always possible to obtain infinite speed with WRSM. The final power versus speed characteristic will look similar to figure 3.5.

However for traction drive a higher current is always striven in order to improve the torque density of motor, this results in a larger current circle. Meanwhile, the rotor excitation is limited due to thermal problem and direct inductance should be kept as large as possible, since here flows the main magnetic flux. The origin of voltage ellipse is hard to be positioned outside the maximum current circle. But shifting the origin of voltage ellipse towards outside of current circle is still beneficial for improving power factor in field-weakening region.

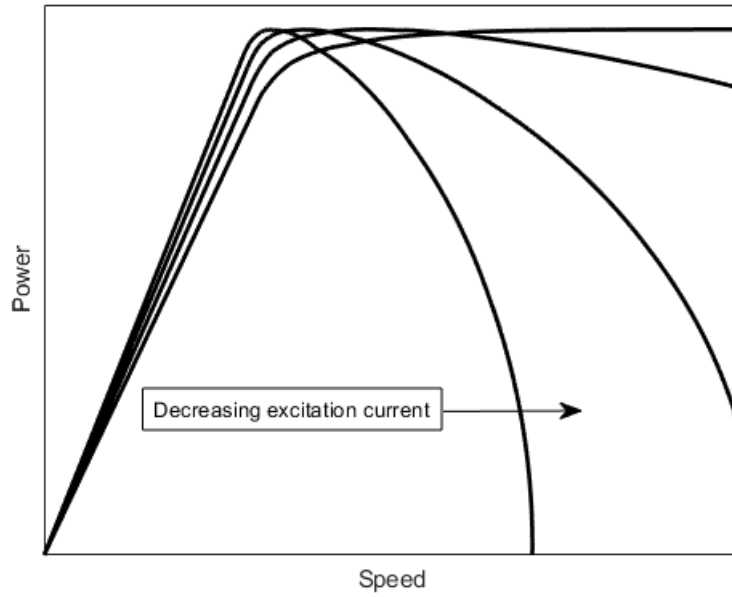


Figure 3.4: Power versus speed for decreasing excitation current

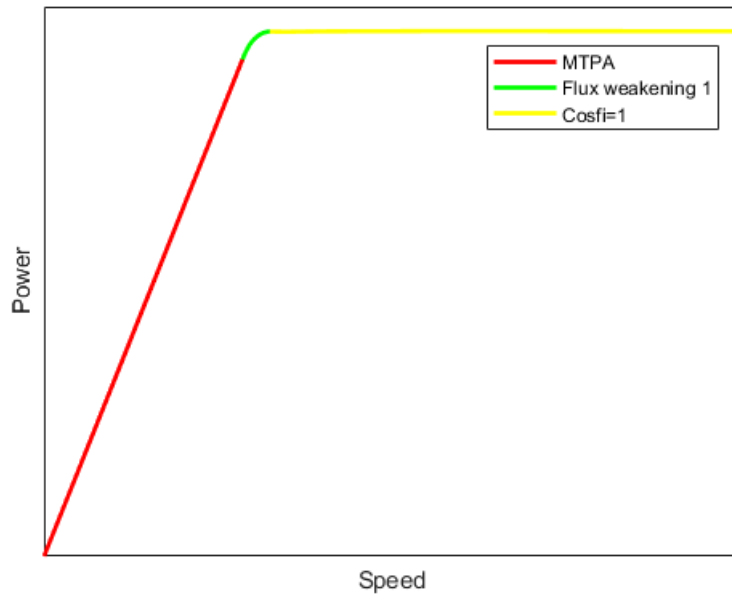


Figure 3.5: Power versus speed with optimal control

3.2 Excitation system

In order to transmit electrical power to the rotor it is necessary to use a system capable of coupling a moving part, the rotor, and a fixed part, the DC power supply. The two most used systems in the field of high powers are the brushes and slip-ring system and the rotary transformer.

3.2.1 Brushes and slip-ring

It is a traditional system, also used in large synchronous generators of production plants where the rotor excitation winding is used to vary the active and reactive power for voltage and frequency regulation. Two conductive rings are keyed on the rotor shaft on which two brushes slide, these are connected respectively to the positive and negative pole of the DC power supply. Further, these slip rings, which are insulated from the shaft, are connected with the terminals of the field winding. It is important to note that in AC motors there is no reed collector and therefore the commutation phenomenon does not occur. This is why the system is much more reliable and long lasting than DC motors. An exemplary drawing is shown in figure 3.6.

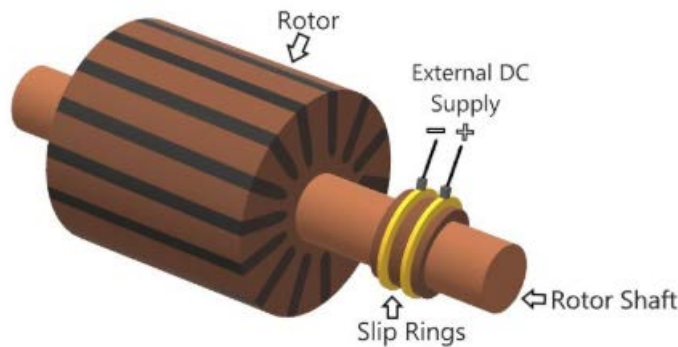


Figure 3.6: Slip-rings and brushes keyed on the rotor [37]

Slip-ring

The slip ring must have three fundamental characteristics, especially for high speed and high current density applications [34]:

- high resistance to mechanical wearing, which guarantees a long operating life;
- a reduced electrical contact resistance which allows an optimal power transfer;
- resistance to oxidation. The high friction and temperature conditions make the phenomenon of oxidation much heavier leading to a rapid deterioration of the materials.

To obtain both characteristics multiple materials are used. Typically the ring is composed of steel on which one or more very thin layers ($3 - 5 \mu m$) of noble metals are deposited. Gold, rhodium and palladium are widely used, thanks to their excellent electrical conductivity and oxidation resistance [34], [35].

Brushes

Also brushes must have the same characteristics as the slip ring. Almost all commercial brushes are metal-graphite brushes. They consist of a graphite matrix to which other materials are added to improve their performance. Graphite has a high wearing resistance and is able to withstand

high temperatures. Furthermore, having a molecular structure composed of many parallel planes joined by weak bonds, it also acts as a lubricant to reduce friction. The other materials added to the graphite matrix are typically metals with high electrical conductivity, especially silver, copper, gold and palladium [36], [34]. In addition, external lubricant is sprayed onto the rings and brushes to reduce friction; typically syntetic fluid ester is used [34].

3.2.2 Rotary transformer

The main disadvantage of traditional WRSM in electric traction is due to the cumbersome presence of the brush-collector excitation system. Slip-rings and brushes constitute a major reliability issue because they wear due to mechanical friction, and produce dust that contaminates the motor insulation. These issues are aggravated by the high-speed operation (up to 20000 rpm) of traction motors, in addition, the efficiency is further reduced. For this reasons it is convenient to replace that system with a rotating transformer and a rotating rectifier. Rotary transformers allow contactless power transfer through the inductive coupling between primary and secondary windings to rotating parts of a system including rotor windings of electric machines. This technology has the potential to enable very cost-effective non-permanent-magnet electric machines like wound rotor synchronous machines for traction applications. A concept of integration of the rotary transformer and rotating rectifier into a WRSM is presented in figure 3.7 [17].

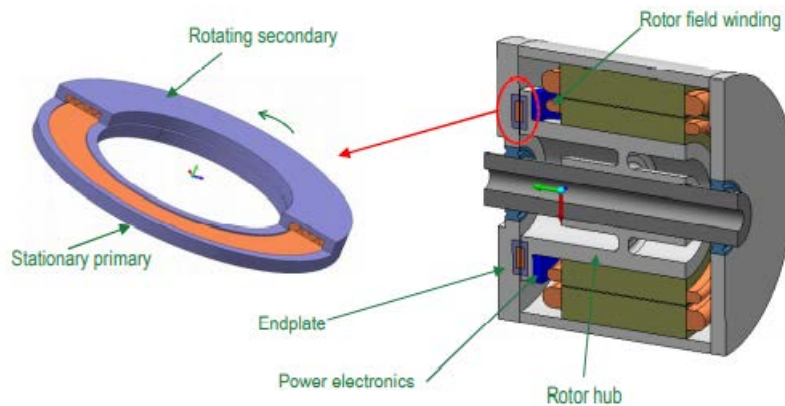


Figure 3.7: Integration concept of a rotary transformer inside a wound-rotor synchronous machine

The rotary transformer is a single-phase transformer with an axial symmetry and an air gap between the primary side and the secondary side. The air gap allows the rotation of one half of the core, without influencing the flux lines and the inductive power transfer between the primary and secondary side. There are different typologies of rotary transformers, the shape of the magnetic core can changes, as well as the relative position of the windings and their collocation inside slots. The two most used typologies are the pot core and the axial rotary transformers, they are shown in figure 3.8 [16].

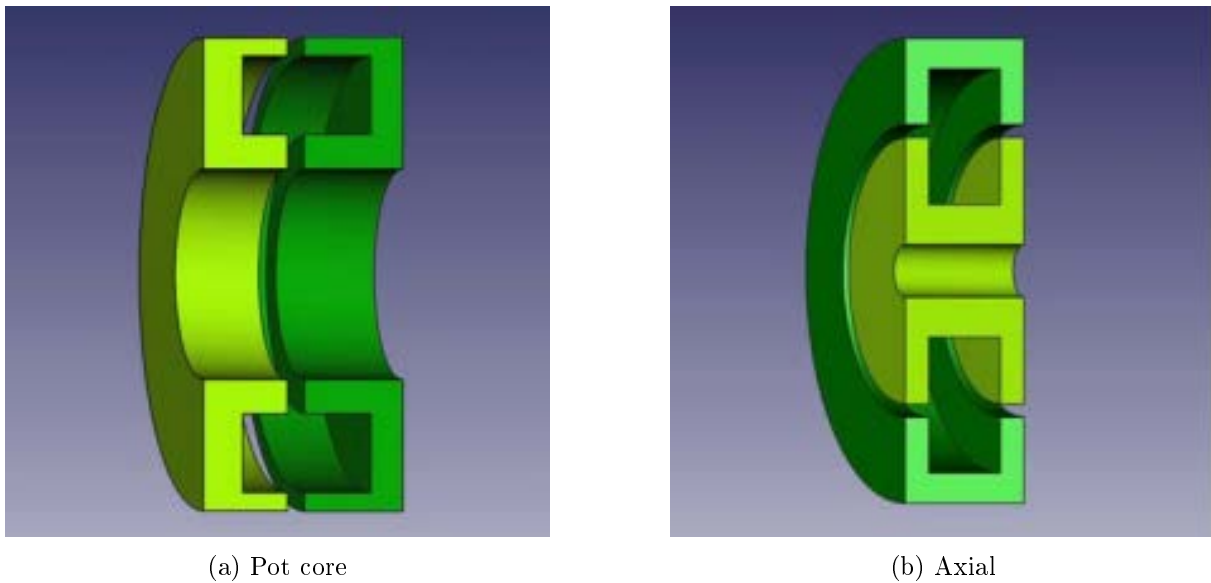


Figure 3.8: Rotary transformer configurations

Both transformers have the secondary side (in light green) splined on a shaft; the primary side (dark green) is kept still and it is connected to the power supply. The secondary side powers the rotating load, in our case the excitation winding of a synchronous machine. The coils are wrapped around the magnetic core, but they can be placed inside the slots in different ways. Windings can be adjacent or coaxial [16]:

- adjacent winding is the most common and easy way to place the coils, because the air gap is completely free and it can be very small. A schematic draw is shown in figure 3.9.

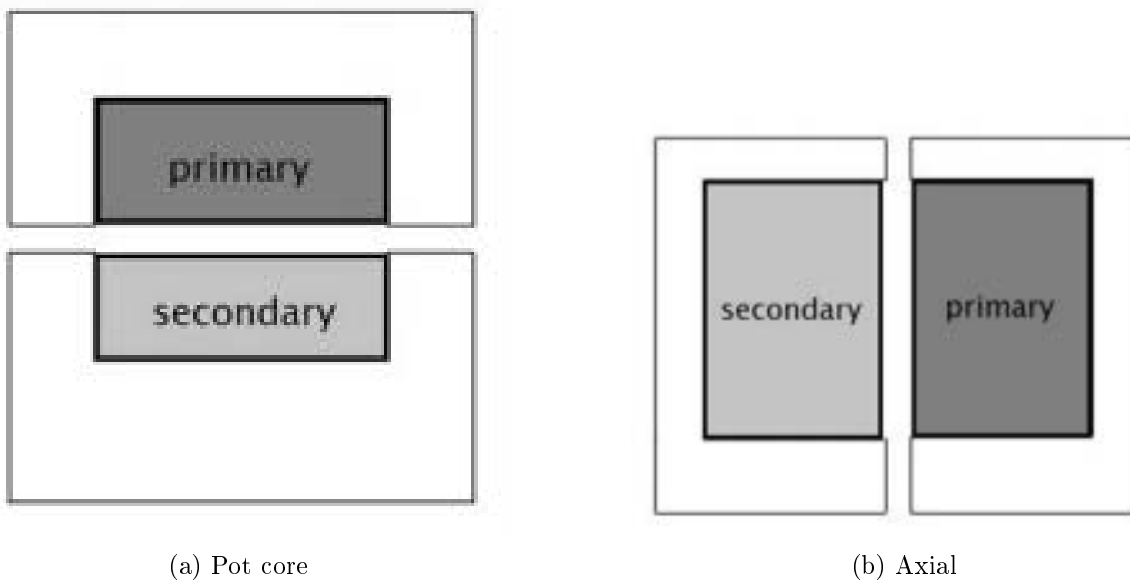


Figure 3.9: Adjacent winding [16]

- coaxial windings allow a better magnetic coupling with a lower value of leakage inductance, but it is difficult to place the coils, above all if there is a small air gap. A schematic draw is shown in figure 3.10.

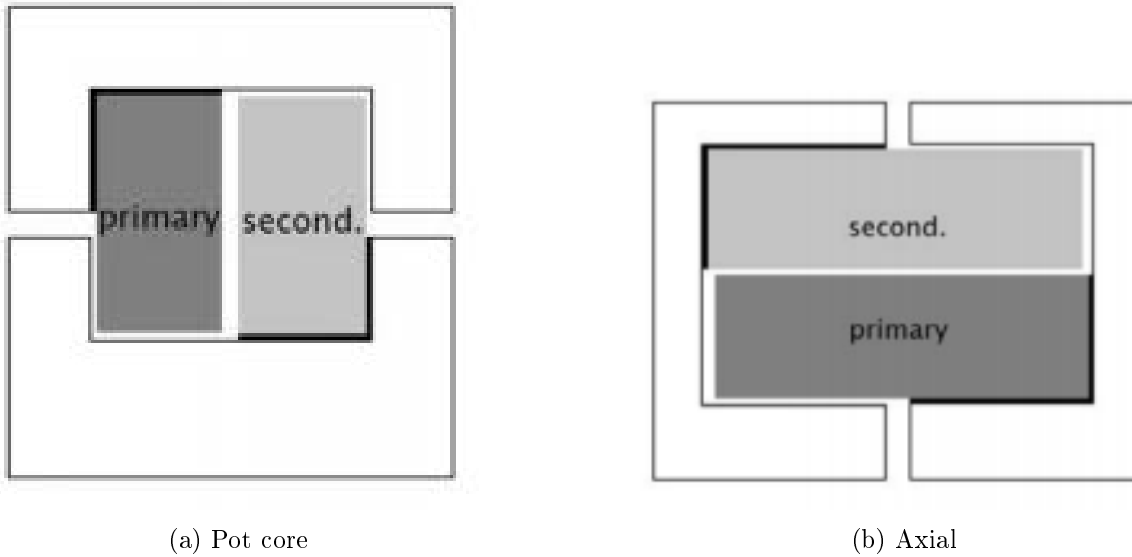


Figure 3.10: Coaxial winding [16]

Effect of the airgap

Although the air gap is mandatory in order to have the rotation, it influences deeply the electromagnetic behavior of the rotary transformer and makes it significantly different from traditional static transformers. The air gap affects both the two main parameters of a transformer: main inductance and leakage inductance.

- main inductance is very small because of the poor coupling, even comparable to the leakage one. This caused a high magnetizing current and therefore high resistive losses in the primary winding;
- leakage inductance is usually very high because there are more leakage fluxes, high leakage inductances caused high voltage drops and problems for power electronics.

Some of this issues can be solved by adding a resonant compensation circuit that significantly increase the power transfer capability, enabling a more compact rotary transformer. As can be seen in figure 3.11 there are two capacitors in series in the primary and secondary winding; they have a capacity that create a series resonance with the primary and secondary leakage inductance thus deleting the reactive impedance. This allows to decrease the voltage drop and the current and therefore also resistive losses thus increasing efficiency. It is also advantageous to use soft switching techniques for electronic converters.

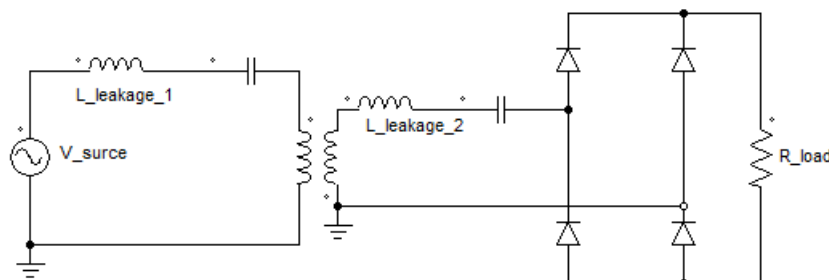


Figure 3.11: Resonant compensation circuit [17]

3.2.3 Comparison

The strengths and weaknesses of the two technologies described above are summarized in table 3.1.

	Brushes and slip-ring	Rotary transformer
State of technology	Very mature	Pretty recent
Dimensions	Cumbersome	More compact
Presence of power electronics	Moderate	Elevated
Maintenance	Moderate	Very low
Transferable power	Very high	Moderate
Efficiency	Quite low	High
Automotive applications	Renault	None

Table 3.1: Rotary transformer versus brushes and slip-ring

3.3 WRSM rotor design

In order to compare more precisely the performances of the IPM motor and WRSM the stator is kept the same and only the rotor is replaced; pole pairs are also unchanged. For the preliminary design, the results obtained by the IPM motor (expecially fluxes) are used, assuming that the two motors work in a fairly similar way. The air gap is chosen equal to

$$g_0 = 0.8 \text{ mm} \quad (3.9)$$

in order to reduce the reluctance of the main flux magnetic path. In fact, the low relative magnetic permeability of air ($\mu_{rel} = 1$) makes it difficult to magnetize paths in such media thus requiring a very high excitation current. Flux density in the airgap is set equal to that of the IPM motor.

$$B_g = 0.7 \text{ T} \quad (3.10)$$

This means that the pole flux is

$$\Phi_p = \frac{B_g \cdot D_{int} \cdot L_{stk}}{p} = 0.00318 \text{ Wb} \quad (3.11)$$

During operation, the complete pole is brought to the same magnetic potential and therefore the air gap flux density assumes a square shape waveform. To obtain a sinusoidal waveform it is necessary to vary the reluctance of the magnetic path in front of the pole by shaping it according to the following equation

$$g(\theta) = \frac{g_0}{\cos(p \cdot \theta)} \quad (3.12)$$

This way the airgap flux density has a sinusoidal waveform

$$B_g(\theta) = \frac{MMF}{R(\theta) \cdot dS} \quad (3.13)$$

where:

- MMF is the magnetomotive force, which doesn't depend on the position;

- $R(\theta)$ is the path reluctance, which varies with a sinusoidal law;
- dS is the infinitesimal area element.

The pole covers $2/3$ of the polar half-step. The height of the pole shoe is calculated with an empirical formula derived from experience:

$$h_{sp} = \frac{1}{4} \cdot \frac{2}{3} \cdot h_s = 2.3 \text{ mm} \quad (3.14)$$

The pole width is chosen so that the machine doesn't saturate during operation. A flux density of 1.5 T is then chosen and the magnetic flux per pole is increased to take into account the leakage fluxes coming from pole shoes and adjacent poles.

$$B_p = 1.5 \text{ T} \quad (3.15)$$

$$\Phi_{p,r} = 1.2 \cdot \Phi_p = 0.003822 \text{ Wb} \quad (3.16)$$

$$L_p = \frac{\Phi_{p,r}}{B_p \cdot L_{fe}} = 20 \text{ mm} \quad (3.17)$$

The yoke height is calculated in similar way:

$$B_y = 0.5 \text{ T} \quad (3.18)$$

$$\Phi_{y,r} = 1.3 \cdot \frac{\Phi_p}{2} = 0.002067 \text{ Wb} \quad (3.19)$$

$$h_y = \frac{\Phi_{y,r}}{B_y \cdot L_{fe}} = 32.5 \text{ mm} \quad (3.20)$$

Finally the pole height must be determined on the basis of the space occupied by the excitation circuit. However, since it is not yet known how many turns are needed, a value is assumed:

$$h_p = \frac{2}{3} \cdot L_p = 13.33 \text{ mm} \quad (3.21)$$

Now instead of proceeding with the drawing of potier-blodel diagram and the analytical analysis, the model is built directly in FEMM to verify its performance. In particular an optimization is carried on in order to evaluate which pole width guarantees the optimal output torque. Since the minimum distance between one pole and the adjacent one must be respected the excitation surface is reduced as the pole width increases thus increasing the excitation current density and excitation losses. As a first approximation all the surface of the excitation is considered conductive. By means of a matlab script the drawing of the pole is carried out automatically with gradually increasing widths, for each width the delivered torque and the excitation current density are calculated. In figure 3.12 the output torque and the excitation current density versus pole width are reported in the same graph. It can be seen that the optimal width is around 26 mm as after this value the derivative of torque with respect to the pole length becomes very small. However the excitation losses increase very quickly thus making thermal management very difficult. It is thus decided to simulate two configuration: the first one has a narrower pole and wider excitation surface while the second one has the optimal output torque.

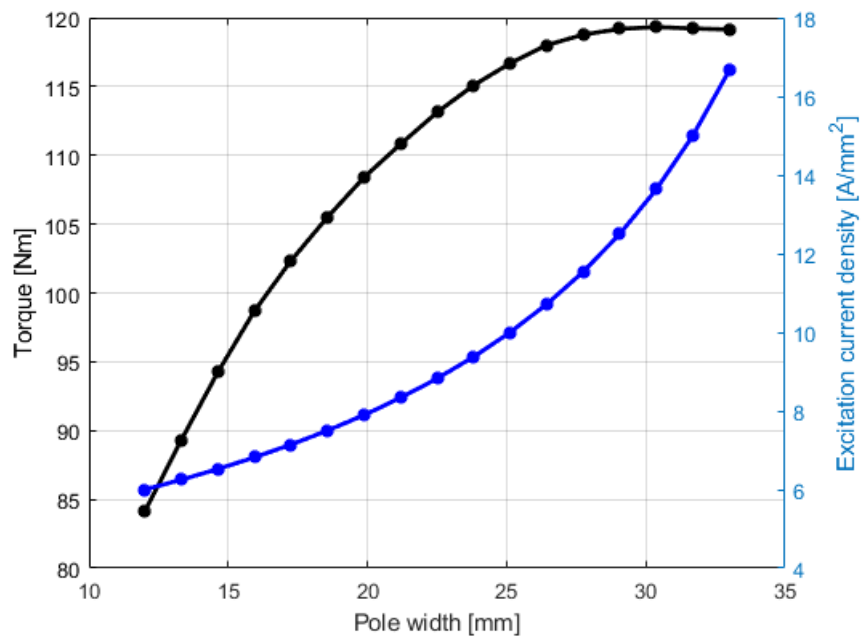


Figure 3.12: Torque and excitation current density versus pole length

The main dimensions of the two configurations are shown in table 3.2 while figure 3.13 show the two geometries built in FEMM.

	Pole width	Pole shoe height	Mesure unit
Narrow pole	20	2.3	mm
Large pole	26	2.3	mm

Table 3.2: Poles main dimensions

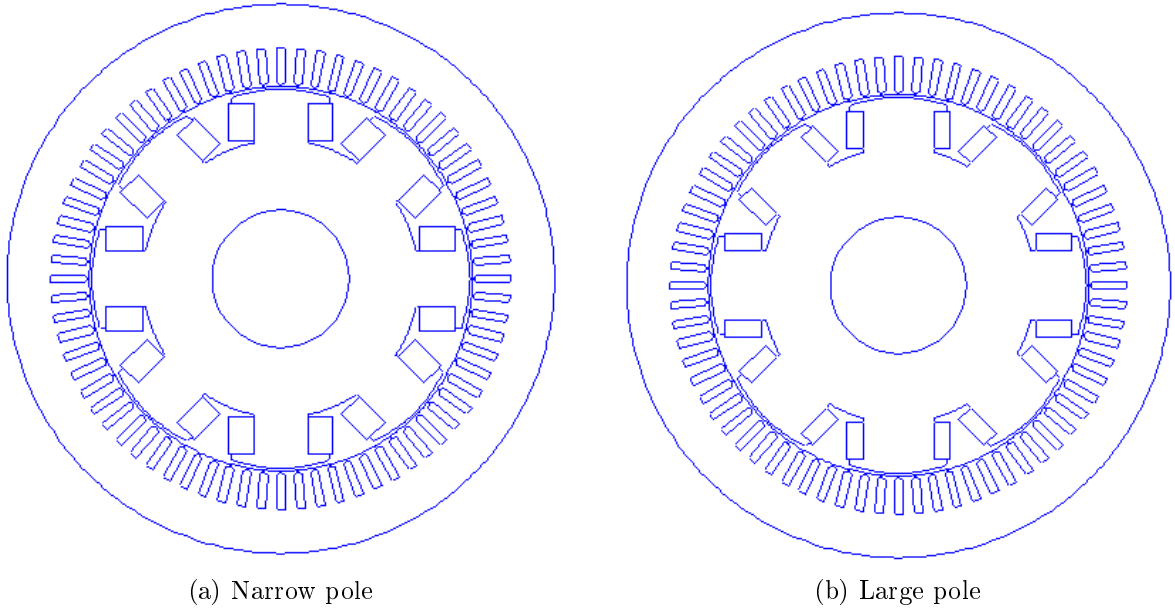


Figure 3.13: Geometries build in FEMM

Excitation winding

To design the excitation winding it is decided to leave 4 mm of distance between the winding of one pole and the next one for thermal and insulation reasons. Commercial ribbon wire are used, with 0.1 mm of insulation on each side. Conductors have a high $\frac{h}{w}$ ratio because it is easier to bend them in the head. On the other hand, however, the removal of heat is more difficult especially for internal ribbons.

	Symbol	Value	Mesure unit
Ribbon wire height	h_{ribbon}	13.2	mm
Ribbon wire width	w_{ribbon}	1	mm
Ribbon surface	A_{ribbon}	13.2	mm ²
Insulated ribbon wire height	$h_{ribbon,in}$	13.4	mm
Insulated ribbon wire width	$w_{ribbon,in}$	1.2	mm
Insulated ribbon surface	$A_{ribbon,in}$	16.08	mm ²

Table 3.3: Ribbon characteristics

For the narrow pole configuration it is possible to make $N_{exc,narrow} = 8$ turns while for the large pole configuration only $N_{exc,large} = 5$ turns as shown in figure 3.14. This means that the total copper section for the two configurations is:

	Symbol	Value	Unit
Narrow pole	$S_{cu,ecc,narrow}$	105.6	mm ²
Large pole	$S_{cu,ecc,large}$	66	mm ²

Table 3.4: Excitation net surface

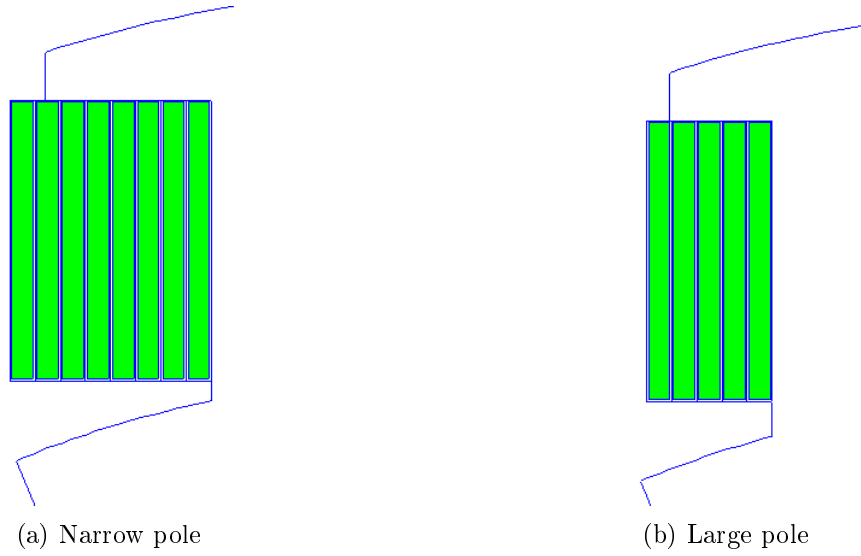


Figure 3.14: Excitation winding

Preliminary tests are carried out with various excitation currents to see the corresponding current densities and losses. This is done to see how much current can be injected into the excitation circuit without causing excessive overheating. A range from 0 to 1500 amperturn is analyzed, current density is computed as follow:

$$J_{exc} = \frac{I_{exc}}{N_{exc} \cdot S_{A_{ribbon}}} \quad (3.22)$$

For losses calculation the following equation is applied:

$$P_{exc} = \rho \cdot J_{exc}^2 \cdot Vol_{exc} \quad (3.23)$$

Excitation volume can be computed as follow:

$$L_{exc} = (L_p + N_{exc} \cdot w_{ribbon,in}) \cdot 2 + (L_{stk} + N_{exc} \cdot w_{ribbon,in}) \cdot 2 \quad (3.24)$$

$$Vol_{exc} = N_{exc} \cdot A_{ribbon,in} \cdot L_{exc} \quad (3.25)$$

The main dimensions for losses computation are shown in table 3.5

	Number of turns	Excitation perimeter [m]	Excitatio volume [m^3]
Narrow pole	8	0.338	$3.57 \cdot 10^{-5}$
Large pole	5	0.336	$2.21 \cdot 10^{-5}$

Table 3.5: Excitation main dimensions

Figure 3.15 shows the excitation current density in the two configurations with variable excitation current while figure 3.16 shows the excitation losses.

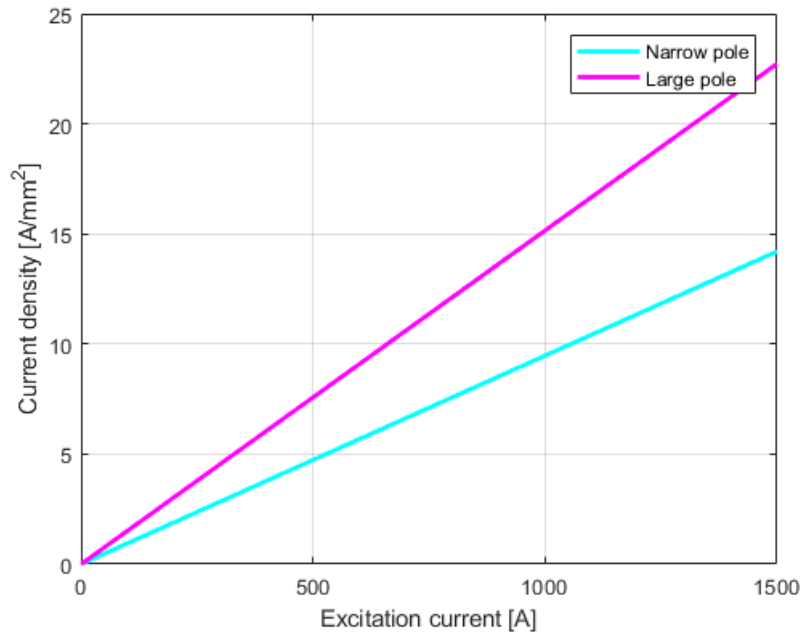


Figure 3.15: Current density versus current

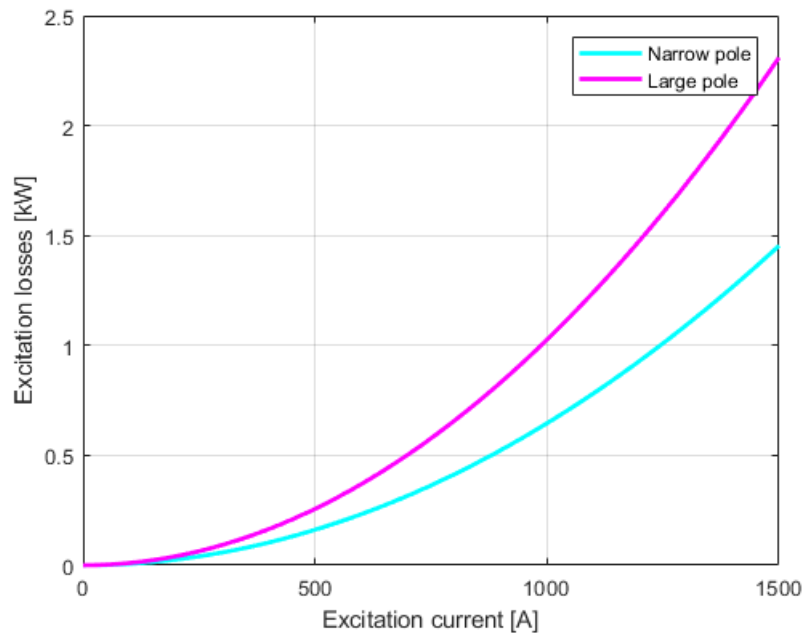
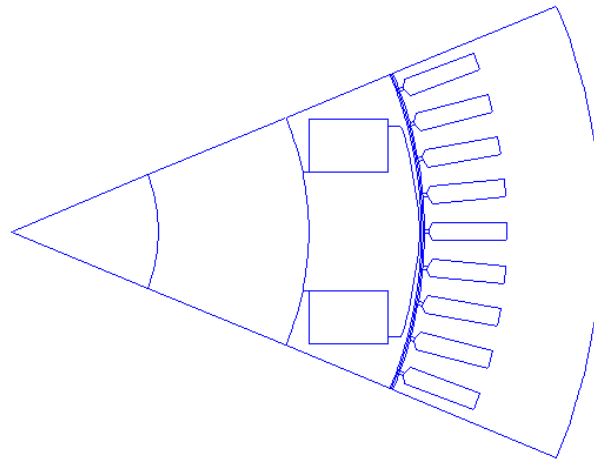


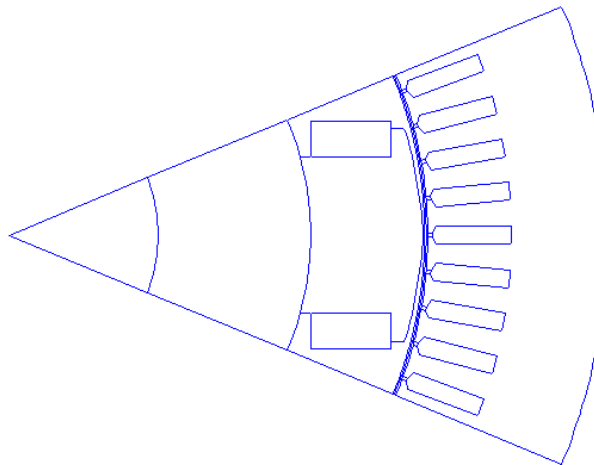
Figure 3.16: Losses versus current

3.4 WRSM analysis

The analysis of the motor proceeds in a way completely identical to what has already been done for the IPM motor. The stator has the dimensions indicated in table 2.3 and the slot matrix is the same as the IPM, also the study is performed on a single pole, imposing anti-periodic conditions. The two configurations (showed in figure 3.17) will be analyzed in parallel.



(a) Narrow pole



(b) Large pole

Figure 3.17: Geometries simulated in FEMM

3.4.1 No load analysis

No load analysis is carried out for different values of excitation current. From figure 3.18 can be seen that the large pole configuration has a wider linear region so it is possible to use higher current without risk of saturation. Furthermore, for quite low excitation current values (i. e. < 600 A) the linkage flux is practically identical in the two configurations as the machine is operating in the linear zone. From this it can be understood that the configuration with a wider pole is capable of exhibiting superior performance only for very high excitation currents, which would be unusable with the narrower pole. Obviously high currents imply high losses, above all because in the wide pole configuration the excitation section is very poor. It should also be noted that for a current of 600 A the linkage flux is 0.038 Vs, very similar to that produced by the IPM,

therefore it is decided to continue the analysis with that excitation current.

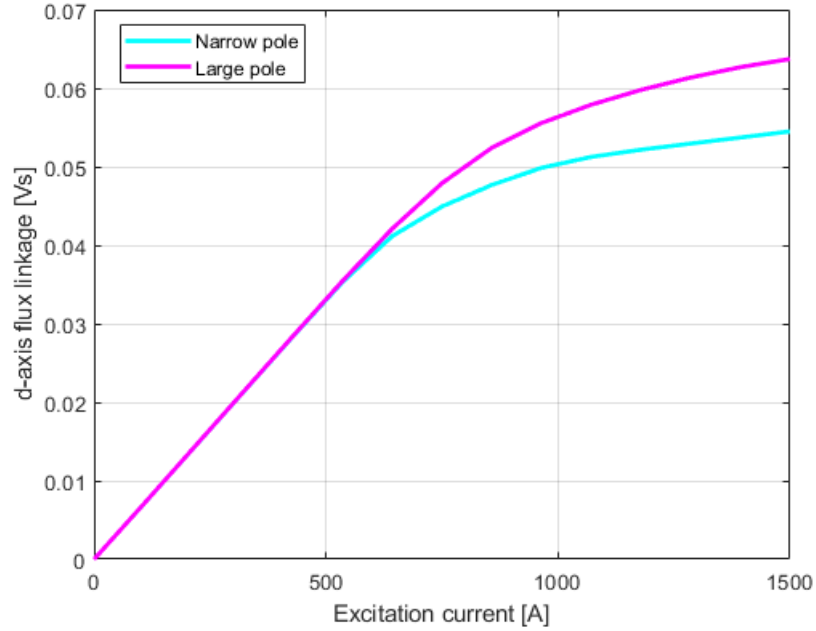


Figure 3.18: Linkage flux versus excitation current

Airgap

The airgap flux densities are shown in figure 3.19, while flux density harmonics are shown in figure 3.20. As can be seen there are not big differences between the two but there is a big difference with IPM waveform because the rotor shape is completely diverse.

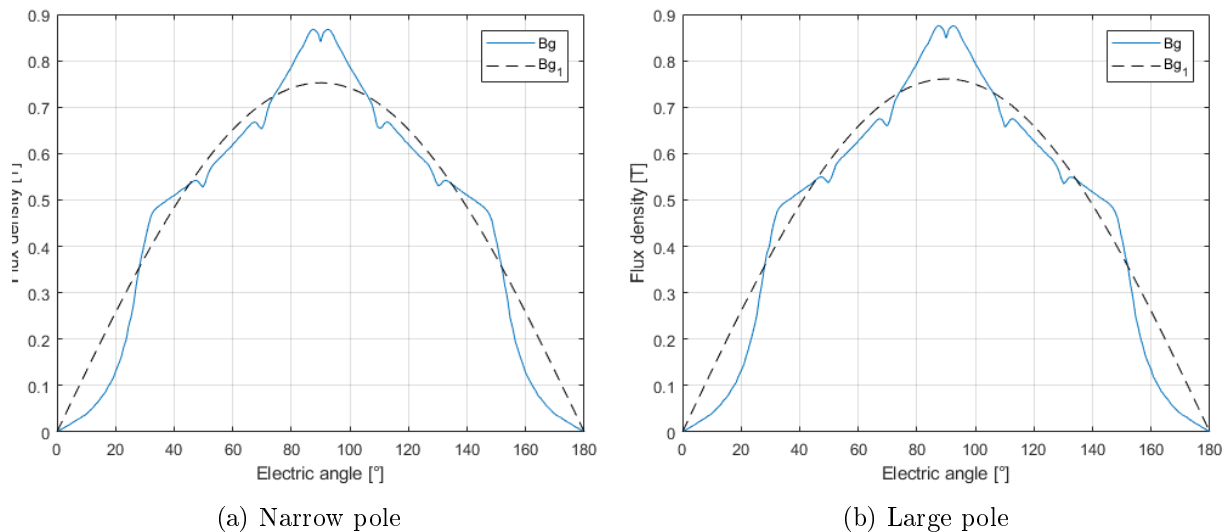


Figure 3.19: Airgap flux density

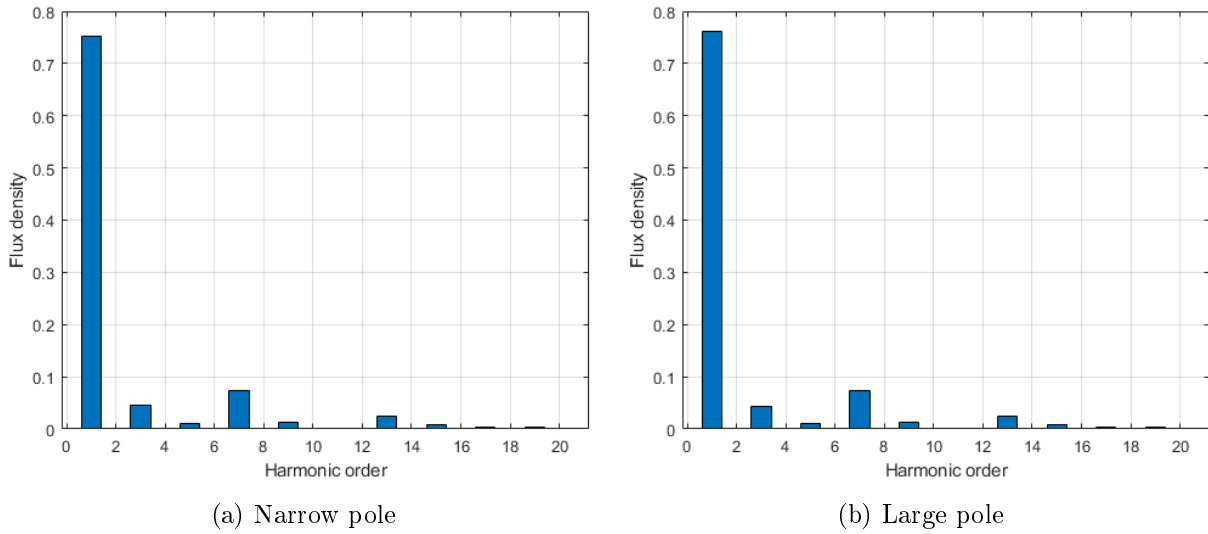


Figure 3.20: Airgap flux density harmonics

Cogging torque

Cogging torque for both geometry is shown in figure 3.21 again computed in two different modes. Since the number of stator slots and the number of poles have not changed, the WRSM also has a 5° torque oscillation period. No differences are noticed between the two geometries.

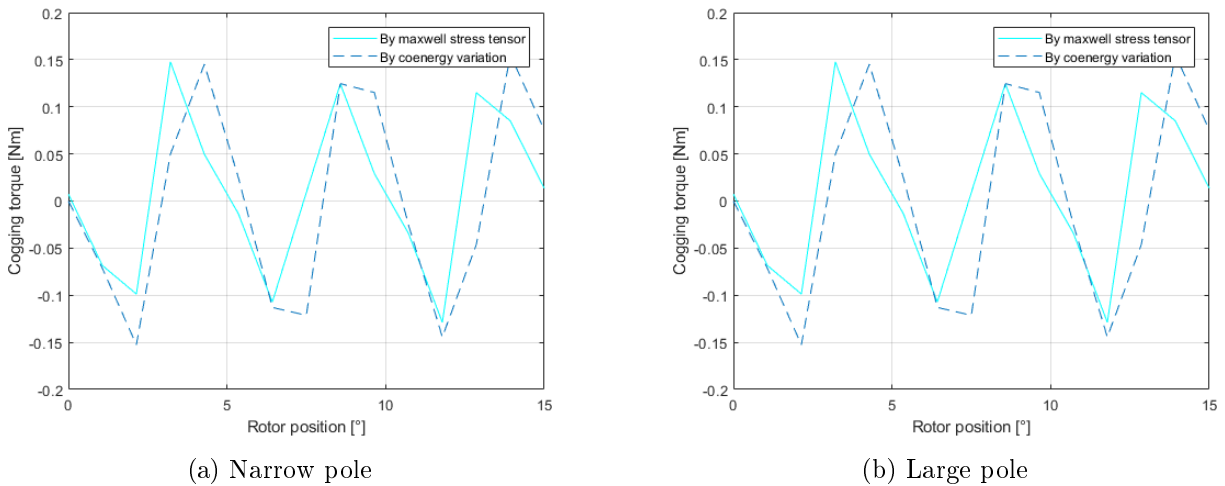


Figure 3.21: Cogging torque

Linkage fluxes and emf

Linkage fluxes by the three phases are calculated at various rotor positions and reported in figure 3.22. It can be seen that the rotor d-axis is aligned with the phase *a* axis and that the two figures are identical. That's because with excitation current $I_{exc} = 600 A$ the machine works in linear zone and fluxes are the same (see figure 3.18).

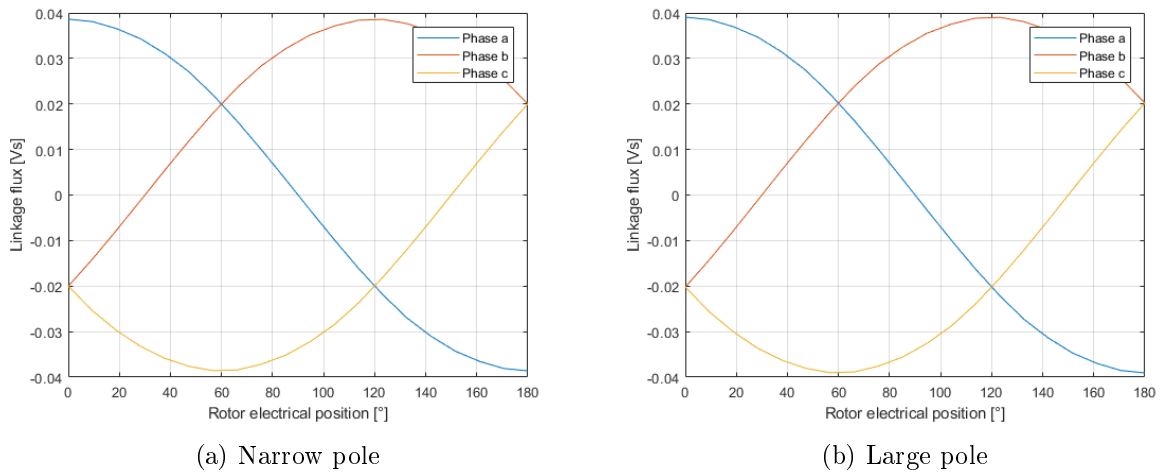


Figure 3.22: Linkage fluxes

By breaking down the waveform of the flux linkage of phase *a* into its series of fourier, it is possible to obtain the harmonic spectrum of figure 3.23, only one configuration is reported since it was already observed that they are indetical. As for the IPM motor very low harmonic content can be noted.

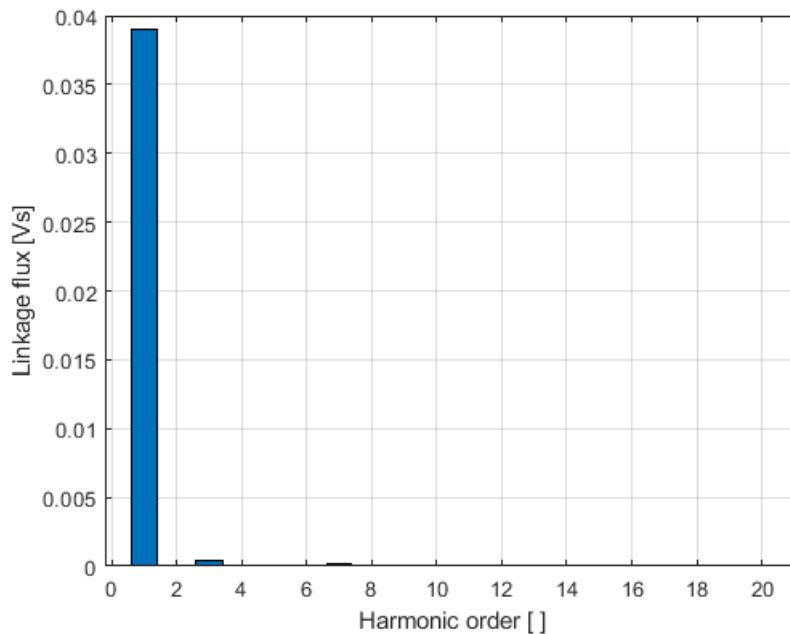


Figure 3.23: Linkage flux armonics

Induced voltage at constant speed $n = 5000 \text{ rpm}$ is shown in figure 3.24. The induced voltage is slightly higher than the IPM motor but still a difference small enough to be negligible.

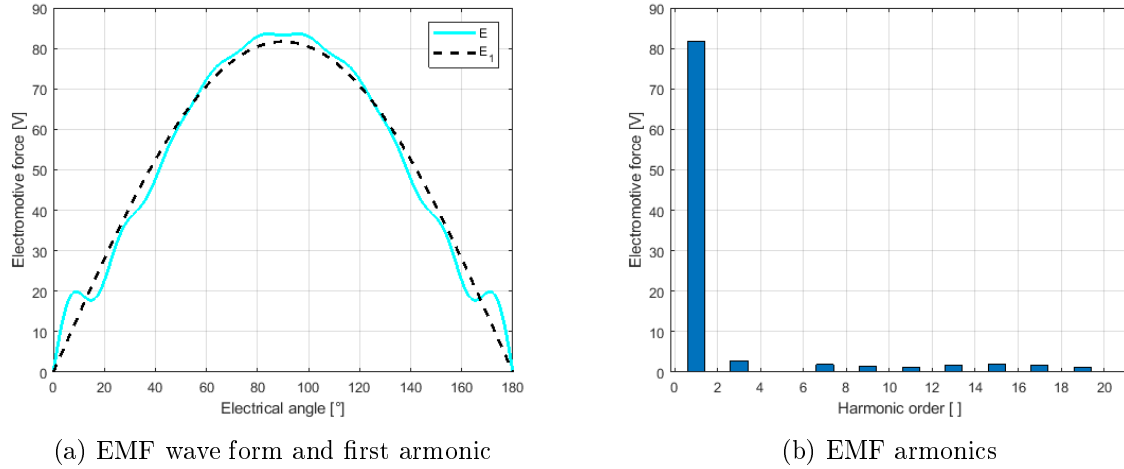


Figure 3.24: No-load phase back electromotive force

Finally, the flux density map for the two configurations is shown in figure 3.25. It is clearly seen that the wide configuration has much lower flux density values in the pole.

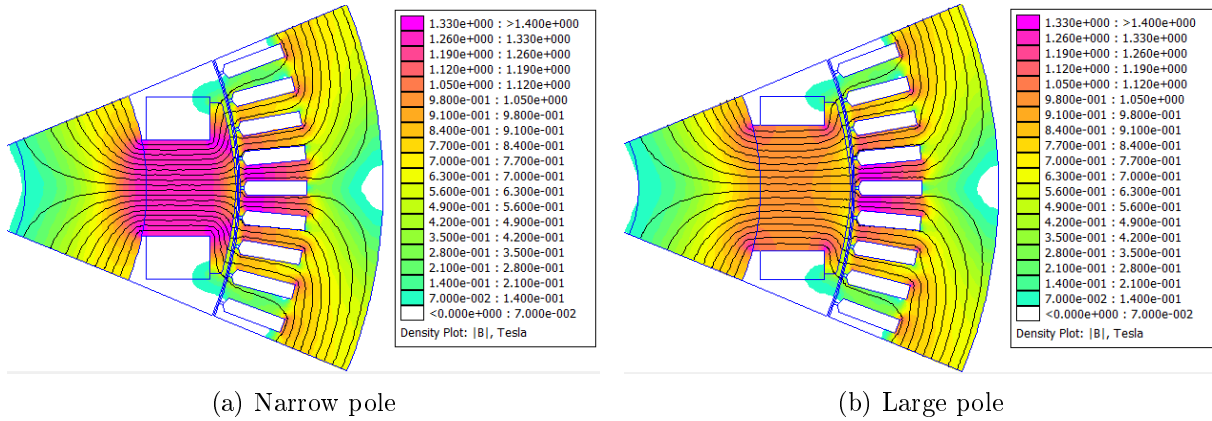


Figure 3.25: Flux density map

3.4.2 Inductances

As for the IPM motor, we define a d-axis and a q-axis inductance. d-axis inductance can be calculated by putting to zero the excitation current and supplying the stator with a d-axis current computing the d-axis flux linkage and then applying the following equation

$$L_d = \frac{\Lambda_d}{I_d} \quad (3.26)$$

Alternately it can be calculated via the total magnetic energy $A \cdot J$ (energy plus co-energy) with the following equation

$$L_d = \frac{2 \cdot 2 \cdot \int A \cdot J}{3 \cdot I_d^2} \quad (3.27)$$

Figure 3.26 shows d-axis inductance for various d-axis current for both configuration. It can be seen that values are very closed between the two geometry.

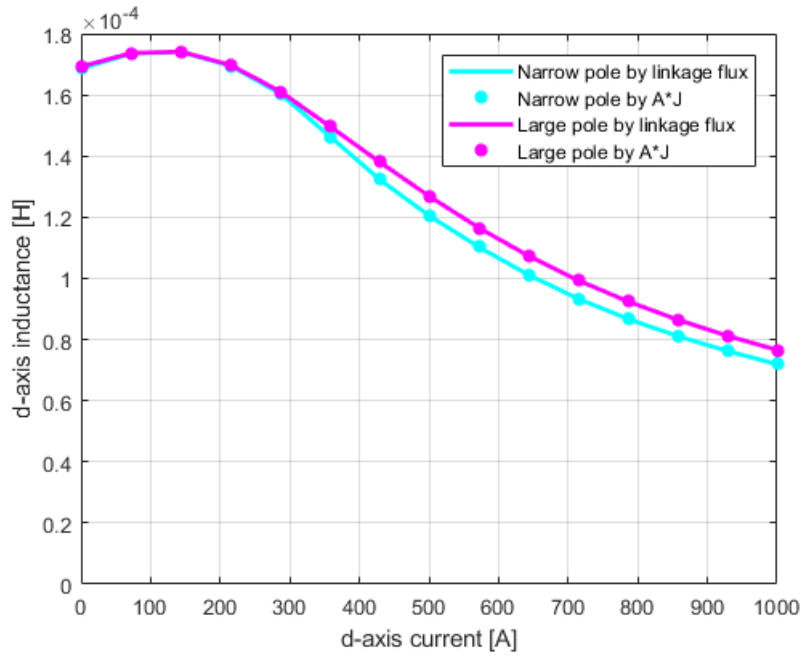


Figure 3.26: d-axis apparent inductance versus d-axis current

A similar procedure is done for the q-axis, once again it can be seen that inductances are similar between the two configurations (figure 3.27).

$$L_q = \frac{\Lambda_q}{I_q} \quad (3.28)$$

$$L_q = \frac{2 \cdot 2 \cdot \int A \cdot J}{3 \cdot I_q^2} \quad (3.29)$$

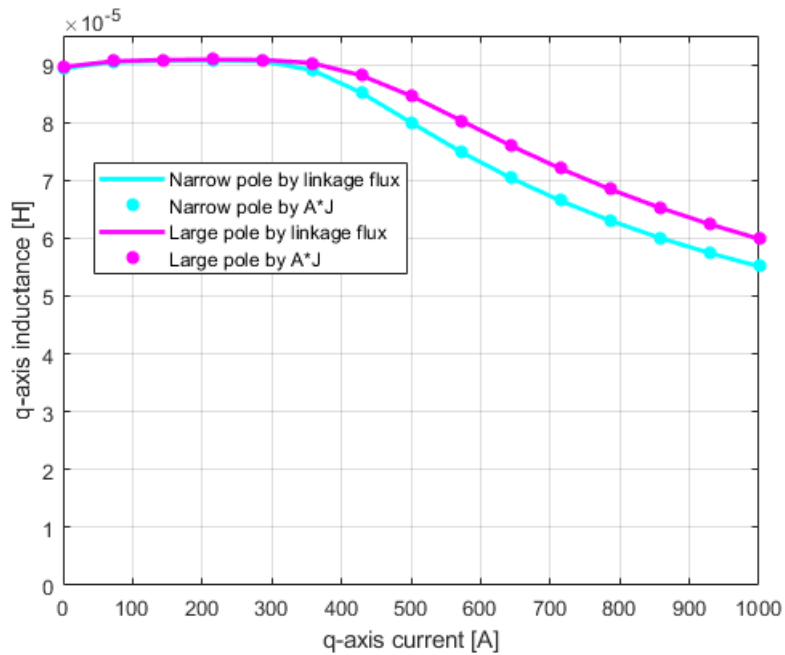


Figure 3.27: q-axis apparent inductance versus q-axis current

In figure 3.28 saliency ratio $\frac{L_d}{L_q}$ is shown. Unlike IPM motor, the d-axis inductance is greater than the q-axis inductance, moreover the saliency ratio is lower. This means that, for the same current and flux, the reluctance torque of the WRSM is less than that of the IPM. It can also be seen that saliency ratio is almost equal between the two configurations.

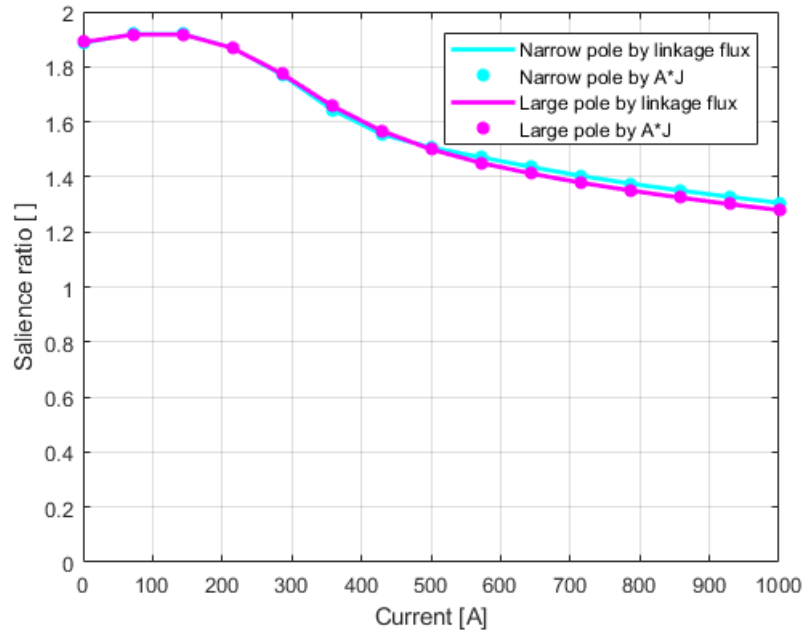


Figure 3.28: Saliency ratio versus current

As for IPM cross coupling is not considered. Given the results obtained regarding the inductances of the two configurations, a fairly small difference is expected in terms of performance between the two.

3.4.3 On load analysis

As already done for the IPM motor, the d-q current plane is mapped. This time, however, a positive and negative d-axis current must be mapped. In fact, as can be seen from figure 3.2, the control of the WRSM machine also requires negative d-axis currents. Figure 3.29 shows the location of the MTPA calculated analytically, using equation 2.19, and the one calculated numerically as already illustrated for the IPM motor. The analytical calculation leads to a trajectory of the MTPA somewhat different from the numerical calculation but in any case such as to confirm the correctness of the analytical formulas. It is also noted that with the same excitation and stator current the large pole configuration develops, as expected, an higher torque.

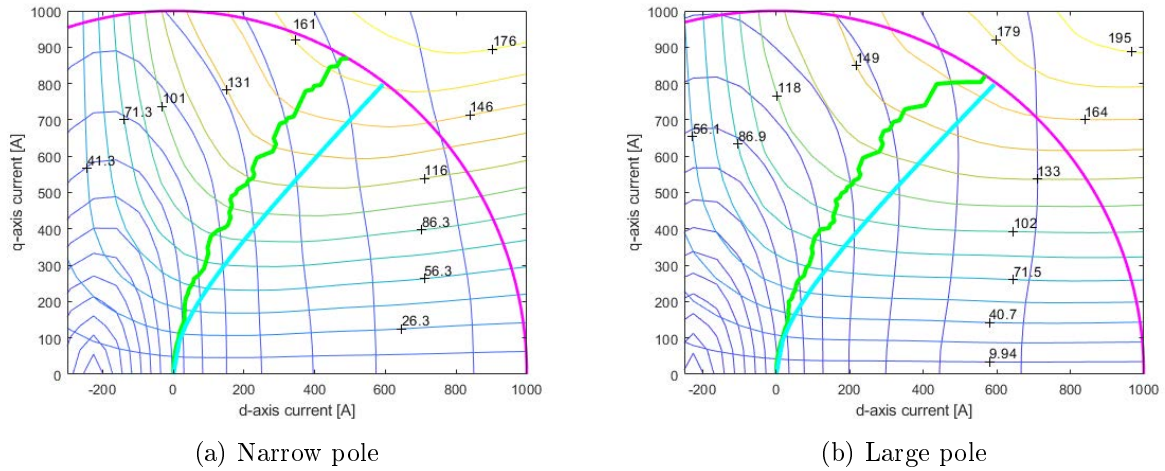


Figure 3.29: d-q current plane, numerical MTPA (green) and analytical MTPA (light blue) at $I_{exc} = 600 A$

In the same way as for IPM motor, the MTPV locus is calculated both numerically and analytically (through equation 2.20) and shown in figure 3.30. It can be seen that the two curves are very similar and therefore the analytical equation is a good approximation of the real trend.

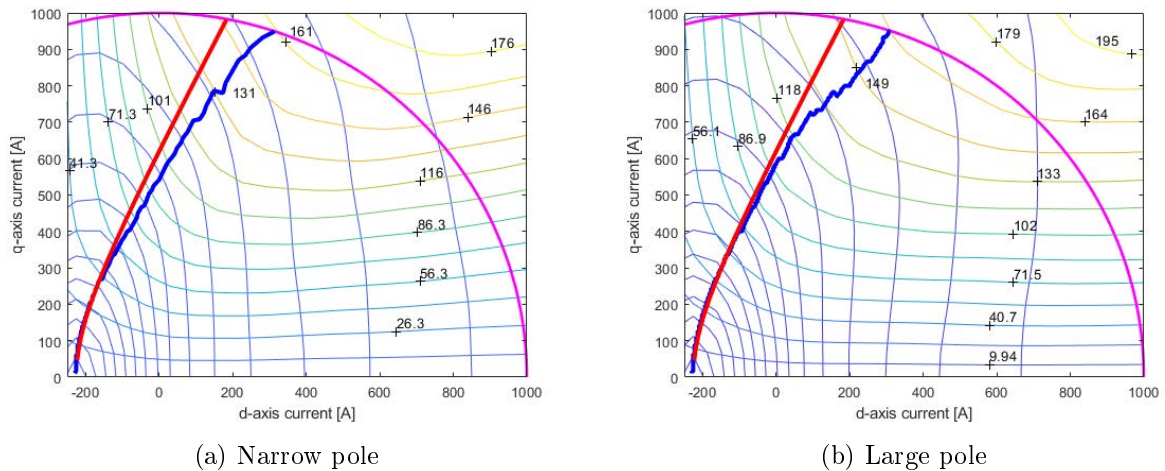


Figure 3.30: d-q current plane, numerical MTPV (blue) and analytical MTPV (red) at $I_{exc} = 600 A$

In figure 3.31 numerical MTPA and MTPV loci are shown.

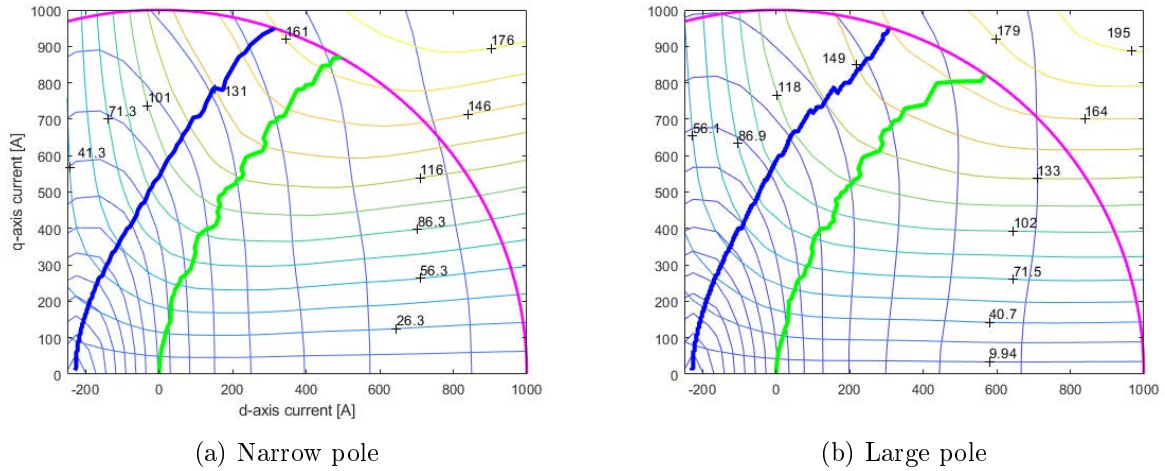


Figure 3.31: Numerical MTPA (green) and numerical MTPV (blue) at $I_{exc} = 600 A$

For WRSM, MTPA and MTPV depend on the excitation current. This means that the calculation of the map must be performed for each excitation current value that is intended to be use. The analysis of the torque delivered as a function of rotor position is now presented. As done for the IPM motor, the calculation is performed by means of maxwell stress tensor and d-q torque plus coenergy variation. The trends for various excitation current are shown below in figure 3.32, 3.33 and 3.34.

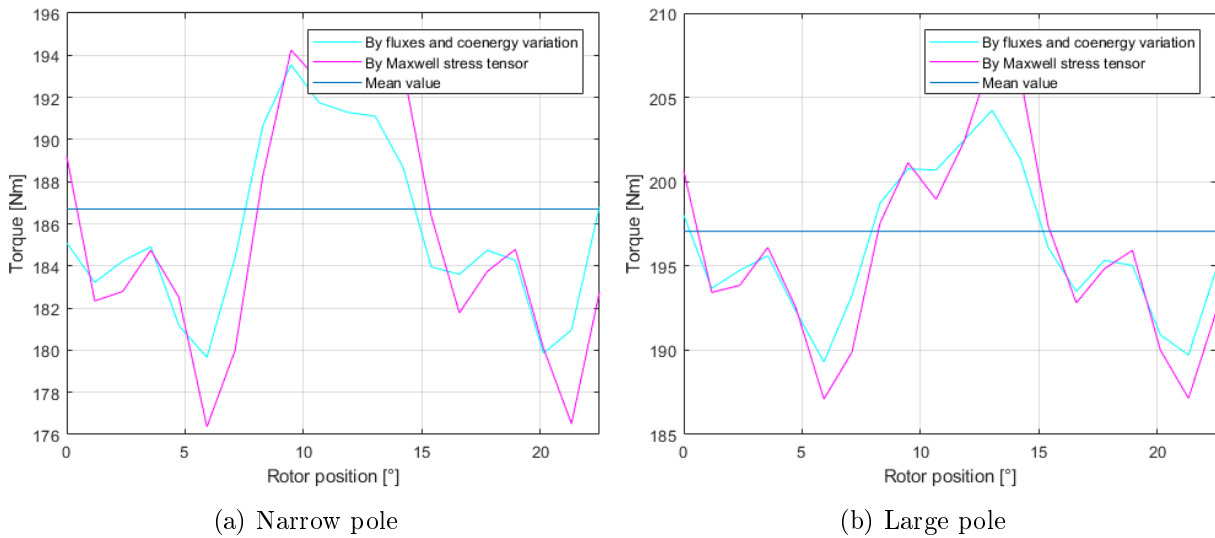


Figure 3.32: Torque at $I_{exc} = 1000 A$ and $\hat{I} = 800 A$

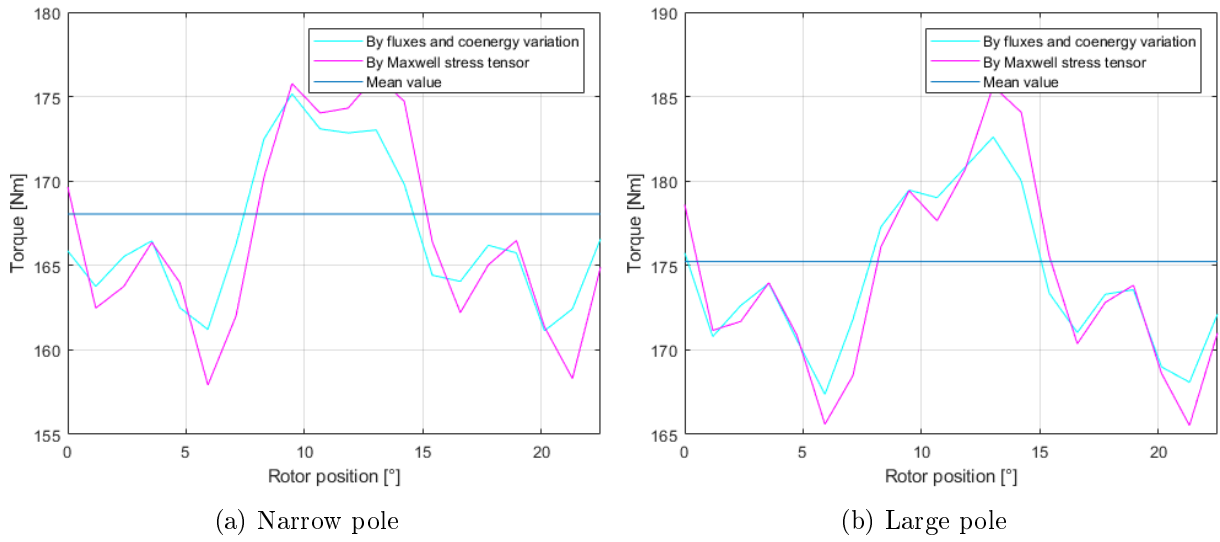


Figure 3.33: Torque at $I_{exc} = 800 A$ and $\hat{I} = 800 A$

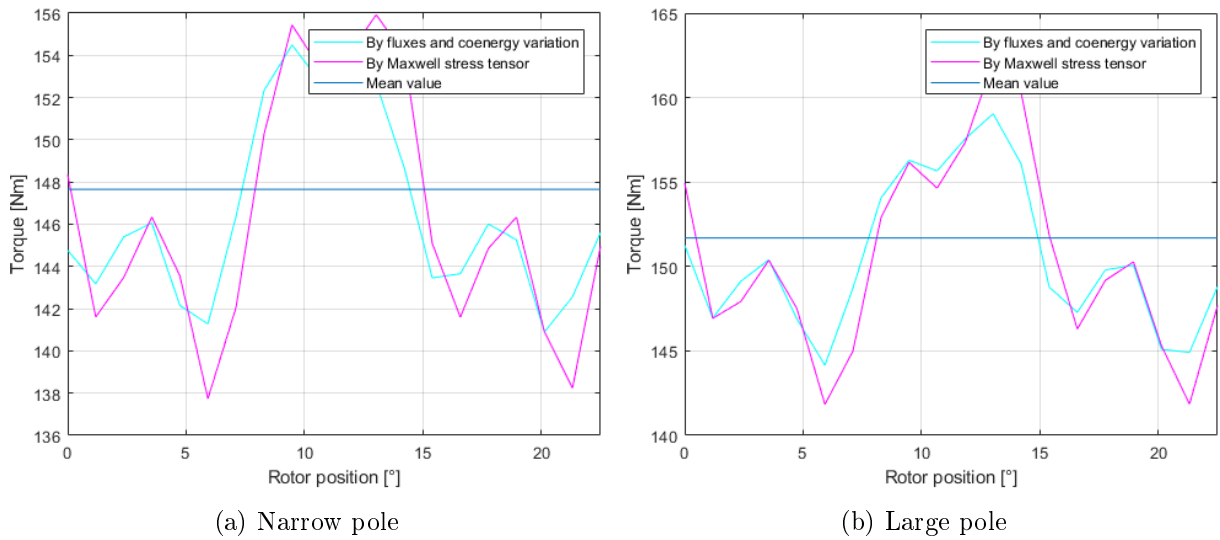


Figure 3.34: Torque at $I_{exc} = 600 A$ and $\hat{I} = 800 A$

Flux density maps with maximum stator current and maximum excitation current are then shown in figure 3.35. The maximum induction reaches 2 T.

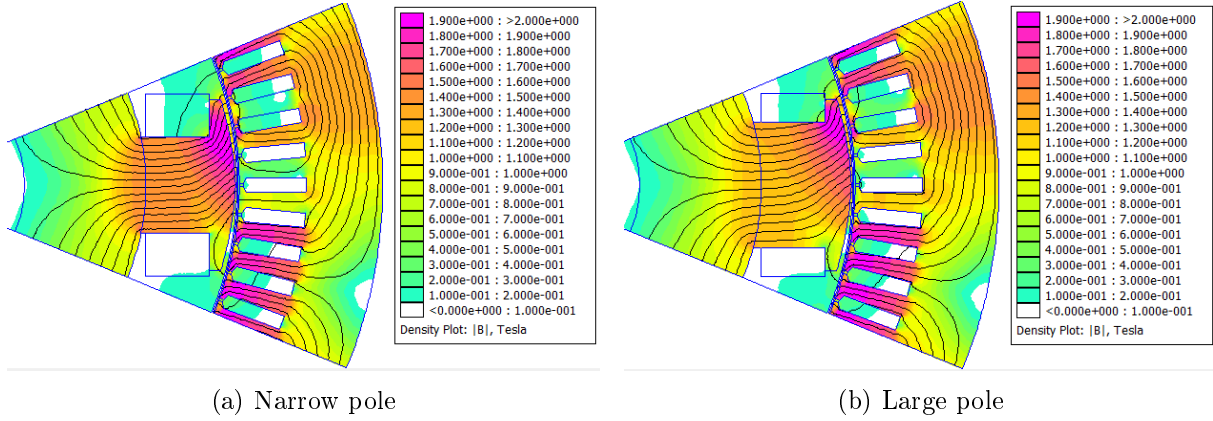


Figure 3.35: Flux density map at $I_{exc} = 1000 A$ and $\hat{I} = 800 A$

Mechanical characteristic

To trace the mechanical characteristic, it is necessary to identify the most effective control strategy. Figure 3.36 shows the locus of the currents used for the analysis.

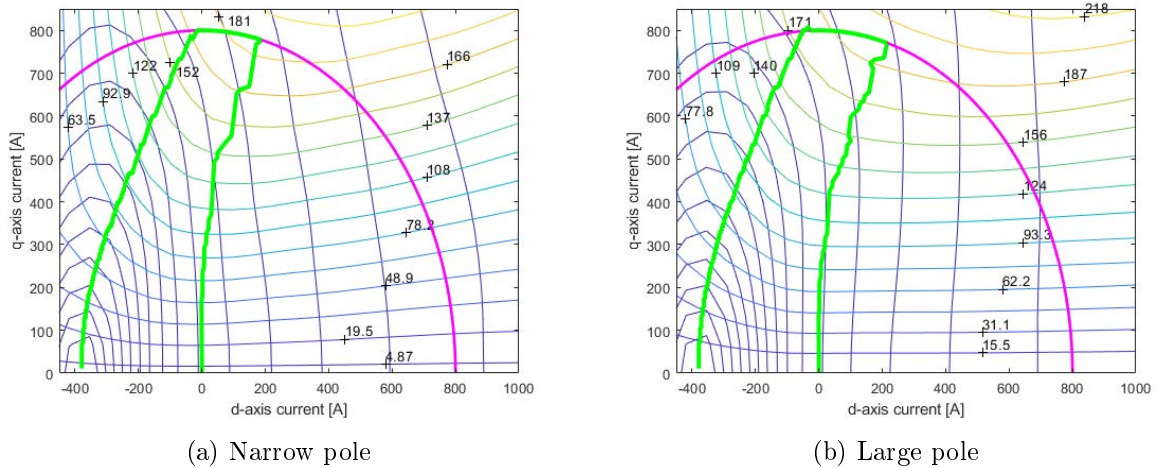


Figure 3.36: Current control path

Given the high number of variables involved, in order not to make the chapter too heavy, only the characteristics obtained at maximum stator current and maximum excitation currents are reported. Figure 3.37 shows the torque versus speed characteristics of the two configurations, figure 3.38 the power versus speed curve and lastly the supply current versus speed in figure 3.39. From the point of view of the performances exhibited there is not much difference between the two geometries.

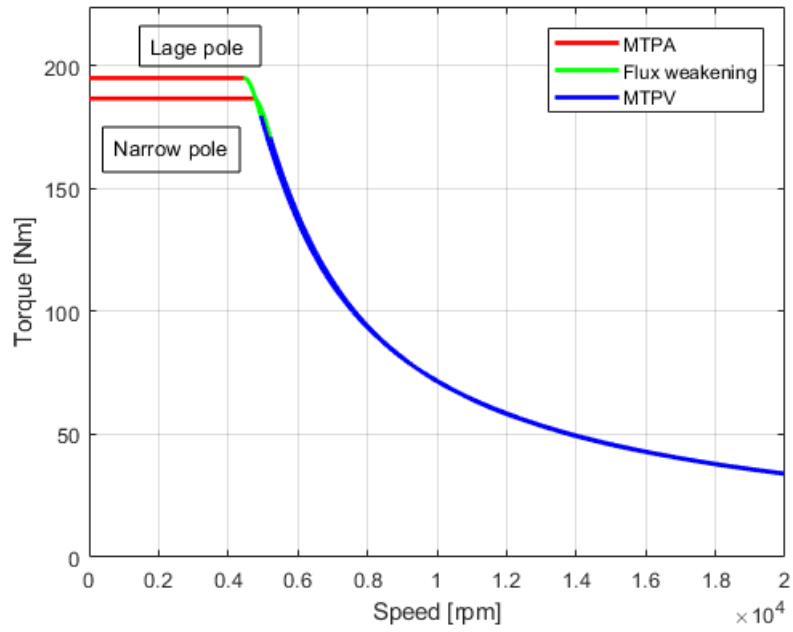


Figure 3.37: Torque versus speed

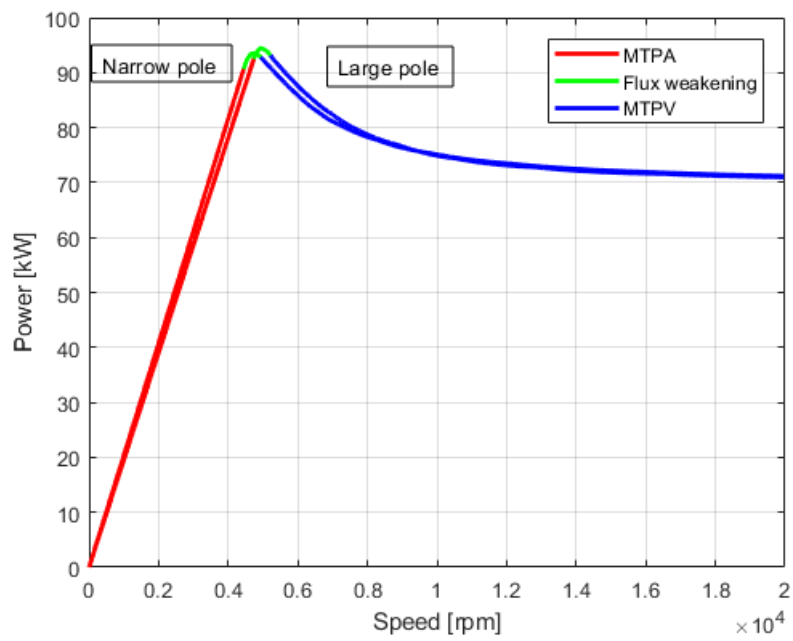


Figure 3.38: Power versus speed

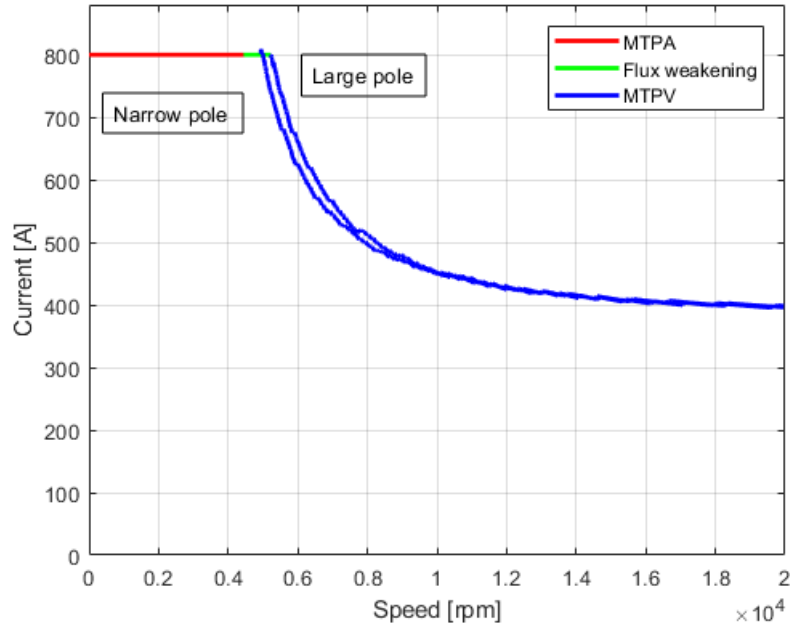


Figure 3.39: Current versus speed

Figure 3.40 shows the map with all the possible working points of the machine.

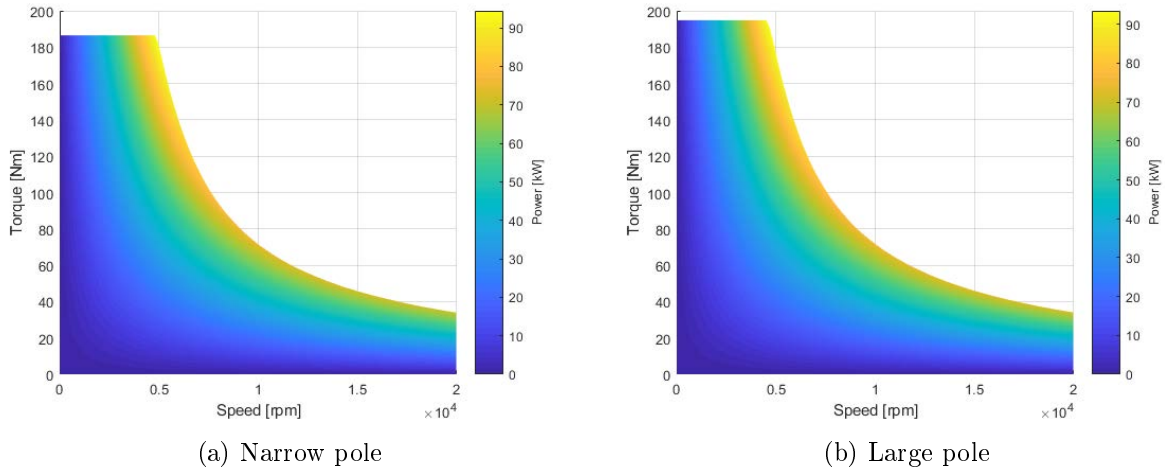


Figure 3.40: Map of the working points

Given the results obtained so far, it is decided to abandon the large pole configuration as the difference in performance is very small. On the other hand, the smaller available excitation surface makes the use of high currents very disadvantageous due to the reduction of the efficiency and the difficulty in the heat removal.

Variable current limit circle

The characteristics obtained for various limit current values are then reported. In figure 3.41 current versus speed behavior is shown, in figure 3.42 torque versus speed is shown while in figure 3.43 power versus speed is reported. Note that the curves obtained with lower current limit ($\hat{I} = 267 A$) have been calculated with a reduced excitation current, equal to $I_{exc} = 600 A$. This is because in doing so the center of the voltage limit ellipses has moved towards values of lower d-axis current allowing the exploitation of the MTPV which would have been otherwise not available. This also allowed to reach the maximum speed.

Unitary cosfi control strategy

To complete the characterization of the motor, the case of a reduced current limit circle, such as to have the center of the ellipses outside the current circle, is reported. In this case it is possible to control the machine in an optimal way obtaining a unitary cosfi (see section 3.1). In figure 3.44 and 3.45 the torque and power characteristics for various current values are shown respectively. It is noted how the unit cosfi control allows to obtain a much flatter constant power region which indicates an optimal control in flux weakening. The currents imposed in the analysis are then shown. The modulus of the stator current space vector remains constant throughout the speed range (figure 3.46) while the d-q components and the excitation current are adapted to always obtain the maximum power condition (figure 3.47a, 3.47b and 3.47c). It is also noted that this control strategy has another benefit, that is the reduction of the excitation current for high speeds which lightens the heat losses to be removed in the rotor.

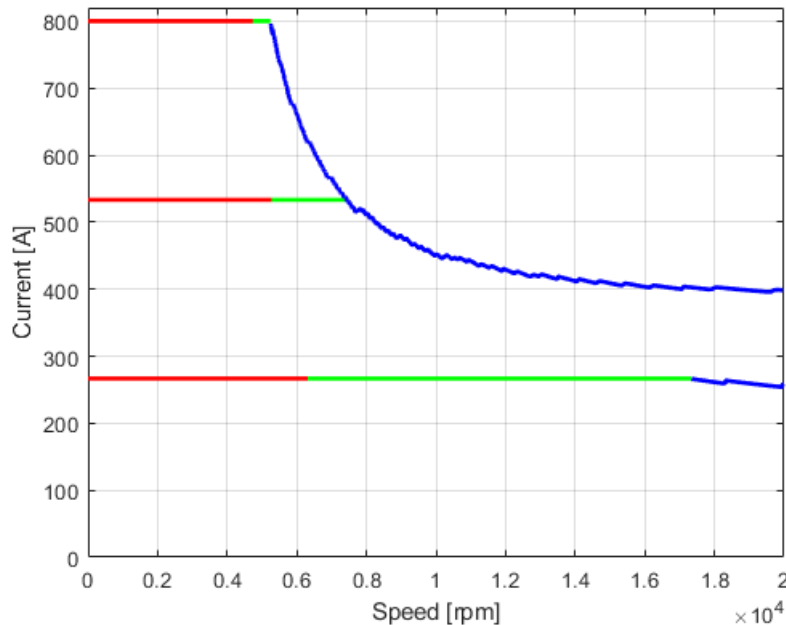


Figure 3.41: Current versus speed for various current limits

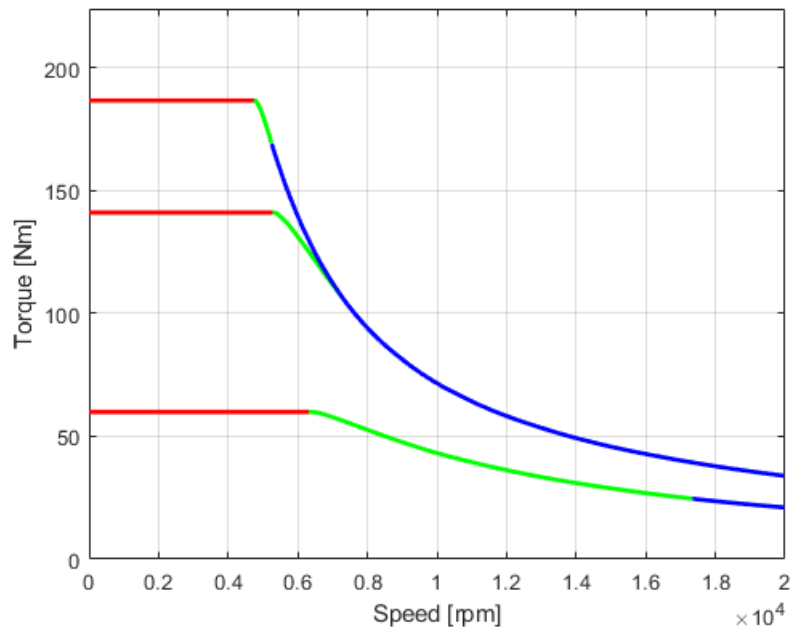


Figure 3.42: Torque versus speed for various current limits

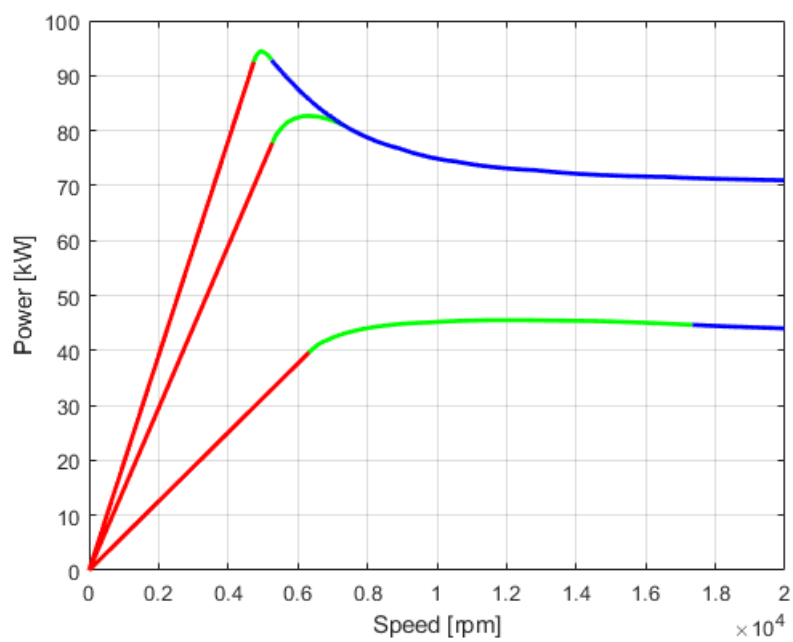


Figure 3.43: Power versus speed for various current limits

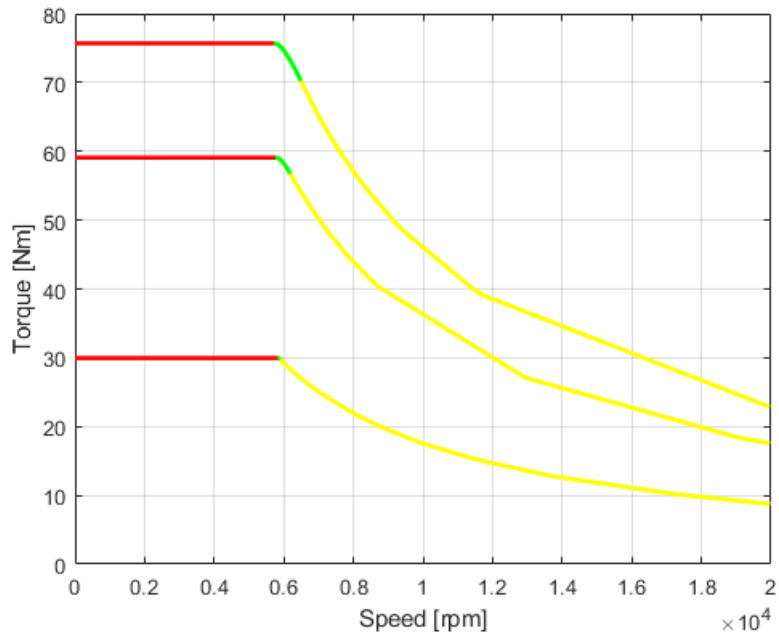


Figure 3.44: Torque versus speed for various current limits

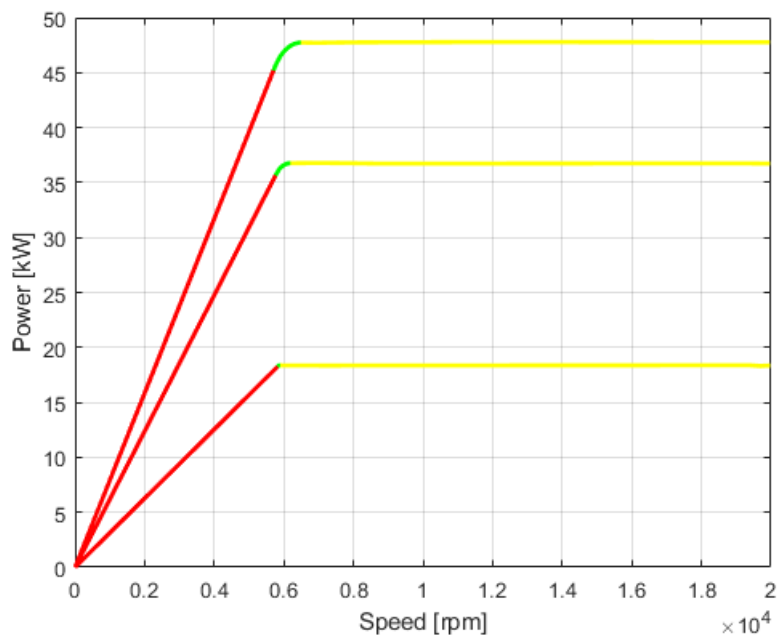


Figure 3.45: Power versus speed for various current limits

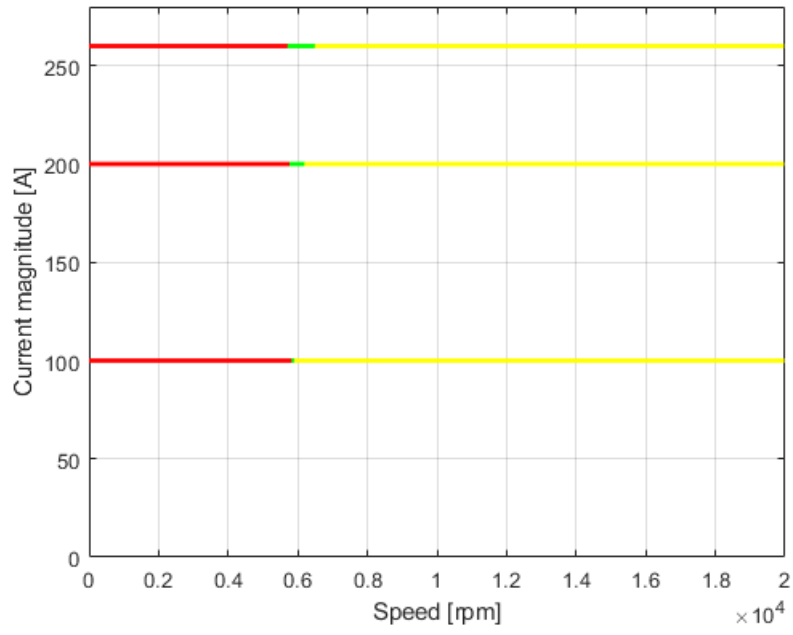
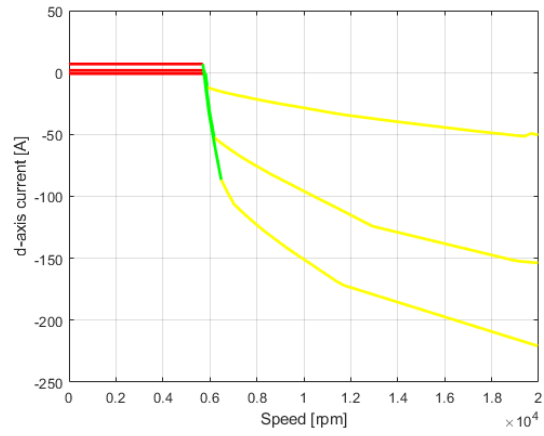
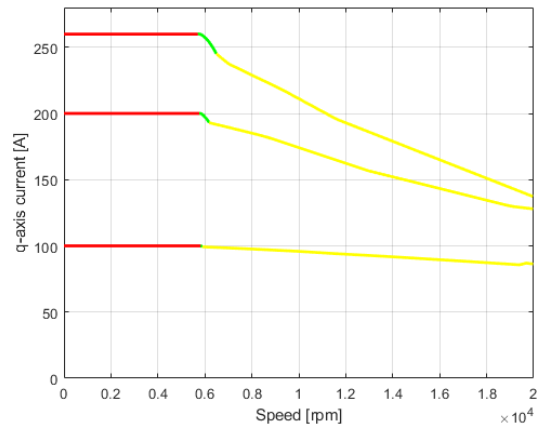


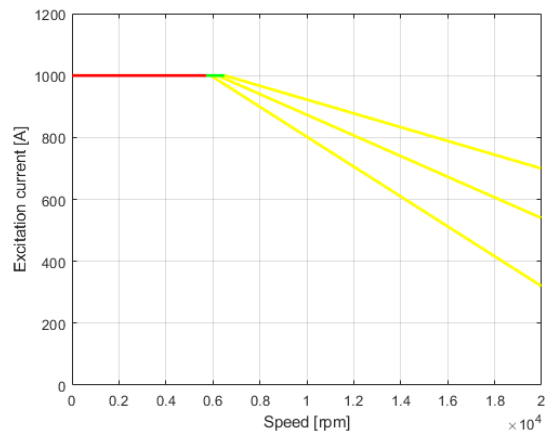
Figure 3.46: Stator current magnitude



(a) d-axis current



(b) q-axis current



(c) Excitation current

Figure 3.47: Control currents for $\cos\phi_i=1$ strategy

3.4.4 Losses

A WRSM has four main sources of losses during operation:

- copper losses due to the current flowing in the stator windings;
- iron losses due to the variable induction in the stator;
- excitation losses due to the current flowing in the excitation winding;
- mechanical losses due to air and bearings friction;
- rotor losses (neglected);

The analysis proceeds in the same way as that already proposed for the IPM motor.

Copper losses

The increase in resistance due to the working frequency is identical to that already calculated since the stator is the same and also the speed range. Figure 3.48 shows the distribution of losses due to the joule effect for all working conditions. It can be seen that the greatest losses are concentrated in the constant torque zone as the motor operates for a wide range in MTPV with reduced currents.

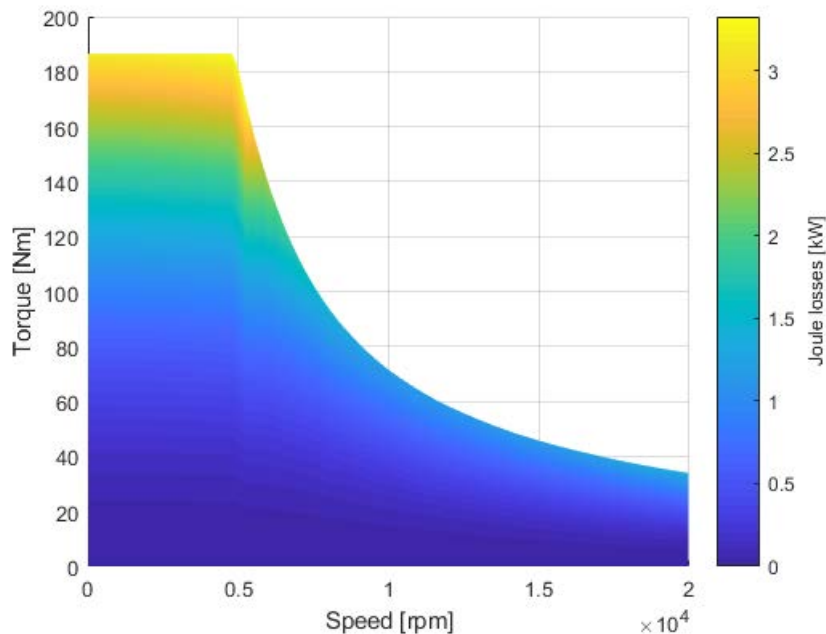


Figure 3.48: Joule losses distribution

Iron losses

Figure 3.49 shows the distribution of iron losses in the stator for all working conditions. It can be seen that the greatest losses occur at high speeds.

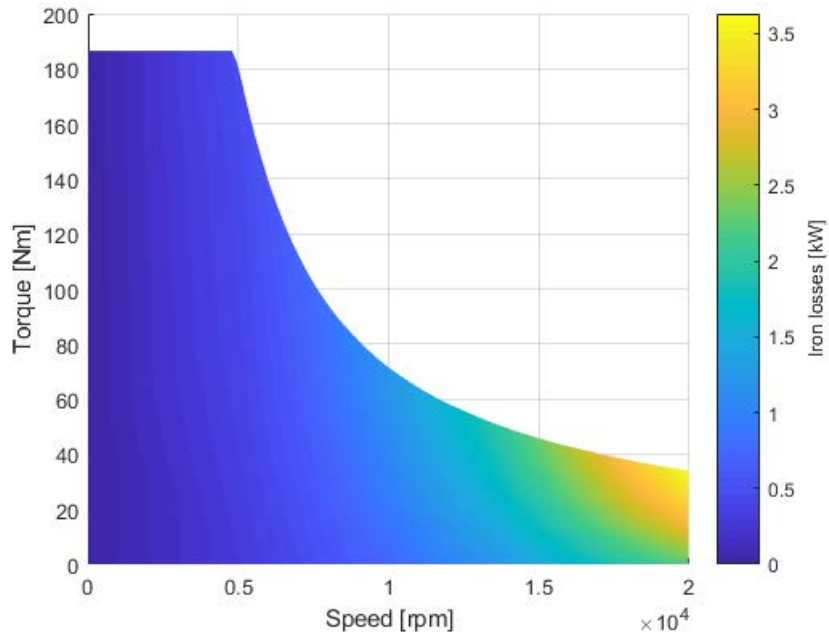


Figure 3.49: Iron losses distribution

Mechanical losses

Mechanical losses computation will be presented in detail in chapter 4, here the results are shown as a map (figure 3.50) for each machine operating point. Obviously mechanical losses do not depend on the torque delivered but only on the rotation speed.

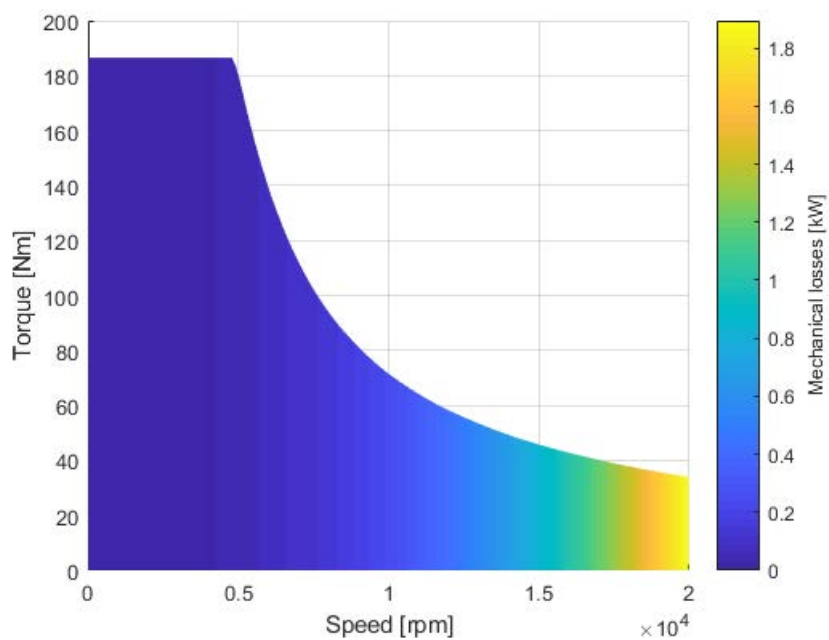


Figure 3.50: Mechanical losses distribution

Excitation losses

The excitation losses do not depend on the load torque nor on the rotation speed but only on the excitation current. In this case, since the $\cos\phi=1$ control is not possible, the excitation current is kept constant at $I_{exc} = 1000 A$ for all operating points.

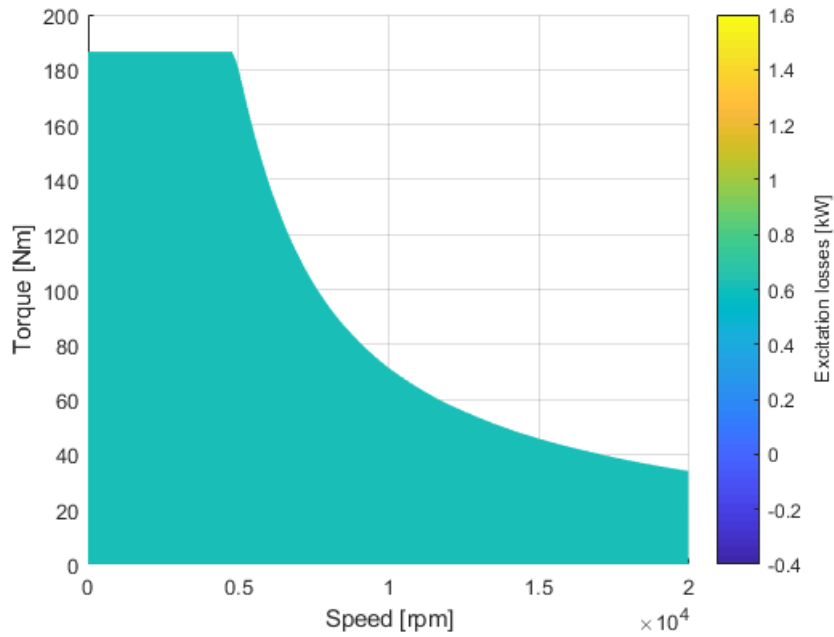


Figure 3.51: Excitation losses distribution

Total losses and efficiency

Total losses are obtained by summing up all losses previously calculated and multiplying them by a safety factor which takes into account any non-calculable contribution. The efficiency map is shown in figure 3.52; it can be seen how the machine works optimally for medium speeds and high load torques.

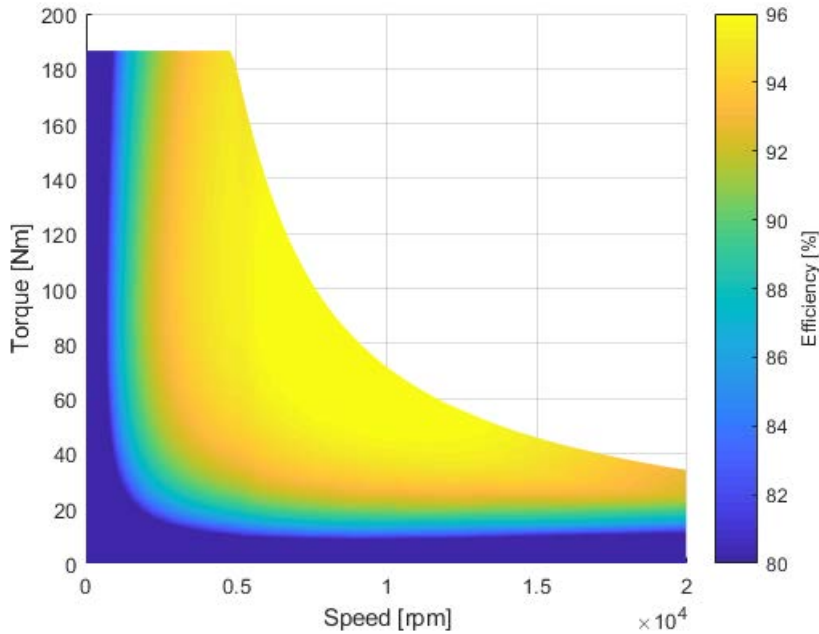


Figure 3.52: Efficiency map

3.5 Comparison

The two motors previously analyzed are now compared. The mechanical characteristics at rated current ($\hat{I} = 400 A$) are shown in figure 3.53. It is noted that the IPM motor has a higher torque in the MTPA region while in the flux weakening region the two machines perform almost in the same way. For high speeds ($n > 15000 rpm$) the WRSM is capable of providing an higher torque.

Power curves are shown in figure 3.54, it can be seen how the trend reflects what has already been said about the torque and how the WRSM has a region more similar to a constant power zone (excellent for traction).

It is also shown the case of a very low current limit, equal to $\hat{I} = 260 A$. The IPM motor is unable to exploit the MTPV in these conditions and therefore cannot reach the maximum required speed. This is because the center of the voltage limit ellipses is outside the current limit circle. With WRSM, on the other hand, it is possible to reach the required speed simply by reducing the excitation current and consequently moving the center of the voltage limit towards values closer to zero, adopting the $\cos\phi=1$ control strategy. This operation is always possible up to the extreme case where $I_{exc} = 0$ and the motor would behave like a pure reluctance motor. Torque and power characteristics are shown in figure 3.55 and 3.56. Note how when it is possible to implement the unitary $\cos\phi$ control the performance of the WRSM becomes superior to that of the IPM from every point of view.

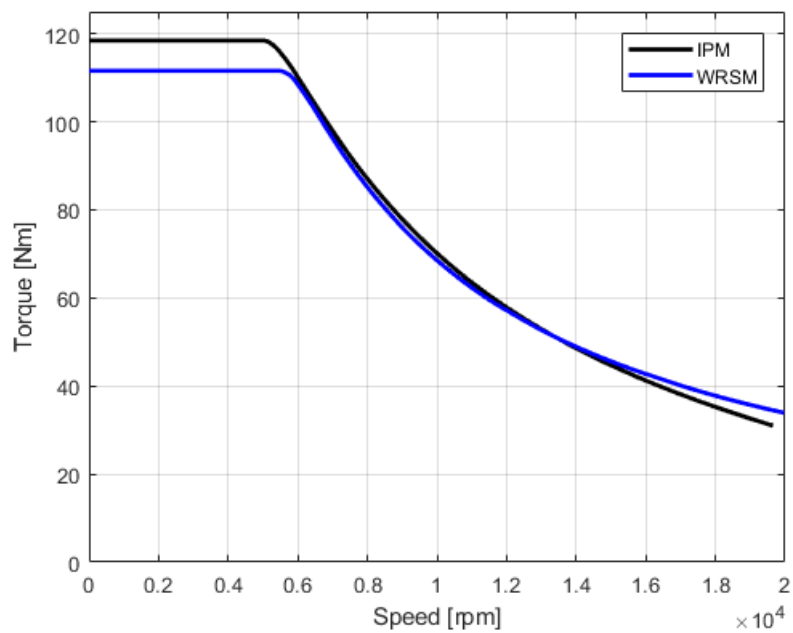


Figure 3.53: Torque versus speed comparison at $\hat{I} = 400 A$

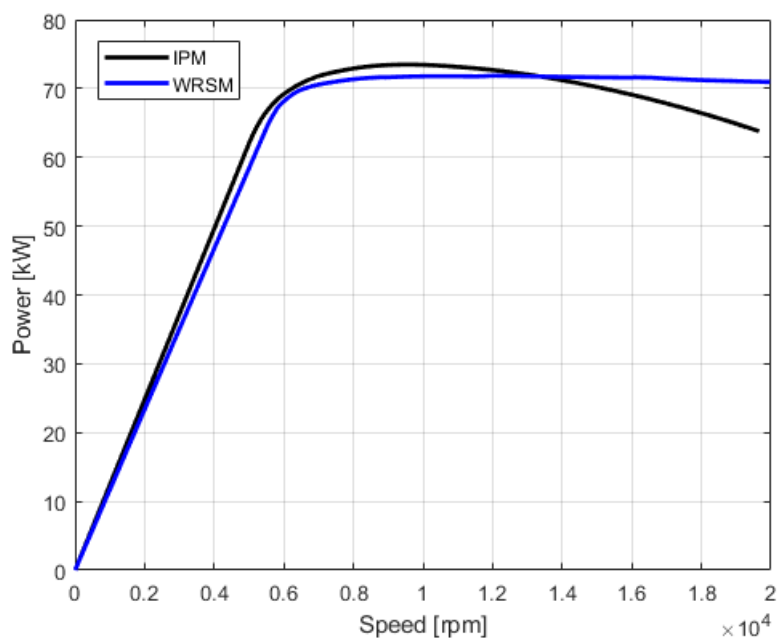


Figure 3.54: Power versus speed comparison at $\hat{I} = 400 A$

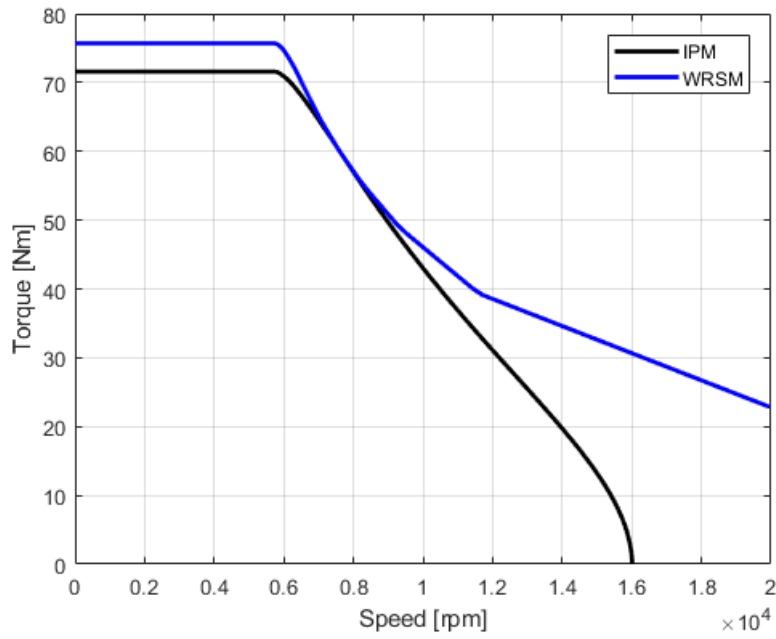


Figure 3.55: Torque versus speed comparison at $\hat{I} = 260 A$

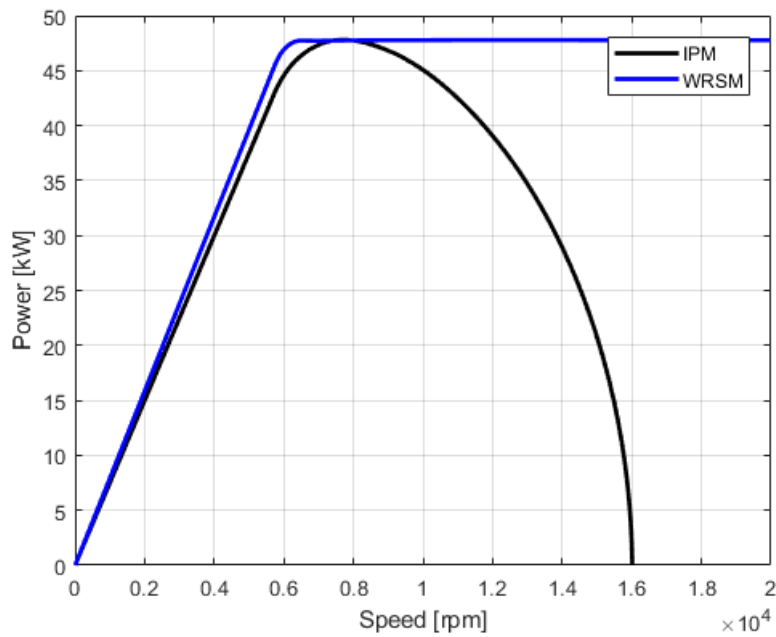


Figure 3.56: Power versus speed comparison at $\hat{I} = 260 A$

Finally, the comparison of efficiency maps at rated current ($\hat{I} = 400 A$) is shown in figure 3.57.

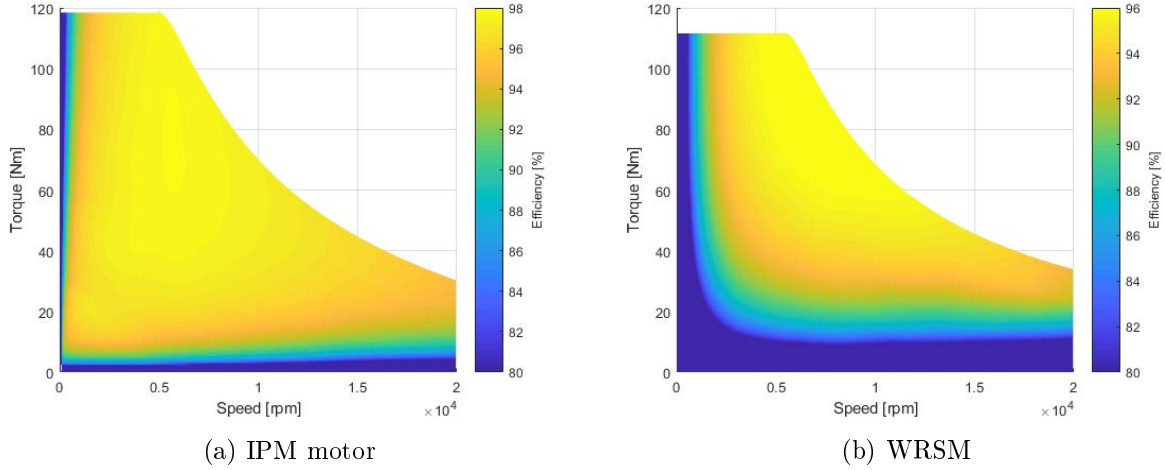


Figure 3.57: Efficiency map at $\hat{I} = 400 A$

It is noted that the IPM motor has a much wider high-efficiency region than WRSM. In addition, both motors have the maximum efficiency region for low speeds and high load torques. However, even at high speeds the efficiency is quite good, always reaching above 85 % for high torque. The IPM motor is certainly more performing in the constant torque area both as regards the torque delivered and the efficiency, this means that for low speeds applications or where there is no need for large flux weakening region, the IPM motor is certainly the best choice. However in the flux weakening zone at high speeds, the WRSM has a higher torque and a flatter power characteristic and therefore closer to the ideal constant power trend. The WRSM also has a great advantage over the IPM which is the possibility of always reaching very high speeds, even for very low current limits thanks to the possibility of regulating the excitation flux. Finally, the possibility of implementing unitary cosfi control makes WRSM an excellent candidate for IPM replacement in automotive applications.

3.5.1 Cost estimation

A very rough estimate of the final cost of the two machines can be obtained by multiplying the weight of each material by the price per kg of that material. Table 3.6 shows the materials making up the motors and the respective prices per kg [38], [39], [40], [41].

Material	Price	Mesure unit
Copper	5.6	$\frac{EUR}{kg}$
NO27 magnetic steel	0.8	$\frac{EUR}{kg}$
Class F insulation	15	$\frac{EUR}{kg}$
NdFeB permanet magnet	93.6	$\frac{EUR}{kg}$

Table 3.6: Material price per kg

Table 3.7 shows the weights (obtained in FEMM) of each material for the two motors. For simplicity of calculation, the contributions of the head connections, the shaft and the bearings will not be considered as they are the same for both motors. The important aspect is in fact the ratio between prices rather than the value itself.

Material	IPM motor	WRSM	Mesure unit
Copper	2.23	4.19	<i>kg</i>
NO27 magnetic steel	24.9	23	<i>kg</i>
Class F insulation	0.21	0.31	<i>kg</i>
NdFeBo permanet magnet	1.38	0	<i>kg</i>

Table 3.7: Material weight in the two motors

By adding up all the contributes and taking the ratio it is

$$Price\ ratio = \frac{IPM\ motor\ price}{WRSM\ price} = \frac{165.2}{46.6} = 3.54 \quad (3.30)$$

As can be seen the WRSM is much cheaper than IPM motor making it perfect for small and hybrid cars.

Chapter 4

Mechanical losses computation

Mechanical losses in industrial machines are normally considered through empirical formulas and tables drawn from experience, which often refer to a nominal operating point. However, the aforementioned machines hardly exceed 3000 rpm of rotation speed and therefore in the case of traction motors, which exceed 10000 rpm and have multiple operating points, it is not possible to rely on such relationships. For this reason, in this section a calculation procedure based on a finite element fluid dynamic study using the Ansys Fluent software is proposed and also a simplified analytical model is presented for comparison.

Mechanical losses can be considered composed of two contributions:

- Bearing losses, due to rolling friction;
- Windage losses, due to the resistance that a fluid exerts when a solid moves inside it. In particular, this resistance to motion can be broken down into two contributions.
 - (1) Shape drag: The motion of a body pushes the air in front of it. However, the air cannot instantaneously move out of the way and its pressure is thus increased, resulting in a zone of high air pressure in front of the solid. Correspondingly, the air behind it cannot instantaneously fill the space left by the forward motion of the body, resulting in a zone of low air pressure at back of it. The two different pressure zones create a force that oppose the motion of the body by pushing (high pressure in front) and pulling (low pressure at the back) it backwards. This resulting force is called shape drag. The name "shape" drag comes from the fact that this drag is completely determined by the shape of the body. See for example figure 4.1.

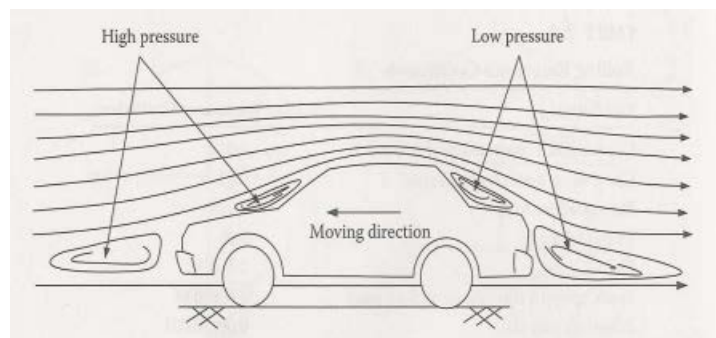


Figure 4.1: High and low pressure zones created when a car moves

- (2) Skin friction: air molecules close to the skin of the solid moves almost at the speed of the solid while air molecules away from it remains still. In between, air molecules

move at intermediate values of speed. The difference in speed between two adjacent layers of air molecules produces a friction that results in the so-called skin friction component of aerodynamic drag

4.1 Bearing losses

A bearing is a machine element that constrains relative motion to only the desired motion, and reduces friction between moving parts [7]. In rotating electric machines they are used to allow the motor shaft, resting on the supporting structure, to rotate freely. The bearings can be of many types, classified base on construction methods, performances, shapes... however in the case of electric motors with high rotation speeds the most used type is called rolling-element bearing [7]. It is a bearing which carries a load by placing rolling elements (such as balls or rollers) between two bearing rings called races. The relative motion of the races causes the rolling elements to roll with very little rolling resistance and with little sliding.



Figure 4.2: A cylindrical roller bearing [10]

Bearings can be composed of different materials, depending on the conditions in which they will have to work and the required performance; typical materials for electric motors applications are [8]

- Chrome-steel bearings, have excellent hardness, surface quality and high load capability; it is also highly resistant to corrosion thanks to the presence of chromium. Chrome Steel is magnetic;
- Stainless steel bearings, contain a martensitic-type stainless steel used extensively in bearing applications that require hardness, dimensional stability, corrosion resistance and toughness. Stainless steel is resistant to corrosion from fresh water, steam, crude oil, gasoline, perspiration, alcohol, blood and food stuffs. Stainless Steel does contain some carbon so it is still slightly magnetic and may eventually rust;
- Ceramic hybrid bearings, have steel races and ceramic balls. Ceramic balls are suitable for applications where high loads, high speeds and extreme temperatures are factors. Long life and the need for minimal lubrication make this material appropriate for extreme applications. Ceramic is non-porous, non-magnetic, non-corrosive and lighter than steel. In ball form, ceramic balls are also harder than steel and because ceramic balls are non-porous they are virtually frictionless and capable of spinning faster than steel balls;
- C-HIP ceramic hybrid bearings, are similar to ceramic hybrid bearings, but these C-HIP bearings utilize ceramic balls that are made with Hot Isostatic Pressing (HIP). These ceramic balls have an even greater density and hardness than a standard ceramic ball.

In many applications, the use of a liquid lubricant is also provided for cooling and further reduction of friction.

Bearing coefficient

Bearings are characterized by a friction coefficient which depends on bearing type, bearing load, rotation speed, lubrication... Reference values for the friction coefficient during stable operation under normal operating conditions are listed in table 4.1 [9].

Bearing type	$k_{bearing}$
Deep groove ball bearing	0.0010 – 0.0015
Angular contact ball bearing	0.0012 – 0.0020
Self-aligning ball bearing	0.0008 – 0.0012
Cylindrical roller bearing	0.0008 – 0.0012
Full complement type needle roller bearing	0.0025 – 0.0035
Needle roller and cage assembly	0.0020 – 0.0030
Tapered roller bearing	0.0017 – 0.0025
Spherical roller bearing	0.0020 – 0.0025
Thrust ball bearing	0.0010 – 0.0015
Spherical thrust roller bearing	0.0020 – 0.0025

Table 4.1: Friction coefficient $k_{bearing}$

4.1.1 Analytical model

Bearing losses computation is based on the model proposed in [2], in which the following equation is used

$$P_{bearing} = 0.5 \cdot \omega_m \cdot k_{bearing} \cdot F_{rotor} \cdot D_{bearing} \quad (4.1)$$

where:

- ω_m is the rotational speed in $\frac{rad}{s}$;
- F is the weight force that presses on the bearing; it is calculated considering that there are two bearings that must support the weight of the entire rotor;
- $D_{bearing}$ is the diameter of the bearings that has been assumed equal to the diameter of the shaft: $D_{bearing} = 50 \text{ mm}$.

In figure 4.3 a schematic representation of a rotor is shown [2].

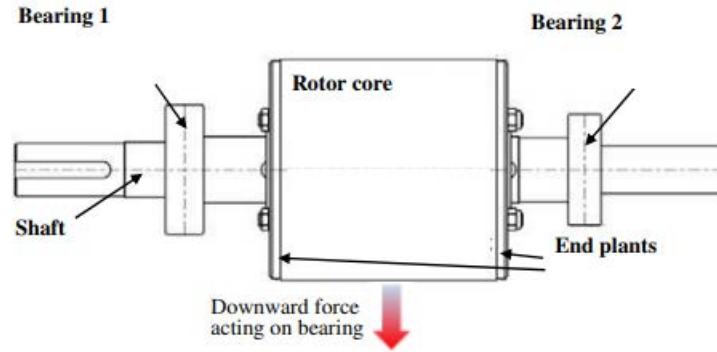


Figure 4.3: Components contributing to the weight of rotor

IPM motor

Considering the IPM motor we have the following volumes and mass weights (table 4.2 and 4.3).

Rotor iron volume	$1.47 \cdot 10^{-3}$	m^3
Shaft iron volume	$5.1 \cdot 10^{-4}$	m^3
Magnets volume	$1.87 \cdot 10^{-4}$	m^3
Iron density	7800	$\frac{kg}{m^3}$
Magnet density	7400	$\frac{kg}{m^3}$

Table 4.2: IPM motor volumes

Rotor iron weight	11.5	kg
Shaft iron weight	4	kg
Magnets weight	1.4	kg
Total rotor weight	16.9	kg

Table 4.3: IPM motor mass weight

Weight force is calculated with the well known: $F_{rotor} = m_{rotor} \cdot g = 165.78 N$.

WRSM, narrow pole

Considering the narrow pole WRSM we have the following volumes and mass weights (table 4.4 and 4.5).

Rotor iron volume	$1.22 \cdot 10^{-3}$	m^3
Shaft iron volume	$5.1 \cdot 10^{-4}$	m^3
Excitation circuit volume	$2.5 \cdot 10^{-4}$	m^3
Iron density	7800	$\frac{kg}{m^3}$
Copper density	8900	$\frac{kg}{m^3}$

Table 4.4: Narrow pole WRSM volumes

Rotor iron weight	9.5	kg
Shaft iron weight	4	kg
Copper weight	2.2	kg
Total rotor weight	15.7	kg

Table 4.5: Narrow pole WRSM mass weight

Weight force is calculated: $F_{rotor} = m_{rotor} \cdot g = 154.01 N$.

WRSM, large pole

Considering the large pole WRSM we have the following volumes and mass weights (table 4.6 and 4.7).

Rotor iron volume	$1.31 \cdot 10^{-3}$	m^3
Shaft iron volume	$5.1 \cdot 10^{-4}$	m^3
Excitation circuit volume	$1.66 \cdot 10^{-4}$	m^3
Iron density	7800	$\frac{kg}{m^3}$
Copper density	8900	$\frac{kg}{m^3}$

Table 4.6: Large pole WRSM volumes

Rotor iron weight	10.2	kg
Shaft iron weight	4	kg
Copper weight	1.47	kg
Total rotor weight	15.67	kg

Table 4.7: Large pole WRSM mass weight

Weight force is calculated as: $F_{rotor} = m_{rotor} \cdot g = 153.72 N$.

Given the almost equal weight between the two geometries of the WRSM, the narrow pole is considered for the following comparisons.

Comparison

Bearing losses are calculated for the whole range of working speed leading to figure 4.4. It can be seen how the IPM motor has slightly higher losses because of its higher weight. It can also be noticed that bearing losses are very small compared to the other loss sources.

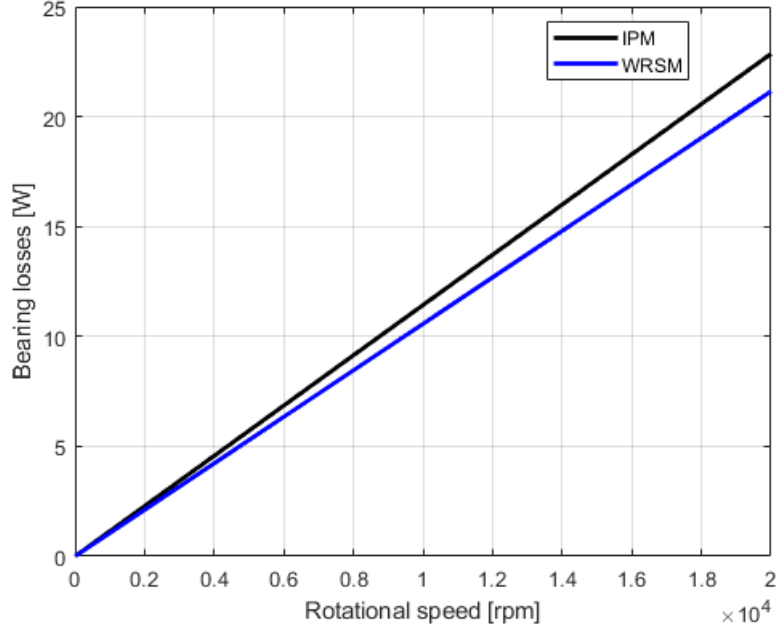


Figure 4.4: Bearing losses: IPM versus WRSM

4.2 Windage losses

Two approaches are proposed for windage losses computation:

- analytical approach through a simplified model;
- numerical approach through finite element simulation with Ansys software.

4.2.1 Analytical model

The motor is modeled as two coaxial cylinders, the external one is held still (stator) while the internal one is rotating (rotor). The model used is described in [2] and it calculates the power dissipated as the product between the drag torque and mechanical rotation speed.

$$P_{windage} = 0.03125 \cdot \omega_m^3 \cdot \pi \cdot k_{tc} \cdot k_r \cdot \rho_{air} \cdot D_r^4 \cdot L_{stk} \quad (4.2)$$

where:

- k_{tc} is the torque coefficient;
- k_r is the roughness coefficient (indicated in the range 1-1.4);
- ρ_{air} is the air density;
- D_r is the rotor diameter;

- L_{stk} is the stack length;

To determine the torque coefficient Reynolds number must be computed in the case of coaxial cylinders, the equation used is the following [2]

$$Re = \frac{\rho_{air} \cdot \omega_m \cdot D_r \cdot g}{2 \cdot \mu_{air}} \quad (4.3)$$

where

- g is the airgap length;
- μ_{air} is the air dynamic viscosity.

To calculate the torque coefficient (k_{tc}) two different equations are used based on the Reynolds number previously calculated. In particular for Reynolds numbers in the range $64 < Re < 500$ the following equation is applied [2]:

$$k_{ct} = 2 \cdot \frac{\left(\frac{2 \cdot g}{D_r}\right)^{0.3}}{Re^{0.6}} \quad (4.4)$$

while for Reynolds $500 < Re < 50000$ the following is used [2]:

$$k_{ct} = 1.03 \cdot \frac{\left(\frac{2 \cdot g}{D_r}\right)^{0.3}}{Re^{0.5}} \quad (4.5)$$

4.2.2 Numerical model

A CFD model is used to calculate the velocity map and other useful parameters. The flow of an incompressible fluid is described by the Reynolds Averaged Navier-Stokes Equation (RANS)

$$\rho \cdot \frac{\partial U}{\partial t} - \eta \cdot \nabla \cdot \nabla U + \rho \cdot U \cdot \nabla U + \nabla P + \nabla(\rho \cdot u' \otimes u') = F \quad (4.6)$$

$$\nabla \cdot U = 0 \quad (4.7)$$

where

- η is the dynamic viscosity;
- U is the average velocity field;
- ρ is the fluid density;
- P is the pressure;
- F is the volumetric force vector;
- $\nabla(\rho \cdot u' \otimes u')$ represents fluctuations around a mean flow and it is called the Reynolds stress tensor;

In order to solve equation 4.7 some assumptions are necessary, some of those lead to the so called $k - \epsilon$ model which is used when a lot of wall interaction must be considered. The final system that has to be solved is in the form

$$\rho \cdot \frac{\partial U}{\partial t} - \nabla \left[\left(\eta + \rho \cdot C_\mu \cdot \frac{k^2}{\epsilon} \right) \cdot \left(\nabla U + (\nabla Q)^T \right) \right] + \rho \cdot U \cdot \nabla U + \nabla P = F \quad (4.8)$$

$$\nabla \cdot U = 0 \quad (4.9)$$

where:

- k is the turbulent kinetic energy;
- ϵ is the dissipation rate of the turbulent energy.

Windage losses can then be calculated using [4]

$$P_{wind} = \pi \cdot C_f \cdot \rho_{air} \cdot \omega_m^3 \cdot \left(\frac{D_r}{2}\right)^4 \cdot L_{stk} \quad (4.10)$$

where

- C_f is the friction coefficient.

It can be computed using [5]

$$C_f = \frac{\tau}{q} \quad (4.11)$$

where

- τ is the sheer stress on the rotor surface. For a Newtonian fluid, the shear stress at a surface element parallel to a flat plate at the point y is given by:

$$\tau(y) = \mu \cdot \frac{\partial u}{\partial y} \quad (4.12)$$

In our case it is calculated directly by the software through a surface integral.

- q is the dynamic pressure, it is associated with the kinetic energy per unit volume

$$q = \frac{\rho_{air} \cdot u^2}{2} \quad (4.13)$$

It is again computed with a surface integral.

Ansys setting

The two models are built in Ansys CAD (DesignModeler), a two-dimensional study is chosen considering only the air gap as the calculation domain, in this way it is possible to save calculation resources and fall within the limits imposed by the student version. Furthermore, to simulate the movement of the rotor, a boundary condition called "moving wall" is used which allows to assign a rotation speed to a wall; this allowed the use of a stationary study which requires much less computation time than a transitional study. The two geometries built in Ansys are shown in figure 4.5 and 4.6. It can be seen that the WRSM motor does not have stator slots. This is because, as will be seen later, by analyzing the IPM motor it has been noticed that the presence of slots openings is negligible (see figure 4.8). The fact of not having to consider slots openings in the calculation domain is very advantageous as it saves resources and avoids numerical errors facilitating the creation of the mesh which is particularly problematic in domains with very acute angles. Finally, since the two configurations of the WRSM motor are identical from the point of view of the overall dimensions of the pole and the excitation, the mechanical losses are in turn identical and only the narrow pole geometry is considered.

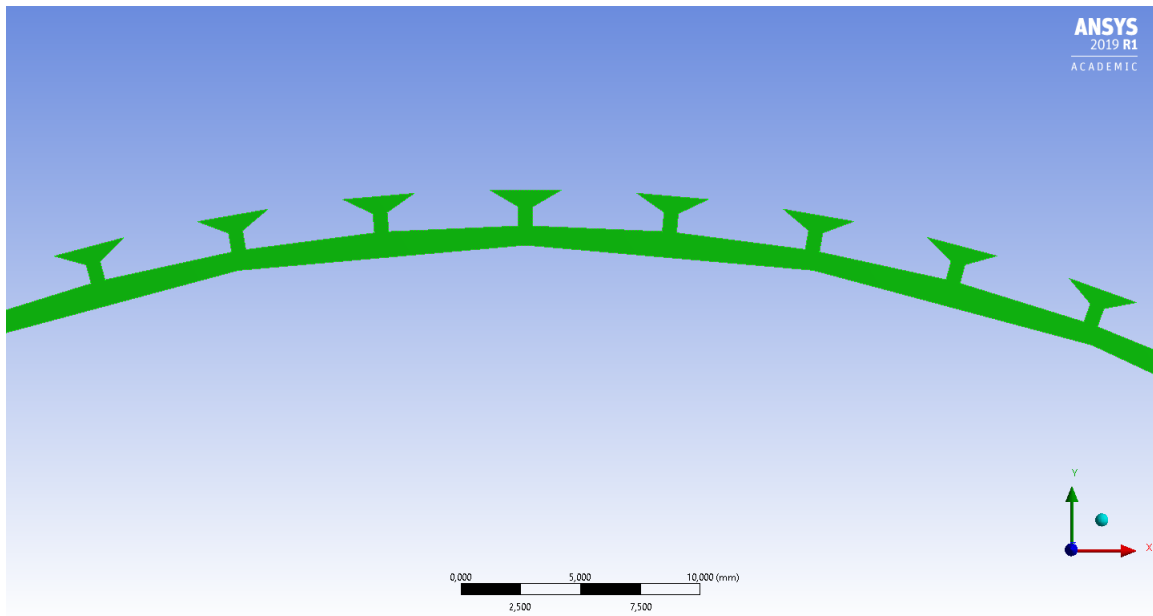


Figure 4.5: IPM geometry in Ansys

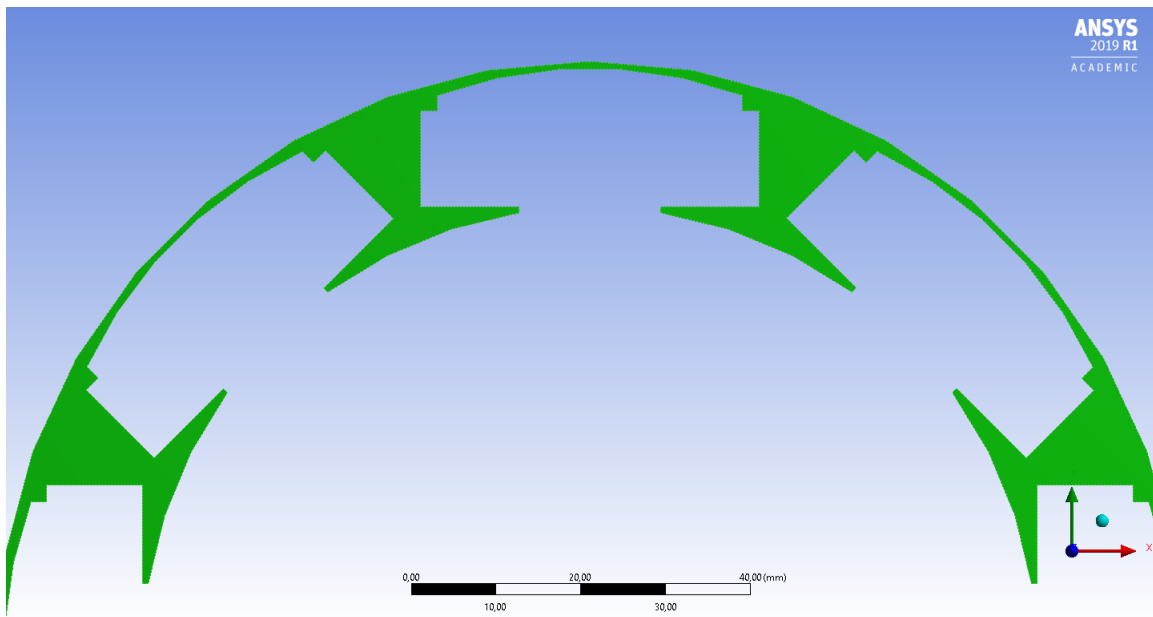


Figure 4.6: WRSM geometry in Ansys

4.2.3 Comparison

First, the results obtained from the analytical model and those obtained by Ansys are compared. As shown by figure 4.7, there is an excellent agreement between the two proposed approaches. Clearly, the WRSM is not taken into consideration as its geometry is too different from the hypotheses of two coaxial cylinders.

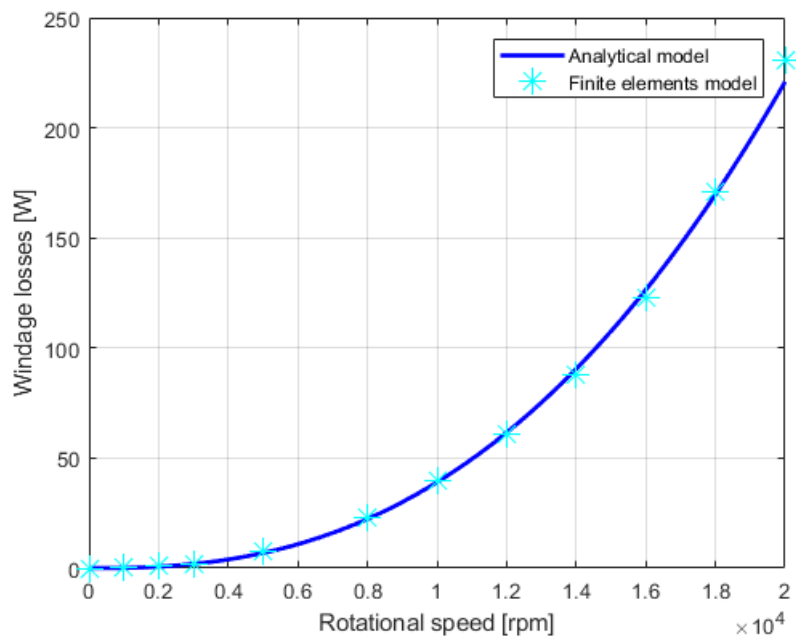


Figure 4.7: Comparison between Ansys results and analytical results

It is also shown in figure 4.8 how the presence of slots openings is almost irrelevant from the point of view of mechanical losses with maximum relative error less than 5%. The fact is also confirmed by figure 4.11 in which it is noted that the air inside the slots openings is practically stationary.

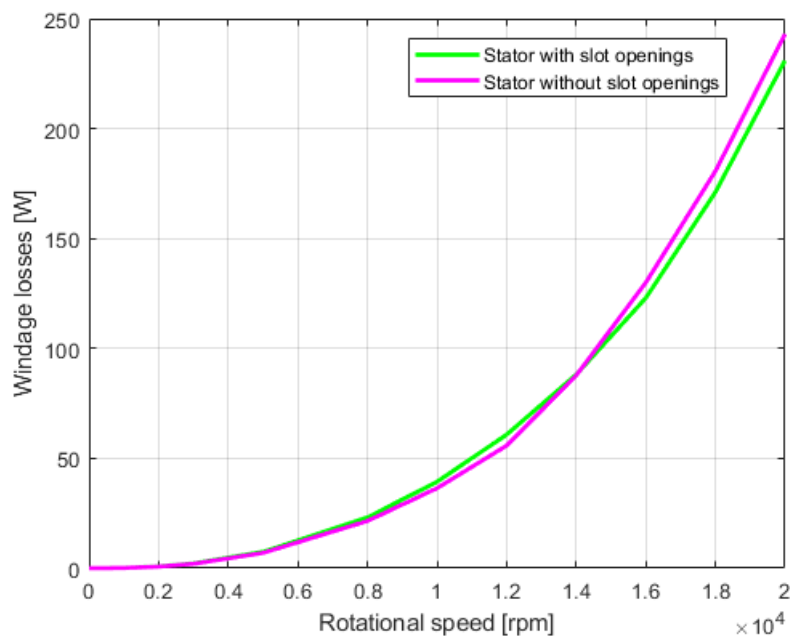


Figure 4.8: Slotted IPM versus smooth stator IPM

Figure 4.9 shows the comparison between windage losses of the IPM motor and WRSM. It is noted that the latter is decidedly disadvantaged compared to the former with very high losses.

The reason for this difference is due to the poorly aerodynamic shape of the WRSM rotor which generates conspicuous air movements and turbulence during rotation and therefore large pressure differences that hinder movements (figures 4.12 and 4.13). In the IPM motor the motion of the fluid is much more uniform (figure 4.10 and 4.11).

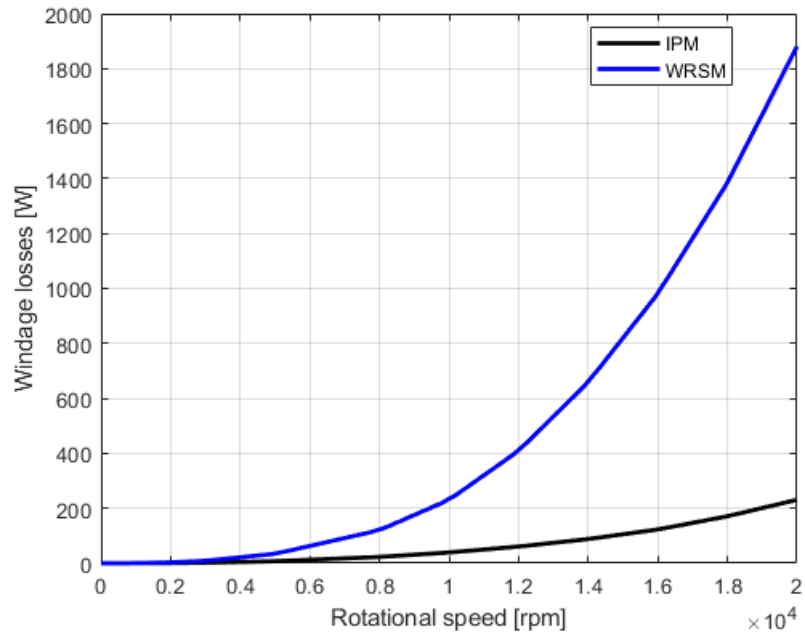


Figure 4.9: Windage losses: IPM versus WRSM

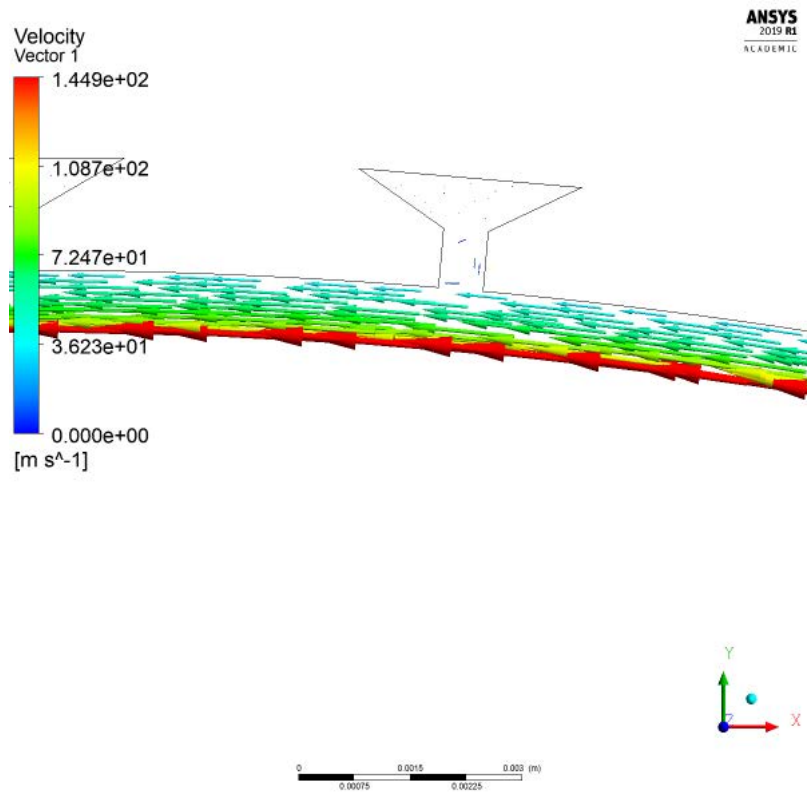


Figure 4.10: IPM arrow plot at $n = 20000 \text{ rpm}$

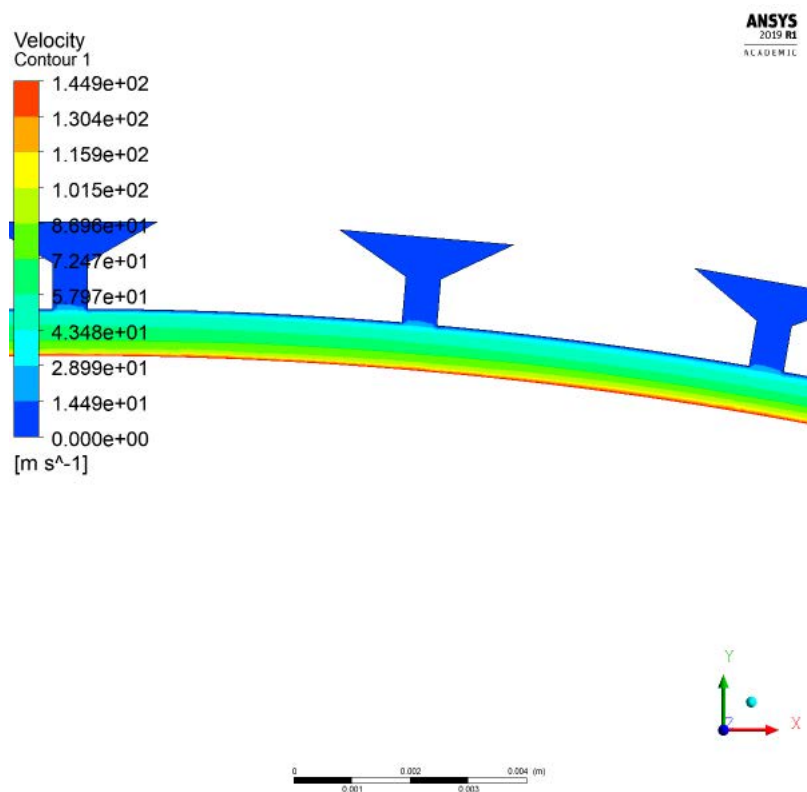


Figure 4.11: IPM velocity contour plot at $n = 20000 \text{ rpm}$

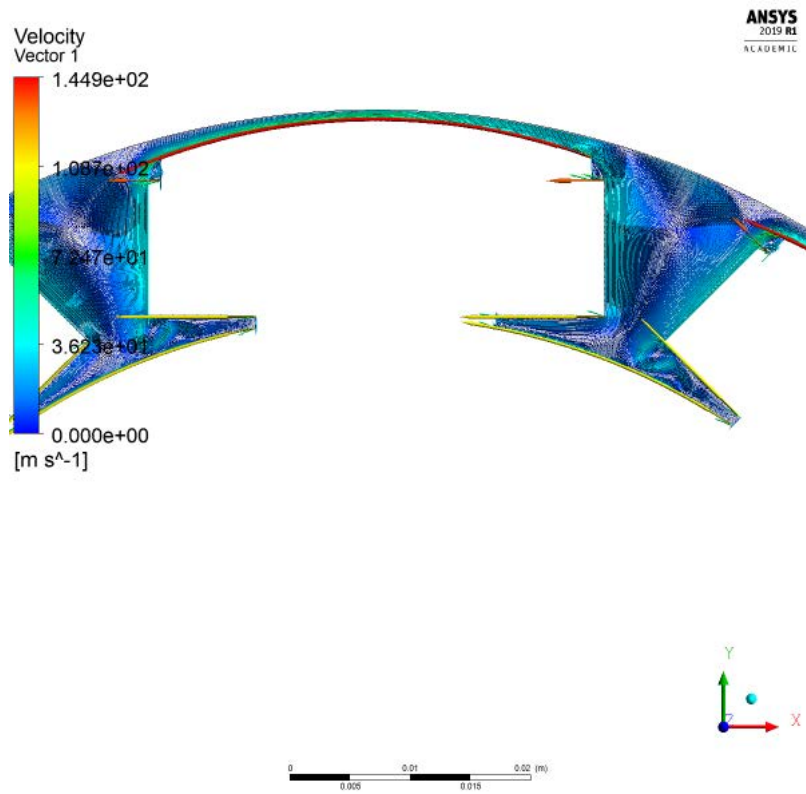


Figure 4.12: WRSM arrow plot at $n = 20000 \text{ rpm}$

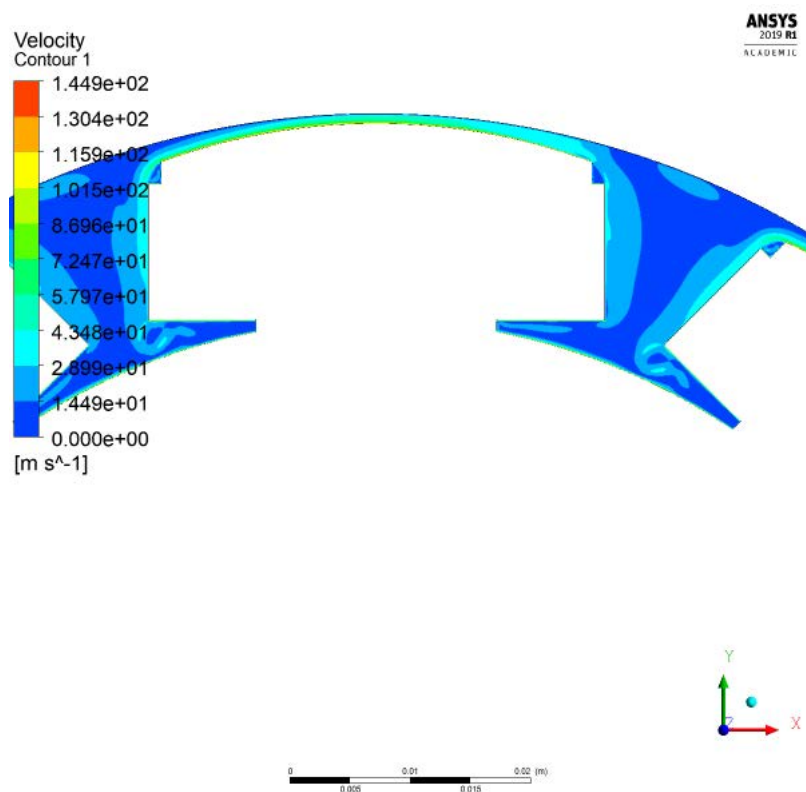


Figure 4.13: WRSM velocity contour plot at $n = 20000 \text{ rpm}$

Finally, the total mechanical losses for the two motors are shown in figure 4.14.

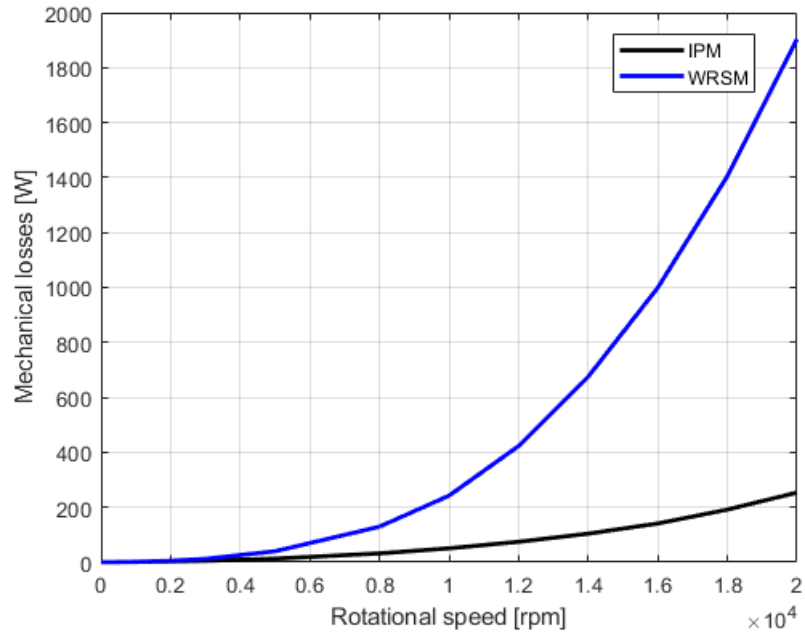


Figure 4.14: Mechanical losses: IPM versus WRSM

Since the losses of the WRSM are caused by the high movement of air that is established between the poles of the machine, covers could be inserted between one pole and the other in order to make the final shape more similar to a cylinder and significantly reduce windage losses.

Chapter 5

Thermal analysis

In recent years, the demand for electric motors with more and more power density has required particular attention to the thermal aspects of those machines. In particular, the reduction in size, and therefore in the heat exchange surfaces, makes heat dissipation particularly problematic. Traditional methods such as finned cases, fans for air recirculation and gas cooling are no longer sufficient for new requests. Liquid cooling systems are becoming increasingly important because the greater density and specific heat of fluids compared to gases makes them much more effective in heat dissipation. Some solutions adopted which make use of liquid for cooling are reported below [13].

- water jackets with various design types (axial and circumferential ducts) and stator and rotor water jackets;
- submersible cooling in which the motor is operating in a liquid environment such as water, oil, or a mixture of water, oil, and air;
- wet rotor and wet stator cooling is where a fluid is passed down the airgap of the machine and over the shaft and end-winding surfaces in the end-cap regions of the machine.
- Spray cooling, when the cooling fluid is passed down a hole on the shaft and is sprayed directly at the inner surface of the end-windings due to the centrifugal forces;
- Direct conductor cooling, e.g., slot water jacket where a cooling fluid is flowing through the slots; it is possible to have internal ducts within the slot to contain the fluid, or the fluid is just completely flowing between conductors.

Finally, systems have been developed that exploit the phase change of a liquid for cooling. During the phase transition, in fact, much higher heat exchange coefficients are obtained than in the single phase cases, allowing a high heat dissipation even for modest temperature differences. The design, analysis and optimization of the aforementioned systems is very complicated as it requires the solution of a three-dimensional multiphysics system. Although there are simplified models and analytical relationships, an accurate study requires the use of finite element (or similar) software that allow a numerical solution of the governing equations.

5.1 Introduction to convective heat transfer

5.1.1 General features

During the study of convection heat transfer, determining the type of motion exerted by the fluid plays a fundamental role. In particular, two types of motions are identified:

- laminar flow, when the layers of fluid flow over each other in an orderly manner;
- turbulent flow, when the fluid moves chaotically generating vortices

In figure 5.1 it can be seen how a flow over a flat plane start as laminar and then become turbulent.

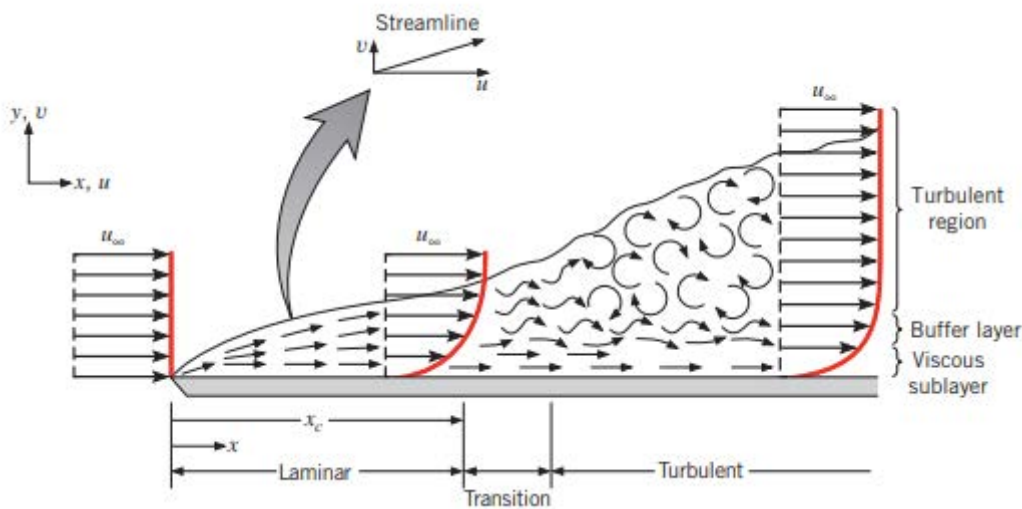


Figure 5.1: Flow over a flat plane

When the fluid is used to remove or give heat, the turbulent flow is usually preferable as it is characterized by higher values of the heat exchange coefficients. Equations describing the fluid and the parameters involved take on a very different form based on the type of flow considered. To distinguish the two types of motion, the Reynolds number is used. It is a dimensionless number that expresses the relationship between inertial forces and viscous forces of the fluid. The Reynolds number is calculated with different equations based on the considered geometry, however a general form is the following [12]:

$$Re = \frac{\rho \cdot v \cdot D}{\mu} = \frac{v \cdot D}{\nu} \quad (5.1)$$

where:

- ρ is the fluid density;
- v is the fluid velocity;
- D is the geometry main dimension;
- μ is the dynamic viscosity of fluid;
- $\nu = \frac{\rho}{\mu}$ is the cinematic viscosity of fluid.

The value of Reynolds number beyond which turbulent motion begins to occur is called *critical value*. It strongly depends on the geometry considered; for example in the case of a flow over a flat plate the critical value is around $5 \cdot 10^5$. Our case of interest is the motion of a fluid inside a pipeline, for which the main dimension is the hydraulic diameter. It is defined as follows:

$$D_{hyd} = 4 \cdot \frac{A}{P} \quad (5.2)$$

where:

- A is the tube cross section;
- P is the wet perimeter.

In the case of circular pipes, the hydraulic diameter coincides with the geometric one while for rectangular pipes it can be expressed as:

$$D_{hyd,rect} = \frac{2 \cdot b \cdot h}{b + h} \quad (5.3)$$

where:

- b is the base;
- h is the height.

For pipes, the type of motion of the fluid is characterized as follows:

- $Re < 2300$ laminar flow;
- $2300 < Re < 10000$ both laminar and turbulent flow;
- $Re > 10000$ fully developed turbulent flow.

It is convenient to express the Reynolds number as a function of the flow rate of the pipeline instead of the velocity so the following relationship is used:

$$Re = \frac{\dot{m} \cdot D_{hyd}}{A \cdot \mu} \quad (5.4)$$

Regarding the thermal aspect there is another number typically used called the Nusselt number. It expresses the relationship between the heat transfer coefficient by convection and conduction.

$$Nu = \frac{h \cdot D}{k} \quad (5.5)$$

where

- h is the convection heat transfer coefficient;
- D is the main dimension of considered geometry;
- k is the thermal conductivity.

The Nusselt number is usually calculated in order to trace the convection coefficient. Another dimensionless parameter widely used is the Prandtl number; it expresses the relationship between the tendency of the fluid to store heat compared to the tendency to exchange heat. It only depends on fluid properties.

$$Pr = \frac{\mu \cdot c_p}{k} \quad (5.6)$$

where:

- c_p is the specific heat at constant pressure

For the case of convective exchanges within pipelines, numerous empirical equations have been proposed for the calculation of the Nusselt number. Only the equations used for subsequent analysis are shown below.

- Dittus-Boelter equation:

$$Nu = 0.023 \cdot Re^{0.8} \cdot Pr^{0.4} \quad (5.7)$$

valid for $Re > 10000$. The estimated error is less than 25 %.

- Pethukov equation:

$$Nu = \frac{\frac{f}{8} \cdot Re \cdot Pr}{1.07 + 12.7 \cdot \left(\frac{f}{8}\right)^{0.5} \cdot (Pr^{\frac{2}{3}} - 1)} \quad (5.8)$$

valid for $10^4 < Re < 5 \cdot 10^6$. The estimated error is less than 10 %.

- Gnielinsky equation:

$$Nu = \frac{\frac{f}{8} \cdot (Re - 1000) \cdot Pr}{1.07 + 12.7 \cdot \left(\frac{f}{8}\right)^{0.5} \cdot (Pr^{\frac{2}{3}} - 1)} \quad (5.9)$$

valid for $3 \cdot 10^3 < Re < 5 \cdot 10^6$. The estimated error is less than 10 %

It should be noted that the properties of the fluid on which the dimensionless parameters depend are variable with the temperature, therefore to obtain precise estimates it will be necessary to introduce the value corresponding to the operating temperature. Also in the previous equations there is the term f . It is a friction coefficient that represents the resistance that the fluid encounters in its motion, moreover it is a factor that influences the type of flow assumed by the fluid. Typically, the Colebrook equation is used to determine the f coefficient [12]:

$$\frac{1}{\sqrt{f}} = -2 \log \left(\frac{\frac{\epsilon}{D_{hyd}}}{3.7} + \frac{2.51}{Re \cdot \sqrt{f}} \right) \quad (5.10)$$

where:

- ϵ is the surface roughness.

Looking at equation 5.10, it can be noticed that the coefficient f is both the argument of a square root and a logarithm, therefore the equation does not have an explicit form. f can be determined by iteratively solving the equation from the Moody diagram shown in figure 5.2 or from the following Halland equation [12].

$$\frac{1}{\sqrt{f}} \approx -1.8 \cdot \log \left(\frac{6.9}{Re} + \left(\frac{\frac{\epsilon}{D_{hyd}}}{3.7} \right)^{1.11} \right) \quad (5.11)$$

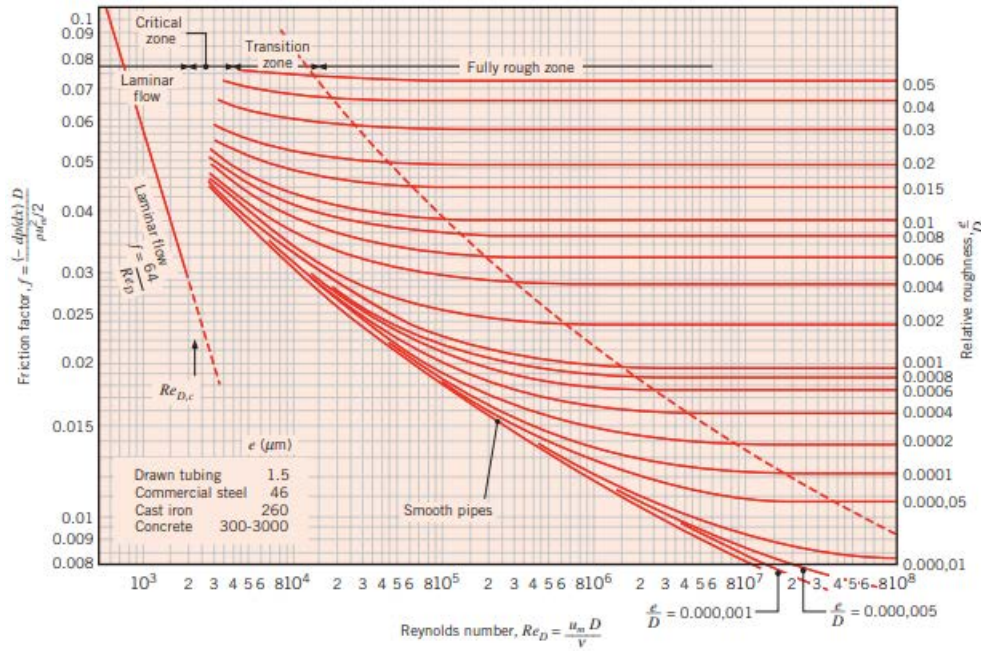


Figure 5.2: Moody diagram

For smooth pipes f can also be computed as follow [12]:

$$f = (0.79 \cdot \log(Re) - 1.64)^{-2} \quad (5.12)$$

From the knowledge of the f coefficient it is possible to determine the pressure drop along the pipe:

$$\Delta P = - \int_{p_1}^{p_2} dP = f \cdot \frac{\rho \cdot v_{mean}}{2 \cdot D_{hyd}} \cdot \int_{x_1}^{x_2} dx = f \cdot \frac{\rho \cdot v_{mean}}{2 \cdot D_{hyd}} \cdot (x_1 - x_2) \quad (5.13)$$

and also the power needed to push the fluid inside the pipe:

$$P = \frac{\Delta P \cdot \dot{m}}{\rho} \quad (5.14)$$

5.1.2 Internal flows

The study of water cooling systems falls into the category of so-called internal flows in which the fluid cannot freely develop its motion but is forced into a pipe. Problems of this type are very complicated to study analytically and often require the adoption of appropriate boundary conditions to simplify the treatment. When a fluid at a certain temperature T , considered uniform over the whole section, enters a pipeline, a region called *thermal entrance region* (figure 5.3) is established. During this phase the convection coefficient h varies exponentially and then assumes a constant value at a certain distance from the entrance 5.4.

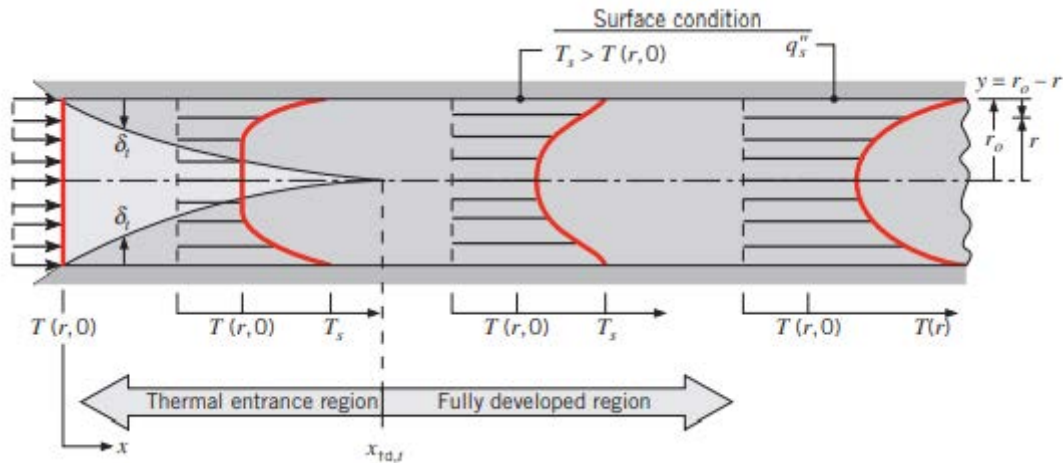


Figure 5.3: Thermal entrance region

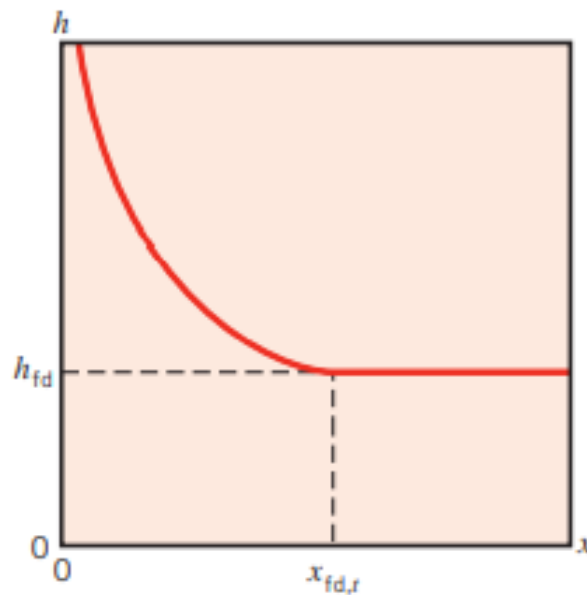


Figure 5.4: h coefficient along thermal entrance region

In the case of laminar flow the *thermal entrance region* depends on the Reynolds and Prandtl numbers while in the case of turbulent motion it is constant and calculable with the following relationship

$$\frac{x_{fd,t}}{D_{hyd}} = 10 \quad (5.15)$$

Usually for pipes of much longer length than the length of the *thermal entrance region*, h coefficient is considered constant. Assuming that the temperature of the fluid is variable only along the longitudinal direction of the tube, it is possible to obtain the difference in temperature between the inlet and outlet using the following equation

$$Q = \dot{m} \cdot c_p \cdot (T_{out} - T_{in}) \quad (5.16)$$

where:

- Q is the total power transferred to the fluid;
- T_{in} and T_{out} are the mean temperature at inlet and outlet.

The calculation of the temperature difference between the inlet and outlet is very important to keep the cooling system efficient and to avoid changes of state (evaporation) inside the system. In fact, equation 5.16 is often used by imposing a maximum difference in temperature between the inlet and outlet and calculating the required fluid mass flow.

$$\dot{m} = \frac{Q}{c_p \cdot (T_{out} - T_{in})} \quad (5.17)$$

Actually the temperature of the fluid also varies along the radial direction. In fact, if we consider the case of a tube in contact with a heat source, the fluid inside will be warmer on the surface and colder towards the inside. To simplify the analytical model, an average temperature is calculated and assigned to the whole section of the tube; it can be calculated from the energy balance equation.

$$T_{mean} = \frac{\int_{A_s} \rho \cdot C_p \cdot u(r, x) \cdot T(r, c) dA_s}{\dot{m} \cdot C_p} \quad (5.18)$$

Applying equation 5.16 to the differential control volume of figure 5.5 we obtain

$$dQ_{conv} = \dot{m} \cdot c_p \cdot [(T_{mean} + dT_{mean}) - T_{mean}] \quad (5.19)$$

or

$$dQ_{conv} = \dot{m} \cdot c_p \cdot dT_{mean} \quad (5.20)$$

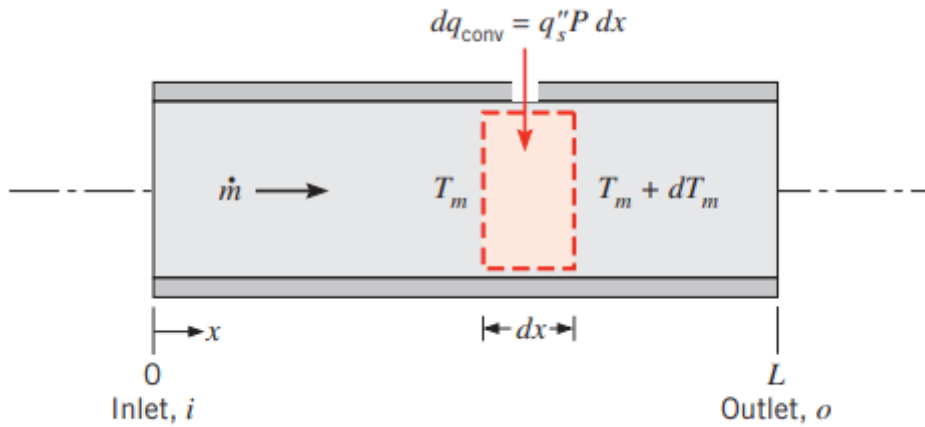


Figure 5.5: Differential control volume

By expressing the rate of convection heat transfer to the differential element as $dq_{conv} = q_s'' \cdot P \cdot dx$, where P is the surface perimeter, we get

$$\frac{dT_{mean}}{dx} = \frac{q_s'' \cdot P}{\dot{m} \cdot c_p} = \frac{P \cdot h \cdot (T_s - T_{mean})}{\dot{m} \cdot c_p} \quad (5.21)$$

Equation 5.21 allows to determine the variation profile of the fluid temperature along the longitudinal direction. Considering both the heat flux and the surface temperature as dependent on the variable x would make the equation complicated to solve. For this reason, two simpler but still very frequent situations are considered: constant heat flux and constant surface temperature.

Constant heat flux

Equation 5.21 become

$$\frac{dT_{mean}}{dx} = \frac{q_s'' \cdot P}{\dot{m} \cdot c_p} \quad (5.22)$$

which can be solved very easily

$$T_{mean}(x) = T_{mean,i} + \frac{q_s'' \cdot P}{\dot{m} \cdot c_p} \cdot x \quad (5.23)$$

Accordingly, the mean temperature varies linearly with x along the tube (figure 5.6). Moreover, we also expect the temperature difference $(T_s - T_{mean})$ to vary with x , as shown in Figure 5.6. This difference is initially small (due to the large value of h near the entrance) but increases with increasing x due to the decrease in h that occurs as the boundary layer develops. However, in the fully developed region h is independent of x . Hence it follows that $(T_s - T_{mean})$ must also be independent of x in this region. It should be noted that, if the heat flux is not constant but is, instead, a known function of x , equation 5.21 may still be integrated to obtain the variation of the mean temperature with x .

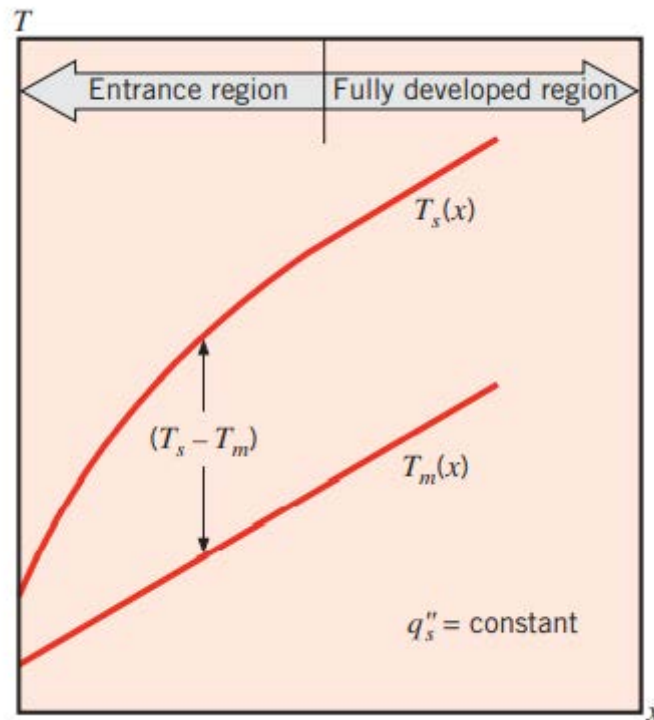


Figure 5.6: Axial temperature variations for heat transfer in a tube with constant heat flux

Constant Surface Temperature

Equation 5.21 become

$$\frac{dT_{mean}}{dx} = -\frac{d(\Delta T)}{dx} = \frac{P \cdot h \cdot \Delta T}{\dot{m} \cdot c_p} \quad (5.24)$$

where:

- $\Delta T = T_s - T_{mean}$

or

$$\ln \frac{\Delta T_o}{\Delta T_i} = -\frac{P \cdot L}{\dot{m} \cdot c_p} \cdot \left(\frac{1}{L} \cdot \int_0^L h \cdot dx \right) \quad (5.25)$$

Solving equation 5.24 we get

$$\frac{T_s - T_{mean}(x)}{T_s - T_{mean,i}} = e^{-\frac{P \cdot x \cdot h(x)}{\dot{m} \cdot c_p}} \quad (5.26)$$

temperature difference ($T_s - T_{mean}$) decays in an exponential fashion with distance along the tube (5.7).

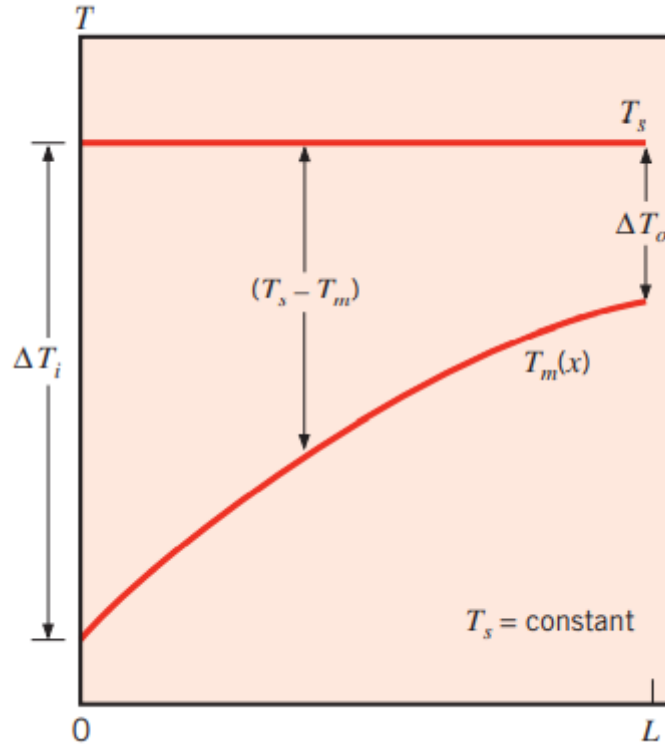


Figure 5.7: Axial temperature variations for heat transfer in a tube with constant surface temperature

Determination of an expression for the total heat transfer rate q_{conv} is complicated by the nature of the temperature decay. Expressing equation 5.19 in the form

$$q_{conv} = \dot{m} \cdot c_p \cdot [(T_s - T_{mean,i}) - (T_s - T_{mean,o})] = \dot{m} \cdot c_p \cdot [\Delta T_i - \Delta T_o] \quad (5.27)$$

and substituting for $\dot{m} \cdot c_p$ from equation 5.25, we obtain

$$q_{conv} = h \cdot A_s \cdot \Delta T_{lm} \quad (5.28)$$

where:

- $\Delta T_{lm} = \frac{\Delta T_o - \Delta T_i}{\ln \frac{\Delta T_o}{\Delta T_i}}$ is called *logarithmic mean temperature difference*.

Equation 5.28 is a form of Newton's law of cooling for the entire tube, and ΔT_{lm} is the appropriate average of the temperature difference over the tube length. The logarithmic nature of this average temperature difference (in contrast, e.g., to an arithmetic mean temperature difference) is due to the exponential nature of the temperature decay.

5.2 Stator cooling system analysis

A steel jacket resting directly on the stator is chosen as the cooling system. This way the thermal resistance between the external surface of the stator and the water flowing in the channels of the jacket is minimal. Two configurations for the jacket are analyzed, one with tangential water flow and one with longitudinal water flow. Both are shown in figure 5.8 [11].

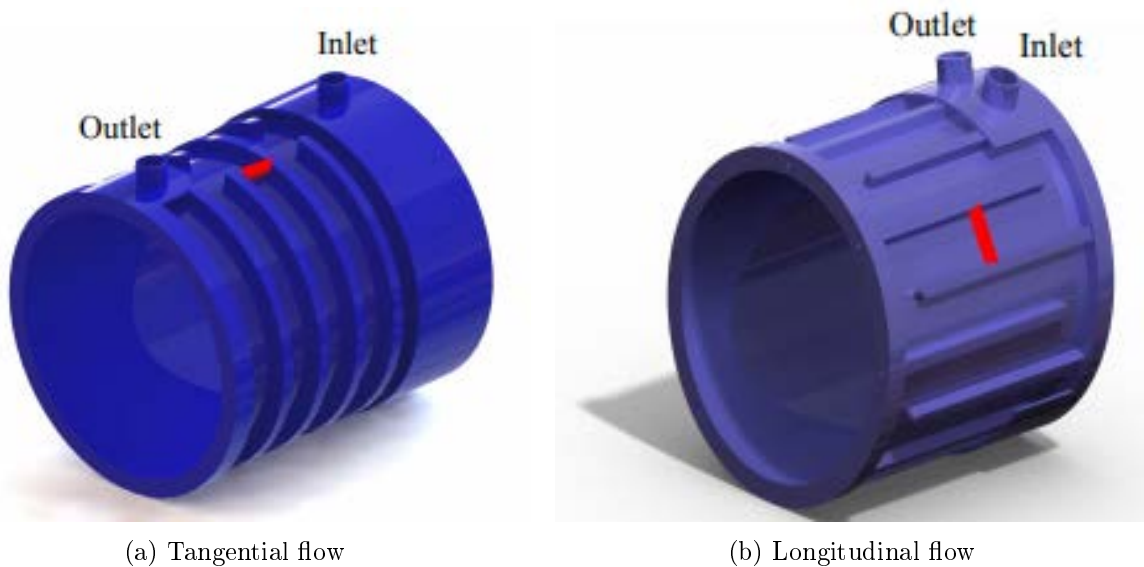


Figure 5.8: Cooling frame geometry

Main dimensions of the frames are listed in table 5.1.

	Value	Mesure unit
External diameter	240	<i>mm</i>
Internal diameter	200	<i>mm</i>
Axial length	130	<i>mm</i>
Pipe width	23.75	<i>mm</i>
Pipe height	10	<i>mm</i>
Hydraulic diameter	14.1	<i>mm</i>
Pipe cross section	237.5	<i>mm</i> ²
Pipes total lenght	2764	<i>mm</i>
Number of pipes	4	/

Table 5.1: Frames main dimensions

Given the high number of conditions in which the machine can work, the map of the stator losses (iron+copper) for each working point is reported in figure 5.9. For this analysis the IPM motor will be taken as a reference as it is subject to greater losses in the stator.

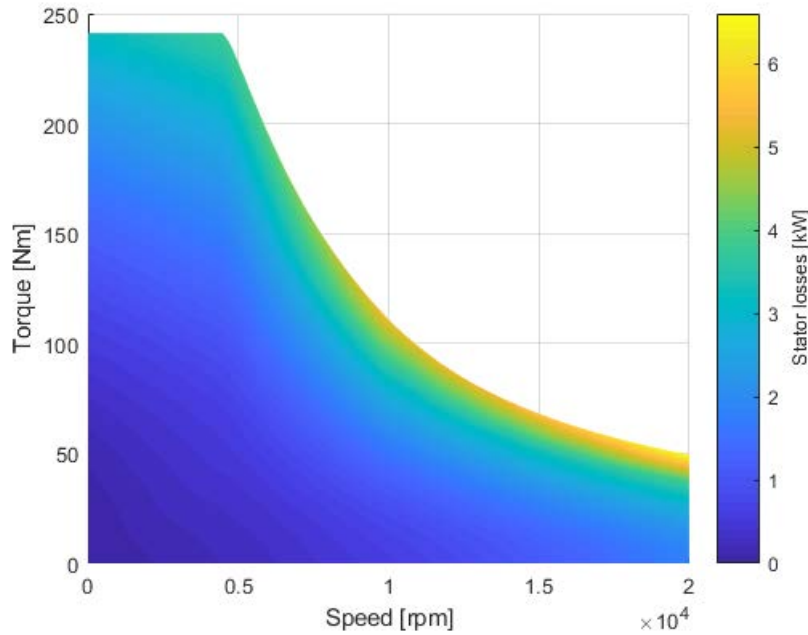


Figure 5.9: Stator total losses at every working point

Clearly the machine does not work continuously at every point, in particular the highest torque (and current) conditions are sustained only for short periods, for example during abrupt accelerations. Given the enormous difference between the electrical and thermal time constants, an overload condition can be sustained for a short period of time without a high increase in temperature. For this reason the cooling system will have to remove only the losses corresponding to the regime operating points. The total stator losses are imposed in the analysis as surface thermal fluxes exiting from the external surface of the stator. To obtain these fluxes the following

equation is applied:

$$Q_{flux} = \frac{P_{stator}}{\pi \cdot D_{ext} \cdot L_{stk}} = \frac{P_{stator}}{0.08168} \quad (5.29)$$

It is decided to consider two operating conditions: base speed and nominal torque, maximum speed and medium torque. The first could represent an uphill driving while the second could be a highway driving. The main parameters for the two conditions are shown in figure 5.2.

	First condition	Second condition	Mesure unit
Peak current	400	170	<i>A</i>
Rotating speed	5000	20000	<i>rpm</i>
Torque	118	25	<i>Nm</i>
Juole losses	0.9	0.8	<i>kW</i>
Iron losses	0.5	1.96	<i>kW</i>
Total losses	1.4	2.76	<i>kW</i>
Heat flux	17.14	33.8	$\frac{kW}{m^2}$

Table 5.2: Losses for two working points

Since the most severe conditions occur at high speed, the second situation will be taken as a reference.

5.2.1 Analytical model

The analytical model simplifies the curved geometry of the frame by considering it rectilinear and composed of a single tube. The water inlet temperature is 40 °C. First a comparison is made between equations 5.7, 5.8 and 5.9 in calculating the Nusselt number and the corresponding heat transfer coefficient as reported in figure 5.10 and 5.11. It can be seen how values are quite similar to each other, anyway equation 5.8 has been used to carry out the analysis.

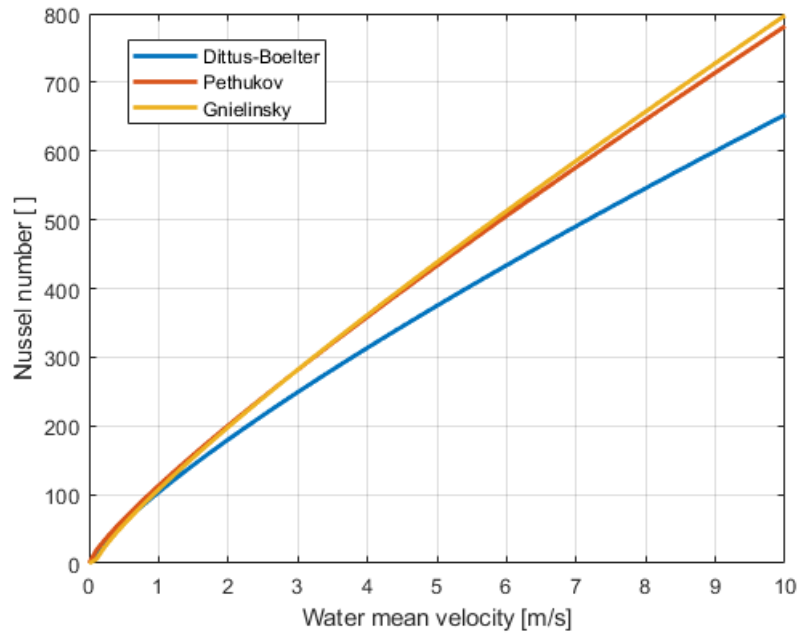


Figure 5.10: Comparison on Nusselt number

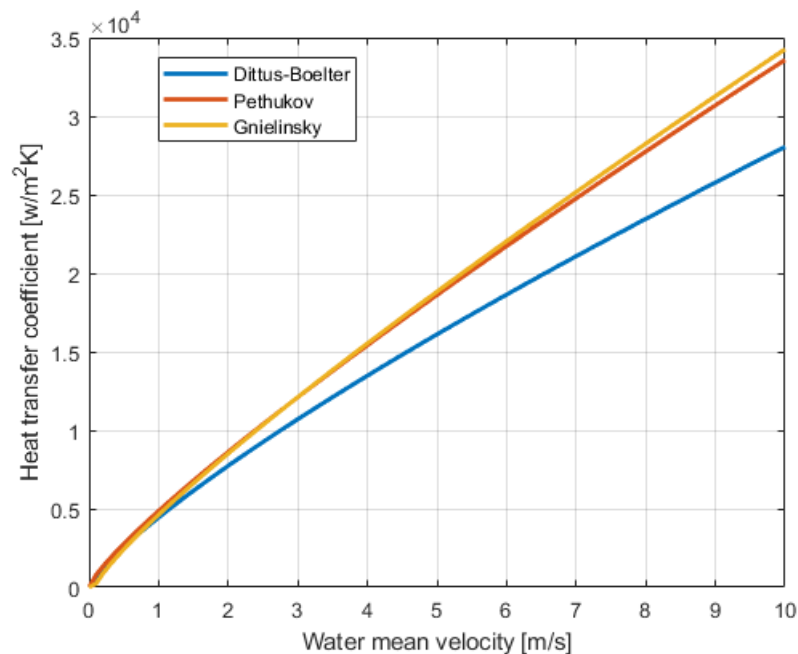


Figure 5.11: Comparison on h coefficient

Then the fluid temperature difference between the inlet and outlet is calculated for various fluid velocity using 5.16 and results are reported in figure 5.12.

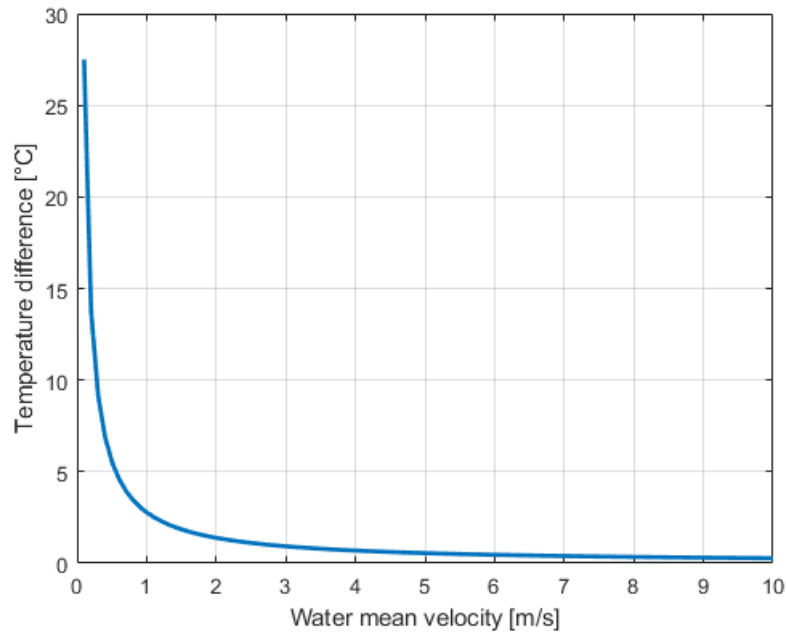


Figure 5.12: Temperature difference between intel and outlet

In figure 5.13 Reynolds number is shown as a function of water velocity. It can be seen that for $v > 0.7 \frac{m}{s}$ there is a fully developed turbulent flow.

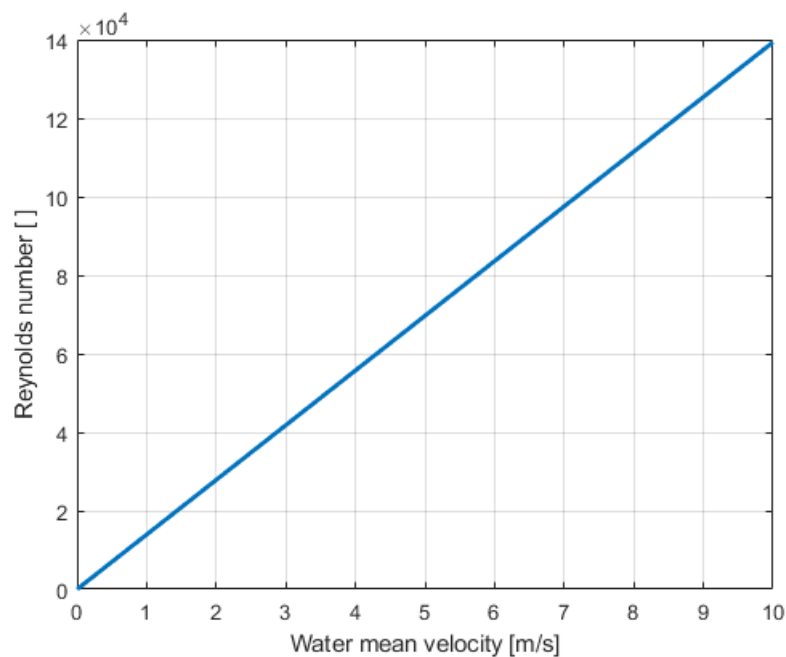


Figure 5.13: Reynolds number versus water mean velocity

The pressure drop between inlet and outle can also be computed by applying equation 5.13

as a function of mass flow rate (figure 5.14).

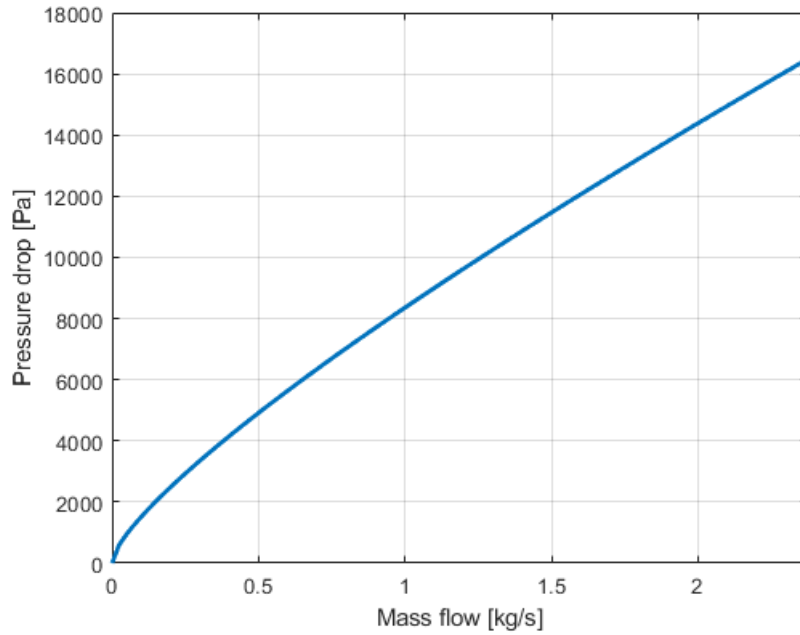


Figure 5.14: Pressure drop

Figure 5.15 shows the pump power needed to push the water into the pipe for various flux rate. Results are obtained using 5.14

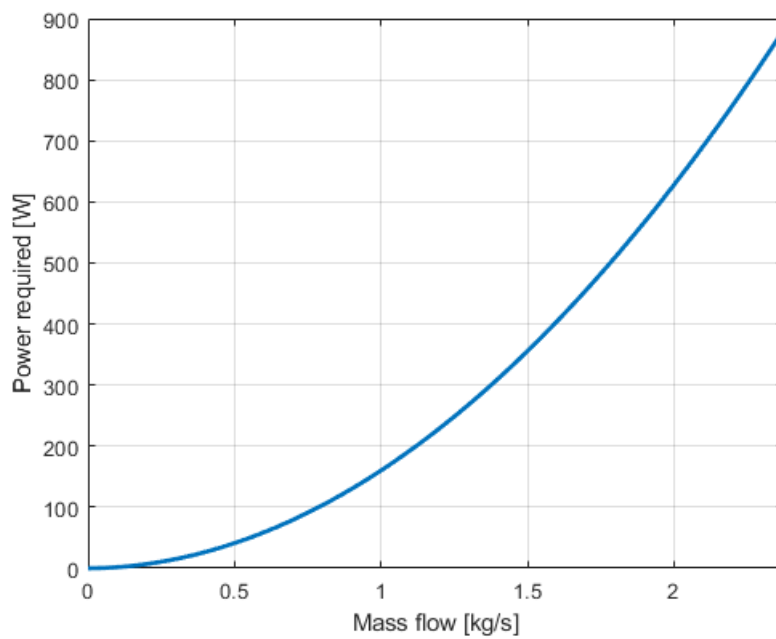


Figure 5.15: Power needed

A mass flow rate of $0.15 \frac{kg}{s}$ is chosen for three reasons:

- water temperature difference between inlet and outlet is about 4.41 °C so the fluid can be consider incompressible;
- fluid velocity is 0.63 $\frac{m}{s}$ so a good convection coefficient is achieved;
- there is not an excessive pressure drop between inlet and outlet.

Constant heat flux

By applying the equations of section 5.1.2 it is possible to obtain the trend of the temperature of the fluid and of the surface of the tube as a function of the position inside the tube itself as shown in figure 5.16. Note how it is supposed that only the bottom surface of the tube exchanges heat with the stator.

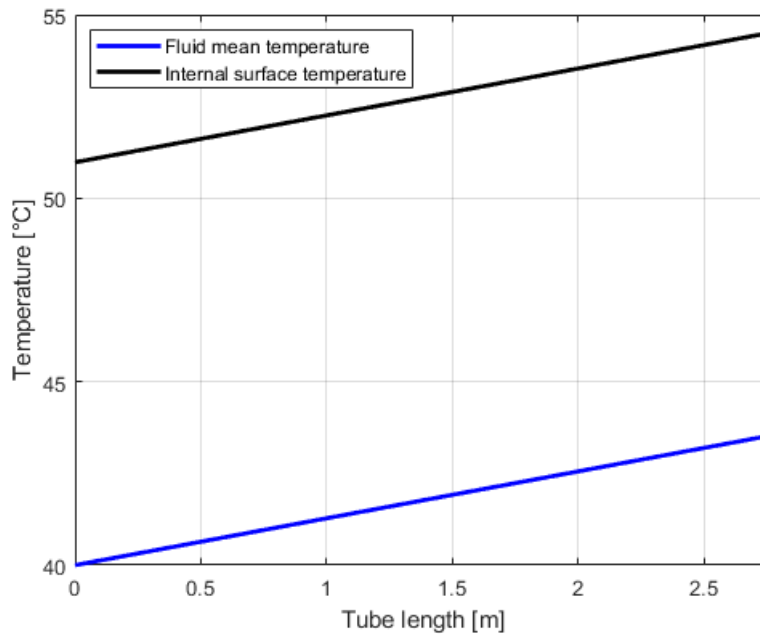


Figure 5.16: Temperature distribution in the tube

It can be seen how the external temperature of the stator reaches a maximum of 54.5 °C which allows good performances. Furthermore, the temperature difference between the pipe wall and the water is 11 °C which corresponds to a thermal convection coefficient

$$h = \frac{Heatflux}{T_{surface} - T_{water}} = 3070 \frac{W}{m^2 \cdot K} \quad (5.30)$$

Pressure drop is also computed using equation 5.13: $\Delta P = 2023 Pa$

Constant surface temperature

We refer now to section 5.1.2. In this case, the approach will be an iterative one, where various (constant) surface temperatures will be analyzed and then the one of interest will be obtained from the calculation of the corresponding heat flux. In figure 5.17 some analyzed cases are shown.

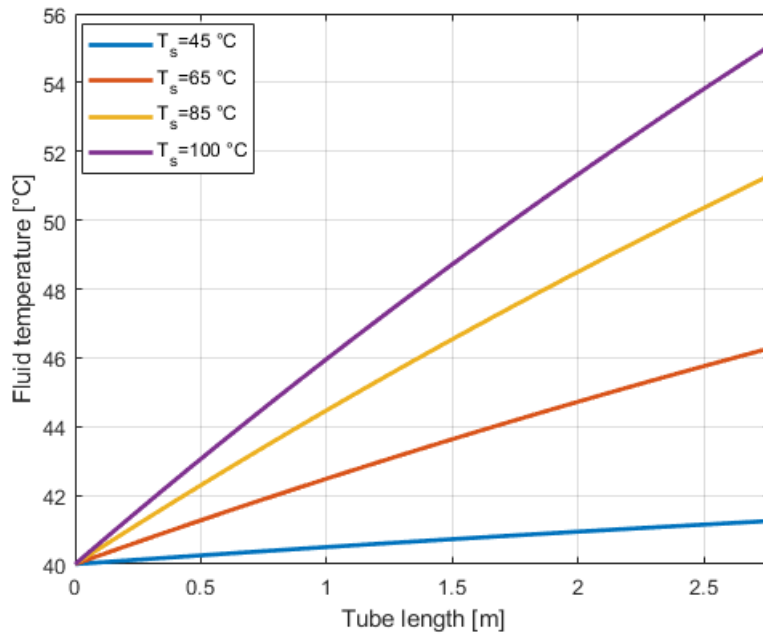


Figure 5.17: Fluid temperature for various tube surface temperature

Then the heat flow removed is calculated as a function of the surface temperature. In figure 5.18, it can be seen that to completely remove the heat flux imposed in table 5.2 the surface of the tube reaches 52.84 °C.

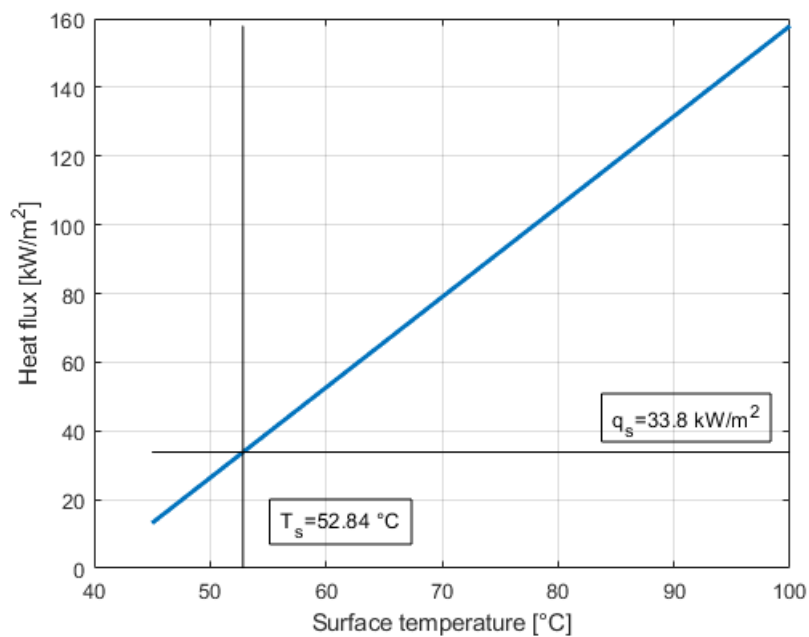


Figure 5.18: Surface temperature calculation

The same thing can be done using total heat insted of heat flux (figure 5.19).

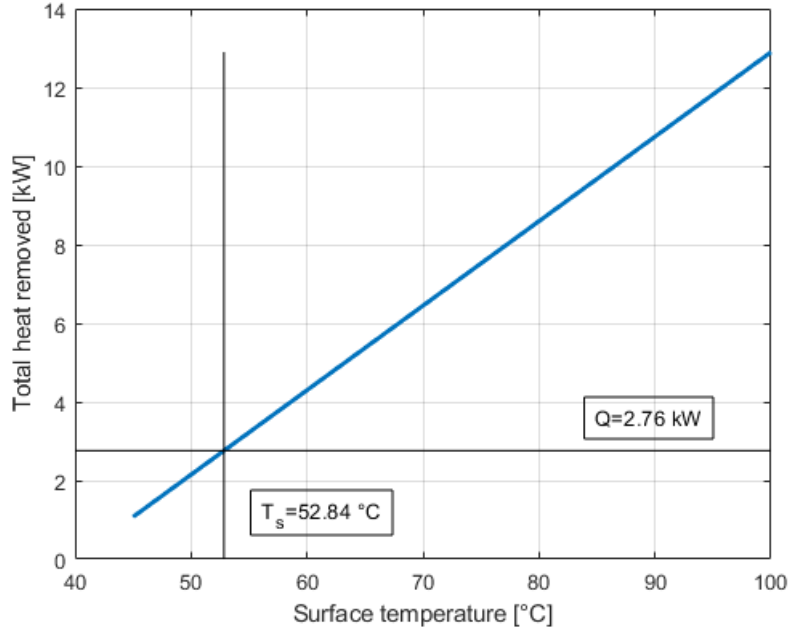


Figure 5.19: Surface temperature calculation

The corresponding heat transfer coefficient is

$$h = \frac{Heat\ flux}{T_{surface} - T_{water}} = 3040 \frac{W}{m^2 \cdot K} \quad (5.31)$$

Pressure drop results: $\Delta P = 2023 Pa$. It can be seen that the results obtained are very close even if they are based on different initial conditions. In the following comparisons the method with constant surface temperature will be taken as a reference.

5.2.2 Numerical model

The geometry of the frame is built directly in Ansys using the internal CAD software *DesignModeler* and is shown in figure 5.20. It is decided to analyze two types of frames, one with tangential flows and the other one with longitudinal flows to see which one has the best performances [11]. The initial conditions are the same as those imposed in the analytical analysis.

	Value	Mesure unit
Inlet water temperature	40	$^{\circ}C$
Mass flow rate	0.15	$\frac{kg}{s}$
Heat flux on the internal surface	33.8	$\frac{kW}{m^2}$

Table 5.3: Initial conditions

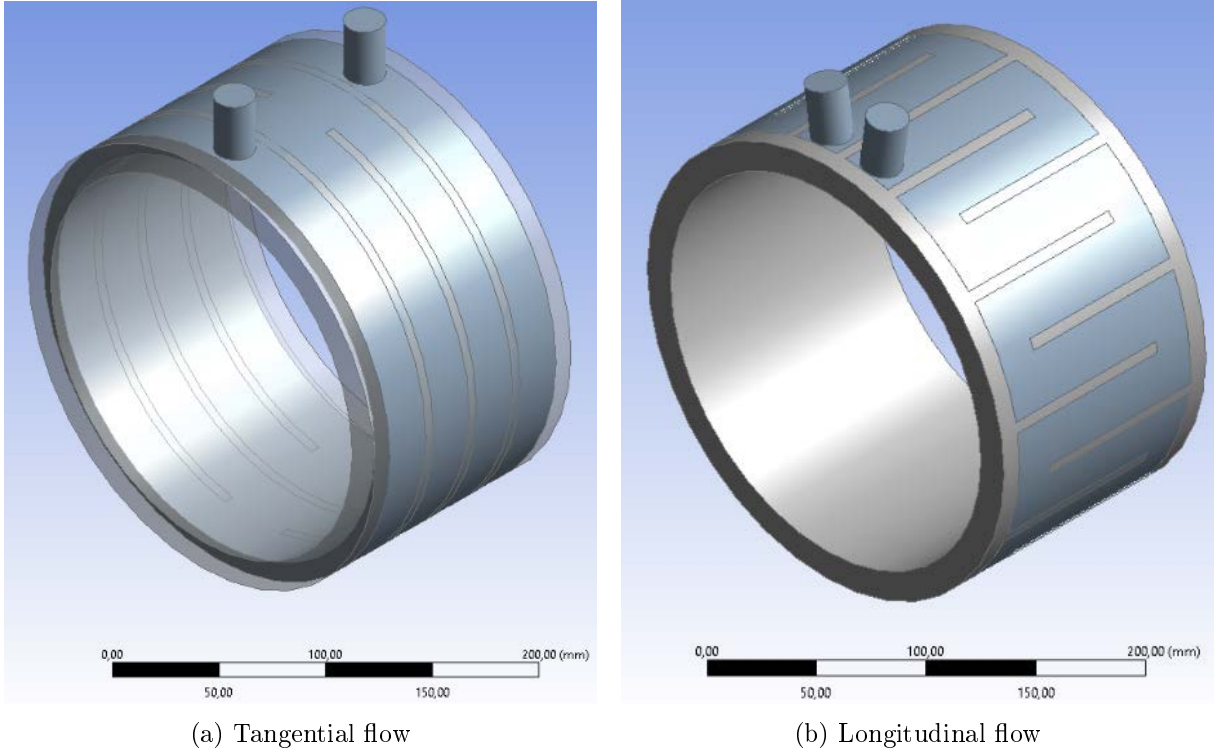


Figure 5.20: Gemetry built in DesignModeler

Physical model

A multiphysics coupled CFD heat-transfer model is used for a simultaneous estimation of the thermal and turbulent properties of the fluid in the frame. The flow of an incompressible fluid is described by the Reynolds Averaged Navier-Stokes Equation (RANS)

$$\rho \cdot \frac{\partial U}{\partial t} - \eta \cdot \nabla \cdot \nabla U + \rho \cdot U \cdot \nabla U + \nabla P + \nabla(\rho \cdot u' \otimes u') = F \quad (5.32)$$

$$\nabla \cdot U = 0 \quad (5.33)$$

where

- η is the dynamic viscosity;
- U is the average velocity field;
- ρ is the fluid density;
- P is the pressure;
- F is the volumetric force vector;
- $\nabla(\rho \cdot u' \otimes u')$ represents fluctuations around a mean flow and it is called the Reynolds stress tensor;

In order to solve equation 5.33 some assumptions are necessary, some of those lead to the so called $k - \epsilon$ model which is widely used for fluid flowing in pipes. The final system that has to be solved

is in the form

$$\rho \cdot \frac{\partial U}{\partial t} - \nabla \cdot \left[\left(\eta + \rho \cdot C_\mu \cdot \frac{k^2}{\epsilon} \right) \cdot \left(\nabla U + (\nabla Q)^T \right) \right] + \rho \cdot U \cdot \nabla U + \nabla P = F \quad (5.34)$$

$$\nabla \cdot U = 0 \quad (5.35)$$

where:

- k is the turbulent kinetic energy;
- ϵ is the dissipation rate of the turbulent energy.

Thermal field model must also be solved. According to the energy conservation law, the governing equation of transient heat conduction can be expressed as [11]

$$\rho \cdot c_p \cdot \frac{\partial T}{\partial t} = \nabla \cdot (k \cdot \nabla T) + P \quad (5.36)$$

where

- T is the temperature;
- ρ is the mass density;
- c_p is the specific heat capacity;
- k is the thermal conductivity;
- P is the heat generation rate.

For the water cooled thermal field, the typical boundary conditions of convection and radiation can be used

$$-k \cdot \left(\frac{\partial T}{\partial t} \right)_f = h \cdot (T_f - T_w) \quad (5.37)$$

where

- T_f is the frame temperature;
- T_w is the water temperature;
- h is the convective heat transfer coefficient between the frame and fluid.

Radiation heat is negligible so only convection is involved in the heat transfer

$$P = h \cdot A \cdot (T_f - T_w) \quad (5.38)$$

where

- A is the inner surface of the frame.

The h coefficient is computed directly by Ansys.

Results

In figure 5.21 the temperature distribution on the inner surface of the frame is reported. Some hot spots caused by local turbulence can be seen and moreover it is noted that the configuration with longitudinal flows is more efficient from the thermal point of view.

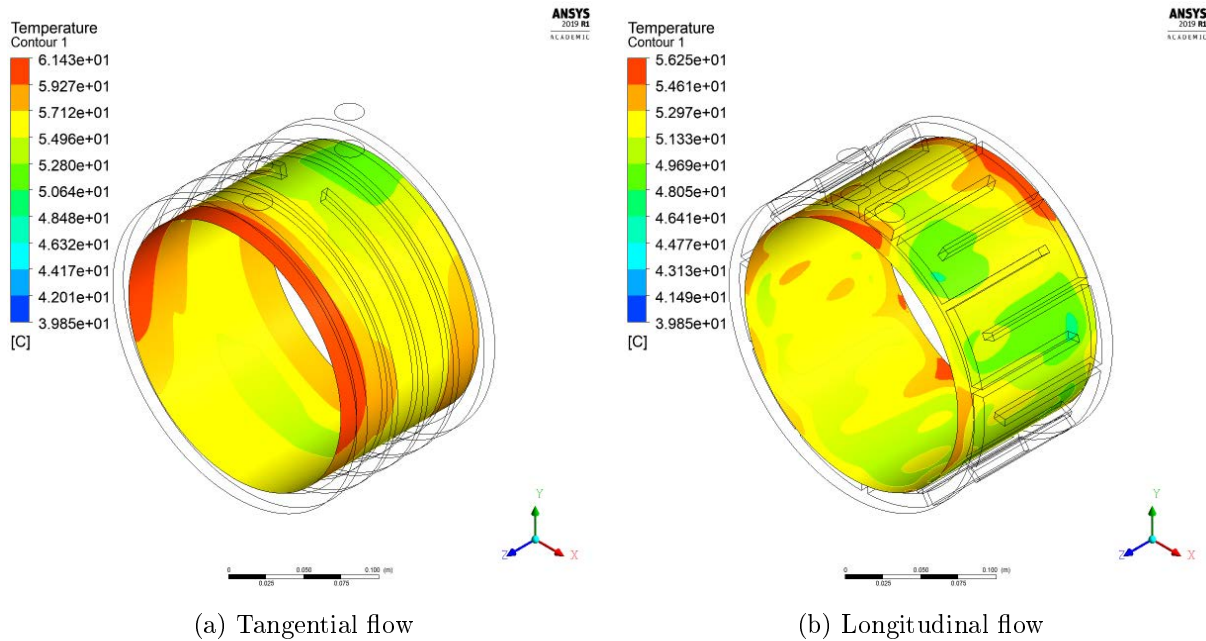


Figure 5.21: Internal surface temperature distribution

In figure 5.22 the streamlines of water are shown; the fluid velocity is not constant along the frame, this causes local points where h coefficient is lower and thus local hot spots. It can be seen how much higher speed peaks are achieved in the longitudinal flow configuration, this leads to greater local losses and therefore the need for greater pressure to push the water into the channels.

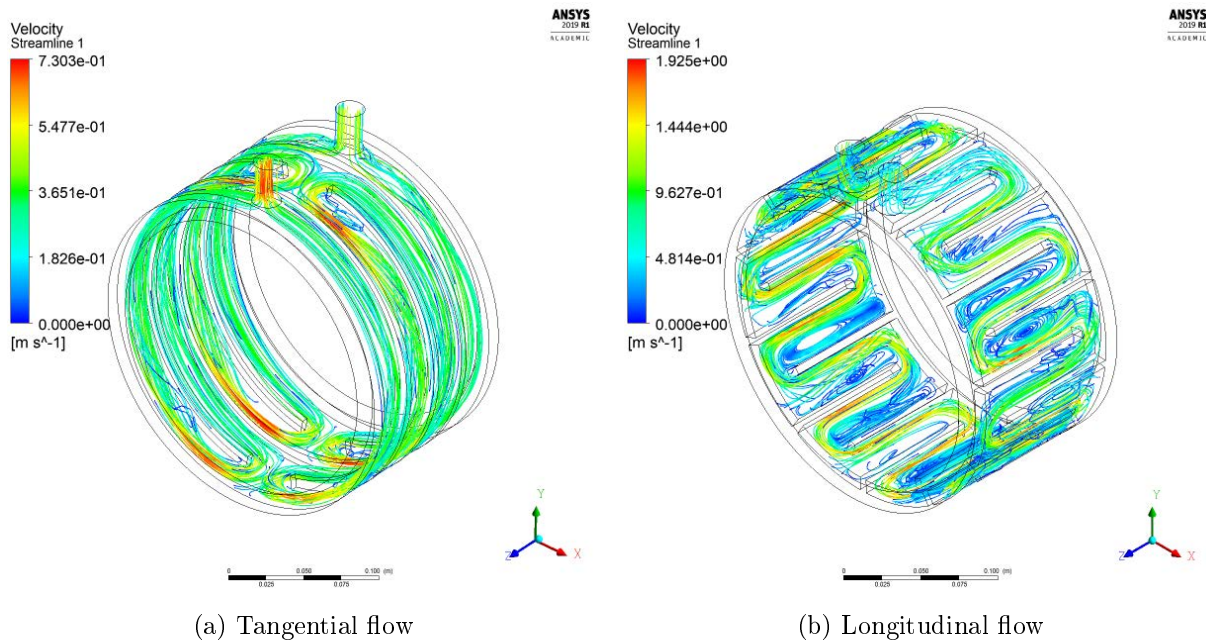


Figure 5.22: Water streamlines

5.2.3 Comparison

Table 5.4 compares the results obtained by the analytical method at constant surface temperature, by the tangential flow jacket and the longitudinal flow jacket.

	Constant temperature	Tangential flow	Longitudinal flow
Flow rate ($\frac{kg}{s}$)	0.15	0.15	0.15
Inlet temperature ($^{\circ}C$)	40	40	40
Outlet temperature ($^{\circ}C$)	43.44	44.18	43.01
Temperature difference ($^{\circ}C$)	3.44	4.18	3.01
Internal surface heat flux ($\frac{kW}{m^2}$)	33.8	33.8	33.8
Internal surface temperature ($^{\circ}C$)	52.84	56.6	51.67
h coefficient ($\frac{W}{m^2 \cdot K}$)	3040	2330	3323
Pressure drop (Pa)	2023	777	22868

Table 5.4: Comparisons

A good agreement can be noted regarding the difference in temperature between the inlet and outlet. As regards the temperature of the internal surface, a small difference between the analytical methods and the FEM analysis can be seen. This may be due to the fact that the analytical model considers the fluid directly in contact with the surface from which the heat flow is emitted while in the real model there is a 5 mm steel layer. The thermal convection coefficient is quite different, perhaps because of the errors of the empirical formulas used and the multiple speed changes within the channels that the simplified model does not take into account. Finally, the pressure difference is also very different between the analytical model and FEM one so the simplified approach cannot be trusted. As regards the two cooling frames analyzed, it can be seen

that the one with longitudinal flows has higher thermal performances with the same water flow rate. However, due to the very tortuous path, with sharp curvatures, the losses in the pipeline are very high and a substantial pressure drop is therefore required to be able to guarantee the massflow. For this reason it is concluded that the tangential flow configuration is the better geometry and will be taken as the cooling system. In any case, I would like to underline how the FEM model requires the resolution of a multi-physical model in three dimensions, with a high number of degrees of freedom and requires some time and computational resources. The analytical model, on the other hand, although not very accurate, is very simple to implement and requires very few resources, making it excellent for a first orientation design.

5.2.4 Stator thermal analysis

After checking that the temperature of the external surface is maintained at an acceptable value, it is necessary to check at what temperature the internal parts of the machine are subject. In particular, electrical insulators are the most delicate parts and are not able to tolerate high thermal stresses. The ability of an insulator to withstand temperature is assessed according to the IEC60034-1 standard which divides the insulators into thermal classes (table 5.5) [22]. Obviously the classes with greater tolerance are more expensive. In our case we consider a class F insulation (typical for rotating electric machines) and therefore a maximum operating temperature of 150 °C for greater safety.

Thermal class	Temperature [°C]
Y	90
A	105
E	120
B	130
F	155
H	180
200	200
220	220
250	250

Table 5.5: Thermal classes and their maximum temperature

It is noted that a high temperature is also problematic for permanent magnets; in fact, as already stated in chapter 2, the risk of demagnetization increases with increasing temperature while remanence induction decreases. Finally also the copper is more performing at a lower temperature because it presents a lower electrical resistance. The thermal study is carried out through the use of software FEMM. Only the stator is analyzed as the rotor which will be analyzed separately. In the model, visible in figure 5.23, an air layer of 3 mm has been added beyond the external surface of the stator. It represents the very thin layer of still air that is interposed between the cooling jacket and the external surface of the stator since perfect adhesion is not physically feasible. This tiny layer of air is the cause of important temperature differences and it is therefore mandatory to introduce it in the simulation. However, to avoid having problems in creating the mesh, the air layer is reported 10 times larger than the real one with a thermal conductivity also increased by 10 times. Furthermore, zero thermal flux conditions are imposed

in order to study only one pole of the machine and a fixed temperature is imposed on the external surface, maintained by the cooling system.

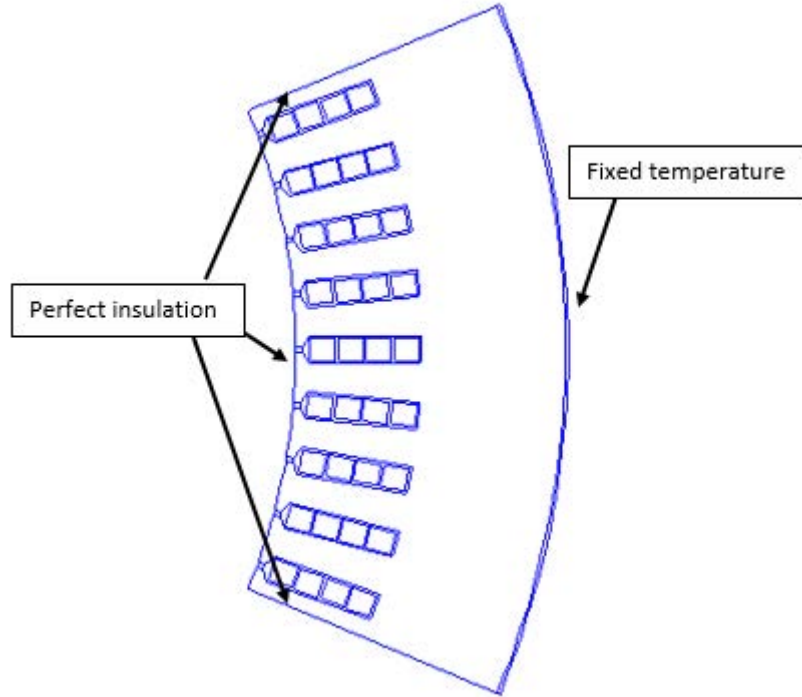


Figure 5.23: Thermal model and boundary conditions

In the software the sources are introduced as volumetric powers, in table 5.6 they are reported for both considered situations.

	First condition	Second condition	Mesure unit
Copper volume	$2.515 \cdot 10^{-4}$	$2.515 \cdot 10^{-4}$	m^3
Copper volumetric losses	3.57	3.18	$\frac{MW}{m^3}$
Iron volume	$17.15 \cdot 10^{-4}$	$17.15 \cdot 10^{-4}$	m^3
Iron volumetric losses	0.291	1.14	$\frac{MW}{m^3}$
External surface temperature	56.6	56.6	$^{\circ}C$

Table 5.6: Source losses in FEMM

Figure 5.24 shows the temperature distribution in the stator, temperatures are reported considering the inlet temperature of the cooling water as reference ($40^{\circ}C$). It is noted that in both situation the maximum thermal limit of $155^{\circ}C$ is widely respected. This means that the insulation class chosen is adequate. It is also noted that the temperature of the internal surface of the stator is about $91^{\circ}C$ in the first situation and about $120^{\circ}C$ in the second one, these parameters will be used in the rotor thermal analysis.

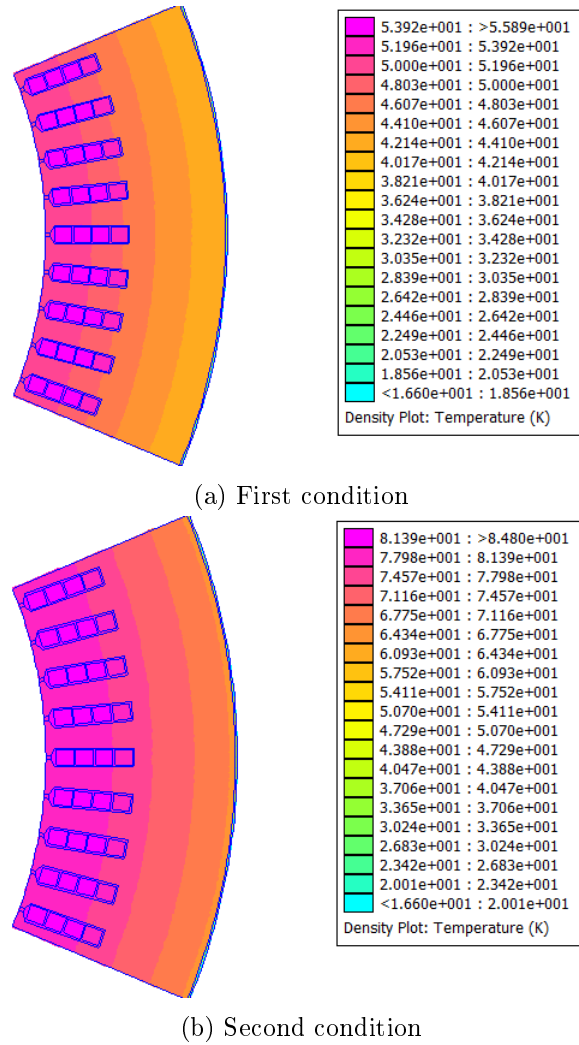


Figure 5.24: Stator temperature distribution

5.3 Thermal transient

In addition to thermal regime analysis, transient analysis is also important. In fact, the operating temperature is reached after a certain time which depends on the physical properties of the materials considered.

5.3.1 Conduction model

The governing equation of conduction in isotropic solids is the following

$$\rho \cdot c_p \cdot \frac{\partial T}{\partial t} - \nabla \cdot (k \cdot \nabla T) = q_{vol} \quad (5.39)$$

where

- ρ is the density;
- c_p is the specific heat;
- T is the temperature;

- t is the time;
- k is the thermal conductivity;
- q_{vol} is the volumetric heat source.

Considering the one-dimensional case, equation 5.39 can be rewritten as

$$\rho \cdot c_p \cdot Vol \cdot \frac{dT}{dt} - \frac{\sigma \cdot S}{L} \cdot T = Q \quad (5.40)$$

which can also be written as

$$\frac{dT}{dt} - \frac{1}{R_{th} \cdot C_{th}} \cdot T = \frac{Q}{C_{th}} \quad (5.41)$$

where

- $C_{th} = c_p \cdot \rho \cdot Vol$ is the thermal capacity and represents the body's ability to accumulate heat with respect to its increase in temperature. In other words, a very high thermal capacity allows the body to absorb a high amount of thermal energy by slightly increasing its temperature.
- $R_{th} = \frac{L}{\sigma \cdot S}$ is the thermal resistance and represents the resistance that the body opposes to the passage of heat. A high thermal resistance makes the passage of heat difficult and determines strong temperature gradients;
- Q is the total source power.

The product $\tau = R_{th} \cdot C_{th}$ is a time in dimensional terms and is called *thermal time constant*. It indicates the time it takes for the transient to run out, in particular after about 5-8 time constants, the transient can be considered totally exhausted and the process is said to be at steady state. It is interesting to note that the equation is mathematically identical to the charge or discharge equation of a capacitor through an ideal current generator. In fact, by replacing the temperature with the voltage, the heat source with the electric current, the thermal resistance with the electric one and the thermal capacity with the electric one we obtain:

$$\frac{dV}{dt} - \frac{1}{R_{el} \cdot C_{el}} \cdot V = \frac{I}{C_{el}} \quad (5.42)$$

which is representative of the electrical circuit shown in figure 5.25

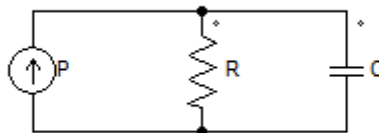


Figure 5.25: Electric circuit for charging of a capacitor

From the resolution of the network in figure 5.25, in the case of charging (or heating), a trend of the type shown in figure 5.26 is obtained

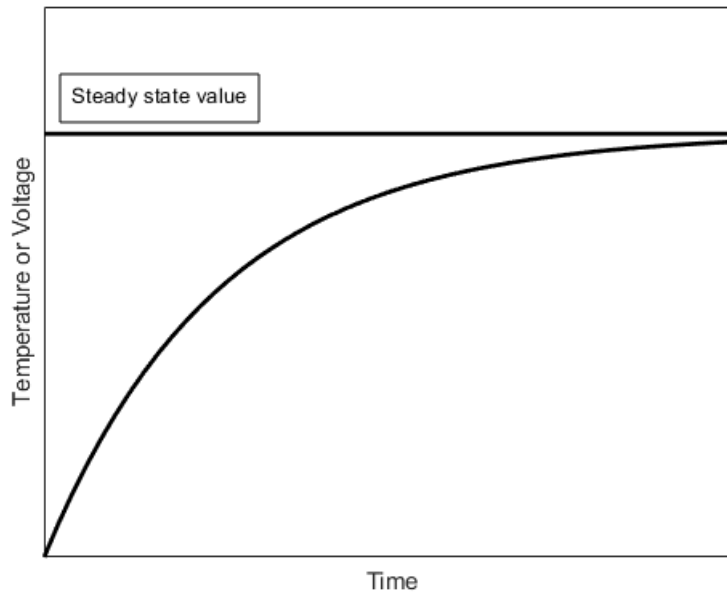


Figure 5.26: Temperature (or voltage) versus time

It is therefore possible to study thermal transients through electrical networks. This is advantageous because it is possible to have a zero dimensional model of the process and moreover the computation of the solution is very simple and fast, especially by using some software (i.e. PSpice). Although the mathematical equation is the same, the time constants present are very different. In particular, we speak of time constants in the order of milliseconds for the electric model while we speak of minutes or even hours (especially for very large machines) in the case of the thermal model. This difference can be exploited to operate the machine in points that would not be sustainable at steady state but for short periods of time, less than the thermal regime time, they are. In this way, the design of the cooling system is much less expensive as it is dimensioned for the regime power only. Although the thermal model obtained from the equivalent electrical network is very convenient from a computational point of view, it does not allow to determine the actual temperature distribution in the materials but only an average value. However, in thermal analysis it is crucial to identify any hot spots where the temperature can be very high to avoid local damage (especially to insulators) which can then lead to large-scale failures. For this reason, the thermal analysis is carried out using the finite element software Ansys.

5.3.2 Numerical model

To decrease the calculation domain and therefore speed up the solution times, only one section of the motor is analyzed, corresponding to $\frac{360}{Q_s} = 5$ mechanical degrees. To make the model representative of the whole machine, perfect insulation conditions (zero heat flux) are imposed on the side and bottom walls, while fixed temperature is imposed on the upper part. As already done in section 5.2.4 an air layer is added to represent the small gap between the cooling frame and the stator. In figure 5.27 the geometry analyzed is shown.

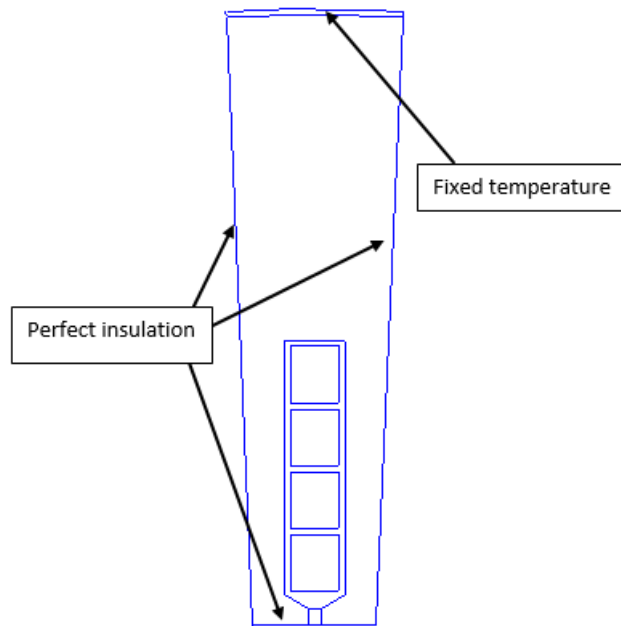


Figure 5.27: Geometry simulated in Ansys and boundary conditions

The two limit conditions reported in table 5.7 are analyzed. The first condition could represent a standstill start with high acceleration while the second a high speed overtaking.

	First condition	Second condition	Measure unit
Current	800	682	<i>A peak</i>
Speed	5000	20000	<i>rpm</i>
Torque	241	46	<i>Nm</i>
Juole losses	3.28	3.2	<i>kW</i>
Iron losses	0.53	3.42	<i>kW</i>
Copper volumetric heat	13	12.7	$\frac{MW}{m^3}$
Iron volumetric heat	0.31	2	$\frac{MW}{m^3}$

Table 5.7: Study conditions

Figure 5.28 shows the temperature distributions in the first condition in three different time instants.

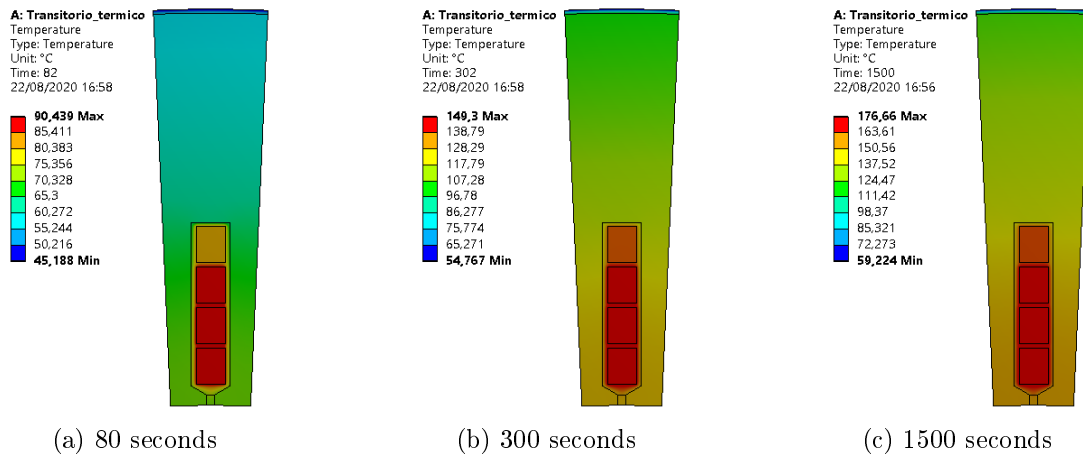


Figure 5.28: Temperature distribution for the first condition

Since the temperature is not uniform in the materials (see figure 5.28), the trend of the maximum temperature in iron, copper and insulating varnish is shown in figure 5.29 in order to consider only the worst case. Copper and insulating varnish have a practically equal temperature and therefore it is not possible to distinguish them. This must not seem strange, in fact the temperatures considered are the maximum. The first thin layer of insulation directly in contact with copper is clearly at the same temperature as copper.

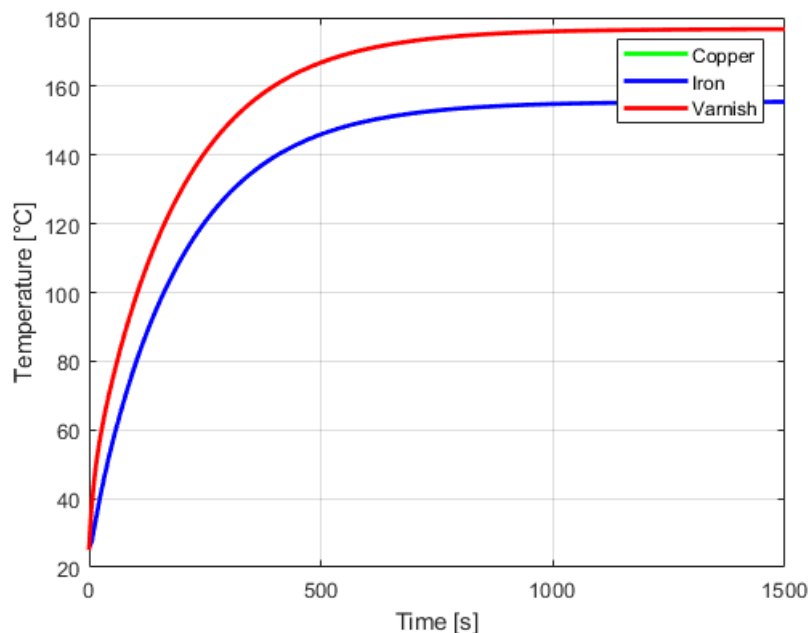


Figure 5.29: Maximum temperature versus time at $T = 241 Nm$ and $n = 5000 rpm$

It can be seen how the temperature of 155 °C is reached for $t = 344 s$. This means that the motor is able to run at maximum torque and base speed for about 5.5 minutes (starting from room temperature) without exceeding the thermal limit. For completeness, the trends of

the minimum temperatures are shown in figure 5.30, however these values are not taken into consideration.

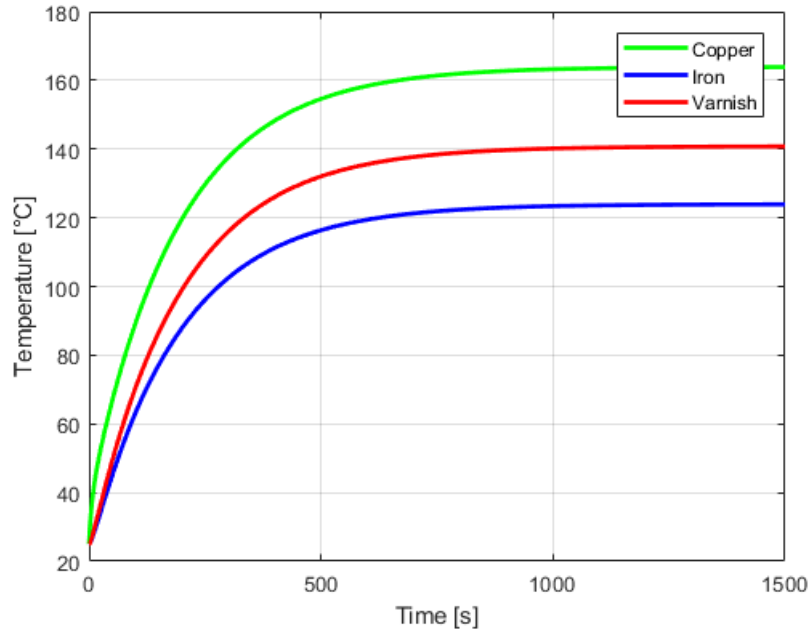


Figure 5.30: Minimum temperature versus time at $T = 241 Nm$ and $n = 5000 rpm$

Figure 5.31 shows the temperature distributions in the first condition in three different time instants.

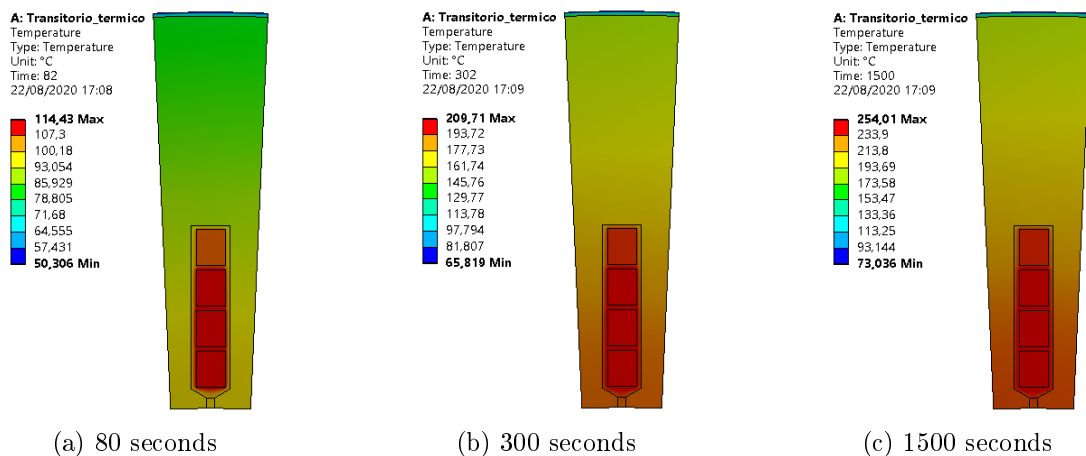


Figure 5.31: Temperature distribution at $\hat{I} = 682 A$ and $n = 20000 rpm$

The trend of the maximum temperature in iron, copper and insulating varnish is shown in figure 5.32

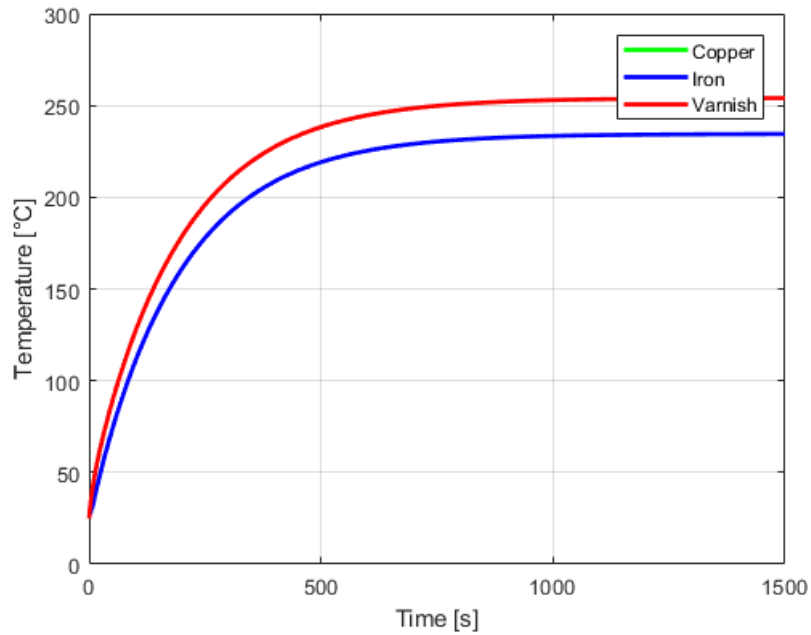


Figure 5.32: Temperature versus time at $T = 46 Nm$ and $n = 20000 rpm$

It can be seen how the temperature of $155\text{ }^{\circ}\text{C}$ is reached for $t = 148\text{ s}$. This means that the motor is able to run at maximum speed with maximum available torque for about 2.5 minutes (starting from room temperature) without exceeding the thermal limit. The trends of the minimum temperatures are shown in figure 5.33, however these values are not taken into consideration.

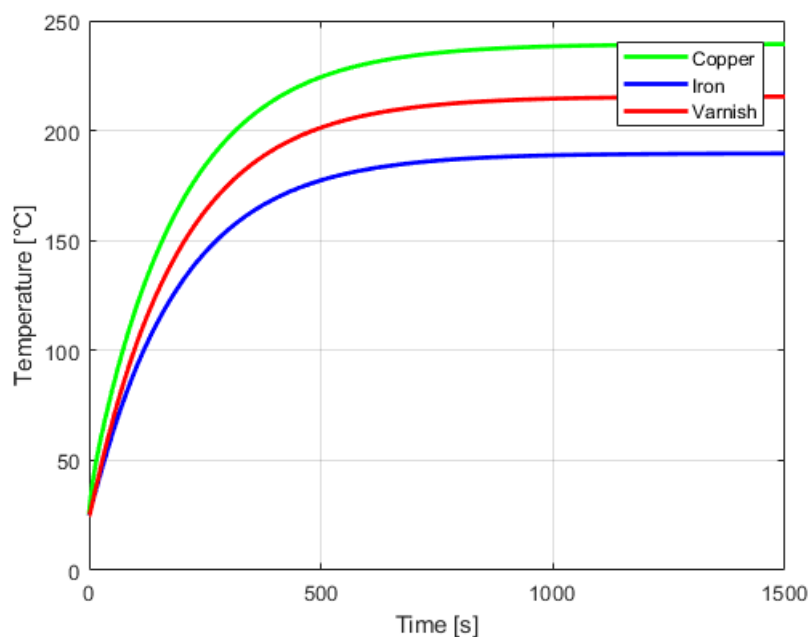


Figure 5.33: Minimum temperature versus time at $T = 46 Nm$ and $n = 20000 rpm$

5.3.3 Analytical model

To validate the finite element simulation and obtain a simplified zero-dimensional model, the equivalent thermal network of the stator is constructed. Only the section shown in figure 5.34 is taken into consideration in order to obtain greater precision. PSim software is used for a quick network solution. The most important resistances and thermal capacities are considered concentrated in a single point (zero-dimensional model). The thermal resistances and capacities are calculated by means of equations 5.43 and 5.44 while the resistance representing the convective exchange is calculated with equation (5.45). Finally, the power to be imposed on the current generators is calculated by dividing the total losses among all the considered sections.

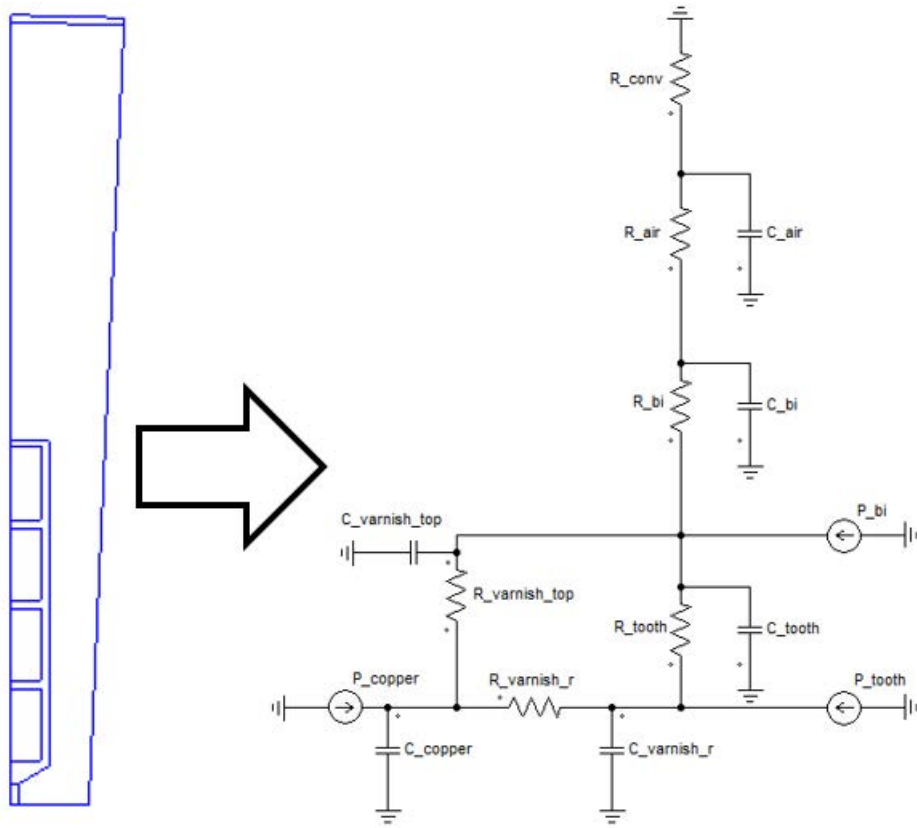


Figure 5.34: Thermal network

$$R_{thermal} = \frac{L}{\sigma \cdot S} \quad (5.43)$$

$$C_{thermal} = c_p \cdot Vol \cdot \rho \quad (5.44)$$

$$R_{convection} = \frac{1}{h_{convection} \cdot S} \quad (5.45)$$

Table 5.8 shows the parameters to be included in the network while table 5.9 shows the values assigned to the current generators.

	Value	Mesure unit
$R_{varnish,r}$	0.923	$\frac{K}{W}$
R_{tooth}	1.2652	$\frac{K}{W}$
$R_{varnish,top}$	7.6923	$\frac{K}{W}$
R_{bi}	0.7692	$\frac{K}{W}$
R_{air}	2.6366	$\frac{K}{W}$
R_{conv}	0.0762	$\frac{K}{W}$
C_{cooper}	5.98	$\frac{J}{K}$
$C_{varnish,d}$	1.59	$\frac{J}{K}$
$C_{varnish,top}$	0.1909	$\frac{J}{K}$
C_{tooth}	10.41	$\frac{J}{K}$
C_{bi}	28.077	$\frac{J}{K}$
C_{air}	0.0000209	$\frac{J}{K}$

Table 5.8: Thermal network parameters

	First condition	Second condition	Mesure unit
P_{copper}	22.77	22.22	W
P_{tooth}	1.17	7.53	W
P_{bi}	2.52	16.2	W

Table 5.9: Sources

The results obtained in the two load conditions considered are shown in figure 5.35.

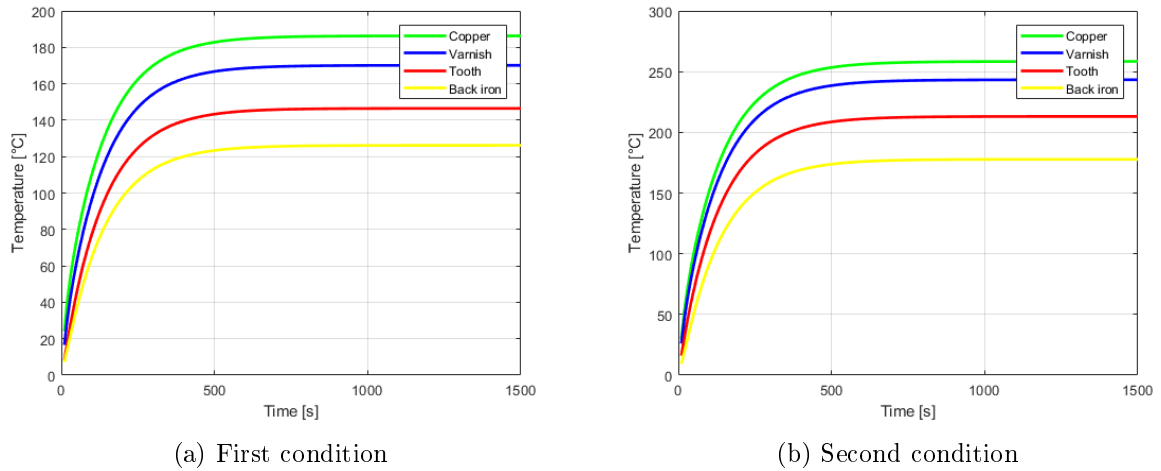
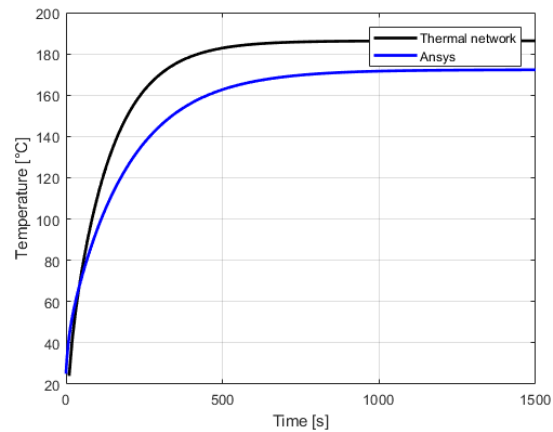


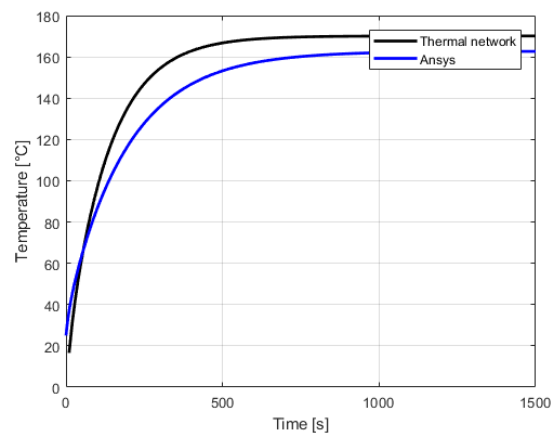
Figure 5.35: Temperature versus time for different parts of the stator

Finally, the results obtained from the two methods used are compared; for a fairer comparison,

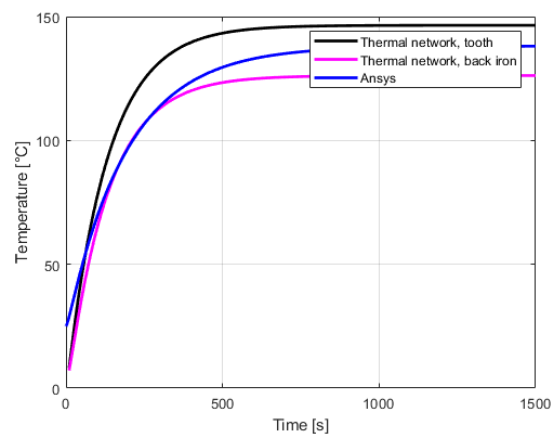
an average temperature of all the material is considered in the case of finite element simulation. In figure 5.36 the first condition is shown while in figure 5.37 the second one is shown.



(a) Copper

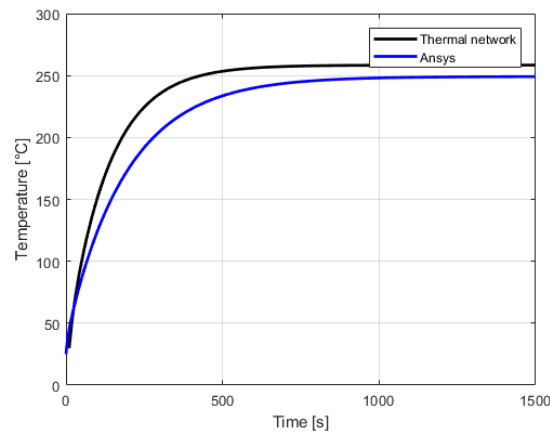


(b) Insulating varnish

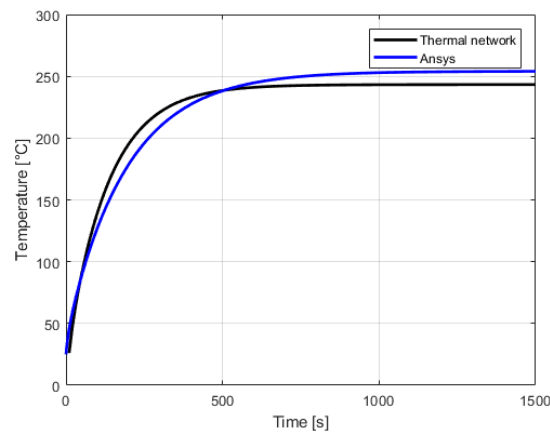


(c) Iron

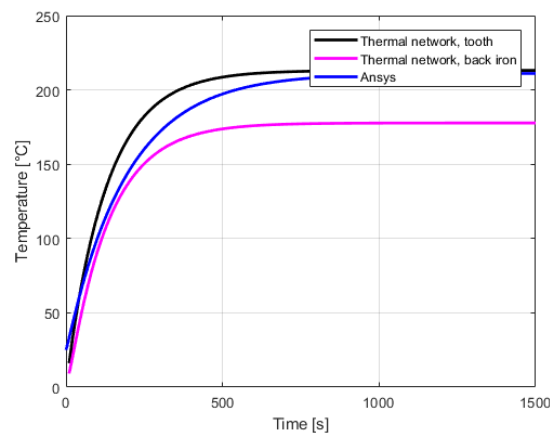
Figure 5.36: Comparison between Ansys and the equivalent thermal network, first condition



(a) Copper



(b) Insulating varnish



(c) Iron

Figure 5.37: Comparison between Ansys and the equivalent thermal network, second condition

A discreet agreement can be noted between the two methods, even if the thermal network is a bit inaccurate. This is due to the fact that the model is very simplified compared to the real situation. In fact, the losses are certainly not concentrated in a single point but distributed and the same can be said for the thermal resistances and capacities. Furthermore, as already mentioned, the temperatures calculated by the heating network are average values which therefore

cannot take into account any local critical issues. In reality, a more precise study would be possible by dividing the geometry into smaller elements to which assign capacities and resistances closer to reality. However, I think it is not a practical choice since Ansys is able to give an even more precise solution with much less effort.

5.4 Rotor cooling

Rotor cooling can be very problematic as the rotor is located in a tight space, where there is not much surface available for heat exchange and it is very complicated to install an effective cooling systems due to the moving parts. Furthermore, for both motors analyzed, the high rotor temperatures risk degrading the performances

- IPM motor has permanent magnets housed in the rotor and, as already mentioned in chapter 2, with high temperatures the magnets are less performing and have a greater risk of demagnetization;
- WRSM has the excitation windings housed in the rotor and the high temperatures can cause the electrical insulation to fail causing short circuits.

5.4.1 IPM motor rotor

In IPM motors the rotor is subject to losses mainly caused by two factors:

- Windage losses, analyzed in chapter 4;
- Eddy current losses due to high order magneto motive force harmonics, analyzed in chapter 2. In the case under consideration, given the small dimensions of the machine and the lamination of the rotor, these losses are neglected.

For the finite element study only the air gap is simulated in order to save computing resources (figure 5.38). The "moving boundary" boundary condition is set on the inner surface in order to simulate rotation without the need for a transient analysis, while a fixed temperature is set on the outer surface, corresponding to what has been identified in section 5.2.2. Windage losses are imposed as a constant heat flux on the rotor surface.

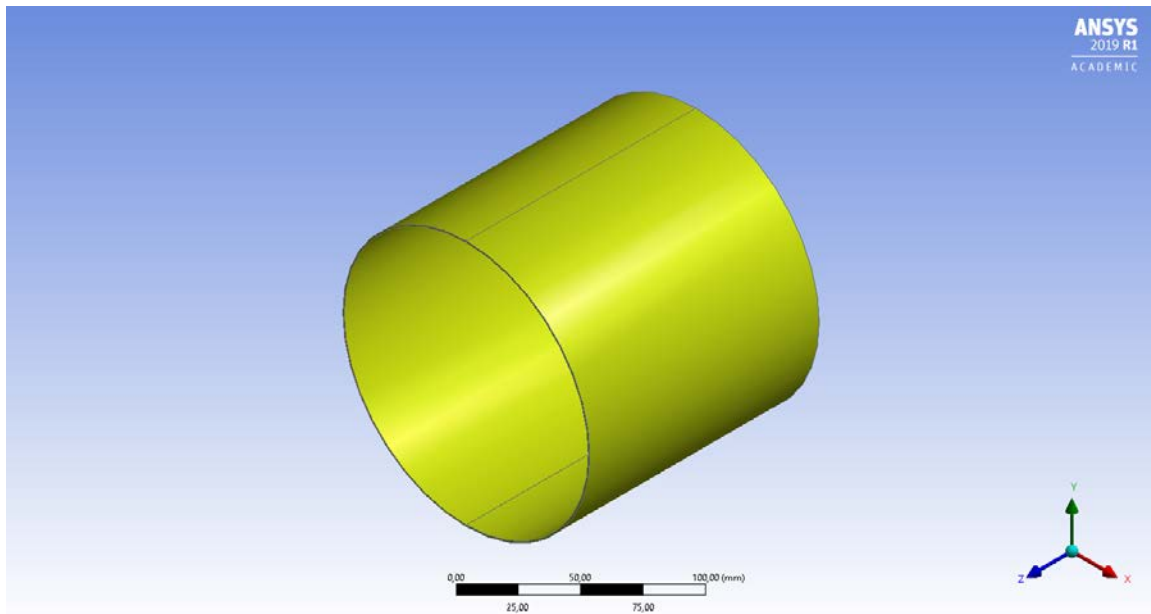


Figure 5.38: 3D model simulated in Ansys

Two working conditions are considered, the same indicated in section 5.2.4; the main parameters for the analysis are indicated in table 5.10.

	First condition	Second condition	Mesure unit
Windage losses	0.0076	0.231	kW
Heat flux	0.13	4.08	$\frac{kW}{m^2}$
Stator temperature	91	120	$^{\circ}C$

Table 5.10: Initial conditions

The temperature distribution on the rotor surface is shown in figure 5.39. At reduced speed the motor works at temperatures well below the maximum allowed by the magnets and therefore does not require special attention. As far as the maximum speed is concerned, it is noted that the surface temperature is quite high even if in any case lower than the maximum working temperature of the magnet ($180\text{ }^{\circ}C$). However, in this condition the risk of demagnetization, especially in the case of major failures or overloads, is decidedly higher. There are also anomalous temperature bands at the ends of the rotor, these are due to the interaction between the moving air and the fictitious walls that are inserted in the simulation to close the calculation domain but do not exist in reality; in fact, in the simulation at a lower speed the phenomenon is much less pronounced.

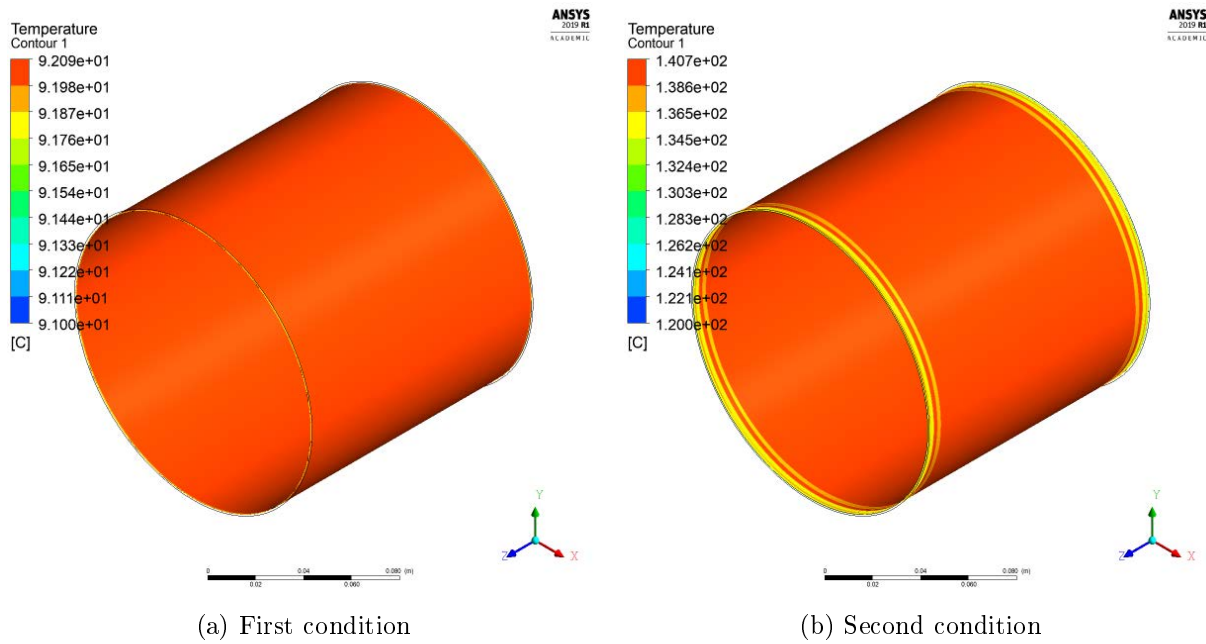


Figure 5.39: IPM rotor surface temperature distribution

In figure 5.40 a vector plot of speed is shown, this type of graph is very useful to verify that the boundary conditions have been entered correctly, in fact the speed of the air on the rotor wall coincides with the tangential speed of the rotor itself.

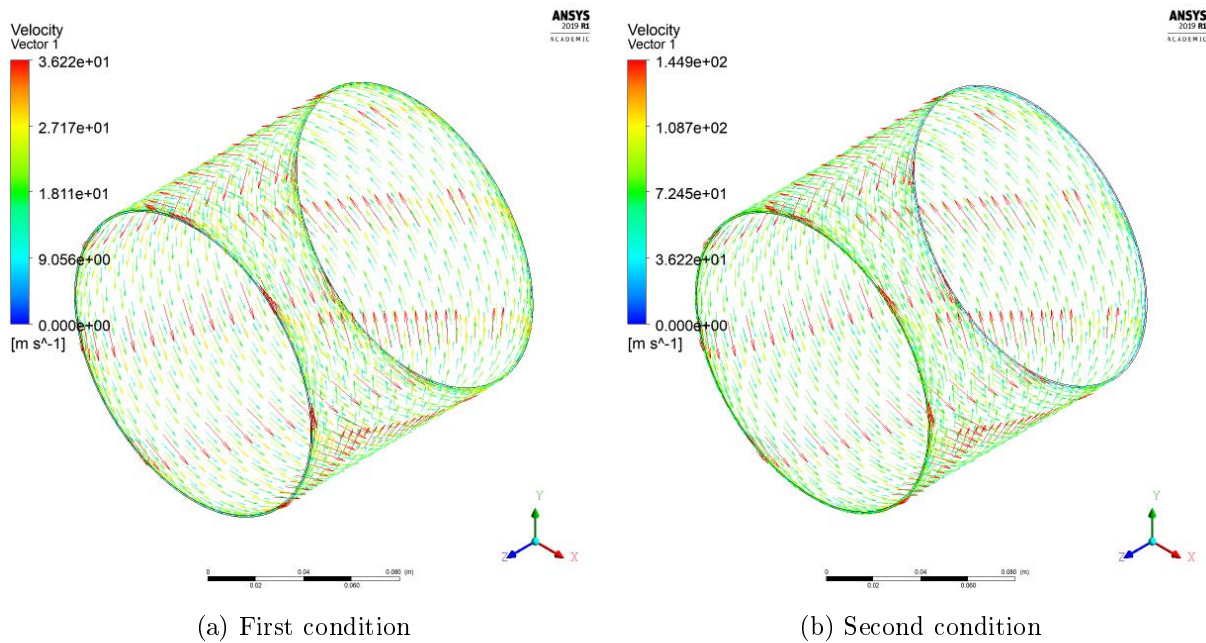


Figure 5.40: Velocity arrow plot

In figure 5.41 the air temperature of the air gap is shown.

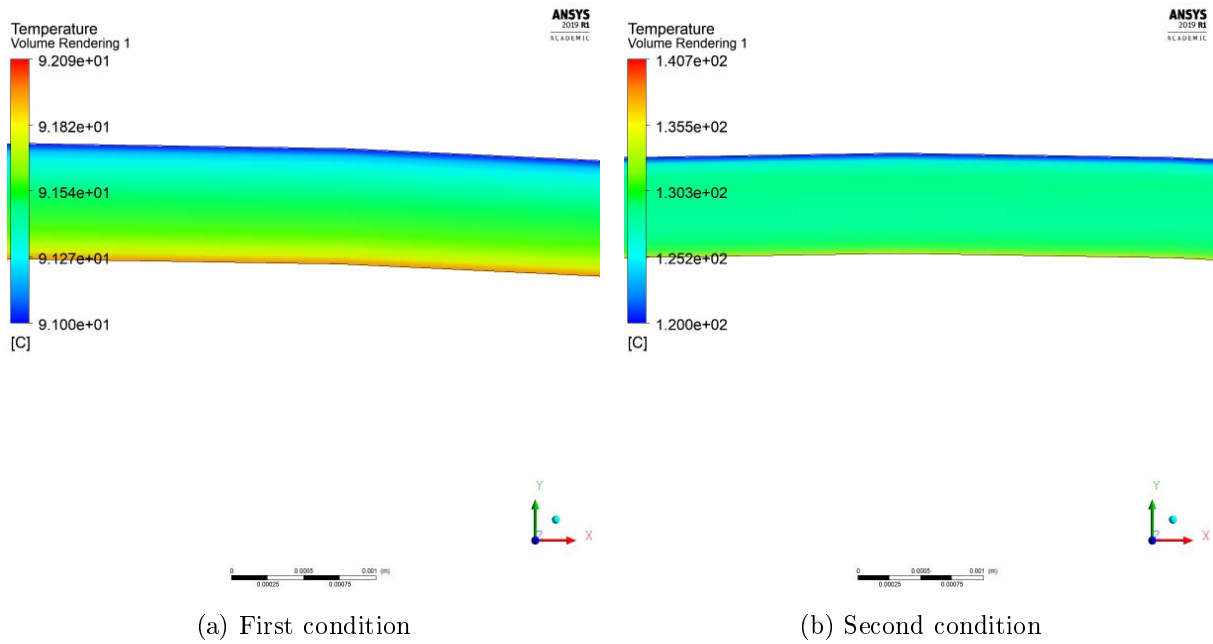


Figure 5.41: Air gap temperature

Table 5.14 summarizes the average parameters obtained from the simulations.

	First condition	Second condition	Mesure unit
Rotor surface mean temperature	92	137.7	$^{\circ}C$
Air mean temperature	91.49	128.8	$^{\circ}C$
Convection coefficient	260	911	$\frac{W}{m^2 \cdot K}$

Table 5.11: Thermal analysis results

Temperature inside the rotor

To study the temperature distribution inside the rotor, a 2D simulation is carried out using the FEMM software. The geometry studied and the boundary conditions imposed are shown in figure 5.42 while table 5.12 shows the properties assigned to materials.

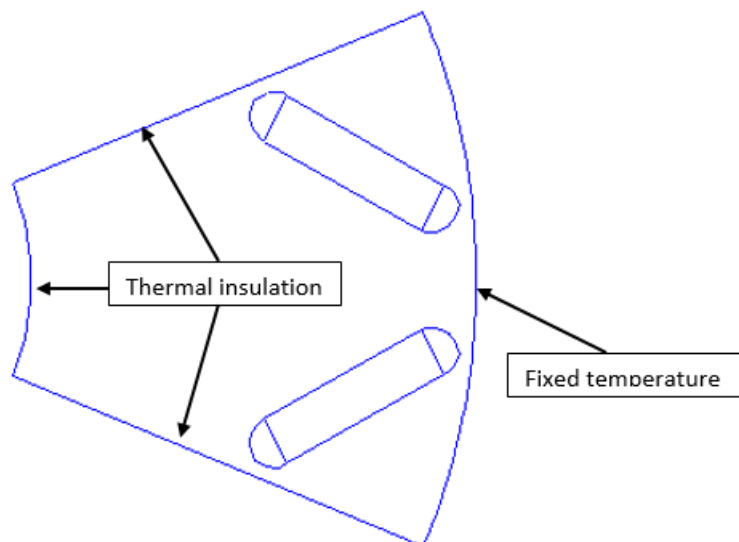
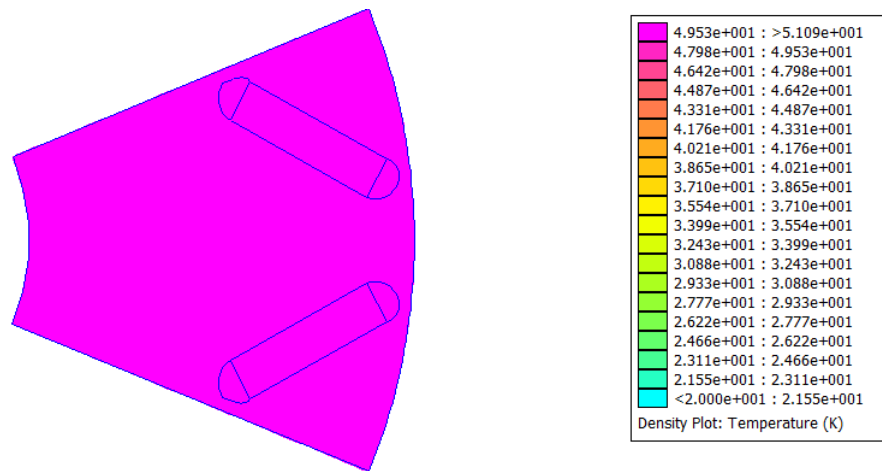


Figure 5.42: FEMM model of the IPM rotor

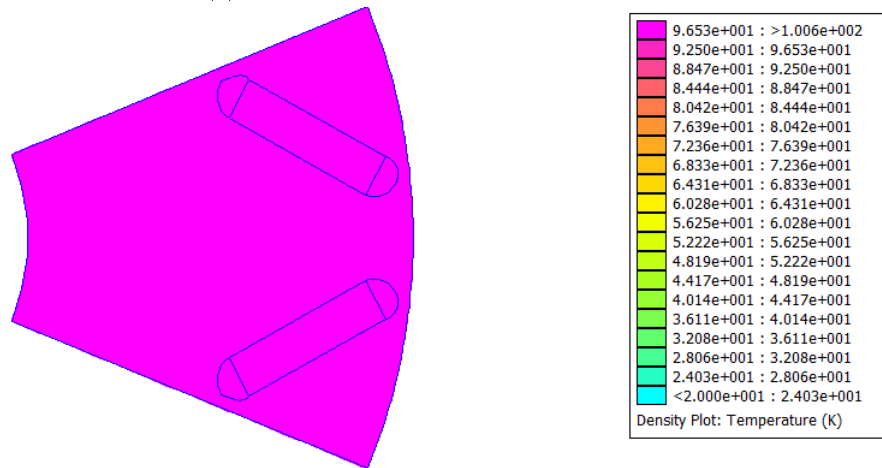
	First condition	Second condition	Mesure unit
Magnet thermal conductivity	8.95	8.95	$\frac{W}{m \cdot K}$
Rotor thermal conductivity	45	45	$\frac{W}{m \cdot K}$
Air thermal conductivity	0.02	0.02	$\frac{W}{m \cdot K}$
Rotor outer temperature	91	120	$^{\circ}C$

Table 5.12: Material properties imposed in FEMM simulation

The simulation results are shown in figure 5.43. The temperatures are reported considering the inlet temperature of the cooling water as reference (40 $^{\circ}C$).



(a) First condition



(b) Second condition

Figure 5.43: Rotor temperature distribution

5.4.2 WRSM rotor cooling

Once again only the air gap is simulated in order to save computing resources (5.44). The "moving boundary" boundary condition is set on the inner surface in order to simulate rotation, while a fixed temperature is set on the outer surface, corresponding to what has been identified in section 5.2.2.

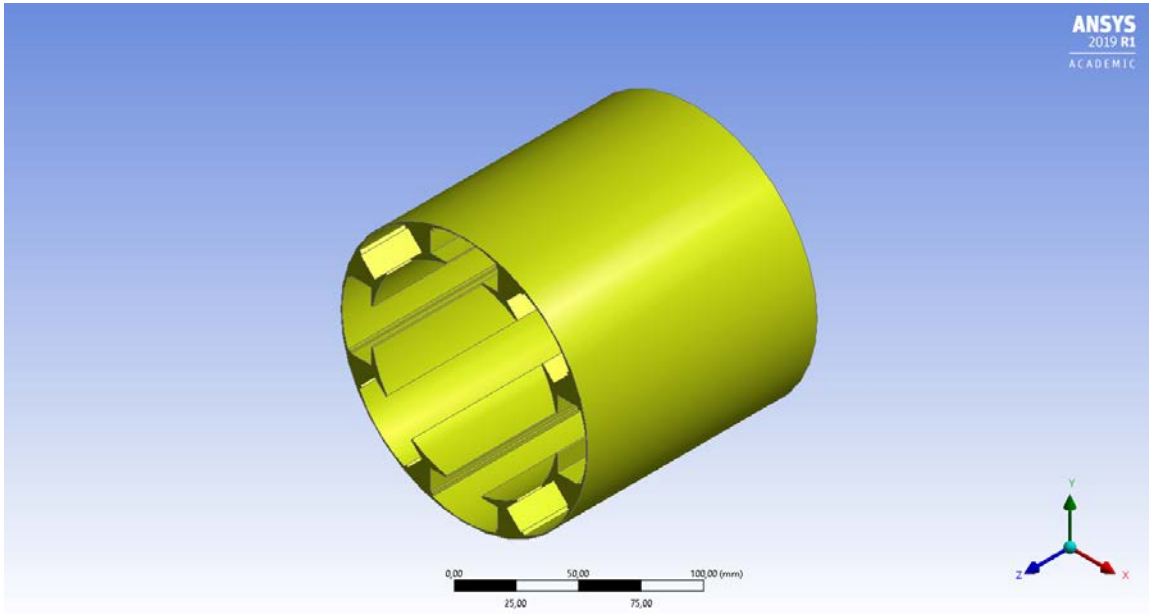


Figure 5.44: WRSM rotor 3D model built in DesignModeler

An excitation current of 1000 A is considered, i.e. the maximum allowed for not having excessive saturation. In the software, excitation losses are imposed as surface power density. Table 5.13 shows the initial data of the simulation. The conditions considered are those presented in section 5.2.2.

	First condition	Second condition	Mesure unit
Excitation losses	0.6	0.6	kW
Heat flux	10.8	10.8	$\frac{kW}{m^2}$
Windage losses	0.0356	1.88	kW
Heat flux	0.3	16.5	$\frac{kW}{m^2}$
Stator temperature	91	120	$^{\circ}C$

Table 5.13: Initial conditions

The temperature distribution on the rotor surface is shown in figure 5.45. Very high temperatures are noted in both situations. Furthermore, at low speeds, even if the average temperatures are lower than at higher speeds (table 5.14), hot spots with very dangerous conditions may be noticed. This is due to the fact that the reduced speed does not allow a good heat exchange with the air and the "hidden" areas, for example the lower side of the excitation, are poorly ventilated and lead to much higher temperatures.

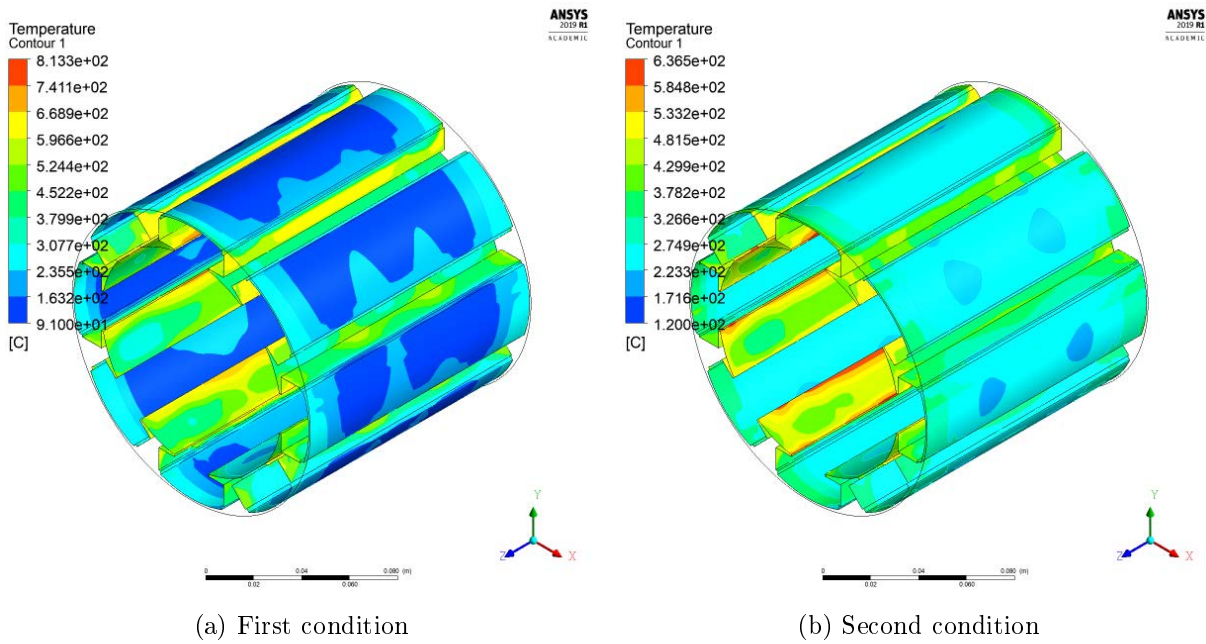


Figure 5.45: WRSM rotor surface temperature distribution

In figure 5.46 a vector plot of speed is shown, again it confirms that the boundary conditions are set correctly.

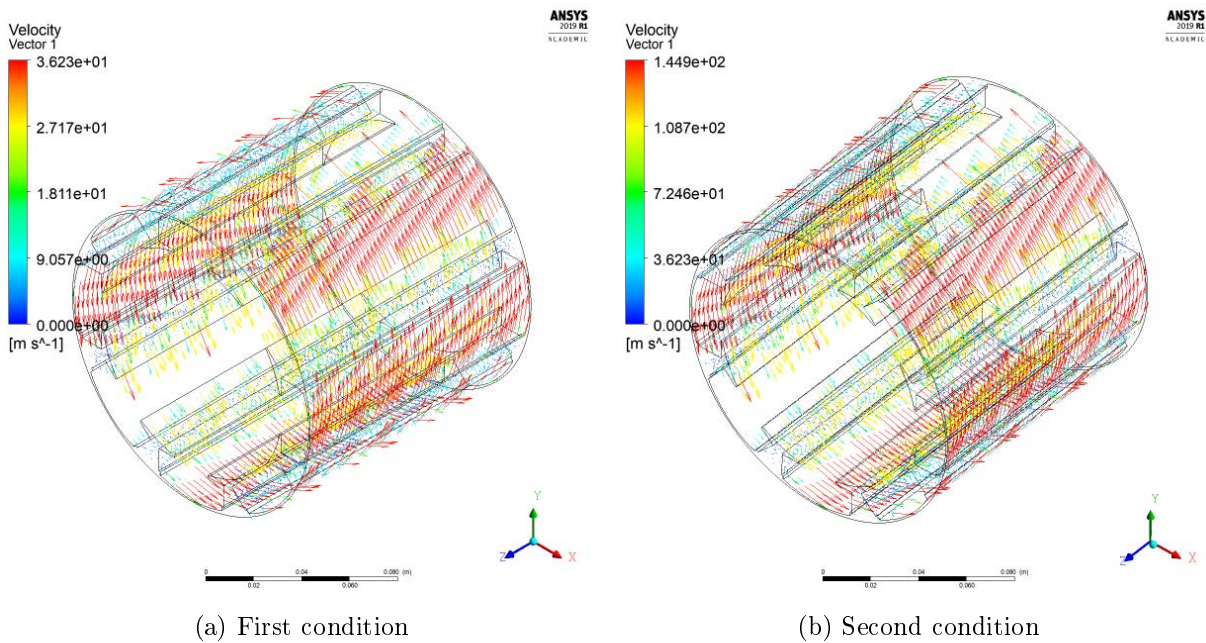


Figure 5.46: Velocity arrow plot

In figure 5.47 the air temperature of the air gap is shown.

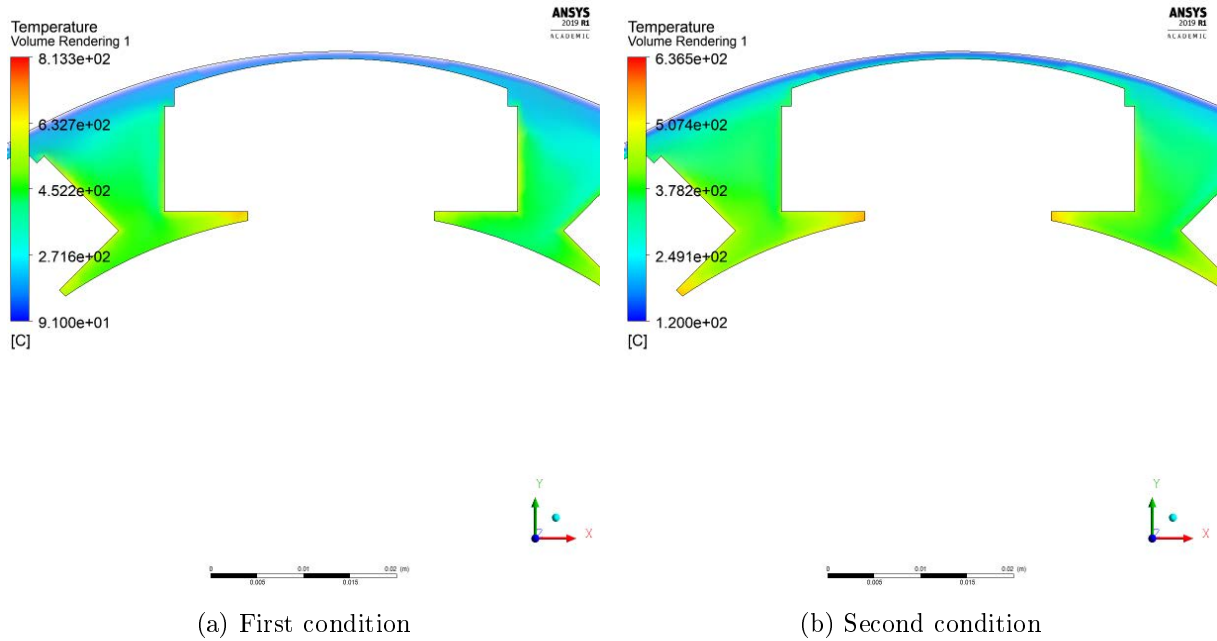


Figure 5.47: Air gap temperature

Table 5.14 summarizes the average parameters obtained from the simulations.

	First condition	Second condition	Mesure unit
Excitation surface mean temperature	515	386.28	$^{\circ}C$
Rotor surface mean temperature	288	324	$^{\circ}C$
Air mean temperature	301.8	286.7	$^{\circ}C$
Convection coefficient	142	393	$\frac{W}{m^2 \cdot K}$

Table 5.14: Thermal analysis results

Given the results obtained, it is necessary to adopt a specific cooling system for the rotor since the stator jacket alone is not sufficient. A first solution could be the adoption of a longitudinal axis fan, however the temperatures involved are much higher than the limit ones and it is therefore more appropriate to opt for a liquid cooling system. Furthermore, the presence of a longitudinal air flow risks further worsening the windage losses.

Liquid cooling

It is decided to use the technology already mounted in the Tesla model S electric motor [15]. A hollow shaft into which water is pumped to cool the rotor. In figure 5.48 the front and longitudinal views are shown respectively while in figure 5.49 the longitudinal view of the system complete with pump and liquid collection tank is shown.

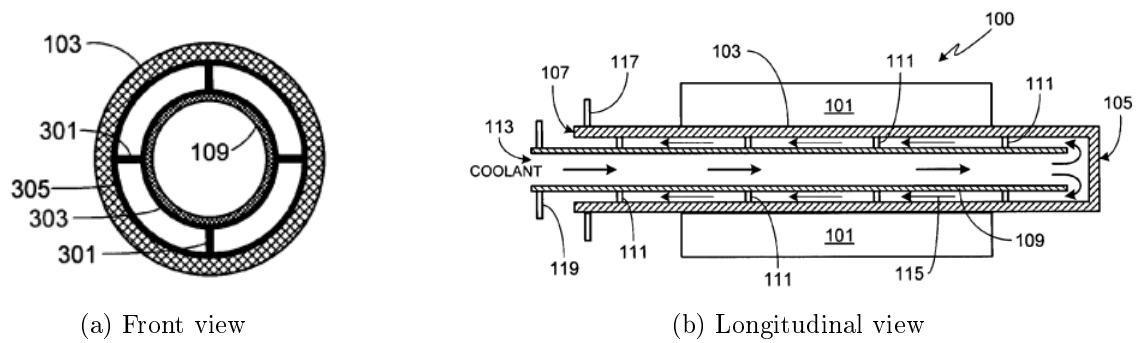


Figure 5.48: Hollow shaft for rotor cooling

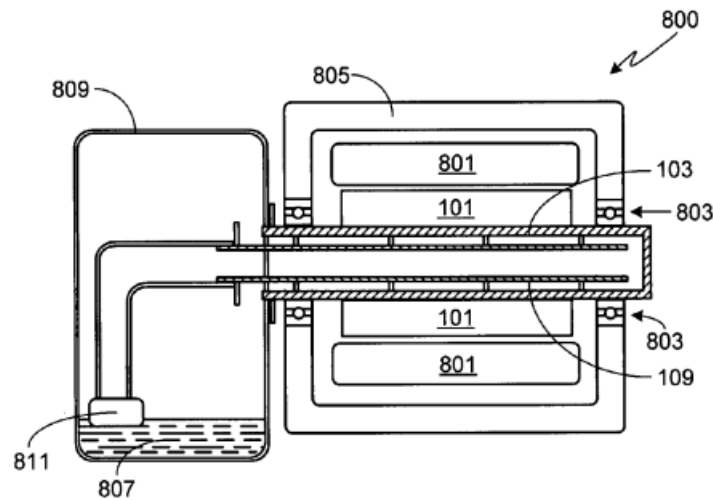


Figure 5.49: Complete cooling system

For the simulation it is assumed that all rotor losses are removed by the water circulating in the hollow shaft and therefore the system is studied by imposing the total heat flux to be removed on the shaft surface. The data used in the simulation are shown in table 5.15. Again the two conditions of section 5.2.4 are considered.

	First condition	Second condition	Mesure unit
Excitation losses	0.6	0.6	kW
Windage losses	0.0356	1.88	kW
Shaft surface	0.0267	0.0267	m^2
Heat flux	23.8	92.88	$\frac{kW}{m^2}$
Inlet mass flow	0.7	0.7	$\frac{kg}{s}$
Inlet temperature	40	40	$^{\circ}C$

Table 5.15: Simulation data

Numerical model The analysis of the cooling system is performed in Ansys fluent by building the gemetry showed in figure 5.50.

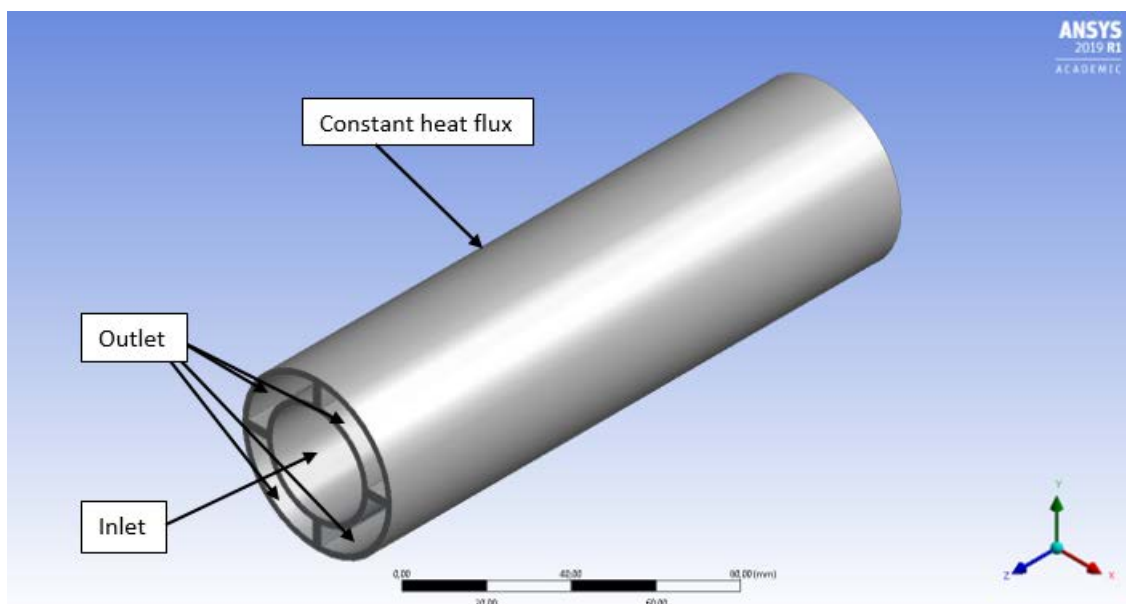


Figure 5.50: Geometry built in DesignModeler

The main geometric dimensions of the cooling system are listed in table 5.16

Shaft outer diameter	50	mm
Shaft inner diameter	30	mm
Tube thickness	2	mm
Frames thickness	1.5	mm
Inlet surface	705	mm^2
Outlet surface	682	mm^2

Table 5.16: Rotor cooling system main dimensions

The fluid dynamic model set is the same used in section 5.2.2. Figure 5.51 shows the temperature distribution on the shaft surface. A very uneven distribution can be noted due to fluid velocity changes. Velocity streamlines are also shown in figure 5.52. It is noted that the slowing of the fluid at the end of the shaft and the reversal of direction are the cause of the hot spots found in figure 5.51.

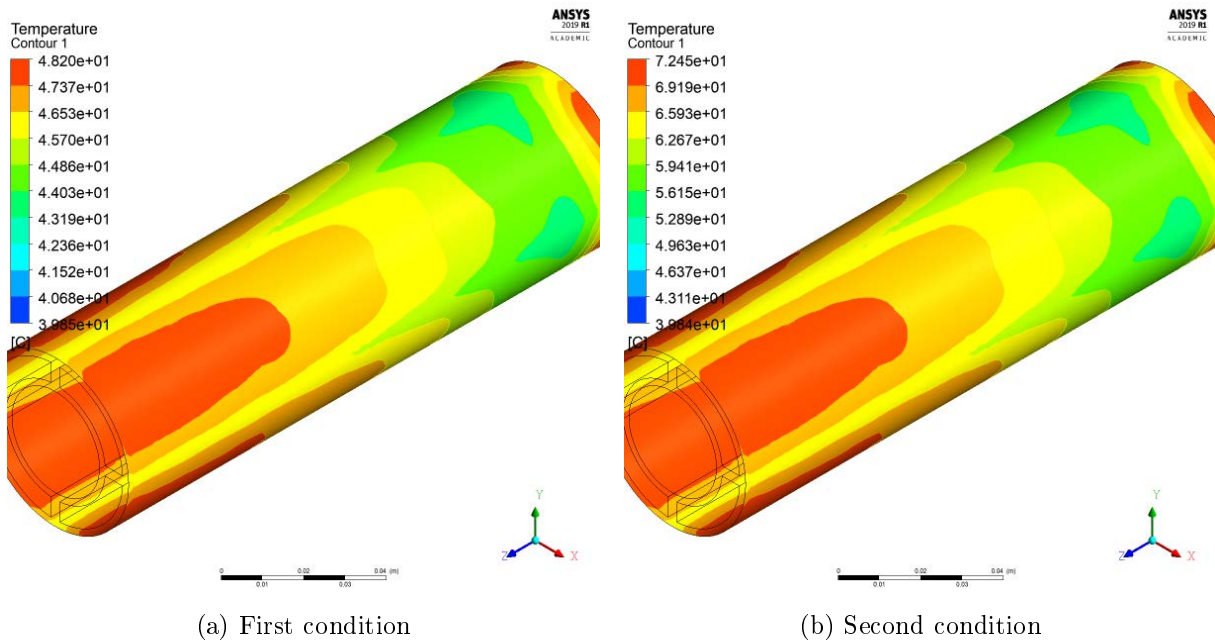


Figure 5.51: Shaft surface temperature distribution

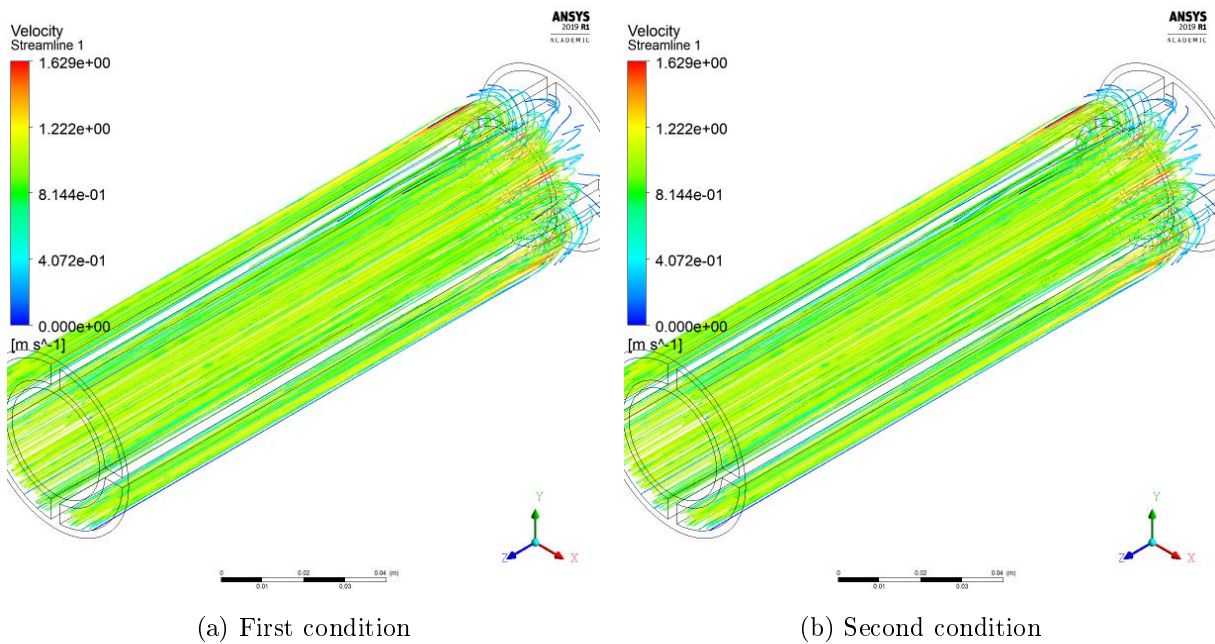


Figure 5.52: Velocity streamlines

Other important results of thermal analysis are reported in table 5.17.

	First condition	Second condition	Mesure unit
Outlet temperature	40.22	40.87	°C
Shaft surface mean temperature	46.3	64.4	°C
Convection coefficient	3870	3870	$\frac{W}{m^2 \cdot K}$
Pressure drop	857	857	$\frac{kW}{m^2}$

Table 5.17: Thermal analysis results

Analytical model The analytical model chosen to represent the cooling system is the so-called "Concentric Tube Annulus" [12]. It consists in two concentric tubes in which the fluid flows in the space between them. see figure 5.53.

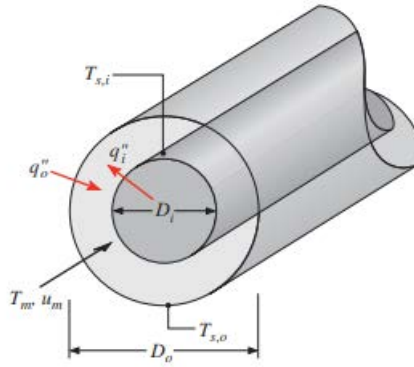


Figure 5.53: Analytical model

The hydraulic diameter is defined by the following relationship [12]

$$D_{hyd} = \frac{4 \cdot \left(\frac{\pi}{4}\right) \cdot (D_{outer}^2 - D_{inner}^2)}{\pi \cdot D_{outer} + \pi \cdot D_{inner}} = D_{outer} - D_{inner} = 20 \text{ mm} \quad (5.46)$$

Reynolds number and Prandtl number are computed using equation 5.4 and 5.6 while Nusselt number is calculated using equation 5.7. The heat transfer convection coefficient can then be calculated as

$$h = \frac{Nu \cdot k}{D_{hyd}} = 4230 \frac{W}{m^2 \cdot K} \quad (5.47)$$

The removed heat flux can then be computed using

$$q = h \cdot (T_s - T_{fluid}) \quad (5.48)$$

Figure 5.54 shows the trend of the heat flux removed as a function of the shaft surface temperature. The heat fluxes removed for the two temperatures obtained in Ansys are also indicated.

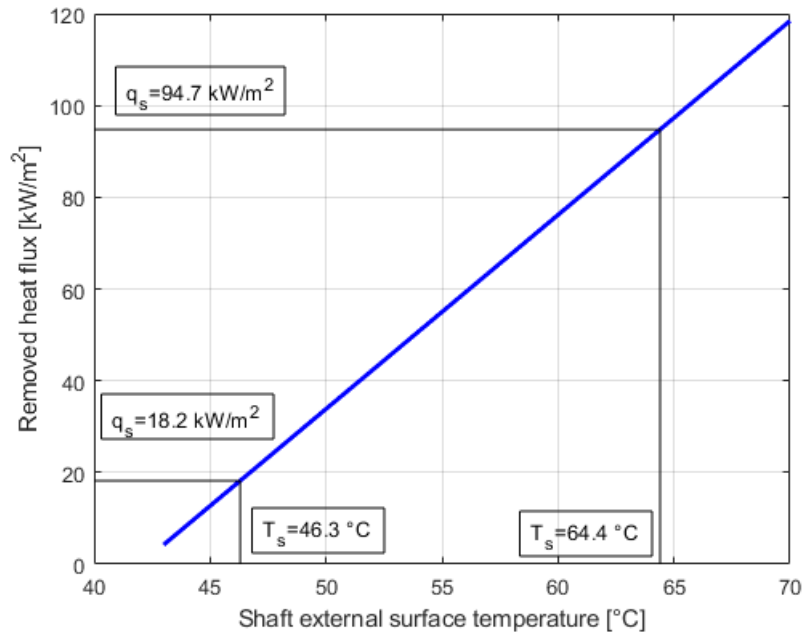


Figure 5.54: Heat flux removed versus shaft surface temperature

Comparison Table 5.18 shows the main results obtained with the two methods described above, the second condition is taken as reference. There is a good agreement between the two methods even if the analytical approach tends to overestimate the cooling capacity of the system as it is not exactly representative of the real model.

	Numerical method	Analytical method	Mesure unit
Water mass flow	0.7	0.7	$\frac{kg}{s}$
Shaft external surface temperature	64.4	64.4	$^{\circ}C$
Convection coefficient	3870	4230	$\frac{W}{m^2 \cdot K}$
Heat flux removed	92.88	94.7	$\frac{kW}{m^2}$

Table 5.18: Comparison between numerical and analytical model

Temperature inside the rotor

To study the temperature distribution inside the rotor, FEMM software is used again. Only the rotor is modeled in order to save computing resources. Figure 5.55 shows the model built in FEMM and the boundary conditions imposed.

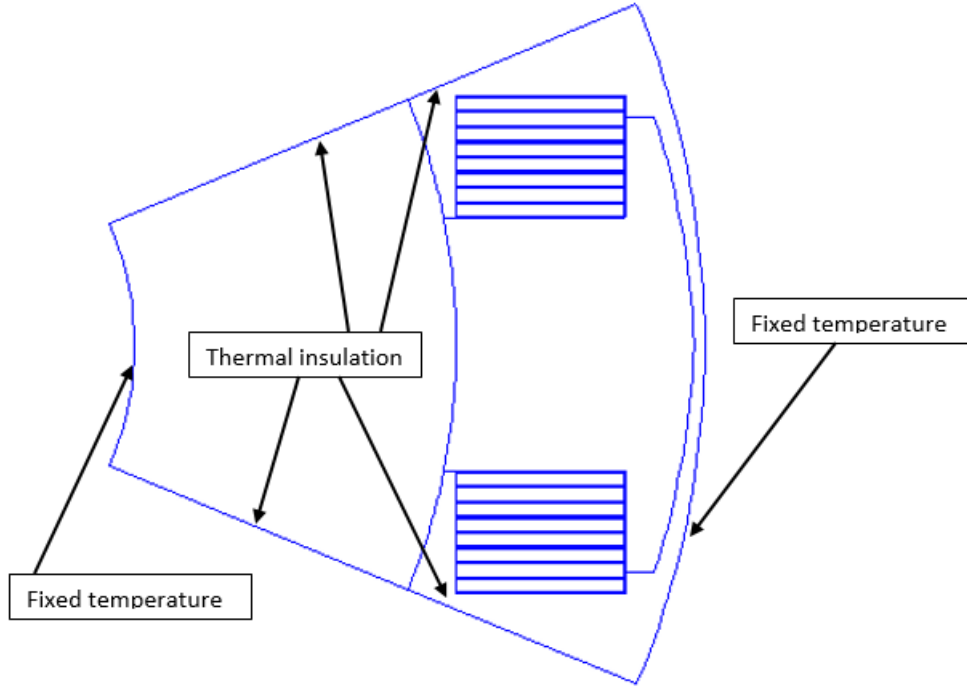


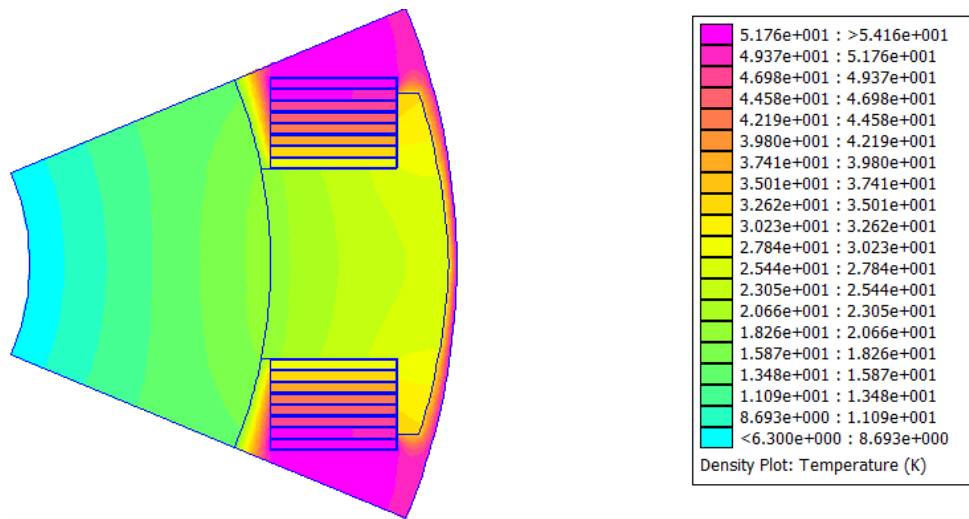
Figure 5.55: Geometry simulated in FEMM and boundary conditions

The properties of materials and the heat sources imposed are shown in table 5.19.

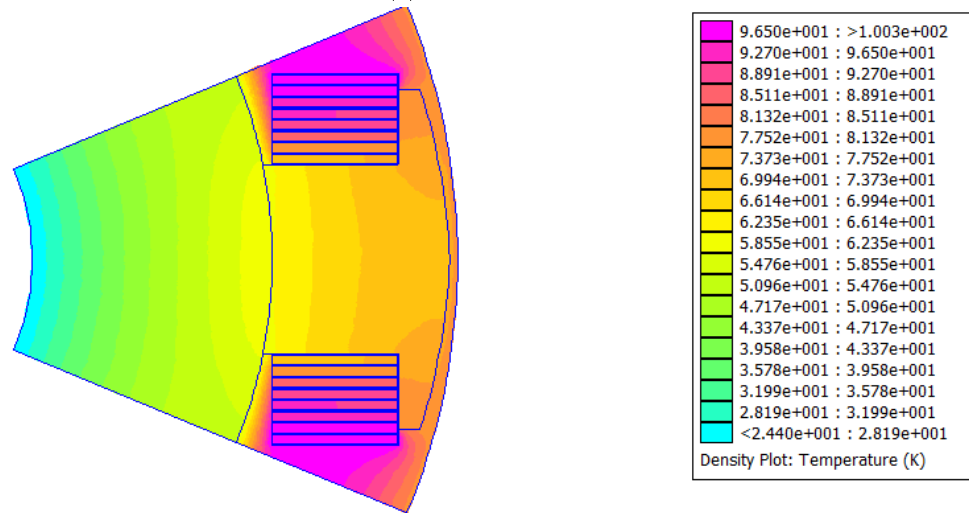
	First condition	Second condition	Mesure unit
Copper thermal conductivity	355	355	$\frac{W}{m \cdot K}$
Rotor thermal conductivity	45	45	$\frac{W}{m \cdot K}$
Excitation losses	2.7	2.7	$\frac{MW}{m^3}$
Windage losses	0.0028	1.5	$\frac{MW}{m^3}$
Stator temperature	91	120	$^{\circ}C$
Shaft temperature	46.3	64.4	$^{\circ}C$

Table 5.19: Material properties and heat sources

By solving the problem for the two configurations considered, the temperature distribution indicated in figure 5.56 is obtained. The simulation results are shown in figure 5.43, temperatures are reported considering the inlet temperature of the cooling water as reference (40 $^{\circ}C$). It is noted that the maximum temperature is reached inside the copper winding and that it is widely within the chosen insulation class and therefore the cooling system is adequate.



(a) First condition



(b) Second condition

Figure 5.56: Rotor temperature distribution

Chapter 6

Conclusion

From the analyzes carried out, it emerged that the WRSM is very promising for automotive applications. In fact, it has a good torque at low speeds and an excellent flux weakening characteristic for high speeds. It also has greater freedom of control, and it is always possible to reach an infinite theoretical speed, regardless of the current limit. The $\cos\phi=1$ control strategy also proved to be very valid so as to make the WRSM better than the IPM motor in terms of performance. However, there are some problems that make WRSM globally inferior to the IPM motor. First of all, efficiency is decidedly lower in all operating points, especially if we consider the overall efficiency, including also the rotating transformer or the brush-slip ring system. Furthermore, the WRSM requires a dedicated cooling system for the rotor which is not required in the IPM motor. It should be noted, however, that this is due to the high excitation current required to obtain very high performances, in the case of applications with more modest power this would not be necessary making the WRSM more competitive. Finally, it is necessary to consider the economic aspect linked to the construction of the two motors. As already noted in the introductory chapter, rare earth permanent magnets can determine up to 40 % of the final cost of a motor and therefore in a model that does not require their presence, costs are considerably reduced (see Chapter 3). It is therefore understood that WRSM is very promising in applications with reduced power, such as small cars or light vehicles, in which low cost and high freedom of control are aspects of primary importance.

Bibliography

- [1] Mat Suli, Liyananadirah and Ibrahim, Wan and Abdul Aziz, Badhrulhisham and Deraman, Mohd Rizauddin and Ismail, Nurul, *A Review of Rare Earth Mineral Processing Technology*, Chemical Engineering Research Bulletin, Vol. 19, 2017
- [2] Rukmi Dutta, Lester Chong, and Fazlur M. Rahman, *ANALYSIS AND EXPERIMENTAL VERIFICATION OF LOSSES IN A CONCENTRATED WOUND INTERIOR PERMANENT MAGNET MACHINE*, Progress In Electromagnetics Research B, Vol. 48, 221–248, 2013.
- [3] Juha Saari, *Friction losses and heat transfer in high-speed electrical machines*, Otaniemi 1996/150.
- [4] Guillaume Burnand, Douglas Martins Araujo, Christian Koechli and Yves Perriard, *Validation by Measurements of a Windage Losses Model for Very-High-Speed Machines* Integrated Actuators Laboratory (LAI), École Polytechnique Fédérale de Lausanne (EPFL), Switzerland, IEEE 2017.
- [5] Frank M. White, *Fluid Mechanics*, McGraw-Hill 2001.
- [6] Co Huynh, Liping Zheng, Dipjyoti Acharya, *Losses in High Speed Permanent Magnet Machines Used in Microturbine Applications*, Journal of Engineering for Gas Turbines and Power, 2009.
- [7] ISO 15
- [8] [https://www.bocabearings.com/products/bearing-and-ball-types/electric-motor-quality-\(emq\)-bearings?ProductType=0](https://www.bocabearings.com/products/bearing-and-ball-types/electric-motor-quality-(emq)-bearings?ProductType=0)
- [9] <https://koyo.jtekt.co.jp/en/support/bearing-knowledge>
- [10] [https://en.wikipedia.org/wiki/Bearing-\(mechanical\)](https://en.wikipedia.org/wiki/Bearing-(mechanical))
- [11] R. Pechánek, L. Bouzek, *Analyzing of Two Types Water Cooling Electric Motors Using Computational Fluid Dynamics*, 15th International Power Electronics and Motion Control Conference, EPE-PEMC 2012 ECCE Europe, Novi Sad, Serbia.
- [12] Theodore L. Bergman, Adrienne S. Lavine, David P. DeWitt, Frank P. Incropera, *Introduction to Heat Transfer*, Sixth Edition-John Wiley and Sons, Inc. (2011).
- [13] Mircea Popescu, David Alan Staton, Aldo Boglietti, Andrea Cavagnino, Douglas Hawkins, James Goss, *Modern Heat Extraction Systems for Power Traction Machines—A Review*, IEEE TRANSACTIONS ON INDUSTRY APPLICATIONS, VOL. 52, NO. 3, MAY/JUNE 2016.
- [14] ANSYS FLUENT 12.0 User's Guide,
https://www.afs.enea.it/project/neptunius/docs/fluent/html/ug/main_pre.htm.

- [15] P. Zhou, El Cerrito, N. R. Kalayjian, S. Carlos, G. D. Cutler, P Koch, Tesla Motors, Inc., San Carlos, CA (US) *LIQUID COOLED ROTOR ASSEMBLY*, US1350954, United States Patent Office, 10 Feb 2009
- [16] Mattia Tosi, *Rotary Transformer Design for Brushless Electrically Excited Synchronous Machines*, 2013-2014.
- [17] Tsarafidy Raminosoa, Randy Wiles, *Contactless Rotor Excitation for Traction Motors*,
- [18] Hongfei Lu, Martin Doppelbauer, *Electrically Excited Synchronous Machine with Additional Permanent Magnets for Traction Application*, 2019 22nd International Conference on Electrical Machines and Systems (ICEMS)
- [19] Samuel Estenlund, Mats Alakula, Avo Reinap, *PM-less machine topologies for EV traction: A literature review*, 2016 IEEE.
- [20] <http://www.die.ing.unibo.it/pers/cristofo/didattica/dispense/13sinc.pdf>
- [21] Winzer, Dipl-Ing Patrick, *Steigerung von Drehmoment und Wirkungsgrad bei Synchronmaschinen durch Nutzung der magnetischen Asymmetrie*.
- [22] N. Bianchi, S. Bolognani, *Metodologie di Progettazione delle Macchine Elettriche*, CLEUP, gennaio 2001.
- [23] N. Bianchi, *Calcolo delle Macchine Elettriche col Metodo degli Elementi Finiti*, CLEUP, gennaio 2001.
- [24] D. Meeker, *Finite Element Method Magnetics: OctaveFEMM User's Manual* 2018.
- [25] N. Bianchi, M. Barcaro, Silverio Bolognani, *Electromagnetic and Thermal Analysis of Permanent Magnet Synchronous Machines, Finite Element Analysis - From Biomedical Applications to Industrial Developments*, Dr. David Moratal (Ed.), ISBN: 978-953-51-0474-2, InTech, Available from: <http://www.intechopen.com/books/finite-element-analysis-from-biomedical-applications-to-industrialdevelopments/electromagnetic-and-thermal-analysis-of-permanent-magnet-machines>.
- [26] N. Bianchi, E. Fornasiero, *Impact of MMF Space Harmonic on Rotor Losses in Fractional-Slot Permanent-Magnet Machines*, IEEE TRANSACTIONS ON ENERGY CONVERSION, VOL. 24, NO. 2, JUNE 2009
- [27] S. J. Galioto, P. B. Reddy, M. EL-Refaie, J. Alexander, *Effect of Magnet Types on Performance of High-Speed Spoke Interior-Permanent-Magnet Machines Designed for Traction Applications*, IEEE TRANSACTIONS ON INDUSTRY APPLICATIONS, VOL. 51, NO. 3, MAY/JUNE 2015.
- [28] <https://www.statista.com/statistics/450164/global-reo-dysprosium-oxide-price-forecast/>
- [29] [https://en.wikipedia.org/wiki/Ferrite-\(magnet\)](https://en.wikipedia.org/wiki/Ferrite-(magnet))
- [30] A. El-Refaie, T. Raminosoa, P. Reddy, S. Galioto, D. Pan, K. Grace, J. Alexander and Kum-Kang Huh, *Comparison of Traction Motors that Reduce or Eliminate Rare-Earth Materials*, 978-1-5090-0737-0/16/31.00 ©2016 IEEE.
- [31] S. Bolognani, *Appunti di Azionamenti elettrici*, 2018

- [32] Y. Wang, N. Bianchi, *Comparison of Synchronous Reluctance and IPM Motors for EV Applications Including Design Approach*
- [33] I. Boldea, N. Tutelea, L. Parsa, D. Dorrell, *Automotive Electric Propulsion Systems With Reduced or No Permanent Magnets: An Overview*, IEEE TRANSACTIONS ON INDUSTRIAL ELECTRONICS, VOL. 61, NO. 10, OCTOBER 2014
- [34] K. Sawa, Y. Watanabe, T. Ueno, M. Masubuchi, *A Supplement to Deterioration Process of AgPd Brush and Au-plated Slip-ring System with Lubricant*, 2019 IEEE Holm Conference on Electrical Contacts.
- [35] C. Holzapfel, P. Heinbuch, S. Holl, *Sliding electrical contacts: Wear and electrical performance of noble metal contacts*, 2010 Proceedings of the 56th IEEE Holm Conference on Electrical Contacts
- [36] D. Kuhlmann-Wilsdorf, D.D. Makel, N.A. Sondergaard, D. Maribo, *On the Two Modes of Operation of Monolithic Ag-C Brushes*, Electrical Contacts, 1988, Proceedings of the Thirty Fourth Meeting of the IEEE Holm Conference on Electrical Contacts
- [37] <https://muniracademy.com/synchronous-generator/>
- [38] <https://www.pecso.it/quotazioni-rame/>
- [39] <https://www.pricepedia.it/it/magazine/article/2018/05/08/il-prezzo-del-lamierino-magnetico-vicino-ai-livelli-record-del-2011/>
- [40] <https://www.magnetapplications.com/content/upload/files/Presentation%20-%20Magnetics%202018.pdf>
- [41] [http://faet.net/_/Materiali – per – avvolgimenti – ULCarte – IsolantiMYLAR – Dupont/Prodotti/003/010/020/](http://faet.net/_/Materiali%20-%20per%20-%20avvolgimenti%20-%20ULCarte%20-%20IsolantiMYLAR%20-%20Dupont/Prodotti/003/010/020/)